Electromagnetic radiation as a tool to determine actual crustal stresses – applications and limitations

Dissertation

zur Erlangung des Doktorgrades

der Mathematisch-Naturwissenschaftlichen Fakultäten

der Georg-August-Universität zu Göttingen

vorgelegt von

Michael Krumbholz

aus Quedlinburg

Göttingen, Januar 2010

D7

Referentin: Prof. Dr. Sharon Webb

Geowissenschaftliches Zentrum der Georg-August-Universität Göttingen

Korreferent: Dr. Axel Vollbrecht

Geowissenschaftliches Zentrum der Georg-August-Universität Göttingen

Tag der mündlichen Prüfung: 22.01.2010

„Jede Wahrheit setzt sich in drei Stufen durch:

Zunächst wird sie belächelt,

dann wird sie bekämpft,

schließlich ist sie selbstverständlich".

Arthur Schopenhauer, German philosopher (1788 – 1860)

Abstract

In the last decades natural Electro Magnetic Radiation (EMR) has gained increasing attention in the fields of material sciences and geosciences. Since EMR precedes material failure, it is used in geosciences as a tool to forecast earthquakes, determine crustal stress directions, and to detect faults. The source mechanisms of natural EMR are diverse and still incompletely understood. Laboratory studies have proved that one mechanism is related to the process of micro-cracking. Crack-related emissions have directional properties: their maximum intensities are parallel to the direction of micro-crack growth. Since micro-crack orientation is controlled by the surrounding stress field, a measurement of the directional properties of the associated EMR in the field offers the opportunity to determine the main horizontal stress direction, σ_H. The Cerescope is a mobile device to measure such intensities, and thus directional properties, of natural EMR in the field. However, this technique is so far only accepted by a small circle of scientists.

The aim of this thesis was therefore to make further tests on the applicability of the EMR method in the field. For this purpose, three case studies were conducted in different geological settings.

The first case study was located in southeast Sweden (**Chapter 3**) to test the EMR method as a tool to determine the orientation of the main horizontal normal stress (σ_H) by measuring the main EMR direction. In addition, the orientation of brittle structures from kilometre down to sub-millimetre scale were analysed to identify those brittle structures that contribute to the emission of EMR relevant in the field. The results of this multi-scale analysis indicate that with decreasing size of the structures, their strike coincides increasingly better with the measured main EMR directions. This supports the results of laboratory studies which suggest that micro-crack formation is associated with EMR. In this case, intraganular cracks, as well as cracking along grain- and phase-boundaries seem to be responsible for the measured EMR. Furthermore, the main EMR directions and the orientation of micro-structures are in good accordance with the in situ σ_H–directions derived from conventional methods. Therefore, this case study strongly supports the applicability of the EMR method.

The second case study (**Chapter 4**) analyses the possibility to detect faults and fault zones with the EMR method. For this purpose, several fault zones, with known extent, were selected in southeast Sweden and central Germany, where EMR intensities were measured along profiles crossing these faults. In addition, the EMR data was coupled with exact geographic coordinates to improve the spatial resolution and the processability of the data. Furthermore, the EMR results for one fault were compared with the results of a conventional method, i.e., the measurement of radon emission. Both methods succeed in locating the fault; however, the EMR measurements are more accurate and were obtained with less effort. This confirms that the EMR method is a useful and reliable tool to detect fault zones. In addition, information about the width and dip of fault zones can be derived.

The third case study (**Chapter 5**) focuses on an analysis of the spatial resolution of the EMR method and of the temporary behaviour of EMR properties. For this, an area of $280.000 \ km^2$ was covered with 52 measurements of the main EMR direction. The obtained data were in

some parts not consistent with stress data as displayed in the World Stress Map. Instead, the main EMR directions form a circular segment with a common focus at the location of a military VLF transmitter. Long-term monitoring of the temporary behaviour of the EMR directions and intensities show irregularities that coincide with the broadcasting times of the VLF transmitter. Furthermore, signal intensities can be correlated to the distance to the transmitter. This causes serious concern about the actual development state of the EMR method. Consequently, results of previous studies based on this method need to be re-evaluated.

In summary, even if the first two case studies gave promising results, the third case study shows that the method in its actual state of development needs to be improved before it can be used for a reliable determination of crustal stresses at the surface. Moreover the successful detection of faults using the EMR method can probably be explained by the well-established VLF method. Since the basic approach of the EMR method is principally correct and promising, in the future the measurement setup has to be improved to overcome the identified technical problems in relation to artificial disturbances.

Zusammenfassung

In den letzten Jahrzehnten fand die Entstehung natürlicher Elektro-Magnetischer Strahlung/Radiation (EMR) immer mehr Beachtung, bevorzugt auf den Gebieten der Materialwissenschaften und der Geowissenschaften. EMR geht mit Materialversagen einher, und wird daher als Möglichkeit zur Erdbebenvorhersage untersucht aber auch zum Detektieren von Störungen und, in jüngerer Zeit, zur Bestimmung von in situ-Hauptspannungsrichtungen. Der Entstehungsmechanismus dieser natürlichen EMR wird noch nicht vollständig verstanden, aber Laborstudien konnten nachweisen, dass der Mechanismus mit der Bildung von Mikrorissen einhergeht. Diese durch Risse hervorgerufene EMR besitzt richtungsabhängige Eigenschaften, und ihre maximale Intensität ist parallel zum verursachenden Mikrorissausbreitung. Da die Mikrorissausbreitungsrichtung durch das umgebende Spannungsfeld diktiert wird, ermöglicht eine Messung der Richtungseigenschaften der rissinduzierten EMR die Bestimmung der Hauptspannungsrichtungen. Das Cereskop ist ein tragbares Messgerät, mit dem derartige Messungen im Gelände vorgenommen werden können. Allerdings wird diese neue Technik bisher nur von einer kleinen Gruppe von Wissenschaftlern eingesetzt.

Ziel dieser Arbeit ist es daher, die Anwendbarkeit der EMR-Methode durch weitere Geländeuntersuchungen zu prüfen. Für diesen Zweck wurden drei Geländestudien in verschiedenen geologischen Regimen durchgeführt.

In der ersten Studie (**Kapitel 3**) wurde die Möglichkeit der Bestimmung der größten horizontalen Normalspannung (σ_H) mit der EMR-Methode überprüft. Zusätzlich wurde eine Richtungsanalyse bruchafter Strukturen in den Größenordnungen vom Kilometer- bis hinunter in den Submillimeterbereich durchgeführt, um jene Sprödstrukturen zu identifizieren, welche Beiträge zur im Gelände gemessenen EMR liefern könnten. Die Ergebnisse zeigen, dass mit abnehmender Größe der Sprödstrukturen, sich ihre Orientierung der Hauptrichtung der EMR immer stärker angleicht. Das stützt Erkenntnisse aus Laboruntersuchungen, die Mikrorisse als EMR-Emittenten identifizieren konnten. Des Weiteren zeigen die Ergebnisse, dass sowohl die Neubildung von intragranularen Mikrorissen als auch Rissausbreitungen an Korn- und Phasengrenzen als Ursache für die gemessene EMR in Frage kommen. Weiterhin stimmen sowohl die bestimmten EMR-Hauptrichtungen als auch die Orientierung der Mikrostrukturen mit in situ σ_H-Richtungen überein, die hier mit anerkannten (konventionellen) Methoden bestimmt wurden. Diese Studie stützt somit die Anwendbarkeit der EMR-Methode zur Bestimmung von σ_H.

Die zweite Fallstudie (**Kapitel 4**) untersuchte die Möglichkeit, Störungen bzw. Störungszonen mit Hilfe der EMR-Methode zu detektieren. Hierzu wurde in Südostschweden und Mitteldeutschland eine Reihe von Störungen mit bekanntem Verlauf ausgewählt, über die auf Querprofil-Linien EMR-Messungen durchgeführt wurden. Zur Verbesserung der räumlichen Auflösung und Auswertbarkeit der Daten wurden die Cereskopdaten mit genauen geographischen Koordinaten verbunden. Des Weiteren wurden die EMR-Daten für eine ausgewählte Störung mit denen Ergebnissen einer etablierten Methode zur Störungsdetektion verglichen. Bei letzterer handelt es sich um die Messung erhöhter Radonentgasung über Störungen. Es war möglich, die Störung mit beiden Methoden zu lokalisierten, wobei sich

zeigte, dass mit der EMR-Methode wesentlich genauere Ergebnisse mit geringerem Aufwand zu erzielen sind. Im Allgemeinen ist die EMR-Methode somit eine nützliche und zuverlässige Methode, um Störungszonen zu lokalisieren. Zusätzlich liefern EMR-Daten Informationen zur Breite und zum Einfallen von Störungszonen.

Die dritte Fallstudie (**Kapitel 5**) beschäftigte sich mit der räumlichen Auflösung und zeitlichen Veränderungen von EMR-Merkmalen. Hierzu wurde auf einer Gesamtfläche von 280 000 km^2 an 52 Standorten die EMR-Hauptrichtung bestimmt. Die daraus abgeleiteten σ_H-Richtungen weichen z.T. deutlich von den in der World Stress Map abgebildeten Richtungen ab. Die gemessenen EMR-Hauptrichtungen bilden überwiegend ein konzentrisches Muster, deren gemeinsamer Mittelpunkt mit der Lage eines militärischen VLF-Senders übereinstimmt. Zudem gibt es eine deutliche Korrelation zwischen gemessenen EMR-Intensitäten und dem Abstand zu diesem Sender. Diese Ergebnisse machen die Anwendbarkeit der EMR-Methode fragwürdig, wenn künstliche Störfaktoren nicht in Erwägung gezogen werden. Ergebnisse früherer Studien, deren Daten auf dieser Methode basieren, müssen daher teilweise überdacht werden.

Zusammenfassend kann gesagt werden, dass trotz der vielversprechenden Ergebnisse der ersten beiden Fallstudien die dritte Studie beweist, dass die EMR-Methode in ihrem momentanen Entwicklungsstand für die Bestimmung von Hauptspannungsrichtungen nicht geeignet zu sein scheint. Im Falle der zweiten Fallstudie kann die erfolgreiche Lokalisierung von Störungszonen auf die bereits bekannte VLF-Methode zurückgeführt werden. Da der generelle Ansatz der EMR-Methode jedoch prinzipiell richtig und vielversprechend ist, muss in Zukunft das Messverfahren überarbeitet werden, um die aufgezeigten technischen Schwierigkeiten überwinden zu können.

Table of contents

1. Introduction

The Electro-Magnetic Radiation (EMR) method is a tool that provides the opportunity to investigate geological structures and related stress configurations in a fast and low-cost way. The method is based on the property of brittle materials to emit electromagnetic waves when subject to mechanical stresses. This phenomenon has been known for some time, but for decades only little effort has been used to analyse the micro-mechanical background and to test its applicability in the field of structural geology. Hence, most investigations have focussed on the processes that generate the EMR in laboratory experiments. Today, amongst a number of possible processes, micro-crack-related charge transfer is assumed to be the main source of the EMR (see Chapter 2.3).

Application of the EMR method was first carried out in Russia and Japan with the aim to forecast earthquakes and volcanic eruptions, and for the (structural) exploration of mineral deposits (see Chapter 2.1). For the former, several stationary observation centres were established to monitor volcanoes and earthquake risk zones all over the planet. More recently, this method has also been applied in underground mining to monitor rockfalls.

For this thesis, the measurement of EMR was conducted using the Cerescope, a portable measuring device. The Cerescope allows the detection of faults and the main horizontal radiation directions that correlate with the orientation of growing micro-cracks and, in this context, with the main horizontal stress direction and loci of stress concentrations. The applicability of this technique to determine the main horizontal stress direction and to detect faults and landslides has been demonstrated during several studies in Chile (Reuther and Moser, 2009), Sicily (Reuther et al., 2002), Germany (Lauterbach, 2005; Lichtenberger, 2005, 2006a, b), and India (Mallik et al., 2008). In addition, Lichtenberger (2005, 2006b) calculated stress magnitudes in tunnels.

However, in spite of these first promising results, the method is still only accepted by a small circle of scientists. One reason for this might be the gap between the results of laboratory studies and field applications. Previous studies only applied the EMR method locally and over short periods of time (days), so that the number of data obtained with this method is still too limited to allow an objective judgement on its applicability. There is also only one study that successfully compared stress determinations obtained with the EMR method with those from established techniques (Reuther et al., 2002). Furthermore, the procedure of data acquisition and interpretation used by different authors is inconsistent and thus, in some cases, questionable.

1.1 Motivation and aims

The main motivation for this study was a comprehensive evaluation of the background, applicability, and possibilities of the EMR method. This was achieved by applying the EMR method over a larger area, for longer periods of time, and in different types of geological settings. The following issues were addressed:

(1) The results of the measurements of main EMR directions have to be interpreted in a consistent and reasonable way to accurately determine the main stress direction.

(2) The graphic evaluation and spatial resolution of the method have to be enhanced to achieve more accurate measurements of faults.

(3) The structures that emit the EMR, as measured in the field, have to be identified to close the gap between the results of laboratory studies and field measurements of EMR.

(4) Stress determinations obtained with the EMR method have to be carried out in an area where the stress field is well known from conventional stress measurement techniques. The results from both approaches have to be compared.

(5) The EMR method has to be applied in areas with known locations of faults to evaluate the practicability of fault detection with this method. In addition, the results have to be compared with established methods, such as radon emission.

(6) Spatial variations of the main EMR direction have to be identified by a regional study to identify the scale on which variations occur and if there are any changes in the vicinity of faults.

(7) The possibility of temporal variations of the main EMR direction has to be surveyed. Since previous measurements cover daily fluctuations (Lauterbach, 2005; Lichtenberger, 2005) but fail to explain the reasons, the main EMR directions should be monitored over a longer time scale to detect possible long-term changes.

1.2 Overview of the chapters

In order to assess the above mentioned aims, different case studies were conducted as part of this study. In general, the measuring process using the Cerescope with regards to data acquisition and interpretation was studied and could be enhanced in places. Section 2.4.2 introduces some of the improvements concerning the interpretation of measured main EMR directions and in the spatial resolution and graphic evaluation of data.

Chapter 3 describes the results of a field study in the Västervik area in southeast Sweden, which determined the main EMR directions over a large region, and a multi-scale analysis of brittle fractures (from map- to micro-scale) to identify the scale of fractures that may

contribute to the emission of EMR. Furthermore, this area offers a capacious dataset of main horizontal stress directions obtained from conventional methods, which can be compared with those obtained with the EMR method.

In Chapter 4, exemplary studies of faults using the EMR method are presented. These studies demonstrate the applicability of the method to identify the location and attitude of faults. Furthermore, the EMR-based detection of a fault is related to measurements of radon emissions associated with faulting. The EMR measurements in this chapter make use of the enhanced technique to couple the Cerescope with a GPS device to link the recorded EMR with exact geographic coordinates during continuous runs (see Section 2.4.2.4). Therefore, it is not only possible to identify faults or locations of stress concentration, but also their attitude.

Chapter 5 presents the results of a regional study of the spatial variation of the main EMR direction between central Germany and southern Sweden. The results are compared with the orientation of the main horizontal stress σ_H, as displayed on the World Stress Map (Heidbach et al., 2008). Furthermore, the temporal variations of EMR main directions were monitored over the last two years. The results of both spatial and temporal variations cast serious doubt on the EMR method in its current application, as well as on the results of previous studies.

2. Methodology

2.1 EMR method history

Effects associated with the occurrence of EMR have been known for a long time, especially in connection with earthquakes. These effects include earthquake lights, the strange behaviour of animals prior to earthquakes, and the breakdown or disturbances of radio communication. The same effects are often observed in connection with volcanic eruptions. For a long time scientists have ignored or doubted the existence of these effects. This first changed when photographs by Yakuta Yasui undoubtedly proved the occurrence of earthquake lights during the Matsushiro earthquake swarm in 1965 in Japan (Derr, 1986). Anomalies of the Earth's electromagnetic field, such as strong fluctuations of its direction and increased intensities that occur hours to days before an earthquake, were first discussed by Milne (1890). These perturbations, later observed by ground measurements (e.g. Gokhberg et al., 1982; Asada et al., 2001) and satellite observations (e.g. Larkina et al, 1989; Parrot, 1994; Trigunait et al., 2004), are sometimes associated with the breakdown or disturbances of radio communication (King, 1983), as, e.g., during the 2003 Hokkaido Tokachi-oki earthquake in Japan (Nagamato et al., 2008), the Tangshan earthquake 1976 (M 7.8), or the Longling earthquakes in China (M 7.5 and 7.6) (Huang and Deng, 1979), where also earthquake lights were sighted. Since then several EMR monitoring stations have been constructed, especially in earthquake-risk zones, to improve the method with the aim to develop a new tool for earthquake prediction.

Further studies concentrate mostly on EMR-based exploration methods, phenomena such as increased EMR intensities above faults, the usage of the EMR method for the analysis of underground mine stability (Red`kin et al., 1985; Scitovich and Lazarevich, 1985; Markov and Ipatov, 1986; Frid, 1997a,b; Frid, 2000; Scott et al., 2004), and monitoring and mapping of potential landslides (Lauterbach, 2005). Krakovetzky et al. (1984a, b) explain the strange behaviour of Aurora Borealis above deep-seated faults, where the Aurora Borealis changed its typical direction relative to the latitude and aligned parallel to faults, with natural EMR. Nikiforova et al. (1989) were the first to recognise strong increases of electromagnetic emissions above faults with mobile devices during a long-time measurement campaign with the main focus on earthquake prediction in the Kirghiz S.S.R. Other studies showed the association of electromagnetic emissions with loci of higher stress in mines, e.g. Frid (1997a, b; 2000). EMR is also generated during artificial explosions (Nardi et al., 2003; Sobolev et al., 1984). The emissions generated during blasting are used in Russia as a standard method for

the exploration of quartz veins and ore bodies that emit typical EMR spectra caused by mechanical waves (Sobolev and Demin, 1980; Sobolev et al., 1984; Kepic et al., 2001).

Most of the current scientific studies focus on laboratory experiments. The first results of stress-related EMR from solid materials were published by Ashton (1901), who generated charges during the deformation of rubber. Stepanow (1933) observed EMR during the deformation of salt crystals. So far, stress-related EMR has been proven in laboratory studies for many different materials, e.g. ice (Fifolt et al., 1993), metal (Jagasivamani and Iyer, 1988), glass ceramics (Bahat et al., 2002), and different rock types (Nitsan, 1977; Warwick et al., 1982; Ogawa et al., 1985; Cress et al., 1987; Yamada et al., 1989; O'Keefe and Thiel, 1995). Despite the increase in scientific attention the occurrence of EMR has gained during the last decades, its source mechanisms are still under debate. The main processes discussed in this context are piezoelectricity and crack-related mechanisms (see Section 2.3). Several investigations evidence correlation of electromagnetic and acoustic emissions, so that micro-crack related processes are regarded as the most probable explanation (Yamada et al., 1989; Koktavy et al., 2004; Rabinovitch et al., 2007; Mori and Obata, 2008). Therefore, today most studies focus on the emitting material, the EMR-generating mechanisms (Rabinovitch et al., 2003; Misra and Kumar, 2004), and the material-related characteristics of EMR (Bahat et al., 2002; Goldbaum et al., 2003; Koktavy et al., 2004; Frid et al., 2006). Recently Koktavy et al. (2004) and Mori and Obata (2008) observed the directionality of EMR on laboratory scale.

With the development of the mobile Cerescope (Section 2.4.1), the EMR method has become more applicable for field studies, especially for the mapping of faults (Mallik et al., 2008) and possible landslides (Lauterbach, 2005; Morgounov and Zdorov, 2007), and for the analysis of stress distributions in tunnels (Lichtenberger, 2005; 2006a, b). In this context, the most significant advancement is the possibility of measurements of the directional properties of EMR to derive information about the actual main horizontal normal stress direction (e.g., Reuther et al., 2002; Lauterbach; 2005; Lichtenberger, 2005, 2006a, b; Mallik et al., 2008; Reuther and Moser, 2009).

2.2 Physical aspects

Electromagnetic waves consist of coupled electric and magnetic fields. In contrast to other waves, e.g. acoustic waves, they do not need a medium to disperse. In vacuum, they disperse independently of their frequency with the speed of light c (about 3×10^5 km/s). Electromagnetic waves can be described as transversal waves, for which the vectors of both components, the magnetic component B [A/m] and the electric component E [V/m], are

perpendicular to each other and to their propagation direction (Fig. 2.1). The direction of the electric component is used to define the polarisation of the electromagnetic wave. Electromagnetic waves have their origin in e.g. an infinitesimal dipole, changes in the atomic energy level (due to movements of electrons between discrete energy bands), or from oscillations and the associated movements of charge carriers in atoms or molecules.
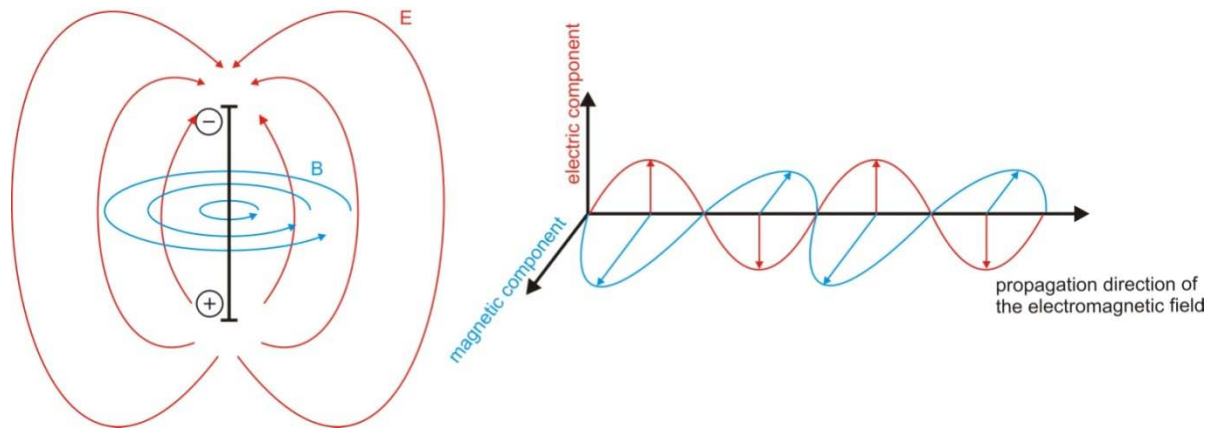
Fig. 2.1: Schematic sketch of an electromagnetic wave (generated by an oscillating dipole) that consists of a magnetic (*B*) and an electric (*E*) component. Both are perpendicular to each other and propagate perpendicular to the dipole axis.

The behaviour of electromagnetic waves in a medium is not only a function of the frequency or the wavelength, respectively. They are subject to effects such as reflection, refraction, and polarisation (see below). Especially the damping in different media, and therefore the penetration depth in rocks, or the atmosphere, and thus the wave propagation direction, are also directly influenced by the electric properties of the medium.

When electromagnetic waves travel through a medium, the velocity *v* depends on the electric properties of the medium [1], namely on the permittivity ε [As/Vm] (dielectric conductivity) and the magnetic permeability μ [Vs/Am] (magnetic conductivity).

$$v = \sqrt{\frac{1}{\varepsilon_r \varepsilon_0 \mu_r \mu_0}} = \frac{1}{\sqrt{(\mu\varepsilon)}} \qquad [\text{m/s}] \qquad [1]$$

where ε_0 [As/Vm] is the permittivity of the vacuum and ε_r is the ratio between ε and ε_0 and therefore dimensionless; accordingly, μ_0 is the magnetic permeability of the vacuum and μ_r [Vs/Am] the ratio between μ and μ_0 and therefore dimensionless. The dielectric permittivity ε describes how far an electric field can penetrate a material, while the magnetic permeability μ describes the penetration depth of magnetic fields.

The skin depth (penetration depth) δ [m] of electromagnetic waves into a material depends on the specific resistivity R [Ωm], the magnetic permeability μ of the material, and on the angular frequency $\omega = 2\pi f$ [Hz], where f [Hz] is the frequency. The skin depth itself is defined as the distance that the wave travels up to a damping of $1/e$ of its original amplitude. This is equivalent to a damping of 8.7 dB or to 63% of the original amplitude. The skin depth can be calculated by the following equations, which are simplifications of the Maxwell equations for electromagnetic fields in conductors [2] and dielectrica [3].

Conductors $\qquad \delta = \dfrac{1}{\sqrt{\left(\dfrac{\mu_0 \omega}{2R} \right)}}$ $\qquad\qquad\qquad\qquad$ [m] $\qquad\qquad$ [2]

Dielectrica $\qquad \delta = \dfrac{2R}{\sqrt{\left(\dfrac{\mu_0}{\varepsilon} \right)}}$ $\qquad\qquad\qquad\qquad$ [m] $\qquad\qquad$ [3]

The relationship between conductors and dielectrica is shown by R;

$$R = \frac{\omega}{\varepsilon}$$ $\qquad\qquad\qquad\qquad\qquad\qquad\qquad\qquad\qquad$ [4]

If R exceeds 1, the material is a conductor at the given frequency; a value of R much lower than 1 defines the material as dielectric. Following equation [4], the conductivity of the material for electromagnetic waves depends not only on its electric properties, but also on the frequency of the electromagnetic waves. Therefore, a material can be a conductor or dielectric at different frequencies. As $R = 1$ does not define a physical limit, but rather a transition zone between dielectrica and conductors, equation [3] for dielectrica is only used for materials with extremely high values for R, e.g. mica or glass. As the skin depth δ is largely controlled by the angular frequency ω, higher frequencies result in a dramatical decrease in skin depth, while a higher specific resistivity R increases the skin depth. Therefore, most rocks (dielectrica) are good conductors for electromagnetic waves, while metals or seawater with low specific electric resistivities are insulators for electromagnetic waves. The electric properties of rocks (especially sedimentary rocks) and soils, e.g. the resistivity, depend on many factors that vary

over a wide range, e.g. fluid content, composition of the fluids, pore space, mineralogy, etc. For this reason, the calculated skin depths are only rough estimations (Fig. 2.2).
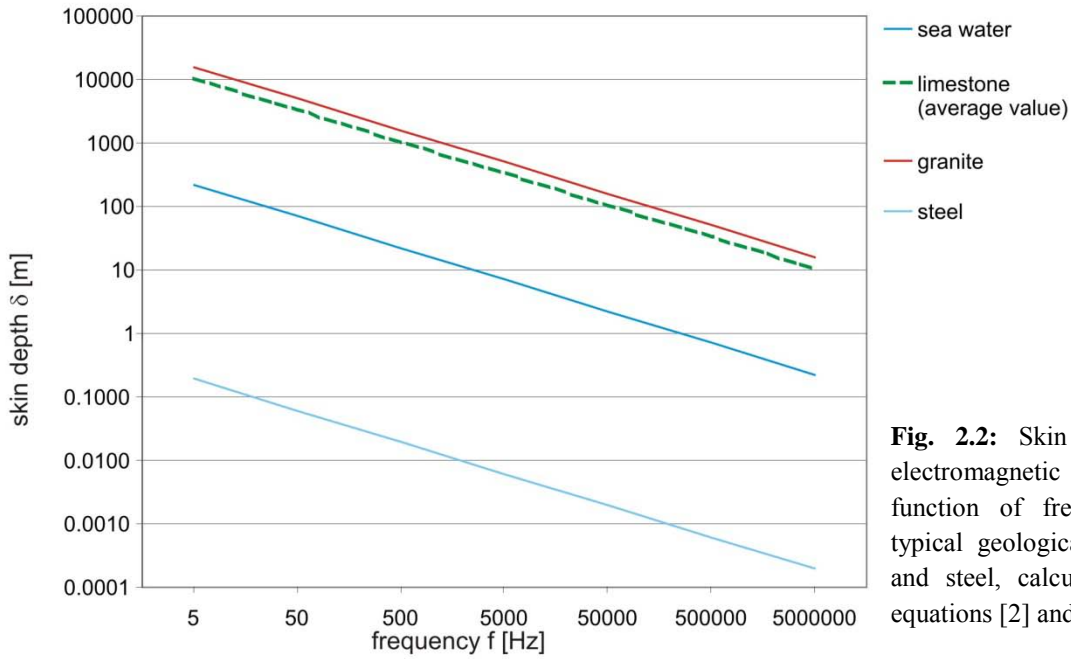
Fig. 2.2: Skin depths of electromagnetic waves as a function of frequency for typical geological materials and steel, calculated using equations [2] and [3].

At the boundary between rocks (medium 1) and atmosphere (medium 2) and at the interface between different rock types, i.e., where electric properties of the passed medium change, the propagation of electromagnetic waves follows Snell's Law [5].

$$\frac{\sin \alpha}{\sin \beta} = \frac{c_1}{c_2} = \frac{\lambda_1}{\lambda_2} = \frac{n_2}{n_1} \qquad [5]$$

where c is the speed [m/s] of the electromagnetic waves in the media 1 and 2, λ is the wavelength [m], n is the refractive index [dimensionless], and α is the angle of the incident wave, while β is the angle of the refracted wave. In the case that at least one of the media is a conductor for electromagnetic waves, the electromagnetic waves are refracted and reflected according to the properties of the adjacent media and dependent on the frequency. Whether the electromagnetic wave is reflected or refracted at the interface between both media, depends furthermore on the angle of incidence, following Snell's Refraction Law [6],

$$\sin \psi = \left(\frac{1}{n_E}\right) \sin \Theta \qquad [6]$$

where ψ is the angle of incidence in medium 1, which becomes critical if the refraction angle Θ reaches $\pi/2$, for which waves propagate parallel to the surface and n_E is the refractive index (Fig. 2.3). If the critical angle ψ_L is exceeded, no refraction occurs, but all waves are reflected back into medium 1 (rocks). Mognashi (2002) calculated for dielectrics (dry rocks, assuming permittivities between 4 and 16) critical angles between 30° and 14.5°. As for conductors, the refractive index n_E also depends on the frequency and resistivity ρ [Ωm], so that the critical angle can be calculated as follows:

$$\psi_L \cong \sin^{-1} \sqrt{2\omega\varepsilon_0\rho} \qquad\qquad [7]$$

Again for incident angles higher than ψ_L, no waves are refracted into the atmosphere (medium 2), whereas the critical incident angle approaches zero at higher frequencies (Mognashi, 2002). This means only waves that propagate almost perpendicular to the Earth's surface are refracted into the atmosphere (Fig. 2.3).
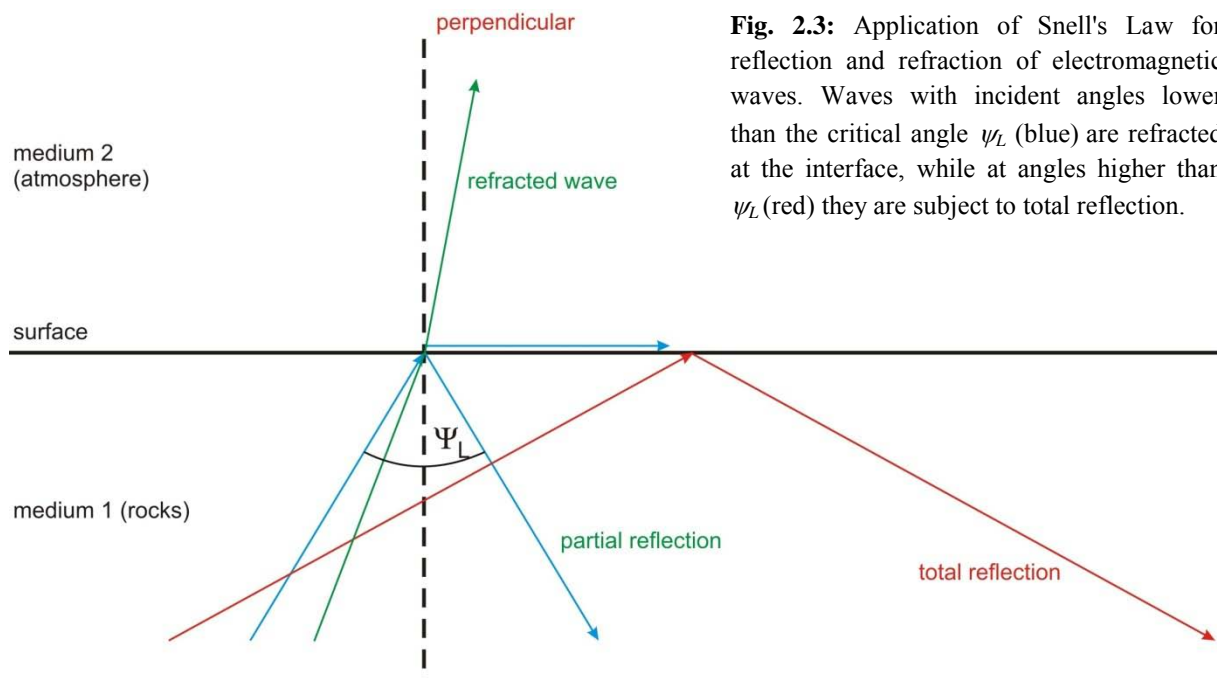
Fig. 2.3: Application of Snell's Law for reflection and refraction of electromagnetic waves. Waves with incident angles lower than the critical angle ψ_L (blue) are refracted at the interface, while at angles higher than ψ_L (red) they are subject to total reflection.

If the electromagnetic waves impinge the interface between medium 1 and 2 (rocks and atmosphere) at an acute angle, they should be totally reflected (Fig. 2.3). However, this is in contradiction with field observations during horizontal EMR measurements, where lower amplification levels are generally sufficient to reach the same intensities as during linear measurements (Section 2.4). This apparent discrepancy might be explained by the "attenuated total reflection", i.e. the incident and the reflected wave interfere with each other at the boundary between both media, resulting in a standing or evanescent wave that is perpendicular to the interface (Fig. 2.4).
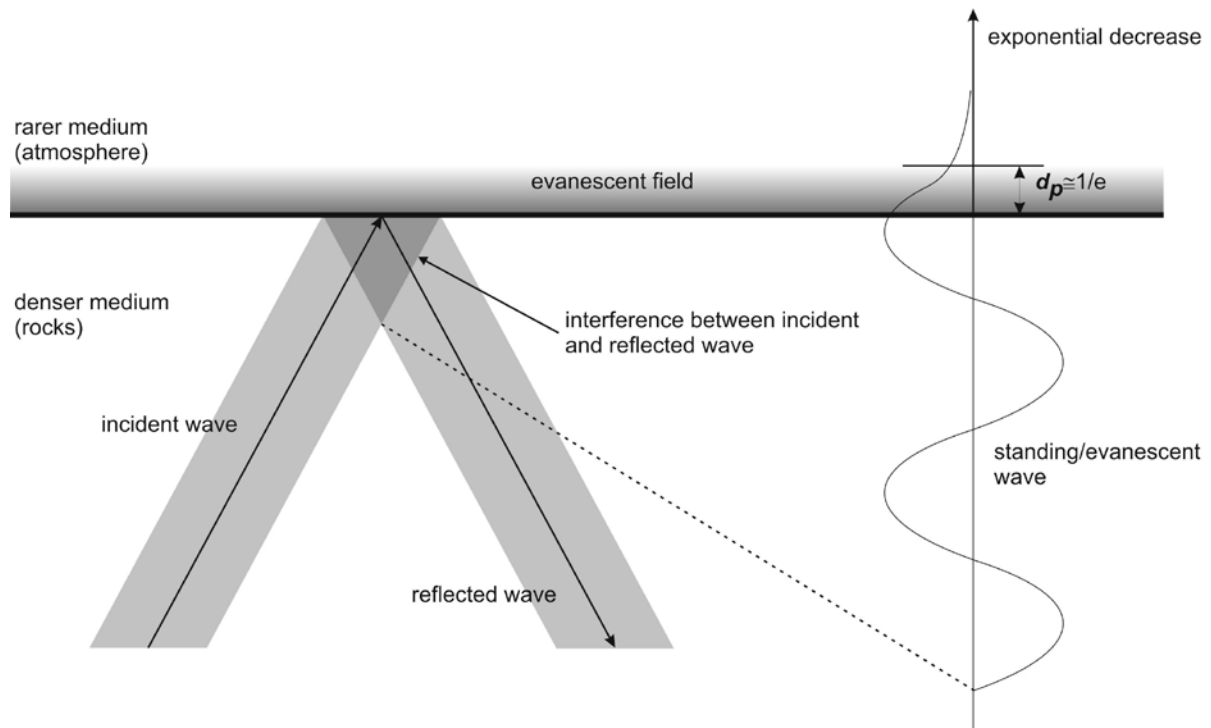
Fig 2.4: Concept of the attenuated total reflection. As a consequence of the interference of the incident and the reflected wave, a standing wave is generated that induces an evanescent field into the rarer medium. Modified after Karabacak et al., 2007.

Since the amplitude of the standing wave is not zero at the interface, an electric field is created in the rarer medium, which decreases with an exponential rate proportionally to the perpendicular distance from the interface. The penetration depth d_p of this evanescent field into the rarer medium is largely dependent on the wavelength within the denser medium λ_1 and lies within the order of the wavelength [8].

$$d_p = \frac{\lambda_1}{2\pi\sqrt{\sin^2\psi - \left(\dfrac{n_2}{n_1}\right)^2}} \qquad \text{[m]} \qquad\qquad [8]$$

Since the frequency range used for EMR measurements is between 5 and 50 kHz (Table 2.1), the wavelengths lie in the range of several hundred metres to some kilometres. Therefore, the attenuation of the evanescent field is negligible for measurements that are carried out directly above the Earth's surface. As the refractive index n for air is 1.00 and according to Mognashi (2002) and Lichtenberger (2005) much higher for rocks, Lichtenberger (2005) calculated, depending on the frequency, refractive index values between 50 and 160 for limestones of the Lower Muschelkalk. Therefore, according to Snell's Law [**5**], the direction of the electromagnetic waves is mostly unaffected by changing medium.

Table 2.1: Overview of frequency spectra and applications of electromagnetic waves and common abbreviations. Frequency bands used in this study in bold letters. Based on Jacobsen (2001).

frequency f [Hz]	wavelength λ [m]	international term	abbrev.	application
$3 \times 10^1 - 30 \times 10^1$	$10 \times 10^6 - \ 100 \times 10^6$	Extremely Low Frequency	ELF	formerly submarine boat communication
$30 \times 10^1 - 300 \times 10^1$	$1 \times 10^6 - \ 10 \times 10^6$	Super Low Frequency	SLF	submarine boat communication, navigation
$300 \times 10^1 - 3 \times 10^3$	$100 \times 10^3 - 1000 \times 10^3$	Voice Frequency	VF	submarine boat communication, navigation
$3 \times 10^3 - 30 \times 10^3$	**$10 \times 10^3 - \ 100 \times 10^3$**	**Very Low Frequency**	**VLF**	**submarine boat communication, navigation**
$30 \times 10^3 - 300 \times 10^3$	**$1 \times 10^3 - \ 10 \times 10^3$**	**Low Frequency**	**LF**	**navigation, AM radio, time signal**
$0.3 \times 10^6 - 3 \times 10^6$	$100 \times 10^1 - 1000 \times 10^1$	Medium Frequency	MF	AM radio
$0.3 \times 10^9 - 3 \times 10^9$	$0.1 \times 10^1 - \ 1 \times 10^1$	Ultra High Frequency	UHF	TV, cellular radio, WLAN, RFID
$3 \times 10^9 - 30 \times 10^9$	$0.01 \times 10^1 - \ 0.1 \times 10^1$	Super High Frequency	SHF	cellular radio, radar, WLAN, directional radio
$30 \times 10^9 - 300 \times 10^9$	$1 \times 10^{-3} - \ 10 \times 10^{-3}$	Extremely High Frequency	EHF	radar, directional radio

After reaching the Earth's surface, the propagation of the electromagnetic waves is again mainly controlled by their frequency. At this point, electromagnetic waves are usually divided into space- and ground waves. Space waves dominate in the range of the short wave band (see Table 2.1) and propagate linearly away from their source. They are unable to follow the curvature of the Earth´s surface. However, as a result of the refraction at the ionosphere, they can travel higher distances. In contrast, ground waves are restricted to the low frequency range (see Table 2.1) and follow the curvature of the Earth´s surface. In this case damping is

very slight, so that they can travel several thousand kilometres, whereas they quickly become attenuated when they propagate into the atmosphere.

2.3 Sources of EMR

The mechanisms of the generation of EMR are diverse and have been discussed by various authors (for references see individual sections). The sources that have been discussed mostly include, e.g., the piezoelectric effect (Section 2.3.1), p-holes (Section 2.3.4), the electrokinetic effect (Section 2.3.6), and micro-cracking (Section 2.3.8). Most of these effects were evaluated in connection with the forecasting of earthquakes and volcanic eruptions, but also for some exploration methods. However, the sources of EMR are still incompletely understood, in particular interactions of individual sources and effects make it difficult to discern one main source for EMR. In the following, the most important possible sources are introduced as discussed by the different authors.

In this context, the main prerequisites for a source of EMR are (1) material-independence; (2) directionality of the emissions; (3) a strong increase in intensity above faults in all tectonic settings; (4) a continuously-acting process not bound to the occurrence of earthquakes or volcanic eruptions; and (5) an explanation for the transient pulse-like character of the emissions.

2.3.1 Piezoelectricity

The piezoelectric effect (from: πιεζω – press/squeeze) was first described by Pierre and Jaques Curie in 1880 for tourmaline crystals. Piezoelectricity occurs when crystals of certain crystal classes are subject to stress. The precondition for piezoelectricity is the lack of a symmetry centre (except in crystal class 432) and the existence of a polar axis. The most important piezoelectric rock-forming mineral is quartz. Some other natural minerals with piezoelectric properties are tourmaline, nepheline, and zincite (Shridar et al., 1999). Furthermore, the piezoelectric effect occurs in some technical minerals, ceramics and some organic materials, e.g. wood (Bazhenov, 1961; Knuffel and Pizzi, 1986). Yoshida and Ogawa (2004) observed electromagnetic emissions during rock fracture experiments of dry and wet granite, and explained their observations with piezoelectricity.

As quartz is an important rock-forming mineral, the piezoelectric effect is briefly described for quartz. The piezoelectric effect is strongest if pressure is applied perpendicular to the crystallographic c-axis and parallel to one of the three a-axes. This pressure induces a relative movement of the charge carriers due to elastic deformation, which results in the creation of an

electric dipole. Quartz-bearing rocks can show piezoelectric properties either by a statistical effect or by their texture (Parkhomenko, 1959, 1971; Wellmer 1971; Bishop, 1981a, b). Statistical effects that have been observed in some laboratory studies results from a deviation from the random orientation of quartz crystals in small samples; but this effect becomes negligible with increasing volume and decreasing grain-size (Ghomshei and Templeton, 1989) and its therefore not of interest in nature. However, Bishop (1981a, b) and Parkhomenko (1971) showed a piezoelectric effect in quartzitic mylonites that exceeds the statistical effect. Even if the texture of the rock is characterised by a strong alignment of the quartz crystals, this is not sufficient for a directed emission of electromagnetic signals. In addition to the alignment of the quartz grains, it is necessary to adjust the a-axes. Furthermore, quartz forms usually dauphine twins and is enantiomorphic, which argues against a true piezoelectric effect in rocks. Therefore to produce a piezoelectric effect, it is necessary to have a preferred crystallographic orientation (CPO) of a-axes with a grouping of the a-axes according to their polarity. However, there are no natural mechanisms of CPO known that can cause this kind of grouping. Tuck et al. (1977) argues that an electric field that acts during the crystallisation might be responsible for an appropriate alignment and grouping of the a-axes. Therefore, rocks subject to stress will induce piezoelectricity, but the random distribution, the twinning, and enantiomorphic occurrence of quartz crystals will cancel the local piezoelectric voltage so that a long-range electromagnetic field cannot be generated (Ogawa et al., 1985; Freund, 2002). Regarding the very special conditions under which a directed electromagnetic field can be generated and that electromagnetic radiation is known from different non-piezoelectric materials like steel, glass ceramics and different rock types without any piezoelectric minerals (e.g. carbonates), it is very doubtful that the contribution of piezoelectricity to the electromagnetic emission is significant. This is also emphasised by Utada (1993) and Takeuchi and Nagahama (2002) who calculated maximum intensities that can be reached under natural conditions and concluded that the observed amplitudes cannot be explained with piezoelectricity, except for strong deformation as during earthquakes (Utada, 1993; Ogawa and Utada, 2000).

2.3.2 Non-classical piezoelectric effect/Stepanov effect/Moving of dislocations

The Stepanov effect belongs to the non-classical piezoelectric effects, i.e., in analogy with the piezoelectric effect, the polarisation results from mechanical stress, but no piezoelectric material is necessary. This effect, first described by Stepanov (1933), is caused by the movement of charged dislocations. Every crystal contains dislocations/defects that are

charged in dielectric materials because of the associated point defects. These point defects are neutralised under static conditions by the Debye-Hückel cloud, i.e. point defects of opposite charge. By applying stress to the material, the dislocations start to move, while the associated Debye-Hückel cloud follows much slower, which result in polarisation (Dologlou, 1993). When subject to shear stress, the dislocations move in two different directions, one of which is the future direction of the crack (Teisseyre, 1992).

This effect could explain the directionality of EMR. However, the dislocations that create the dipoles perpendicular to the future crack need to dominate. Slifkin (1993) suggested large-scale rapid motions of dislocations occur only at high temperatures and under the sudden application of stress, so that this process should play only a minor role in the uppermost crust. On the other hand, Frid et al. (2003) suggested dislocation movements are too slow under the conditions in the upper crust and conclude that dislocations cannot be responsible for charge separation in conductors. Gershenzon and Bambakidis (2001) propose that the effect of moving dislocations is too small, because at normal temperature the density of dislocations is extremely high so that they constrain each other, which makes movement of dislocations almost impossible. This pinning effect is also described by Slifkin (1993), Gershenzon and Bambakidis (2001), and Freund (2003). The effect of dislocations moving is expected to be important only at greater depths (Slifkin, 1996). Additionally, it is known from laboratory experiments that EMR emissions increase with the brittleness of the material (Jagasvamani and Iyer, 1988; Frid et al., 1999), which is also in contradiction to models based on the movement of dislocations.

2.3.3 Piezomagnetic effect

As the piezomagnetic effect is restricted to rocks or other materials that contain ferromagnetic minerals, e.g. pyrrhotite, magnetite and rutile, or other iron- and titanoxides, it mainly occurs in igneous rocks, especially basalt and gabbros that have usually high amounts of ferromagnetic minerals, and in sedimentary rocks of source rocks containing significant amounts of ferromagnetic minerals. During crystallisation, these minerals become remanently magnetised by cooling down below the Curie temperature, where the polarisation/orientation of magnetisation is controlled by the Earth's magnetic field. In analogy, in sediments the ferromagnetic particles can become aligned according to the actual magnetic field during the sedimentation process. However, piezomagnetic properties of these rocks can change with diagenesis and metamorphosis.

The piezomagnetic effect itself is defined as the change of the magnetic properties of the material induced by changes of the applied stress and has been discussed by various authors as a possible source of EMR (e.g. Breiner, 1964; Rikitake, 1968; Abdullabekov et al., 1972; Carmichael, 1977; Gershenzon and Bambakidis, 2001). As a change of the magnetic field causes an induction of an electric current, the piezomagnetic effect is a probable source of electromagnetic radiation or at least can influence the electromagnetic field. Several laboratory studies by e.g. Carmichael (1968) showed that during uniaxial and triaxial experiments, the direction and intensity of the remanent magnetisation and the magnetic susceptibility is affected by mechanical stress. The same effect was observed prior to and during earthquakes and volcanic eruptions (Zlotnicki and Cornet, 1986; Meloni et al., 1998; Mueller and Johnston, 1998), and during long-term monitoring of large fault zones (e.g. the San Andreas Fault; Talwani and Kovach, 1972).

Based on the piezomagnetic effect, Zlotnicki and Bof (1998) calculated changes in the geomagnetic field of the Merapi Volcano, Indonesia, between 1990-1995, that are in good agreement with field measurements of the intensity and spatial distribution of changes of the local geomagnetic field. However, Gershenzon and Bambakidis (2001) proposed that the piezomagnetic effect is strong enough to act as possible source of EMR, but occurs only for a short duration during stress build-up.

For the EMR measured in this study, the piezomagnetic effect is not the preferred source, because (1) it is not material-independent, (2) it cannot account for the directionality of the emissions, and (3) it should occur only locally during short-term changes in the stress field, i.e. associated with volcanic eruptions and earthquakes or during variations in temperature due to changes of the magnetisation of minerals.

2.3.4 Positive holes and free OH-groups

The theory of positive holes as charge carriers in igneous and metamorphic rocks was introduced by Freund (2000, 2003), Freund et al. (2006), Takeuchi et al. (2006), and Takeuchi (2008). Positive holes are crystal defects in the oxygen anion sub-lattice, where some O^{2-} places are occupied by O^-, which produce a positive hole. Since this configuration is unstable, the O^- tends to pair up with another O^- to an $O^- \text{-} O^-$ peroxy link, that in physical terms represents a dormant positive hole (Freund et al., 2004). This so-called p-hole is usually electrically inactive, but can be activated by heating or mechanical stress. In laboratory experiments, the p-holes were activated by the application of mechanical stress to a rock. According to Freund et al. (2004), the p-holes are highly mobile, able to travel macroscopic

distances and to jump grain boundaries. During the experiments, the p-holes moved out of the stressed rock volume into unstressed parts of the rock, resulting in differently-charged areas in a rock volume.

This theory could explain the generation of EMR also in relation to micro-cracks (see Section 2.3.8), where the electric current starts as a result of the mobilisation of p-holes due to vibrations of the crack walls at low mechanical stresses. The current reaches its maximum just before the final failure. This is in accordance with laboratory studies that identify micro-cracks as the main source of EMR (see Section 2.3.8; e.g. Misra and Kumar, 2004; Mori and Obata, 2008). Furthermore, the combination with the micro-cracks in the rock could explain the directionality of EMR: If the commonly aligned micro- and nano-cracks act as insulating barriers, forcing the current of charge carriers in a direction that is parallel to the micro-cracks, the EMR would be directly controlled by the stress field of the Earth's crust that controls the orientation of micro-cracking. However, Freund et al. (2004) found that this theory cannot be confirmed for every material and that electric potentials are only created in rocks that are inhomogeneously stressed. Hence, this theory is probably not unrestrictedly applicable to nature, where inhomogeneous stresses do not occur at scales and magnitudes produced in experiments (cf. Freund et al., 2004). Nevertheless, it is a promising explanation for the large currents that are measured prior to earthquakes and volcanic eruptions or in the vicinity of fault zones.

However, according to Takeuchi et al. (2006), the outflow of charge carriers out of the stressed rock is radial, that would result in a radial electric field around the stressed rock volume. This is not in agreement with the directionality of EMR that is aligned along the main horizontal stress, independent of faults. However, even this theory has as basic weakness the material dependency and is not suitable to explain EMR from materials such as metal.

2.3.5 Contact electrification and triboelectricity

Contact electrification and triboelectricity describe a mechanism that generates charges along contact planes. Contact electrification occurs when two different materials are brought in contact, while the term triboelectricity is commonly used in connection with a frictional component along the surface between the two materials (e.g. Lowell and Rose-Innes, 1980). Since different materials contain different amounts of free charge carriers, even non-conductive materials are not free of charge carriers. By bringing two conductive materials in contact the charges flow between both materials until the concentrations of charge carriers are

equalised, as e.g. shown by Horn and Smith (1992) for the contact between quartz and mica. By separating both materials after contact, the two surfaces are charged with opposite polarities, but at an equal value (Tamatani, 2002). Applied to rocks, the opening of phase boundaries would consequently result in the formation of a dipole and electromagnetic emissions.

Triboelectricity is one type of contact electrification where, due to frictional heating between two surfaces, a charge is generated. By this process, it is also possible to generate plasma (Kamogawa and Ohtsuki, 1999; Muto et al., 2005). The charge depends on properties like the surface asperity, the material, and the temperature. The emitted electromagnetic spectrum is expected to cover the whole frequency spectrum with a constant signal strength (white noise type), which is typical for plasma (Brady and Rowell, 1986; Bahat et al., 2005). According to Lichtenberger (2005), the white noise could be interpreted as a typical EMR spectrum after frequency-dependent damping and filtering of the white noise signal through different rocks. Parkhomenko (1971) therefore suggests triboelectricity as one source of EMR. However, Parrot et al. (1992) expected the discharge energy created by this process as too small to play a major role in the generation EMR. Furthermore, this process is not able to explain electromagnetic emissions from single crystals (e.g. Nitsan, 1977; Khatiashvili and Perel´man, 1989; Hadjicontis et al., 2004), or during experiments on metal (Jagasivamani and Iyer, 1988) or glass ceramics (Bahat et al., 2002), where the required contact planes between different material are absent.

Therefore, contact electrification and triboelectricity can be excluded as sources for the measured EMR.

2.3.6 Electrokinetic effect and streaming potentials

The electrokinetic effect results from the interaction of a flowing liquid with a surface and has been proposed as a main source of EMR (e.g. Gershenzon and Gokhberg, 1993; Gershenzon et al., 1993; Kormiltsev et al., 1998; Clint, 1999; Gershenzon and Bambakidis, 2001).

Due to interaction of the fluid with a surface, a charged interface is generated. According to Shaw (1978), the process that generates the charge is mostly triggered by osmotic effects; the fluid penetrates into the solid generating an electric potential gradient (Zeta-potential). A streaming potential is generated by the movement of the liquid along the surface, or of the charged particles in the fluid phase, respectively.
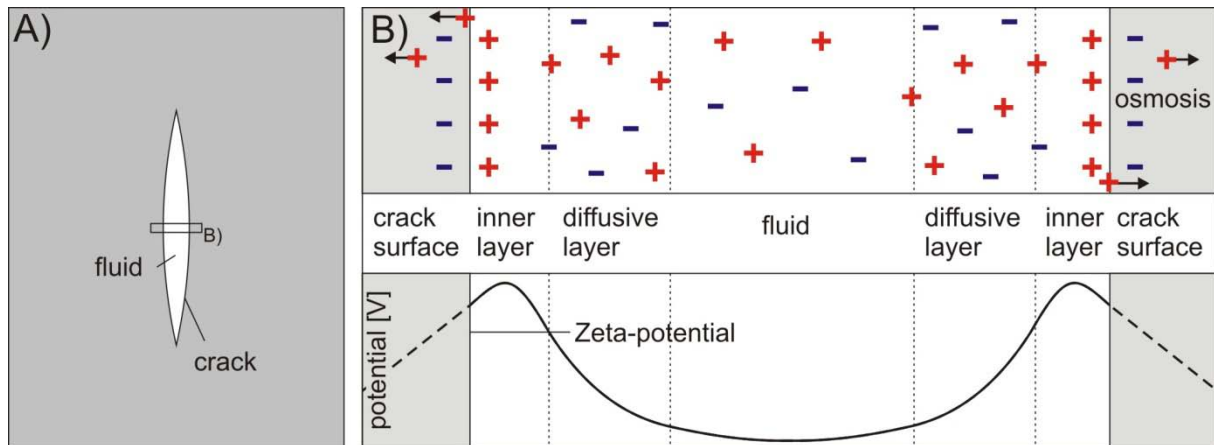
Fig. 2.5: Schematic sketch of the concept of the electrokinetic effect. **A)** While forcing a fluid through a crack, the charge carriers in the fluid interact with the crack walls. **B)** An electric double layer, consisting of the inner and the diffusive layer, with an electric potential is generated at the interface between fluid and solid. The orientation of the resulting electromagnetic field is controlled by the orientation of the interface. + and – represent charge carriers. Black arrows indicate the movement of positive ions into the solid.

Therefore, the streaming potential is a consequence of a potential difference, when a liquid is forced through a porous medium or a capillary tube (Mizutani et al., 1976). While the surface of the solid (the crack wall) is usually negatively charged, the fluid contains both positive and negative ions (Fig. 2.5). Consequently, the positive ions move to the solid surface forming an electric double layer that consists of an outer diffusive layer and an inner layer enriched in positive ions. The highest electric potential is created near the surface of the solid. The value of the electric potential depends mostly on the fluid pressure, the velocity of the fluid, pH, temperature, and ionic charges (e.g. Parks, 1965; Somasundaran and Kulkarni, 1973; Lorne et al., 1999).

Therefore, stress changes prior to and during earthquakes, landslides, and volcanic eruptions that cause movement of pore fluids and pore (crack) volume changes of rocks, are capable to explain EMR. In general, Clint (1999) expects the electrokinetic effect to be the main electrical potential-generating process in the upper crust. According to Gershenzon and Bambakidis (2001), the electrokinetic effect can explain the main features of electrotelluric field anomalies, namely duration, magnitude, and high degree of selectivity. Gokhberg et al. (2007) calculated the electrokinetic effect with respect to the earth tides, with the result that the diurnal variations of the earth tides have a detectable effect on the intensity of the electrokinetic effect. Furthermore, Gershenzon and Gokhberg (1993) suggest the electrokinetic effect as possible mechanism for the generation of an electromagnetic field caused by crustal stresses during the September 13th 1986 earthquake in Kalamata, Greece.

However, even if the electrokinetic effect offers a good explanation for an anomalous behaviour of EMR associated with earthquakes and volcanic eruptions, it is questionable that this effect can explain the results of Cerescope measurements in field. While fluid flow along joints follows the topographic gradient, the flow direction of fluids in micro- and nano-cracks is usually controlled by the regional stress field, where the fluid moves preferentially perpendicular to the main normal stress direction. Thus, fluid flow in micro- and nano-cracks therefore generates an electric field perpendicular and a magnetic field parallel to the main normal stress direction. The effect is also not capable to explain the electromagnetic emissions from dry samples in laboratory experiments (e.g Ogawa et al., 1985; Enomoto and Hashimoto, 1990; Takeuchi and Nagahama, 2001).

The electrokinetic effect is detectable above water pipes with the Cerescope (see Chapter 2.5.1). However, it is unlikely that EMR directions can be explained by groundwater flow, since they are constant over large areas and independent of topography and the orientation of macroscopic fluid pathways.

2.3.7 Atmospheric phenomena

It is widely accepted that atmospheric disturbances of the EMR are secondary effects that precede or accompany earthquakes (e.g. Popov et al., 1989). Atmospheric effects become noticeable as short-duration broadband radio emissions, as interruptions in the propagation of radio waves (e.g. Tate and Daily, 1989), or sometimes as earthquake lights. The observed anomalies that can even affect the ionosphere are in the frequency range of some Hertz up to several MHz (e.g. Fatkullin et al., 1989; Larkina et al., 1989; Lyakhov and Zetser, 2008). As the coupling mechanism between crust and ionosphere is not completely understood, the observed atmospheric interferences were mostly discussed as a result of (1) crustal movements during earthquakes, (2) thermal anomalies due to greenhouse lithospheric gas input into the atmosphere, or (3) an unsteady mass input of lithospheric gas into the atmosphere (Shalimov, 1992; Gokhberg et al., 1994; Pertsev and Shalimov, 1996; Shalimov and Gokhberg, 1998; Molchanov et al., 2004). These sources are thought to be responsible for the indirect coupling of the Earth's crust with the ionosphere by atmospheric and acoustic gravity waves (Nekrasov et al., 1995; Liperovsky et al., 2000; Molchanov, et al., 2004; Koshevaya et al., 2007; Rozhnoi et al., 2007). This coupling induces disturbances in the ionosphere, e.g. plasma depletion or density enhancements (Shalimov and Gokhberg, 1998) that are responsible for the observed electromagnetic anomalies, such as e.g. earthquake lights.

Time-invariant observations of ionospheric anomalies were made by Lyakhov and Zetser (2008) above the recently active Talass-Fergana Fault and the North Tien Shan fracture system (Central Asia). Krakovetzky et al. (1984a, b) observed repeatedly a reorientation of the Aurora Borealis above deep-seated faults in the transition zone between the Siberian platform and the East Siberian plate.

Nikiforova et al. (1989) could not find any evidence that meteorological factors, like air temperature, cloudiness, wind velocity, or atmospheric pressure contribute to anomalously high EMR, with the only exception of thunderstorms (see also Chapter 2.5.2). For this reason, the temporarily-restricted occurrence of atmospheric anomalies, which is furthermore strongly related to events like earthquakes and volcanic eruptions, cannot be the source of the continuously occurring EMR and is not able to explain the directionality of the emissions.

Since it is possible to measure EMR in the sub-surface (see Chapter 2.4.2.3), as demonstrated by e.g. Lichtenberger (2005, 2006a, b), and in electromagnetically-shielded vessels during laboratory experiments (Rabinovitch et al., 1999; Takeuchi and Nagahama, 2006), atmospheric effects can mostly be excluded in such investigations. However, field measurements during sunset and sunrise show an influence of the interaction of solar radiation with the ionosphere layers by unusually high EMR intensities (see Chapter 2.5.2).

In summary, the processes described above are able to explain some of the properties of the measured EMR. However, none of the mechanisms can fulfil all requirements (see Section 2.3; Table 2.2). Consequently, mechanisms related to micro-cracking are favoured (see Section 2.3.8).

Table 2.2: Overview of possible source mechanisms of EMR with advantages and disadvantages in explaining the properties of measured EMR and exemplary references.

Mechanism	Pro	Contra	Reference, e.g.
piezoelectric effect	- stress-induced - piezoelectric minerals are common	- material-dependent - difficulties in explaining directional properties of EMR - for continuous emissions continuous stress changes are necessary - intensities too low	-Gomshei and Templeton, 1989 -Freund, 2002 -Yoshida and Ogawa, 2004
Stepanov effect	- stress-induced -mostly material-independent - can explain directionality of EMR	- material-dependent - in contrast to EMR, decreases with brittleness	-Slifkin, 1993 -Frid et al., 2003 -Teisseyre, 1992

positive holes & free OH-groups	- stress-induced - can explain directionality of EMR	- material-dependent - only in inhomogeneously-stressed materials	-Freund et al., 2004 -Freund, 2000
contact electrification & triboelectricity	- stress-induced - mostly material-independent	- preferably on shear planes - frequency spectrum expected as white noise - not able to explain emissions in single crystals and metals	-Brady and Rowell, 1986 -Muto et al., 2007
piezomagnetic effect	- stress-induced	- material-dependent - cannot explain directionality of EMR -mostly restricted to short-term events	-Carmichael, 1977 -Gershenzon and Bambakidis, 2001
electrokinetic effect & streaming potentials	- directed emissions	- orientation of EMR depends on flow direction - cannot explain emissions from laboratory-dry samples - limited intensities	-Bahat et al., 2005 -Gershenzon and Gokhberg, 1993 -Clint, 1999
atmospheric effects	- observations of EMR disturbances prior to and during earthquakes and volcanic eruptions	- cannot explain directionality of EMR -cannot explain EMR in underground excavations	-Nikiforova et al., 1989 -Fatkullin et al., 1989

2.3.8 Micro- and nano-cracks

Cracks occur in any brittle material. Crack-related models of EMR generation are capable of explaining all significant characteristics of EMR observed in laboratory experiments and field measurements (see Sections 2.3 and 2.3.8.1). For example, since micro- and nano-cracks are generally not randomly oriented, but strongly aligned with respect to the responsible stress field (e.g. Kranz, 1983; Vollbrecht et al., 1999; Blenkinsop, 2000; Zang et al., 1996), they can act as a source of a directed electromagnetic radiation. Therefore, in the last years several laboratory studies have been performed to investigate the role of micro-cracks as a source for EMR (e.g. Egorov et al., 1988; Section 2.3.8.2). These experiments proved that EMR is related to brittle fracturing and the creation of crack surfaces (e.g. Mori and Obata, 2008) from micro- to nano-scale. Although the experiments did detect cracking as one source of EMR, the physical background is nevertheless incompletely understood and still under discussion (see Section 2.3.8.2).

2.3.8.1 Properties of crack-induced EMR

Fracture-related EMR is known to occur during the opening and growth of a crack (e.g. Koktavy et al., 2004) at a very early stage of the loading cycle by subcritical cracking (Yamada et al., 1989; Koktavy et al., 2004; Mori and Obata, 2008). As soon as crack propagation stops, the EMR signal decays. So, crack-related mechanisms need to explain this typical behaviour and different shapes of the signal. Furthermore, micro-crack related EMR implies that the EMR characteristics should depend on the electrical and mechanical properties of the fractured material. Crack-induced EMR usually occurs in short pulses or pulse packages (bursts), whereas single pulses can be related to single cracks (Rabinovitch et al., 1998; Frid et al., 2000; Rabinovitch et al., 2000) and exhibit typical shapes (Fig. 2.6). Therefore, several laboratory studies have worked on the parameterisation of the EMR-related to the material and to the type and size of the emitting micro-cracks. These studies were carried out on different materials like ice (Fifolt et al., 1993; Petrenko, 1993), metal (Misra and Kumar, 2004), single crystals of different materials (Egorov et al., 1988; Hadjicontis et al., 2004), amorphous materials like glass, and different rock types (Yamada et al., 1989; Enomoto and Hashimoto, 1992; Koktavy et al., 2004; Mori and Obata, 2008).

Some of these studies concluded that EMR is independent of the material, under the precondition that the material brittlely deformed.

In addition, the typical shape of EMR pulses can be described by their frequency, amplitude, the time between the initiation of the signal and the maximum amplitude, and the respective decay time and defining energy (Fig. 2.6). Furthermore, Rabinovitch et al. (2000; 2002) and Frid et al. (2003) conclude that the basic shape of EMR pulses is invariant to the loading mode and material. As the maximum EMR amplitude is primarily a function of the crack-surface area, the amplitude also correlates with the elasticity and the strength of the material (Jagasivamani and Iyer, 1988), as well as with the loading rate (Gold et al., 1975; Nitsan, 1977; Khatiashvili, 1984; Frid et al., 1999), i.e. higher fracture toughness and loading rate commonly results in higher EMR amplitudes. For metals, Misra and Kumar (2004) observed an additional influence of the temperature on the maximum amplitude.

The generated single pulses or burst are usually restricted to a narrow frequency band (Frid et al., 2003) and are therefore not of a "white noise type" (see Section 2.3.8.2). Furthermore, Rabinovitch et al. (2002) and Koktavy et al. (2004) demonstrated that the frequency of the EMR is a function of the crack dimensions. According to Rabinovitch et al. (2002), Koktavy et al. (2004), and Mori and Obata (2008), the frequency is related to the crack length and reaches a maximum prior to final failure, whereas Bahat et al. (2005) and Rabinovitch et al.

(1998; 1999) relate the frequency to the crack width. Rabinovitch et al. (1999) showed that there is a general (mainly material-independent) frequency-amplitude relationship in chalk, granite, and glass ceramics; the amplitude is inversely proportional to the signal frequency and thus to crack width (Rabinovitch et al., 1998). Srilakshmi and Misra (2005) came to the same conclusion for metals. Furthermore, the signal amplitude, as well as the number of pulses, increases sharply immediately prior to final failure of the sample (e.g Egorov et al., 1988; Stavrakas et al., 2004).
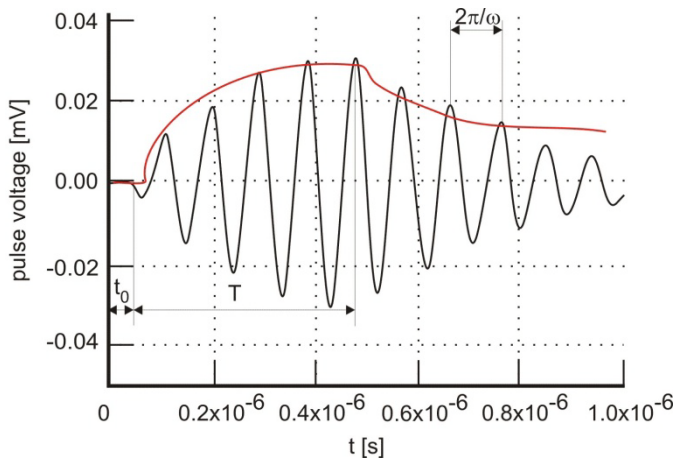
Fig. 2.6: Typical shape of an EMR pulse associated with micro-cracking. The frequency ($2\pi/\omega$) is usually restricted to a narrow band and is mainly a function of crack dimension. The emission starts at t_0 simultaneous with initiation of crack growth. The amplitude increases as long as the crack grows (T). As soon as the crack arrests, the signal decays. Modified from Frid et al. (2003).

Rabinovitch et al. (1999), Koktavy et al. (2004), and Takeuchi and Nagahama (2006) demonstrated that the directional properties of EMR, which are crucial for the method described in this thesis, are related to the orientation of the associated micro-cracks. According to this, the intensity of the measured EMR depends on the angular relationship between the emitting micro-crack and the antenna and is at its maximum when the antenna is oriented parallel to the strike of the crack.

Even though this summary of laboratory results outlines the significant parameters of EMR and their relation to material properties, it should be noted that a comparison of these studies should be taken with care. In particular, the different experimental setups, the use of basically different materials, and the investigation of different frequency ranges make it difficult to compare the results.

The generation process of EMR by micro-cracking is related to the creation of dipoles between the crack walls parallel or perpendicular to the direction of crack propagation. Therefore, it can be assumed that the direction of the emitted EMR is either parallel or perpendicular to crack walls. The EMR parallel to the crack walls is usually defined as longitudinal, while the direction perpendicular to the crack is defined as transversal (Fig. 2.7). Even if both options can easily be explained by the same processes, field observations (e.g. Lichtenberger, 2005; Reuther and Moser, 2009) and laboratory investigations of EMR (e.g.

Koktavy et al., 2004; Mori and Obata, 2008) indicate that the longitudinal propagation of EMR is dominant. The efficiency of generating EMR depending on the types of cracks is still discussed. While Yamada et al. (1989) expect tension cracks (Mode I) to be more efficient as source of EMR, Frid et al. (2003) argue that the fracture mode is insignificant in this context. However, since tension cracks represent the majority of cracks in rocks, they should be the favourable source.

Fig. 2.7: 2D conceptual sketch of the propagation of crack-related EMR illustrated for a Mode I tensional crack. The propagation direction of the electromagnetic waves depends on the orientation of crack propagation and is therefore controlled by the surrounding stress field (indicated by σ_1 as the maximum principal normal stress). The longitudinal propagation direction of the electromagnetic waves is parallel to the direction of crack propagation.
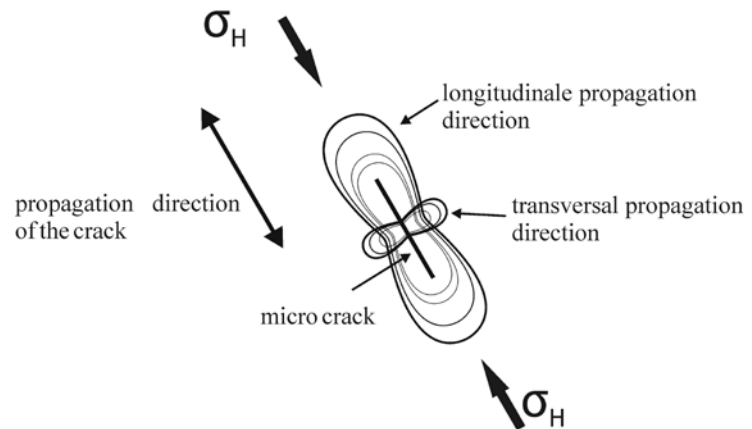

2.3.8.2 Models of crack-related EMR

The most promising theories to explain the generation of EMR induced by brittle fracturing are (1) charge separation processes between (e.g. O´Keefe and Thiel, 1995) or along (Gershenzon et al., 1986) the crack walls associated with micro-cracking, (2) crack-induced movement and reorientation of dislocations (e.g. Misra and Gosh, 1980; Slifkin, 1993), and (3) the surface vibrational-wave model of Frid et al. (2003) and Rabinovitch et al. (2007).

For **Model (1)**, different mechanisms are discussed that give more or less suitable explanations for the generation and the properties of EMR. One of the processes (**Model 1a**) is the charging of the crack walls by the emission of charged particles, such as electrons, ions, atoms, molecules, and other charged particulate matter (e.g. Brady and Rowell, 1986; Enomoto and Hashimoto, 1990) or even the breaking of atomic bonds, resulting in a mosaic-like pattern of differently charged domains (Fig. 2.8; Perelman and Khatiashvili, 1981; Gershenzon et al., 1985; Khatiashivili and Perel´man, 1989; Mognaschi, 2002) producing dipoles along and between the crack surfaces. Statistically, both sides of the crack should carry the same charge, so that they are electrically neutral. However, the signal generated by this process is that of a "white noise spectrum" (Miroshnishenko and Kuksenko, 1980;

Khatiashivili, 1984) that is not consistent with the observations of Rabinovitch et al. (2002), Frid et al. (2003), and Koktavy et al. (2004). These authors attribute the pulse properties, in particular the frequency, to be influenced by the fracture size and the mechanical properties of the material (see Section 2.3.8.1).
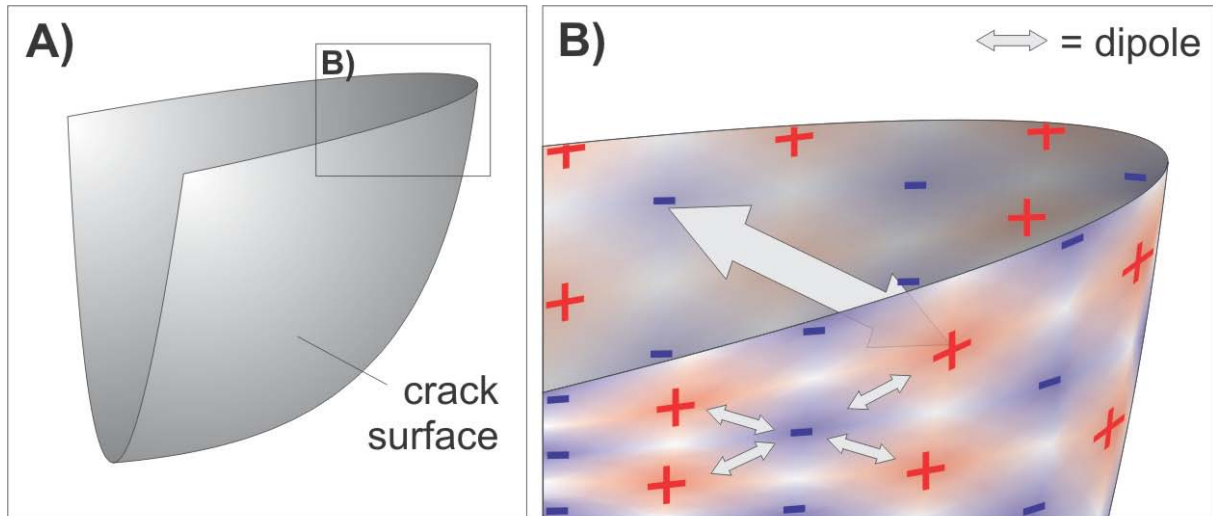
Fig. 2.8: A) Schematic sketch of a section of a crack in its tip area to locate illustration in B). **B)** Schematic sketch of dipoles along crack walls, arranged in a mosaic-like pattern of differently-charged domains (indicated by + (positive) and − (negative) areas). The dipoles are generated by the emission of charged particles (not illustrated) or the breaking of atomic bonds.

The "capacitor model" (**Model 1b**) by O`Keefe and Thiel (1995) deals with a net charge that is created between the crack walls. In contrast to a homogenous non-polarised material, where positive and negative charges are distributed regularly on both crack sides, materials with a pre-polarisation or the application of physical gradients are likely to produce net charges. The physical gradients can be temperature, deformation, impurity density gradients, or external fields (Petrenko, 1993). Temperature gradients can form during crack formation, resulting in different heating on opposite crack walls and a temperature gradient along the crack. There, the warmer side is typically characterised by a negative load (Takahashi, 1983). The resultant net charge produces charge-equalisation currents that flow along and between the crack walls during fracturing (Fig. 2.9). While the currents at the crack surface are expected to cancel out each other, the only current that is able to contribute to the emission of EMR flows at the crack tip (O´Keefe and Thiel, 1995). According to Frid et al. (2003), this model is questionable for the following reasons: (1) The model works favourably only for tensile cracks; (2) the model is not capable of explaining the shapes of the measured signals, and (3) the main radiation direction would have be perpendicular to the main radiation

direction as observed by Rabinovitch et al. (1999), Koktavy et al. (2004), and Takeuchi and Nagahama (2006).
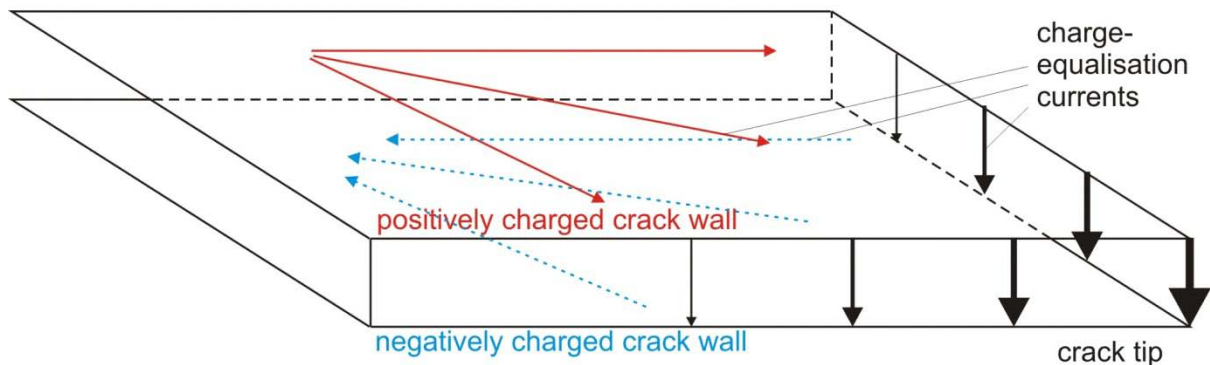
Fig. 2.9: Schematic sketch of the "capacitor model" of charge generation modified after O`Keefe and Thiel (1995). The EMR generated by charge equalisation currents that are parallel to the cracks walls (blue and red arrows), cancel each other out, while EMR results from the current at the crack tip (black arrows).

The second possible source mechanism of EMR (**Model 2**) is related to crack- and deformation-associated movements of dislocations (e.g. Misra and Gosh, 1980; Slifkin, 1993; Teisseyre and Ernst, 2002; Stavrakas et al., 2004; Teisseyre et al., 2004). Under stable conditions, dislocations are surrounded by point defects to maintain charge neutrality (Whitworth, 1975; Teisseyre, 1992). When subject to loading, the local stress conditions in a material change due to crack initiation and propagation. Consequently, the non-uniformly distributed dislocations and the associated "conduction electrons" become unstable and start to migrate and rearrange towards a more stable configuration under the new stress regime. If the "conduction electrons" are stopped, this "braking" process is analogue to the emission of a "bremsstrahlung" (Misra, 1977; Misra and Gosh, 1980) that emits EMR. In addition, the dislocations themselves move faster than the associated charge-compensating point defects (e.g. Slifkin, 1993), resulting in the formation of dipoles. According to Misra (1977), this rearrangement process is assumed to occur during each transition stage of micro-cracking, like fracturing or yield point. In contrast, Molotskii (1980) explains the occurrence of EMR by the changes in total length of dislocations and by their velocity during the transition changes, where the dislocations themselves act as dipoles. As a consequence, the increase in total length of dislocations would result in an increased dipole moment. Frid et al. (2003) doubt these explanations, because the motion of dislocations in brittle materials can mostly be neglected. Furthermore, Jagasivamani and Iyer (1988) and Frid et al. (1999) showed that EMR amplitudes increase with the brittleness of the investigated material and decrease with the transition from brittle to ductile behaviour that is in contrast to the dislocation models.

Model (3) of crack-related EMR is the surface vibrational wave (SVW) model as described by Frid et al. (2003) and Rabinovitch et al. (2007). In this model, the electromagnetic emissions are explained by the oscillation of charge carriers due to the release of mechanical energy by crack growth (Fig. 2.10). Following the breakage of the atomic bonds at the crack tip, the atoms along the crack walls become excited and oscillate around their steady state positions. The oscillating atoms move together in lines with the surrounding atoms. The oscillation direction is parallel and perpendicular to the growth direction of the crack. The resulting vibrations are SVWs. According to Rabinovitch et al. (2007), the positive charges move together, diametrically opposite to the negative charges, while the vibrations decay exponentially within the material. The resulting oscillating dipoles are oriented perpendicular and parallel to the crack walls and could explain the emission of longitudinal waves, as well as transversal EMR waves (cf. Fig. 2.7).
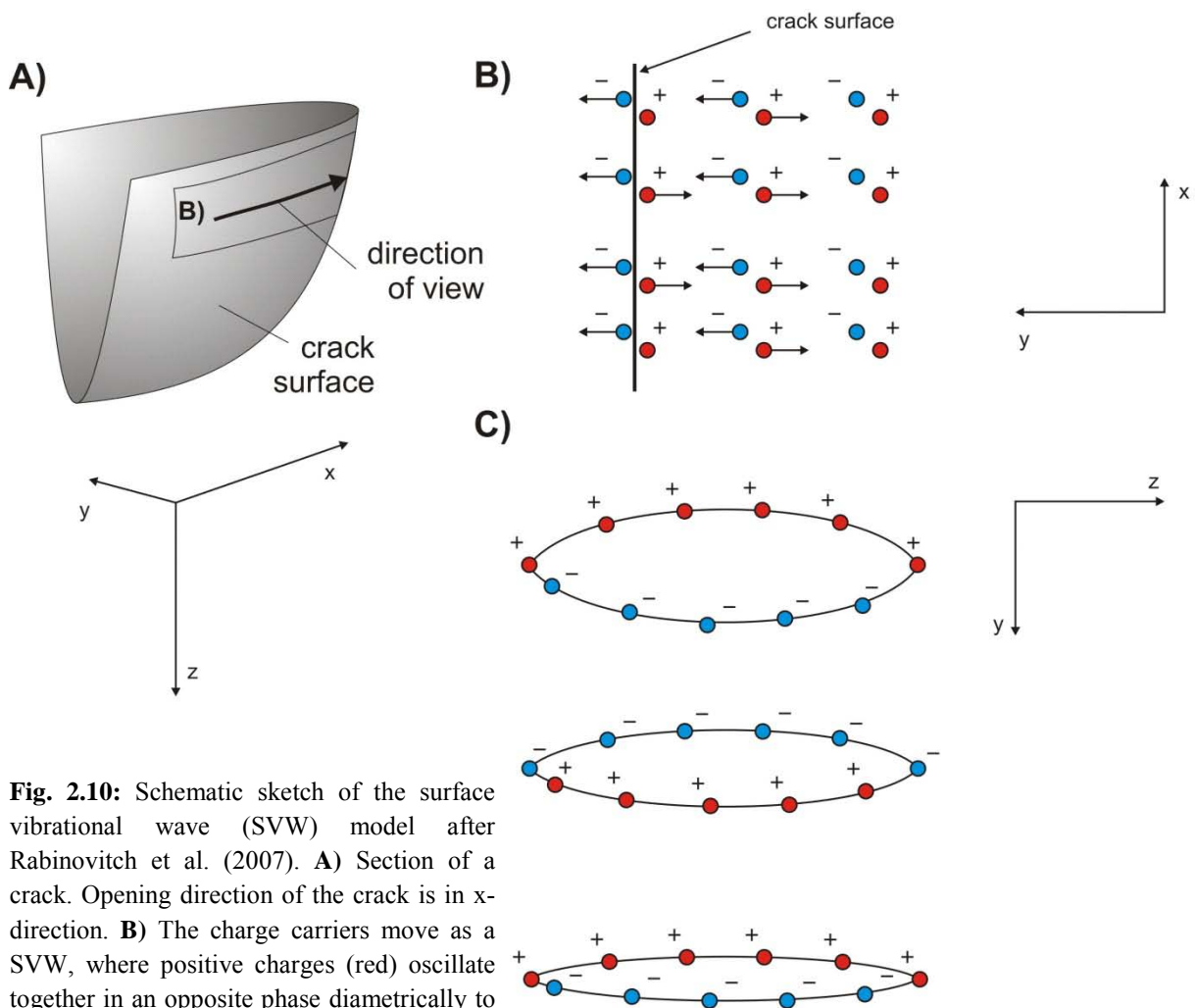
Fig. 2.10: Schematic sketch of the surface vibrational wave (SVW) model after Rabinovitch et al. (2007). **A)** Section of a crack. Opening direction of the crack is in x-direction. **B)** The charge carriers move as a SVW, where positive charges (red) oscillate together in an opposite phase diametrically to the negative charges (blue). **C)** Decay of the SVWs. Figure modified after Rabinovitch et al. (2007).

In summary, **Model (3)** is able to explain the generation of EMR (mostly) independent of the material, as well as the directional properties of the emitted electromagnetic waves, the main requirements of a source mechanism (cf. Section 2.3). Here, no differently-charged crack walls are required, only that the dipoles oscillate. Furthermore, the SVW model is in accordance with further investigations of Frid et al. (1999), Rabinovitch et al. (2000, 2002) and Takeuchi and Nagahama (2006) who are able to explain the properties of the measured EMR waves with the crack dimensions and the material properties. Furthermore, this model is independent of failure scale and loading mode. Koktavy et al. (2004) propose a combination of the charge-separation models (**Model 1**) and the SVW model (**Model 3**). It is therefore probable that more than one mechanism contributes to the generation of EMR associated with micro-cracking (cf. Table 2.3).

Table 2.3: Overview of models of EMR generation related to micro-cracking with advantages and disadvantages in explaining the properties of measured EMR and exemplary references

mechanism	pro	contra	reference, e.g.
Model 1: charge-separation processes			
emission of charge carriers and breakage of atomic bonds (**Model 1a**)	- material-independent - can explain directionality of EMR	-signal of a "white noise"-type	-Brady and Rowell, 1986 -Enomoto and Hashimoto, 1990
capacitor model (**Model1b**)	-material-independent - can explain directionality of EMR	-not capable to explain EMR pulse shape -preferential for tensile cracks	-O`Keefe and Thiel, 1995
Model 2: movement of dislocations	- mostly material-independent	- EMR increases with brittleness of material	-Molotskii, 1980 -Slifkin, 1993
Model 3: surface vibrational waves (SVW)	- material-independent - can explain directionality of EMR - can explain signal shape		-Frid et al., 2003 -Rabinovitch et al., 2007

2.4 Measuring methods

2.4.1 The Cerescope

All EMR measurements discussed in this study were performed with the Cerescope (Fig. 2.11). The Cerescope is a portable device developed by the Ceres GmbH Staffort/Baden in collaboration with the Department of Applied Geology of the University of Karlsruhe and the company "Slawische Brücke" in Dnjeprpetrowsk under the direction of Prof. Dr. W. Dachroth, Dr. H. Obermeyer, and Dr. S. Vagin. Today the Cerescope is manufactured in the "Gesellschaft für Erkundung und Ortung" (GE&O) in Karlsruhe by Dr. H. Obermeyer.

Fig. 2.11: The portable Cerescope for the determination of EMR properties in the field.

The Cerescope consists of a beam antenna/ferrite aerial and a receiver with a frequency range range of 5 kHz to 50 kHz. The beam antenna, with a length of 30 cm, is tuned to this frequency range and most sensitive to a frequency of 12.8 kHz. It provides a strongly pronounced directional receiving pattern. The antenna is most sensitive to the h-component (Section 2.2) of the electromagnetic field, so that the maximum signal is measured if the antenna is aligned parallel to the h-component and therefore to cracks. The Cerescope works with amplifications between 90 and 120 dB and reaches a sensitivity of 5×10^{-6} A/m. It is powered by a 6 V lead-accumulator that allows work for 3 to 4 days without recharging, while the limited capacity of the memory makes it necessary to take along a mobile computer, especially during the measurements along extended linear profiles (Section 2.4.2.1), to download the data.

The signals are measured as single transient pulses. If the pulses occur in a fast succession, the Cerescope measures them as pulse packages, so-called bursts. To distinguish pulses and bursts of presumably geological origin from artificial ones, it is important to adjust the Cerescope carefully. The most important steps of adjustment are the following: (1) The

selection of the frequency range. For this purpose, the spectrum analyser of the Cerescope, which shows the frequency band between 5 and 50 kHz, is used, and the quietest part of the spectrum is selected. (2) The adjustment of the amplification and discrimination level is also carried out in a graphical mode. Usually, the amplification is chosen in such a way that the signal covers 2/3 to 3/4 of the screen height, and the discrimination level is chosen to be between the background noise and peaks of presumably geological origin. The actual measuring duration is 0.1 s, while the time for calculation and storing of data depends on the number of measured counts and can last up to two seconds.

The Cerescope stores the measured and calculated values as Parameters A to E. Parameter A is the number of peaks that cross the defined discrimination level, while Parameter B is the number of bursts. The defining average amplitude of the bursts is stored as Parameter C. Parameter D is the energy of the bursts. Parameter E is the average frequency of the bursts and is only calculated if the measuring interval is at least 3 s (Obermeyer, 2001, 2005).

The data is stored in the non-volatile memory and can be transferred over the RS232 interface of the Cerescope. The download is managed by a plug-in for Microsoft Excel. Table 2.4 shows a typical data sheet. Additionally, every measuring point has a time stamp and a consecutive number. Optionally, the azimuth of the antenna can be stored. Parameters D and A appear to be most useful for meaningful interpretation. Both parameters show the same basic pattern, but the maximum values of Parameter D are commonly better pronounced compared to the background noise.

Table 2.4: Part of a data file in Microsoft Excel recorded with Cerescope. In addition to the measured data (Parameters), the subject and time of each data point is stored.

Object - sudheim_, Profile - 1_____,22.05.2007 16:48:33

Picket	ParameterA	ParametrB	ParametrC	ParametrD	ParametrE	Azimuth	Time
1	214	9	30	87	22	188	22.05.2005 13:30
2	199	6	30	50	22	188	22.05.2005 13:30
3	198	6	31	69	22	188	22.05.2005 13:30
4	261	19	33	408	22	188	22.05.2005 13:30

2.4.2 Measurement procedures

Generally, three different measurement procedures can be performed with the Cerescope. For all of these methods, the directionality of the beam antenna is the key. The three procedures comprise (1) linear measurement (Section 2.4.2.1), (2) horizontal measurement (Section 2.4.2.2), and (3) cross-sectional measurement (Section 2.4.2.3). A fourth type of

measurement, first described in detail in this study, is called "combined linear measurement" that represents a further development of the linear measurement (Section 2.4.2.4).

2.4.2.1 Linear measurements

Linear Cerescope measurements (Figs. 2.12 & 2.13) were first described by Obermeyer et al. (2001) and are taken along linear sections. They are usually carried out to detect the location of faults, landslides, or stress concentrations of other origins. Usually, a linear measurement is carried out in the time-triggered mode of the Cerescope. As a consequence, it is important to move with a constant speed along the profile to achieve a homogeneous distribution of the measuring points. This is often difficult, especially in mountainous areas, along profiles of several kilometres length, or when taking linear measurements with the car. To ensure a regular spacing between individual measurements, a GPS device was used here, which recorded the covered distance per unit time. The Cerescope and GPS data points were then combined. A more detailed description is given in Section 2.3.2.4.

During linear measurements it is crucial that the beam antenna is oriented at a constant angle to the examined object, in this case, perpendicular to the ground. It is important to avoid an oscillating motion of the antenna. Due to the directionality of the antenna, the results would fluctuate in a wide range, resulting in a saw-tooth pattern (Fig. 2.12). This effect can be avoided by fixing the antenna in a vertical position, e.g. on the backpack or on the car.
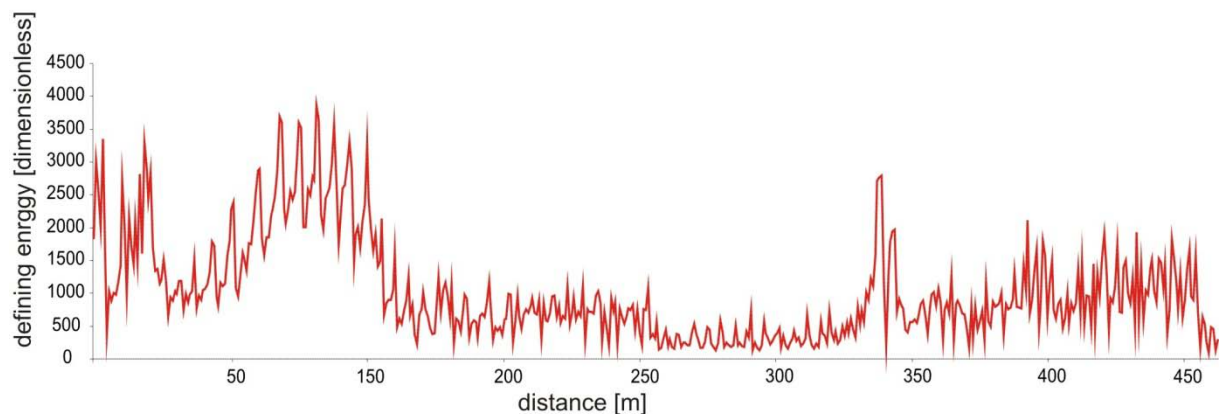
Fig. 2.12: Example of a linear measurement disturbed by oscillating movements of the antenna causing a saw-tooth pattern in the intensities.

With linear measurements, it is furthermore possible to make predictions about the strike and the dip direction of detected faults. To determine the strike direction, it is necessary to combine different linear measurements on a grid crossing the fault. The dip direction can be deduced from the asymmetric shape of the intensity curve. The highest intensities are expected to occur where the fault as EMR emitter is closest to the surface; the intensities

decrease with increasing depth in dip direction since the hanging wall material acts as a damping medium. As shown exemplarily in Fig. 2.13 A, steeply-dipping faults produce sharp increases in the intensities on both sides of the fault. For shallower-dipping faults, the pattern of the curve progression has a strong asymmetry. As emphasised in Fig. 2.13 B, moving against the dip direction of the fault results in a slow increase in intensity approaching the fault trace, followed by a sharp decrease behind the fault trace, falling back to the normal background level on the foot wall.
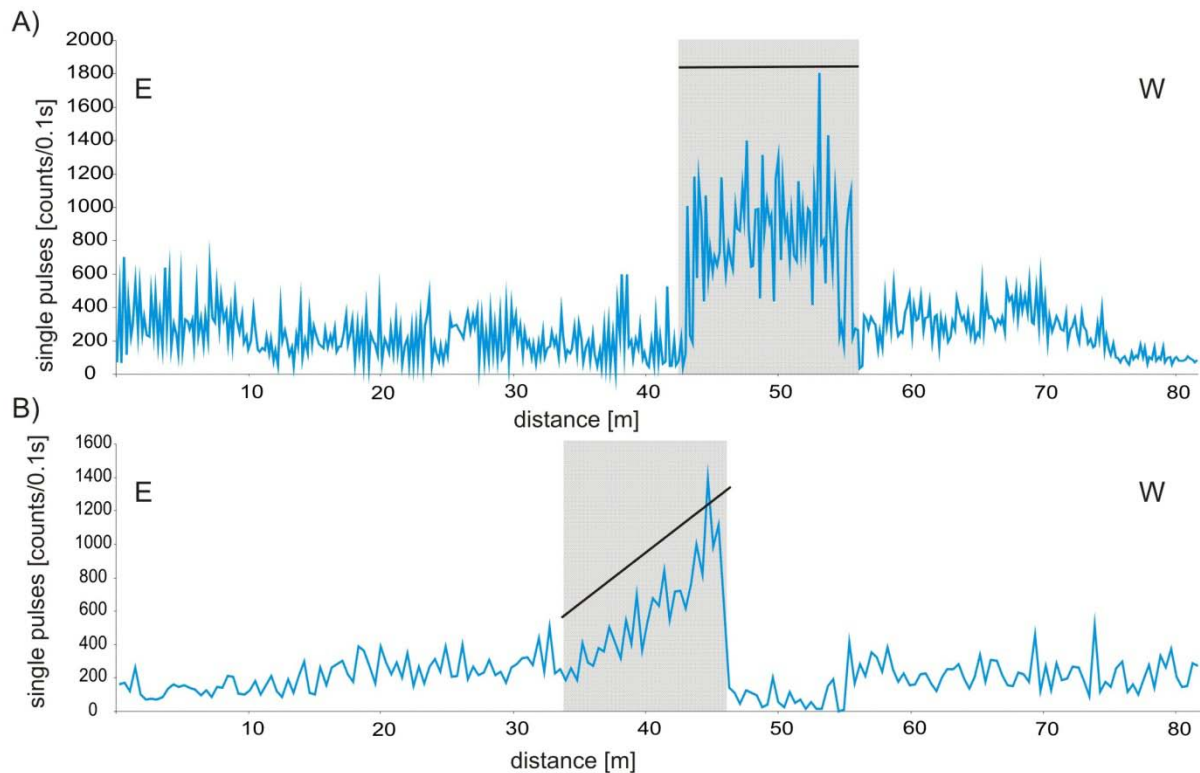
Fig. 2.13: Examples of linear measurements across faults with different dip-angles. Typical EMR signal patterns above the faults are highlighted in grey. **A)** The recorded Cerescope data of a steeply-dipping fault (location indicated by a black line) is characterised by a sharply bordered increase of EMR above the fault. **B)** The recorded data of a profile crossing a shallow-dipping fault is characterised by an asymmetric EMR pattern, increasing slowly by moving towards the foot-wall side of the fault and a sharp decrease of EMR on the foot-wall side of the fault. The dip of the fault is schematically indicated by a black line.

2.4.2.2 Horizontal measurements

With horizontal measurements it is possible to determine the main horizontal direction of EMR. Assuming tensional (mode I) micro- and nano-cracks as the source of EMR, the main radiation direction coincides with the preferred orientation of the cracks and therefore allows the determination of the direction of the main horizontal normal stress direction (σ_H). Horizontal measurements were first described by Reuther et al. (2002). They compared first the results of horizontal EMR measurements with results of conventional methods of in-situ

stress determination like borehole breakouts (SE Sicily) and concluded that horizontal EMR measurements can be used as an alternative method to determine σ_H.

During horizontal measurements the beam antenna is moved in a circle in the horizontal. In this study, two procedures were used. First, using a template with a 360° azimuth, one person rotates the antenna stepwise in 5° intervals, while a second person operates the Cerescope, resulting in 72 single measurements at each measuring location. This assures correct and highly reproducible results. An alternative method used is to mount the antenna onto an automatic turning device. This simplifies the fieldwork and the measurements can be done easily by a single person. The turning device used was equipped with a motor and a manual speed regulation, which turned the antenna with a constant speed, while the Cerescope runs in the time-triggered mode. Hence, the angles between the measurements have to be calculated afterwards according to the speed of the turning device. Furthermore, using the automatic turning device usually results in slightly different numbers of individual measurements at the measuring location. Hence the data are more difficult to compare.

For the determination of the main radiation direction, the data was analysed with a spreadsheet. The individual horizontal measurements were smoothed with the moving average over five values, then the direction with the highest intensities was read out. Usually multiple measurements were carried out at one location, and summed before the main EMR direction was determined to improve the statistics. In Figure 2.14, single pulses (Parameters A) and defining energy (Parameter D), determined during a manual horizontal measurement, are plotted in polar diagrams. Because of its usually stronger pronounced maxima, the defining energy was preferentially used for calculating the main EMR direction.
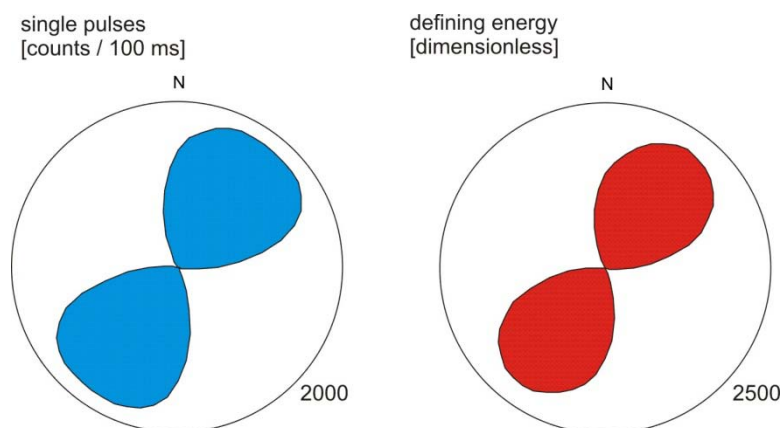
Fig. 2.14: Polar diagrams of typical EMR intensity patterns of single pulses (blue) and defining energy (red) determined during a horizontal measurement. The maximum of the defining energy is usually stronger pronounced.

Additional aspects of the bursts recorded during horizontal measurements

During this study, it has been observed that the bursts (Parameter B) are also valuable, or under special circumstances, even preferable, to determine the main EMR direction. Although previous studies paid no or little attention to the use of these bursts, an immense set of high accuracy data, taken during this thesis, can use the bursts for an easier and more accurate calculation of the main EMR direction and therefore of inferred σ_H. While the intensities of the single pulses and the defining energy are highest in the direction of σ_H (Fig. 2.14), the pattern of the bursts varies from a narrow, "clubbed" distribution (Fig. 2.15 A) perpendicular to the main EMR direction and σ_H (i.e. parallel to σ_h) to a "butterfly shape" distribution (Fig. 2.15 B) with a symmetry similar of the single pulses and the defining energy. There are smooth transitions between these two end-member shapes from a strongly symmetric "swallowtail" (Fig. 2.15 C) to asymmetric patterns (Fig. 2.15 D). It was also observed that high intensities of bursts influence the intensities of the single pulses, while the defining energy is less affected (Fig. 2.16 C & D). In particular, asymmetric patterns of bursts change the distributions of intensities of single pulses in a way that makes determination of the main EMR direction difficult (Fig. 2.16 C & D).
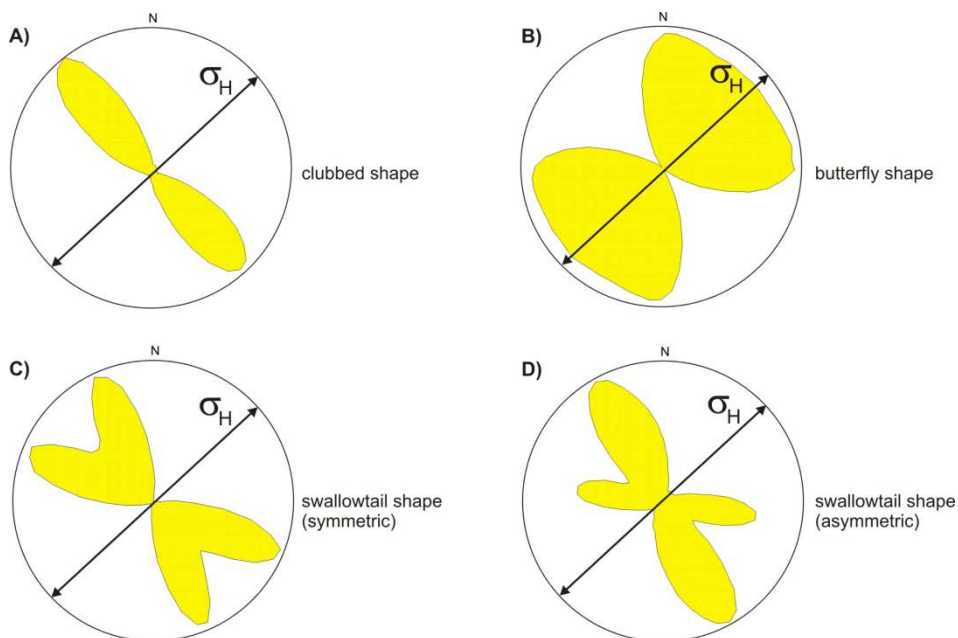
Fig. 2.15: Different shapes of the intensity distribution of the bursts, with respect to the inferred σ_H direction.

Thus the angular relationship between the narrow peaks and minima of the bursts on one side and the intensity distribution of the defining energy and single pulses on the other side can be used for σ_H determination. Furthermore, the intensity distribution of the bursts is

appropriate for an automatic calculation of the exact main EMR direction. For this reason, it is necessary to determine the maxima of the bursts, as shown in Fig. 2.16, which are perpendicular to the main EMR direction. In the case of the "swallowtail" pattern, the acute bisector and the minimum within the acute angle are exactly perpendicular to the main EMR direction. Therefore, especially in cases where of the maxima of the single pulses and the defining energy differ, it is reasonable to use the bursts to determine the main EMR direction.
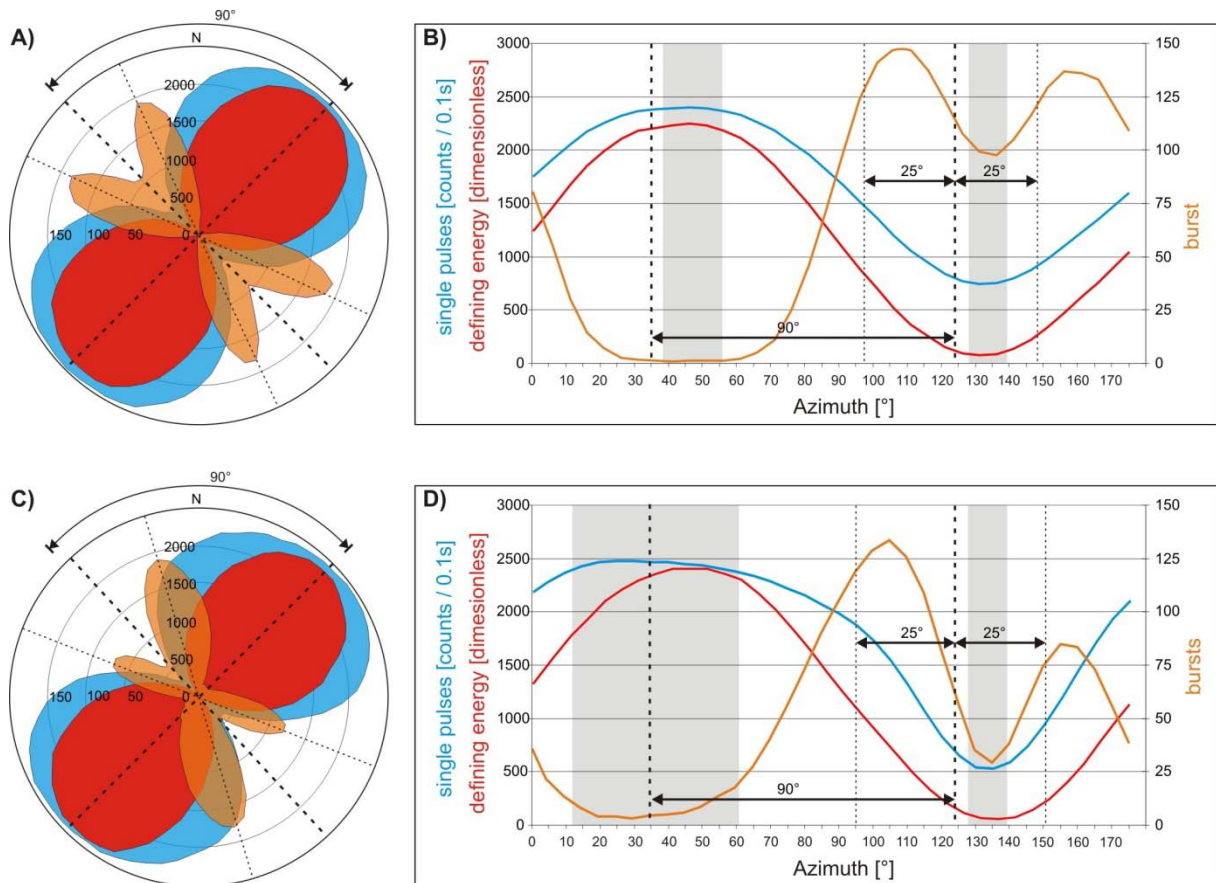
Fig. 2.16: Evaluation of the main EMR direction with respect to the symmetry of the intensity distribution of the bursts (orange). **A) & B)** Determination of main EMR direction for the case of a symmetric "swallowtail" distribution, associated with a symmetric distribution of the intensities of the single pulses (blue) and the defining energy (red). **C) & D)** Determination of the main EMR direction for a case where the distribution of the bursts and of the single pulses is asymmetric.

2.4.2.3 Cross-sectional measurements

Cross-sectional measurements are comparable with horizontal measurements, with the only difference that they are carried out in a vertical circle. For this reason, they are only applicable in tunnels or other underground excavations. Cross-sectional measurements were first described by Lichtenberger (2006a).
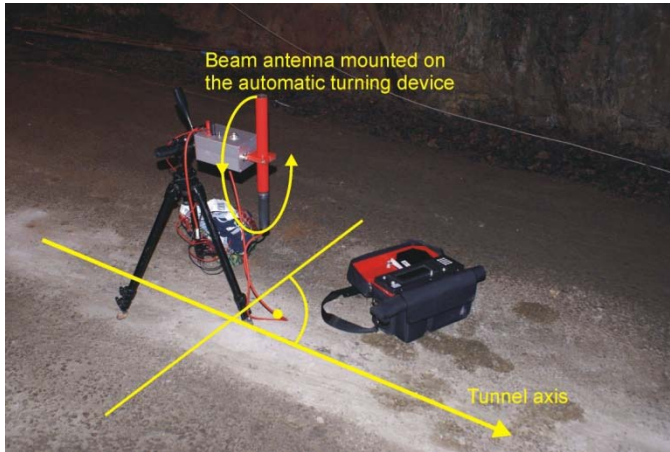
Fig. 2.17: Cerescope set-up during cross-sectional measurements in a tunnel of the Äspö Hard Rock Laboratory, Sweden.

The measurements have to be carried out perpendicular to the tunnel axis. The typical measurement set-up is shown in Fig. 2.17, where the automatic turning device is fixed on a tripod and rotates in a vertical plane. To make the data comparable throughout the whole tunnel, it is important to keep the settings of the Cerescope constant. The evaluation of the data is carried out in the same way as for the horizontal measurements. The data are usually plotted in polar diagrams. The resulting plots give information about the stress distribution along the tunnel wall (Fig. 2.18).
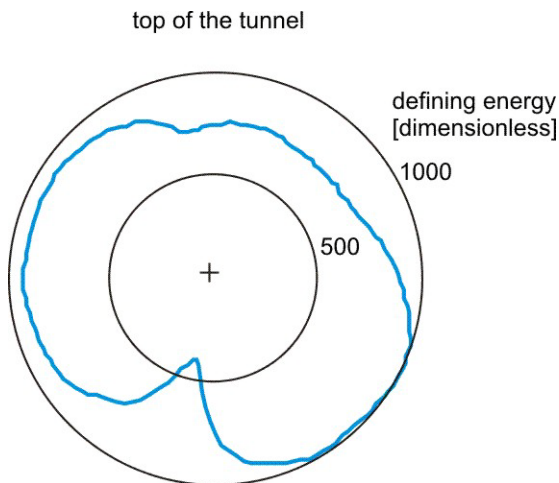
Fig. 2.18: Polar plot of the defining energy of EMR intensities along a tunnel wall, determined by cross-sectional measurements.

As the stress fields in tunnels are composite and influenced by the regional stress field, the overburden pressure, and local stresses related to the orientation, form, and the size of the tunnel, the resulting stress field is characterised by radial and shear stresses. (Hudson and Harrison, 2000). Accordingly, and on the assumption that shear stress values are proportional to EMR intensities, Lichtenberger (2005; 2006a, b) developed a method to determine not only the direction of σ_H, but also quantify its magnitude. The precondition is that a tunnel of known geometry is curved and therefore changes its orientation in relation to the regional σ_H. To calculate the magnitude of σ_H, Lichtenberger uses an approximation technique using the Kirsch Equations (Kirsch, 1898) including the tunnel geometry, its orientation in relation to regional σ_H, and the overburden pressure. For more details, the reader is referred to Lichtenberger (2005; 2006a, b).

2.4.2.4 Combined linear EMR and GPS measurements

This method, which was developed for this study, combines different linear measurements to draw a 3-dimensional plot of structures e.g. faults, which generate areas with increased EMR. For this purpose, GPS measurements were combined with the data recorded with the Cerescope. To attach geographic coordinates to each measured EMR data point, the Cerescope and the GPS measurements were performed in time-triggered mode with the same logging interval. Before combining the data, the time stamp of both measurement devices was synchronised to minimise device errors. Usually the GPS time was used as reference. It could be demonstrated that the pass difference between both devices is insignificant, so that it can be neglected during measurements that last not longer than a day. The data sets were finally combined with a relational database using the time stamp as the primary key. The same results can be achieved with an EXCEL spreadsheet with the function "vlookup".

2.5 Sources of interference/disturbance

The Cerescope is equipped with a filter system that allows the selection of relatively undisturbed frequency spectra using low-, high-, bandpass-, and notch filters (see Section 2.4.1). The measurement device is able to differentiate between artificial- and natural electromagnetic pulses by their shape, periodicity, and amplitude. Despite these filters, it is not possible to avoid interferences or disturbances and to get usable results in all environments. Therefore, it is important to plan measurements carefully with respect to the external circumstances and to critically revise every result during and after the measurement.

Effects that can influence EMR measurements while determining the direction of the stress axes in a negative way, can be divided into natural (Section 2.5.2) and artificial sources (Section 2.5.1).

2.5.1 Artificial sources of interference

Artificial sources that clearly affect the EMR measurements are power lines (irrespective of their voltage), communication lines and television cables, water-, and gas pipelines. Their disturbing signals do normally not reach further than 500 m (high voltage power lines), or only few metres (water pipes), and within these distances, it is, not possible to obtain correct geological results.

The influence of artificial sources of interference manifests in different ways for the different measuring methods. For linear measurements, the effect of artificial sources is in most cases easy to detect, because typical symmetric patterns occur when crossing such sources (Fig. 2.19). This pattern is characterised by a dramatical increase in intensity towards e.g. a power line or water pipe. Typically, directly above or below a power line (or above water- and gas pipes), a significant decrease in intensity occurs. For linear measurements, this symmetric pattern of signals is a clear evidence of an artificial origin. Walking parallel to power or communication lines results in unusually high intensities that vary less than those typical for presumably geological EMR emissions and form a high, plateau-like pattern.
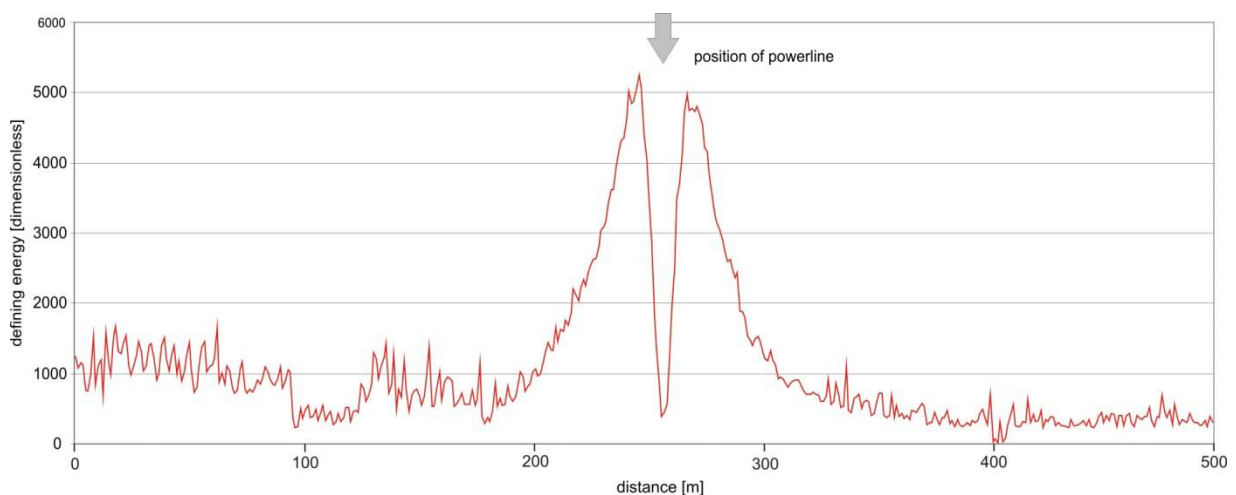
Fig. 2.19: Typical pattern of linear EMR measurement while passing a power line (near Västervik, Sweden). The location of the power line (grey arrow) is marked by an increase of intensity relative to the background noise. A similar pattern is produced by gas- and water pipes.

Furthermore, the intensity of the artificial signals is often significantly higher than the intensity produced by natural sources, such as faults. While natural sources induce intensity increases that commonly exceed the background noise by a factor of 1.5 to 2, the effect of power lines easily reaches a factor 4 and higher. The effect of water- and gas pipes depends on the size of the pipe, but it is generally not as high as the effect of power lines.

The disturbance caused by power lines, water pipes etc. requires careful planning of the location of measurements. While overhead power lines can be easily avoided, underground power lines or telecommunication cables are often located directly under paths or roads and are often only detected during EMR measurements. For this reason, pathways are often not usable to carry out linear measurements.

Other observed disturbances of linear EMR measurements are characterised by distinct changes in intensity when changing the measuring location. This effect exceeds the typical

fluctuation of intensities between two successive measurements by about 30%. These intensity changes generally occur in the vicinity of power lines at a distance of a few hundred metres. A possible explanation may be that the human body (operator) that consists of around 90% of water, acts as a lens for electromagnetic waves; therefore, the arrangement of a power line, the human body, and the antenna may influence the density of the electromagnetic field, and therefore the measurements.

During **horizontal measurements**, artificial interferences are not as easy to recognise as during linear measurements. Main evidence for an uninfluenced measurement is the geometry and the smoothness of measured signals. Typical unaffected intensity diagrams show a nearly mirror symmetric pattern in both directions of maximum intensity (Fig. 2.20).
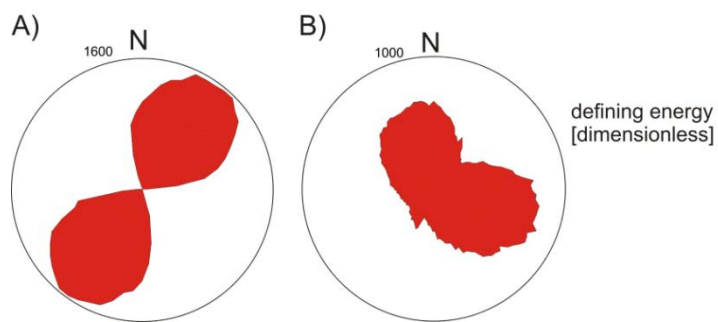
2.20: Two examples of horizontal ɪsurements. **A)** The contour of the is smooth; the intensities show two ɪmetric peaks with a NE-SW strike. Disturbed horizontal measurement, contour of the intensity distribution ɔugher, and the peaks are asymmetric point into different directions.

Another indication for artificial disturbances is the occurrence of significant deviations of the main EMR direction over short distances.

Subsurface gas- and water pipes only seem to have an effect on measurement directly above the pipes. This could be observed during the field studies in the Västervik area in southeast Sweden (see Fig. 2.21). At one point, the measured main radiation direction changed locally (within metres) by about 80°. In this case, neither the symmetry nor the smoothness of plotted measurement showed any irregular pattern; only the intensities were unusually high. By checking the area with a linear measurement, the location of an underground gas pipe could be detected exactly where the horizontal measurement had been made.
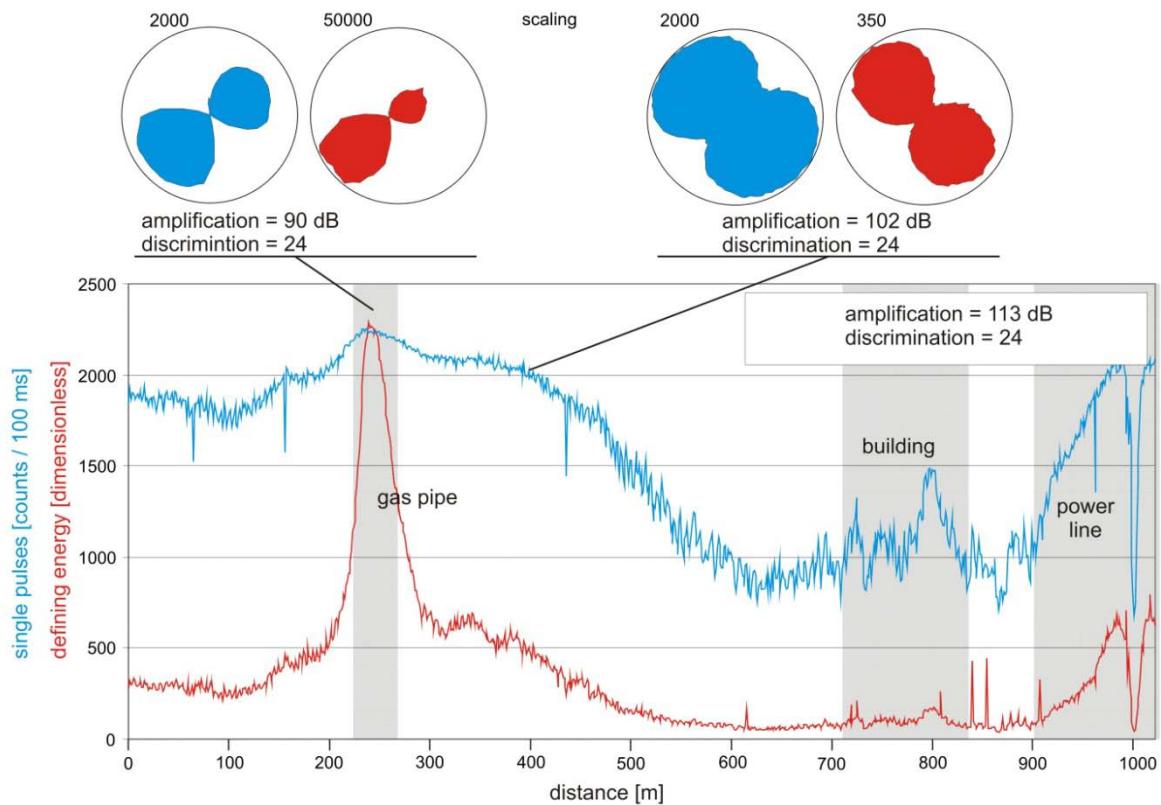
Fig. 2.21: Effect of a gas pipe on horizontal EMR measurements, example from the Västervik area, Sweden. The location of the gas pipe was detected using a linear measurement. Even with a lower amplification, the maximum intensities exceed the usual natural EMR values. The main horizontal EMR direction, measured directly above the gas pipe, coincides with the strike of the gas pipe. Areas shaded in grey show location of sources of disturbance.

In general, horizontal EMR measurements seem to be mainly insensitive to artificial disturbances, as measurements carried out in the direct vicinity of buildings, towns, or main roads showed no dependence on the distance to the object. However, I recommend not to carry out measurements in the direct vicinity of towns or other man-made facilities. Furthermore, I recommend to turn off electronic devices like mobile phones and cameras during measurements, because the effect of the illumination of LCD-displays and of the actuators from lenses can be significant.

In addition, for all types of EMR measurements carried out with the Cerescope, it is essential to be aware that by using higher amplifications, it becomes more important to keep a large distance from sources of disturbances and that the fluctuations during measurements can increase significantly.

Other artificial sources of interference like transmission masts (e.g. for mobile communication) do not seem to have an effect on the measurements. This is possibly the result of the high frequency spectrum (normally at least several MHz) that is not recognised by the Cerescope. As transmission masts act as a point source and if the transmissions would

lie within the measuring range of the Cerescope, they would be easily identifiable by a radial pattern of measured main EMR directions around them.

Several powerful military and civil VLF transmitters work in the used frequency range and are by their nature receivable everywhere. The signal of the VLF transmitters manifests on the display of the Cerescope as a distinct narrow peak. As these transmitters turned out to be an important interference factor, influences on the EMR method are discussed in a separate chapter (see Chapter 5).

2.5.2 Natural sources of interference

Apart from micro-cracking as natural source of EMR, other natural sources that can influence (and disturb) EMR measurements are the Earth tides, interaction with the irradiation from the sun (Lichtenberger, 2005), extreme meteorological conditions like thunderstorms, and extreme topographies, as previously observed by Reuther (personal communication).

As Earth tides behave in a regular, continuous pattern in diurnal and annual cycles and as they affect large areas, it can be assumed that they do not have an effect on horizontal measurements. During this study, no significant changes in direction or intensity of main EMR directions were observed during measurements over a day.

For linear measurements, the daily fluctuations of the Earth tides may have an effect, although this effect is only significant if the measurement is taken over several hours. In order to verify this it is better to carry out linear measurements along long profiles within a relatively short time or to carry out the work over several days at the same time.

During this study, strong natural disturbances that make the measurements useless were only observed during thunderstorms. Figure 2.22 illustrates the results of a time-triggered measurement with 1 second interval during a thunderstorm in the Västervik area, Sweden. The configuration of the Cerescope was such that the beam antenna was oriented in the horizontal and pointed to 060°, with an amplification of 102 dB and a discrimination level of 24. The run started while the centre of the thunderstorm was almost directly above the point of measurement and was stopped when the thunderstorm had moved about 10 km away. Each major peak corresponds to an occurrence of lightening. Every peak within the first 15 minutes could be directly identified with an occurrence of a lightening, while continuously checking the display of the Cerescope. Lightening events out of view were indirectly identified by the related thunder.

In contrast to stable weather conditions, remarkably high background intensities that switched between two different levels occurred during the thunderstorm. The higher level is

characterised by intensities of the single pulses of about 1500 counts per 0.1 seconds and intensities of the defining energy between 250 and 90 (dimensionless). The intensity of single pulses of the higher level is therefore about 50% higher than those of the lower background level. A horizontal measurement at the same point two days later during stable weather conditions, with the same measurement setup, gave single pulse intensities of 1054 and 1211 counts per 0.1 seconds in the directions 060° and 240° and defining energy values of 86 and 144 (dimensionless). Therefore it can be concluded that the lower intensity level observed during the thunderstorms coincides with the normal background level. It is not clear why a repeated switch between the two intensity levels occurred during the thunderstorm. However, it could be demonstrated that EMR measurements during thunderstorms, even at distances of several kilometres, are strongly disturbed and do not give useful results. Similar effects were observed by Nikiforova et al. (1989).
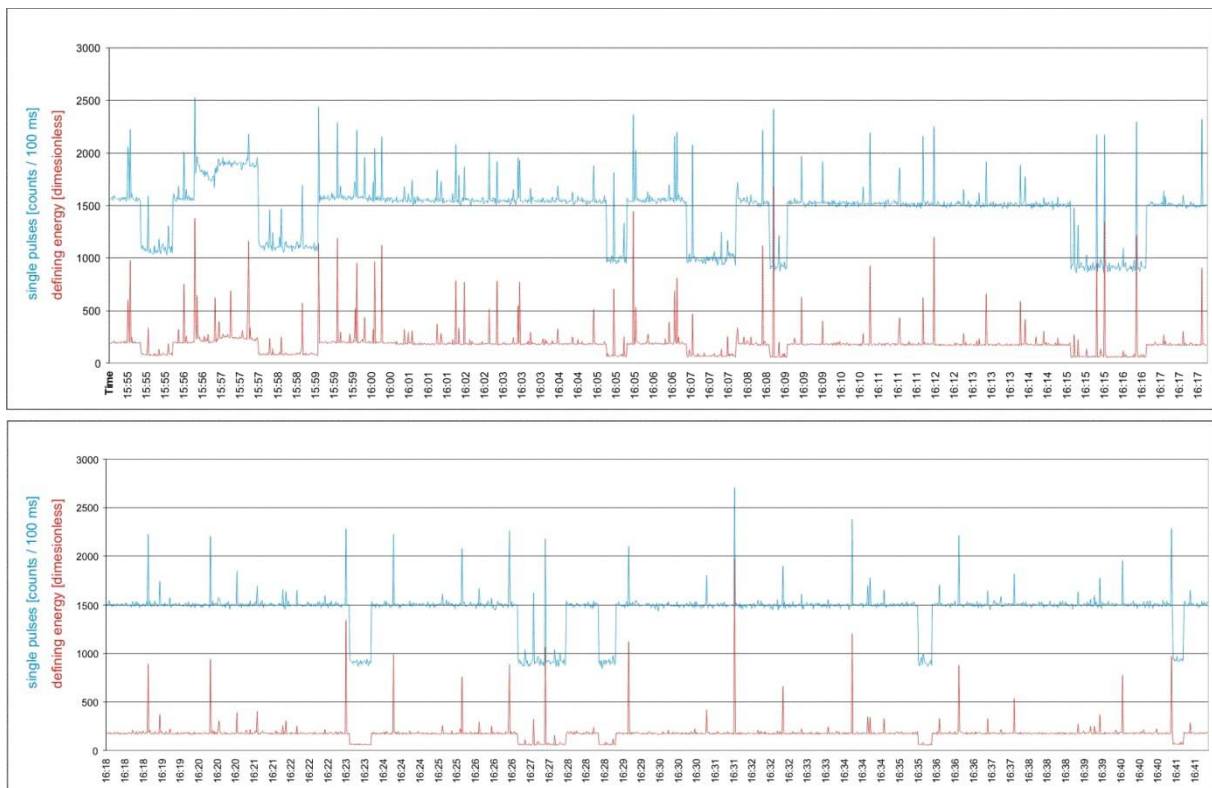
Fig. 2.22: 47 minutes time record of EMR during a thunderstorm on the 2009-05-20 from 15:54 to 16:41 in the Västervik area, Sweden. Every peak in the intensity of the single pulses and the defining energy represents a lightening event. The intensities of the lightening signals correlate with the observed distances of the lightening as determined by the occurrence of the thunder. In addition, two different levels of the background intensity occur.

3. Implications of a multi-scale analysis of brittle structures in southeast Sweden for the generation of Electro-Magnetic Radiation (EMR)

3.1. Introduction

As described in Section 2.4.2.2, the EMR method can be used to determine main horizontal stress directions (σ_H) in the upper crust. The results are in good agreement with those obtained by conventional methods like, e.g., the doorstopper method or focal plane solutions (e.g. Reuther et al., 2002).

Several laboratory studies (e.g. Egorov et al., 1988; Enomoto and Hashimoto, 1992) show that EMR occurs during brittle deformation of different materials (see Chapter 2.3). Furthermore, it is known that the direction of emitted EMR strictly corresponds to the orientation of the related structures (e.g. Rabinovitch et al., 1999; Koktavy et al., 2004), that are, in laboratory-scale samples, cracks in the millimetre and sub-millimetre range. However, the exact mechanism of the EMR generation during brittle fracturing is still under debate (cf. Section 2.3.8, e.g., O´Keefe and Thiel, 1995; Rabinovitch et al., 2007). So far, there have been no detailed studies that consider the relationship between EMR and brittle structures on the regional scale. The aim of this study is, thus, to correlate the main principle stress directions inferred from EMR measurements in the field with brittle structures on different scales in rocks. As a suitable area, the Proterozoic basement of the Västervik area in southeast Sweden was selected (see below).

For this purpose, two methodological approaches were used: (1) horizontal EMR measurements (Section 2.4.2.2) were carried out at 54 locations to determine the main horizontal stress direction over an area of about 1600 km^2; and (2) a multi-scale orientation analysis of brittle structures of the area, which included lineaments at map scale and joint pattern of different rocks. Furthermore, six oriented samples of representative rock types were used for a detailed analyses of brittle structures at meso- to micro-scale. The results of both approaches were then compared to determine, which scale of brittle fractures most likely contributes to the generation of the directed EMR.

The study area was chosen because detailed geological maps are available produced during numerous diploma mappings and because the rocks are very suitable for the analysis of crack fabrics. A further advantage of this area is the low topography with elevation differences of less than 100 m, so that the influence of gravitationally-caused stress fields, as observed in other environments (Reuther, personal communication) can be neglected. Moreover, for this

area, high-quality stress data, measured by conventional methods (SKB report, 2002), are available for comparison with the observed EMR.

3.2. Methods used for the multi-scale structural analysis of brittle fractures

The purpose of the multi-scale analysis was to identify those brittle structures that form as a result of the actual stresses or older structures, which are likely to be reactivated so they could account for the measured EMR directions. Orientation analyses of brittle structures covered a wide range of scales, starting with a lineament analysis (on satellite images), over joints down to intragranular micro-cracks and intergranular cracks along grain- and phase boundaries in sub-millimetre scale using optical microscopy. The focus was purely on the strike of these structures to compare them with the directions of horizontal EMR emissions. This simple correlation is adequate, because the main EMR direction is parallel to the propagation direction of cracks, as observed in laboratory experiments by Rabinovitch et al. (1999), Koktavy et al. (2004), and Takeuchi and Nagahama (2006) (see Section 2.3.8.1), i.e., the dip angle of the structures has no significance.

3.2.1 Lineament analysis

Lineaments are defined as lines or edges of geological origin at a scale visible on remotely-sensed images (Campbell, 1996); or, according to Hobbs (1912), lineaments are "significant lines of landscape which reveal the hidden architecture of the rock basement". The lineament analysis in this study was based on SRTM data, recorded during the "Shuttle Radar Topography Mission" and freely provided by the NASA (http:\\www.nasa.gov) of an area of about 2400 km^2 between 57.3°N 16.3°E and 58.0°N 16.8°E. The resolution of these data is about 90 m cell size. Map-scale lineaments in the Västervik area most likely correspond to the traces of major fault zones. Lineaments were analysed manually in ArcGis9.2 with the free extension "Field Calculator" for the evaluation of their length and strike. The strike of the lineaments was plotted in rose diagrams and the corresponding length distributions in histograms. Since the SRTM data only contain elevation information, lineaments of artificial origin (e.g. roads) were precluded.

3.2.2 Joint analysis

At meso-scale, joints are the most abundant brittle structures in rocks, usually formed by coalescence of micro-cracks. They are defined as fractures with no or little displacement (Price, 1966). Most joints in metamorphic and plutonic rocks, as seen in the Västervik area,

are produced by thermal contraction during uplift and cooling of the basement in a regional (palaeo-)stress field. In addition, non-tectonic joints form by the release of overburden pressure during uplift and erosion. Thus, tectonic joints reflect the regional stress field or local variations at the time of their formation They usually form regular sets over large areas (Hancock, 1985). The main set of these tectonic joints forms as extensional fractures that propagate parallel to σ_1 and is therefore often used as indicator for the palaeostress field orientation (Engelders and Geiser, 1980; Dyer, 1988; Muller and Pollard, 1977; Pollard and Aydin, 1988; Eisbacher; 1996). Consequently, a recent formation of new joints or a reactivation of older joint sets can reflect recent stress directions (Hancock and Engelder, 1989; Eyal et al., 2001).

Most of the joint data used in this study is derived from 34 unpublished Diploma mappings carried out by students of the Geoscience Center Göttingen, which cover an area of about 800 km^2. For the evaluation of the main strikes, only joints with a dip steeper than 60° were selected to minimise measuring errors. Furthermore, joints in meta-sedimentary rocks have been ignored, because their orientation may have been influenced by primary sedimentary structures (mainly bedding planes).

3.2.3 Meso-crack analysis

For this study, meso-cracks are defined as cracks with strike dimensions significantly smaller than that of joints and larger than that of micro-cracks. Thus, the strike dimensions of meso-cracks in the six samples are in the range of some millimetres to some centimetres, i.e., visible with the naked eye.

The orientation and length of meso-cracks were measured on horizontal, polished slices of oriented samples with a calliper and a goniometer. The meso-cracks were measured on the same horizontal slices that were later used for thin sections for micro-crack analysis. The evaluation of the orientation and the length was done without considering age relationships between different sets.

3.2.4 Micro-crack analysis

Micro-cracks are here defined as fractures with lengths in the millimetre to sub-millimetre range. Their strike and trace length in the samples were analysed in two ways: **(1)** From the surfaces of polished horizontal slices (with areas of 50 cm² and 200 cm²) (samples described in Section 3.3.2), photographs of ten representative domains with an total area of 10 cm² where taken with a Carl Zeiss binocular Stemi 200-C, using an AXIOS Camera Axio ICc1. A

grid with 1 cm spacing was lain on every examined sample slice and 10 squares of representative parts of the sample, each with an area of 1 cm^2, were selected. The selected areas were homogenous with respect to fabric and composition. Two photographs with different light exposures were taken of each square to avoid illumination effects and to make sure that as many micro-cracks as possible become visible. The two pictures were stacked and stitched together with the other pictures of the horizontal slice. The composite picture was imported into ArcGis 9.2 to measure the trace lengths and strike of the micro-cracks in the same way as done for the map-scale lineaments (described in Section 3.2.1, Fig. 3.1). Also, the mineralogy of the host grains of micro-cracks was considered. For simplicity reasons, only the major minerals quartz and feldspars (k-feldspar and plagioclase) were taken into account. For micro-crack stress correlation, quartz is the preferred mineral because of its great abundance in different crustal rocks and the lack of twin lamellae or cleavage planes that could strongly affect the direction of crack propagation in a way that it deviates from the regional stress field (e.g. Kranz, 1983; Vollbrecht et al., 1999). Furthermore, several studies show that quartz is highly affected by micro-cracking in different tectonic settings (Vollbrecht et al., 1989).
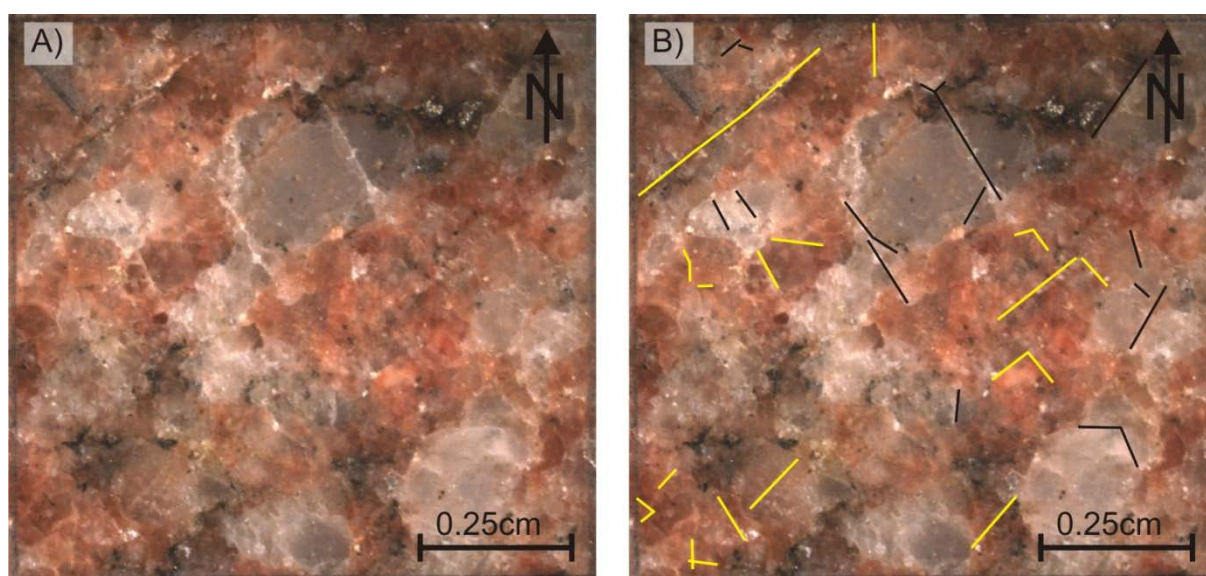
Fig. 3.1: A) Photograph of a 1 cm^2 section of the surface of a horizontal, polished slice of an oriented sample of a metagranite from the Västervik area (sample 87). **B)** Strike and length of micro-cracks on the sample surface were measured and classified according to grain mineralogy (yellow lines mark the traces of micro-cracks in potassium feldspar; black lines mark the traces of micro-cracks in quartz).

The described technique was not used for sample 84/2, because its grain size is too small to observe micro-cracks at this magnification. Therefore a second methodological approach **(2)** was used on sample 84/2. The strike of micro-cracks was analysed in a standard thin section

made of a horizontal slice of the sample. The used magnification was between 5x and 20x, depending on the grain-size. Here, only the strike of micro-cracks was measured using a conventional cross-table.

The micro-cracks measured with both methods were classified according to the mineralogy of the grains. Only open cracks and the most recent generations were measured, which can mostly be distinguished from older cracks that are usually healed or sealed. Healed cracks can be identified from fluid inclusions along the cracks, while the latest generation of open micro-cracks show sharp boundaries without mineral precipitations. Sealed cracks are closed by mineral precipitations such as hematite, which is typical for comparatively young cracks (Vollbrecht et al., 1994) formed close to the surface. Therefore, cracks with hematite-coated walls were also taken into account. Sealing with other minerals was not observed.
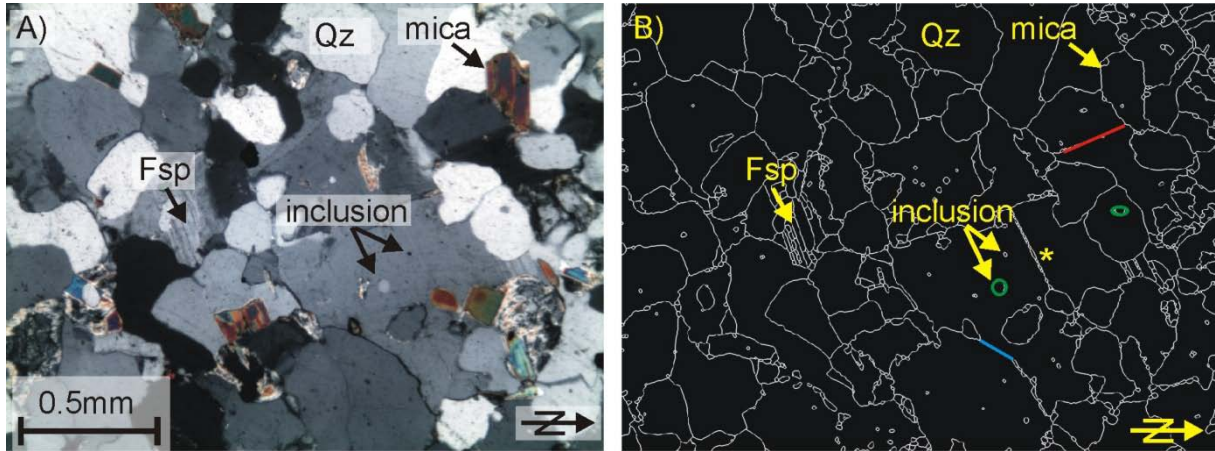
3.2.5 Grain- and phase-boundary analysis

As grain and phase boundaries are preferred loci of intergranular micro-crack initiation, also the grain- and phase-boundary orientation distribution was analysed. For this purpose, the automatic "rotating polarizer stage" was used. Parts of the horizontal sample slices were used for the preparation of thin sections. In each of these thin sections, five representative sections were selected of five of the samples and analysed by microscopy with a magnification of 2.5. Only for sample 104, six sections were analysed because of the large grain size.

For each section, 200 images with different polarisations were automatically captured by the computer-controlled rotating polarizer stage (Fig. 3.2). During this procedure, the polariser within the microscope stage is rotated stepwise (with an interval of 1 gon).

The resulting dataset therefore consists of 200 individual images that were subsequently combined (Fig. 3.2 A) and analysed with the automatic edge-detection routine of the software "GEOVISION 6.0". This routine automatically detects grain and phase boundaries by indentifying contrast gradients in the stacked image and completing these to grain boundaries (Fig. 3.2 B). This works properly with pure quartzites, but it is somewhat problematic if the sample contains larger amounts of other minerals, in this case feldspars and mica, or small inclusions in the minerals. Therefore, the results of the automatic edge-detection were refined manually, e.g. by disregarding twin lamellae identified as grain boundaries, to improve the results (Fig. 3.2 B). It has to be considered that the automatic edge-detection measures each edge length between two triple points (Fig. 3.3). For this reason, particularly longer boundaries are often cut in several sections that are counted separately by the software. As a result, the grain-boundary direction of long grains is statistically falsified by an amplification of the number of grain boundaries parallel to the long axis of the grain. Since each micro-

crack emits an EMR pulse, a wrong number of micro-cracks per direction would falsify the results.

Fig. 3.2: Example of grain- and phase-boundary determination by the automatic edge detection of the software "GEOVISION 6.0". **A)** Photomicrograph of sample 87 under crossed polars. The analysed dataset consists of 200 stacked images captured with the "rotating polarizer stage" assembled by "GEOVISION 6.0". **B)** Image of A) after processing the automatic edge detection with "GEOVISION 6.0" without manual refining. White lines represent the automatically-detected grain and phase boundaries. The yellow asterisk marks an intra-granular micro-crack, identified as a grain boundary by the software, which was deleted during the manual refining. The grain boundary marked by a red line has a curvature factor of 1, while the blue-marked grain boundary has a curvature factor of -1, depending on their orientation in the reference system of the "rotating polarizer stage". The green-marked inclusions have a curvature factor of 0 and are neglected during data analysis.

To quantify this statistical effect, the rose diagrams were (1) plotted separately for different grain-boundary lengths, and (2) an additional analysis was carried out, where the grain-boundary lengths were grouped according to their direction, and the boundary length was summed for all boundaries in each group. Consequently, the true boundary length in relation to the strike of the boundaries could be evaluated.
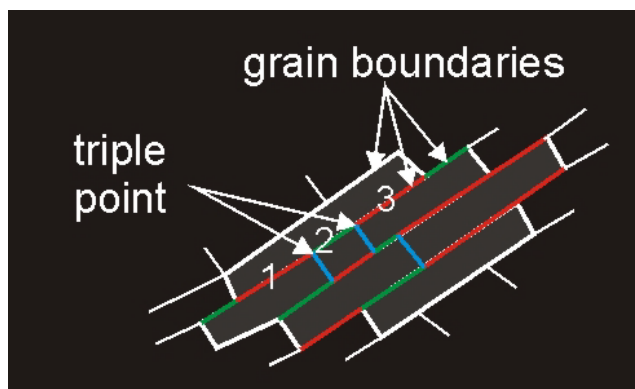
Fig. 3.3: During edge detection with "GEOVISION 6.0" grain and phase boundaries are separated at triple points. Consequently, long grain and phase boundaries are disected more often than short boundaries. Therefore, the direction of the long axis of these long grains appears disproportionally more often in the statistics.

The curvature of the boundary segments detected by the automatic edge-detection represents another statistical problem. Since an EMR contribution by grain/phase-boundary cracks occurs parallel to their strike, curved boundaries can contribute in a more or less wide angular range to the EMR. Furthermore, small inclusions detected by the software and not manually rejected (see Fig. 3.2 B) result in completely round and closed boundaries and have to be ignored in the

evaluation, because no preferred radiation direction can be expected. To quantify this effect, every calculated grain boundary is attributed a curvature factor called R-statistics in "GEOVISION 6.0". The curvature factor has a range of -1 to 1, where -1 and 1 are straight boundaries without curvature. A curvature factor of 0 describes completely circular and closed forms. For the evaluation of the data, only grain/phase boundaries with a curvature factor of 0.8 to 1, and -0.8 to -1 respectively, were used. To ensure that the results were not statistically falsified by this data restriction, the effects were exemplarily tested for sample 83 (Fig. 3.4). For this purpose, the complete dataset was grouped according to curvature factor, and the strike distribution of each group was determined as function of the number of grain boundaries and as a function of the boundary length per direction. The results indicate that about two thirds of the data lie in a range of the curvature factor 0.8 and 1 (and -0.8 to -1) and that this data contributes with about 60% to the total grain- and phase-boundary length. By including boundaries with higher curvature (R < 0.8 and R > -0.8) the results to become less well defined; however, they show the same main trends. In the following, the grain- and phase-boundary data of all samples was filtered by curvature prior to further analysis.
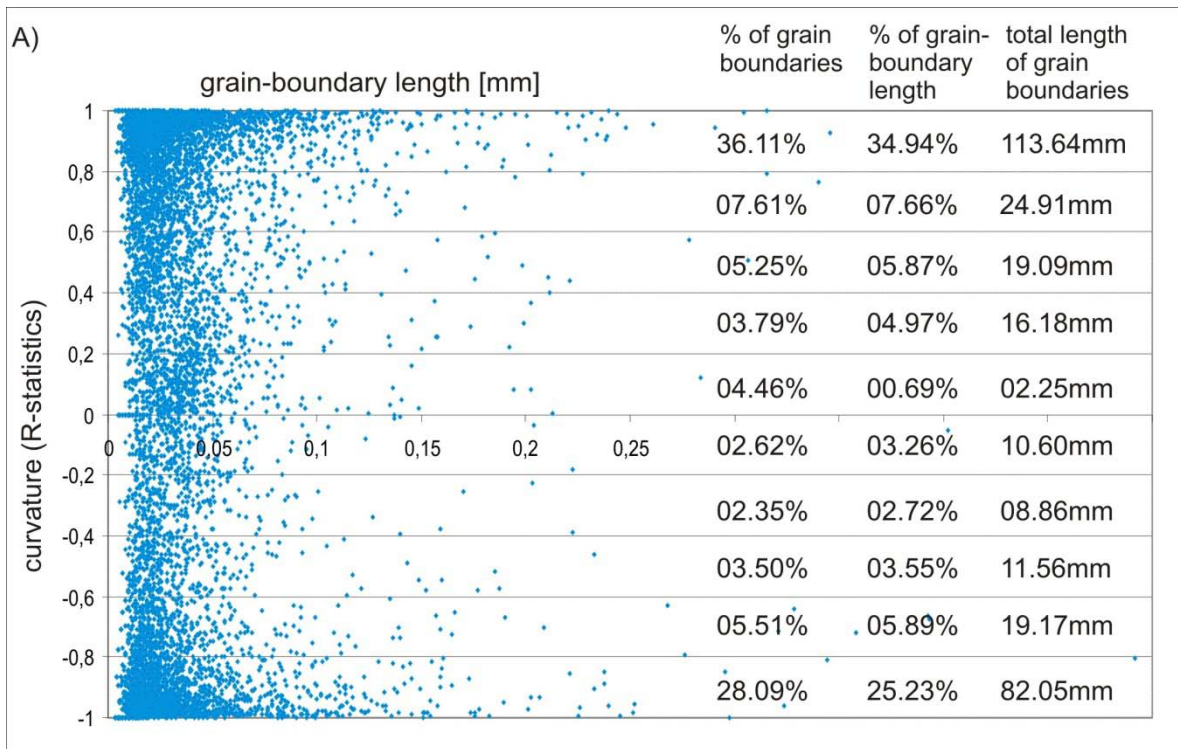
Fig. 3.4: Exemplary statistic test for sample 83: influence of reduced number of data as a result of filtering grain/phase-boundary data as a function of curvature. **A)** For grain/phase boundaries with a curvature factor of 0.8 and 1, and -0.8 and -1 respectively, 65% of grain/phase boundaries and 60% of the corresponding grain/phase-boundary length remain for further analysis. **B) - E)** overpage.
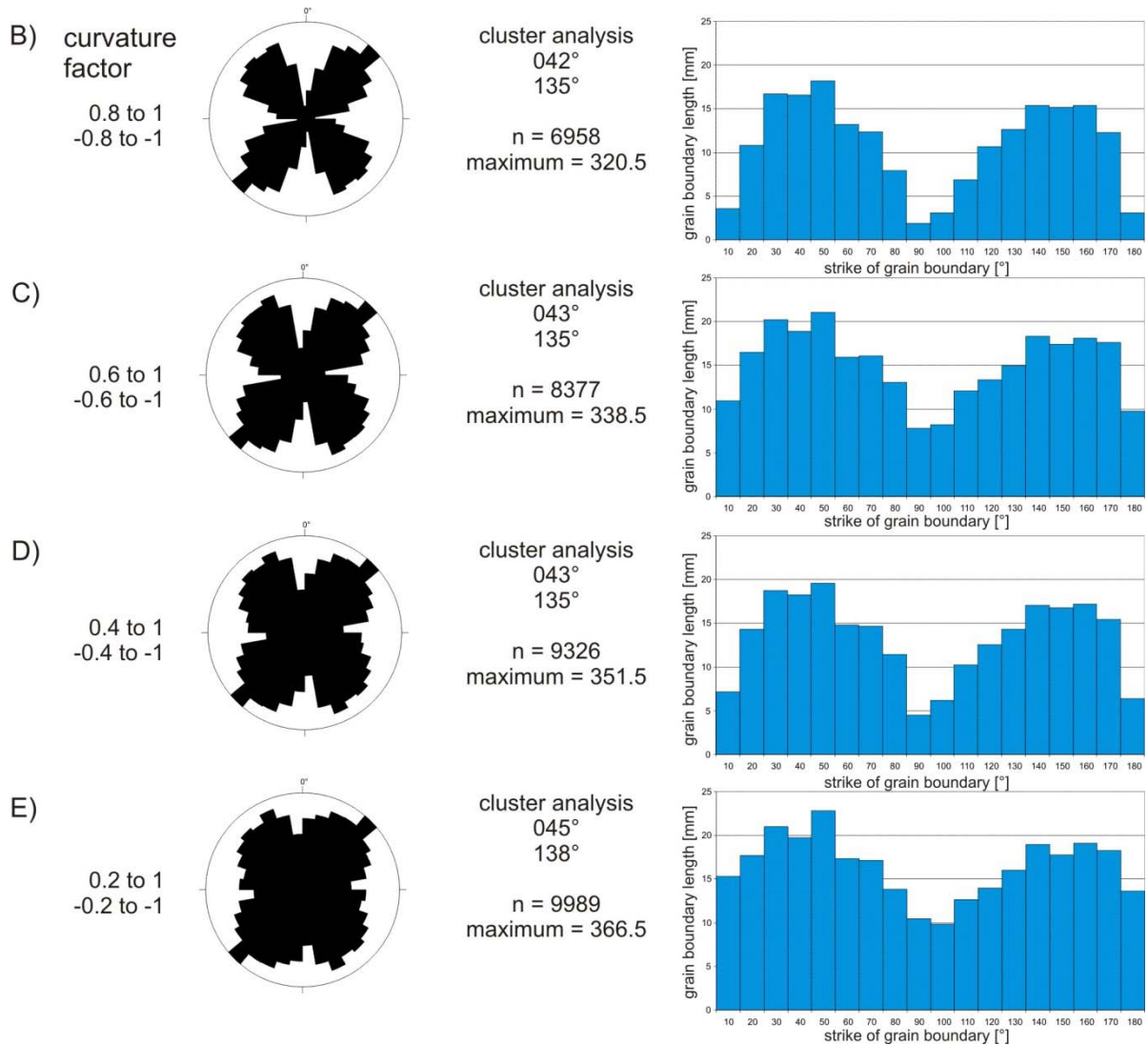
Fig. 3.4: Exemplary statistic test for sample 83: influence of reduced number of data as a result of filtering grain/phase-boundary data as a function of curvature. **B) - E)** A further increase of the data range by adding stronger-curved grain/phase boundaries has no significant effect on the resulting main strike.

3.3 Geological setting

3.3.1 Geological and tectonic evolution of the study area

The study area is located on the Baltic Shield, which is part of the East European Craton. The Baltic Shield consists of four sub-domains that comprise the Archaen Domain, the Proterozoic Svecofennian Domain, the Transscandinavian Igneous Belt (TIB), and the Southwest Scandinavian Domain (Fig. 3.5 A). A fifth unit is represented by the Caledonides that have been thrusted over from the NW onto the Precambrian Basement. The four sub-domains of the Baltic Shield become successively younger towards the southwest. The Svecofennides were accreted to the Archean Domain, the oldest part of the Baltic Shield, during the Svecofennian orogeny between 1.95 Ga and 1.85 Ga (e.g. Gaal and Gorbatschev, 1987; Nironen, 1997; Lahtinen et al., 2005). To the south of the Svecofennian domain, is the

TIB. The TIB is a ~1500 km long N-S extended, and several hundred kilometres wide batholitic complex (e.g. Andersson, 1991; Högdahl et al., 2004) that is separated from the Svecofennides by the Loftahammar-Linköping Deformation Zone (LLDZ; Fig. 3.6), a dextral transpressional, WNW striking shear and suture zone (Högdahl et al., 2004). The TIB formed during a period of intensive magmatic activity between 1.83 and 1.65 Ga (Gorbatschev and Bogdanova, 1993) and consists mostly of granitic, monzonitic, and monzodiortic intrusions (Lindh and Bylund, 1987; Högdahl, et al., 2004), and subordinate meta-volcanic and meta-siliciclastic rocks.

Fig.3.5: Geological maps. **A)** The Baltic Shield and its four sub-domains, the Archean Domain, the Proterozoic Svecofennian Domain, the Transscandinavian Igneous Belt (TIB), and the Southwest Scandinavian Domain. The Proterozoic Svecofennian Domain is subdivided into two volcanic belts (VB) and the enclosed Botnian Basin (BB). Area of B) is marked by a frame. **B)** Southern Sweden with the study area outlined by a frame (detailed geological map see Fig. 3.6). OJB - Oskarsham-Jönköping-Belt; LLDZ - Loftahammar-Linköping Deformation Zone; TTZ - Teisseire-Tornquist-Zone, after Beunk and Page (2001) and SGU (1994).

The Svecofennian Domain is sub-divided into three units: two volcanic belts (VB in Fig. 3.5 A) that were accreted between 1.91 Ga and 1.87 Ga and enclose the third unit, the Bothnian Basin (BB in Fig. 3.5 A), that formed at about 1.95 Ga (Nironen, 1997). The

volcanic belts consist mostly of calcalkaline volcanic rocks, rhyolites, and dacites with intercalated limestones, while the Bothnian Basin comprises mainly meta-greywackes and meta-pelites (Claesson and Lundqvist, 1995).

granite, granodiorite 1.6 - 1.0 Ga
gabbro, diorite 1.87 - 1.66 Ga
basalt 1.87 - 1.66 Ga
granite, granodiorite 1.87 - 1.66 Ga
rhyolite, dacite, andesite 1.87 - 1.66 Ga
granite, granodiorite 1.87 - 1.75 Ga
basalt 1.96 - 1.86 Ga
granite, granodiorite 1.96 - 1.86 Ga
sandstone, greywacke & shale 1.96 - 1.86 Ga
diabase

sample location of meta-sedimentary rocks
sample location of intrusive rocks
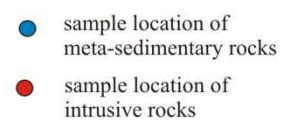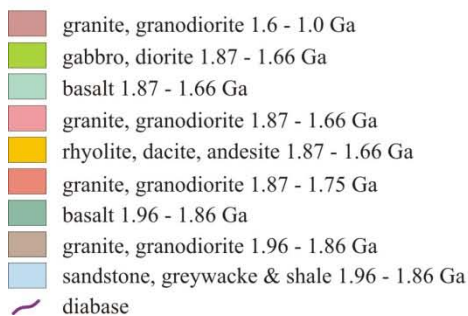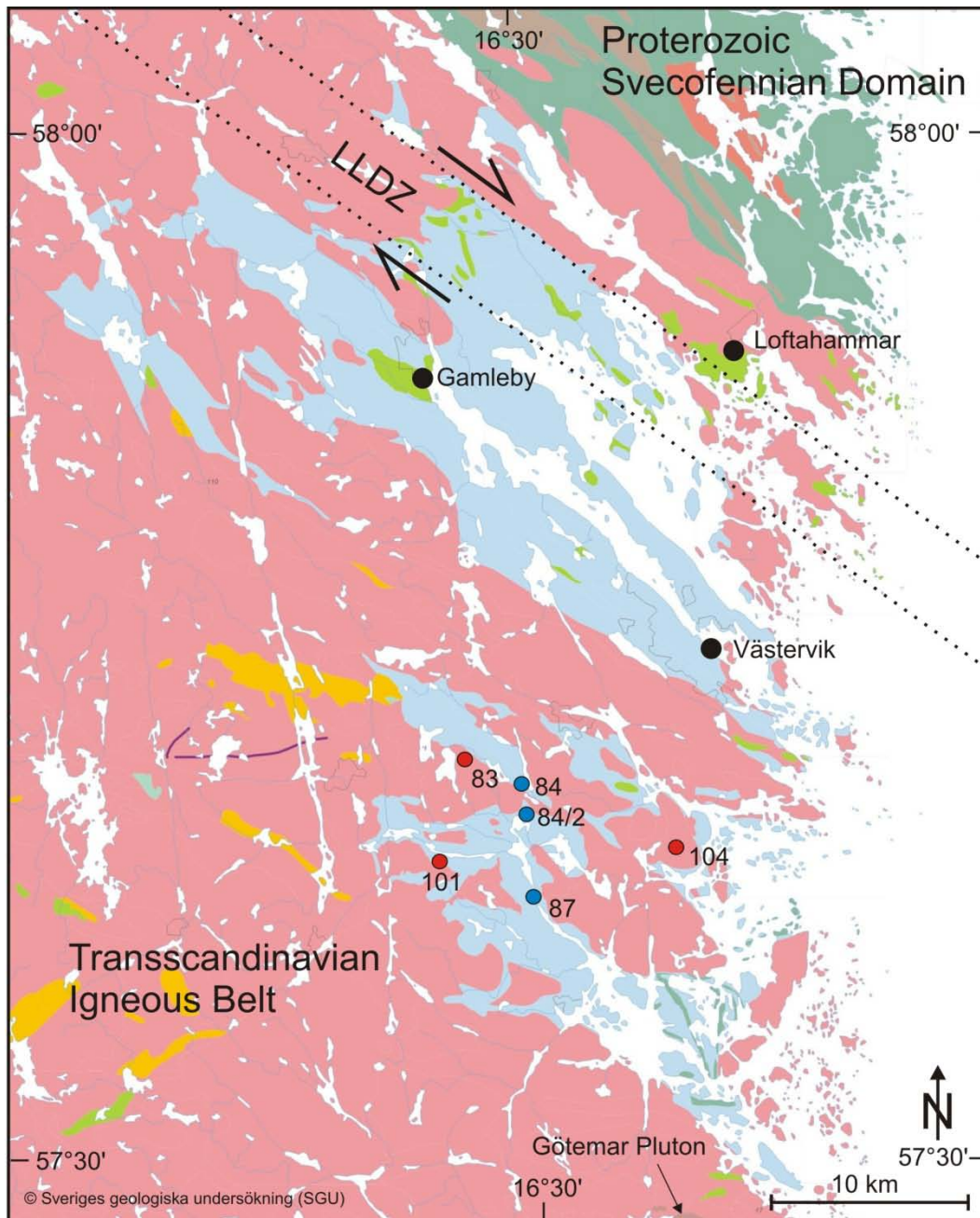
Fig. 3.6: Geological map of the Västervik area, southeast Sweden, with sample locations (see Sections 3.3.2, 3.3.4, 3.3.5, and 3.3.6. Modified after © Sveriges Geologiska Undersökning (SGU).

The study area around Västervik (Fig. 3.6) is part of the transition zone between the TIB and the Svecofennian Domain. The Västervik area itself is located between the Oskarshamm-Jönköping-Belt (OJB) to the south and the LLDZ to the north. The NNW-trending OJB is interpreted as an island-arc complex that consists of sedimentary, volcanic, and intrusive rocks belonging to the TIB (Mansfeld, 1995; Andersson 2006, 2007).

The meta-sedimentary rocks of the area consist predominantly of quarzites that contain sedimentary structures, such as cross-bedding and ripple marks (Gavelin, 1984; Vollbrecht and Leiss, 2008). They have been folded and affected by amphibolite-facies and partly by retrograde greenschist-facies metamorphism. From 1.87 Ga on the meta-sedimentary rocks were intruded by several generations of TIB granitoids, which led to contact metamorphism in the vicinity of the intrusions. Following the intrusion of the TIB granitoids, additional shear zones were formed.

The multi-phase deformations of the area reflects changing stress regimes that resulted in a complex deformation pattern, including folds at all scales, faults, shear zones and distinct foliations (see e.g. Beunk and Page, 2001; SKB-report, 2002 and references therein). The present-day structural inventory is characterised by dominant NW-SE striking structures on all scales.

The recent stress field in Scandinavia (Fig. 3.7A) is mostly affected by the Atlantic ridge-push force (e.g. Gregersen et. al, 1991; Stephanson et al., 1991) and by the continent-continent collision between Africa and Europe (e.g. Fieldskaar et al., 2000). This results is an NW-SE directed compression (Gregersen et al., 1991; Heidbach et. al, 2008), evident from different in-situ stress measurements carried out in Sweden and focal plane solutions (Fig. 3.7B). In addition, the recent crustal dynamics are also affected by postglacial isostatic uplift, which started after the last deglaciation at about 10.000 a ago. The actual isostatic uplift rate is up to 8 mm/a in central Scandinavia; in the study area the rates range between 1 and 2 mm/a (Fieldskaar et al., 2000). As a consequence elastic relaxation occurs resulting in horizontal movements away from the centre of uplift, with velocities in the range of 1 - 2 mm/a (Carlson and Olsen, 1982). These movements preferably take place along pre-existing faults.
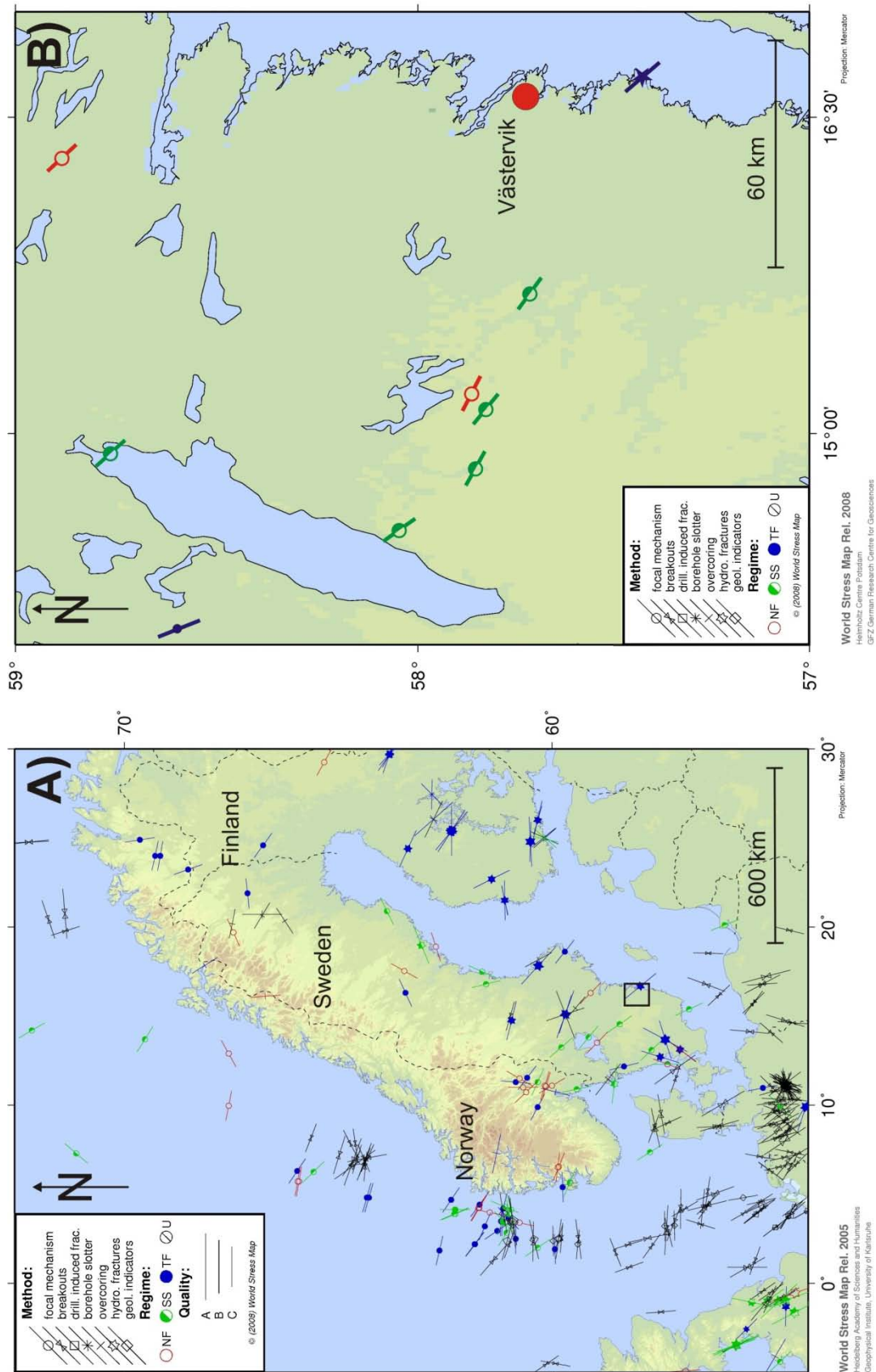
Fig. 3.7: Stress maps. **A)** Direction of the maximum horizontal stress σ_H in northern Europe. Area of B) is marked by a frame. **B)** Orientattion of σ_H in the Västervik area. Maps based on WSM (Heidbach et al., 2008). For method applied to determine σ_H and stress regime, see inset key. Projection: Mercator.

3.3.2 Sample description

The six samples that were used for the analyses of meso-, micro-crack and grain-boundary orientation were taken from an area of about 250 km^2 (Fig. 3.6). To investigate the possible influence of different materials on the generation of EMR, a representative spectrum of different lithologies was considered. Horizontal slices were cut from the oriented samples after reorientation in a sandbox. The sample slices were then polished and furthermore used for the preparation of thin sections. In the following, a short description of the samples is given; a summary of the main features of the samples is given in Table 3.1.

Sample 83

Sample 83 (Fig. 3.8 A&B) is a medium-grained (average grain size ~3 mm) alkali feldspar granite (nomenclature of igneous rocks according to the Streckeisen classification). It contains about 50% quartz and 40% feldspar (k-feldspar, plagioclase), while the remaining 10% are mainly mafic minerals, predominantly hornblende and biotite. Accessory components comprise sphene and opaque minerals. There is no shape preferred orientation of minerals recognisable with the naked eye. The potassium feldspar crystals (average size ~5 mm) form a porphyric fabric with a slight NNW-SSE alignment. The alkali feldspars are mostly unaltered and surrounded by a matrix of quartz and plagioclase grains. Plagioclase crystals (grain size ~2 mm) are rounded and sericitised, while quartz forms polycrystalline aggregates (size of individual grains lies in the sub-millimetre range). Individual quartz grains are equigranular to slightly elongate with a preferred NW-SE orientation. The grain boundaries are interlobate.

Sample 101

Sample 101 (Fig. 3.8 C&D) is a light-reddish alkali feldspar granite with ~ 60% quartz, 35% feldspar (k-feldspar and only a small amount of plagioclase), and about 5% mafic minerals, mainly biotite and hornblende. The average grain size is 0.1 mm. The grain shapes are mainly xenomorphic. The quartz grains occur as polycrystalline aggregates (grain sizes of << 0.1 mm) and as a few single grains with sizes of up to 0.2 mm. As a whole, the quartz grains exhibit a NW-SE shape preferred orientation. In contrast, no preferred orientation of the feldspars crystals is recognisable. Potassium feldspar and plagioclase have average grain sizes of <1 mm. Plagioclase crystals show a weak sericitisation.

Sample 104

Sample 104 (Fig. 3.8 E&F) is a red fine-grained, porphyric alkali feldspar granite (average grain size <2 mm). The rock contains around 50% feldspar (predominantly alkali feldspar), about 40% quartz, and 10% mafic minerals (biotite and hornblende). Quartz occurs as polycrystalline aggregates in the matrix with grain sizes in the sub-mm range. Individual quartz grains are elongate in NW-SE direction. The alkali feldspar phenocrysts (size of individual grains ~3 mm) are hypidiomorphic and show a slight NNW-SSE shape preferred orientation. The plagioclase crystals (crystal sizes ~2 mm) are rounded and their rims are sericitised.

Sample 84/2

Sample 84/2 (Fig. 3.9 A&B) is a fine-grained (average grain size ~0.4 mm), reddish, siliciclastic meta-sedimentary rock with well-preserved bedding. It consists of 80% quartz, 10% alkali feldspar, and 10% biotite. The polygonal quartz grains show a NW-SE shape preferred orientation. The bedding is manifested by the occurrence of biotite crystals with an average grain size of <0.5 mm. Alkali feldspar is sericitised and occurs as sericite aggregates with sizes of ~1 mm.

Sample 87

Sample 87 (Fig. 3.9 C&D) is a fined-grained grey, quartzitic meta-sedimentary rock with well-preserved sedimentary structures. The average grain size ranges from 0.1 to 0.5 mm and varies as a result of preserved graded bedding. The bulk of the sample consists of more than 90% quartz. In contrast, coarser-grained parts contain about 80% quartz. The remaining 10% to 20% consists mainly of feldspar (predominantly plagioclase) and biotite. Quartz grains have lobate grain boundaries and are slightly elongate parallel to the bedding plane. The plagioclase crystals are unaltered and have the same grain size as the quartz crystals. Biotite crystals with sizes similar to those of the surrounding quartz grains occur preferably in the uppermost parts of the graded beds.
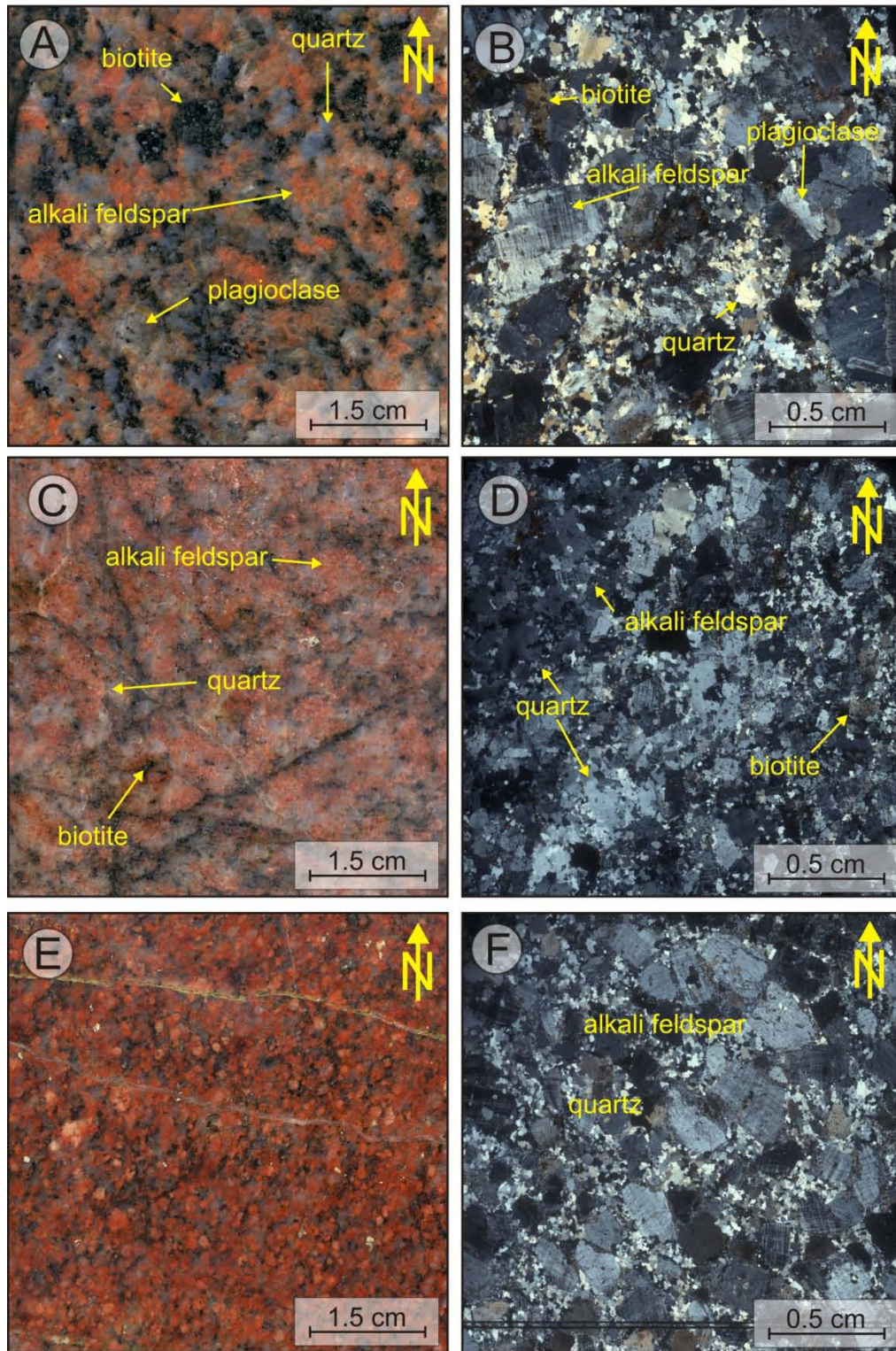
Sample 84

Sample 84 (Fig. 3.9 E&F) is a reddish meta-arkose with about 80% quartz, 10% feldspar (mainly k-feldspar), and 10% biotite. Macroscopically, the rock is characterised by well-preserved parallel and cross-bedding. The average grain size is around 0.3 mm. Quartz grains have polygonal shapes without recognisable shape preferred orientation and seriate interlobate

grain boundaries. The reddish colour of the rock originates from alkali feldspar crystals that are evenly distributed throughout the rock as xenomorphic, ~0.6 mm long crystals with a shape preferred orientation parallel to the bedding plane. Plagioclase crystals that are in size similar to the k-feldspar grains are sericitised. Biotite occurs as crystals that range in size from 2 mm down to sub-mm size and are accumulated preferably on former bedding planes.

Table 3.1: Overview of the main features of the rock samples described in this section.

Sample	Rock type	Texture	Grain size	Mineralogy
83	alkali feldspar granite	porphyric	3 mm	50% quartz 40% feldspar (k-feldspar & plagioclase) 10% mafic minerals
101	alkali feldspar granite	random	0.1 mm	60% quartz 35% feldspar (mainly k-feldspar) 5% mafic minerals
104	alkali feldspar granite	pophyric	2 mm	40% quartz 50% feldspar (mainly k-feldspar) 10% mafic minerals
84/2	siliciclastic meta-sediment	"bedded"	0.4 mm	80% quartz 10% biotite 10% k-feldspar
87	quartzitic meta-sediment	"bedded"	0.1-0.5 mm	80-90% quartz 10-20% feldspar (mainly plagioclase) & biotite
84	meta-arkose	"bedded"	0.3 mm	80% quartz 10% feldspar (mainly k-feldspar) 10% biotite

Fig. 3.8 Photographs of polished horizontal slices (left side) and thin sections (right side, all under crossed polars) of the samples of igneous rocks.

A&B: Sample 83, porphyric alkali feldspar granite. A) The rock consists of 50% quartz, 40% alkali feldspar and plagiclase, and 10% mafic minerals. The average grain size is ~3 mm. B) Alkali feldspar occurs as porphyric crystals surrounded by quartz polycrystals and sericitised plagioclase.

C&D: Sample 101, alkali feldspar granite. C) The rock consists of 60% quartz, 35% alkali feldspar and little sericitised plagioclase, and 5% hornblende and mica. The average grain size is 0.1 mm. D) Quartz occurs as polycrystalline aggregates (grain sizes <<0.1 mm) and as a few larger (~0.2 mm crystals. Alkali feldspar crystals are xenomorphic.

E&F: Sample 104, alkali feldspar granite. E) The rock consists of 50% alkali feldspar, 40% quartz, and 10% mica and hornblende. The average grain size is 2 mm. F) The porhyric alkali feldspar crystals show a slight preferred orientation, while the quartz occurs in polycrystalline aggregates.
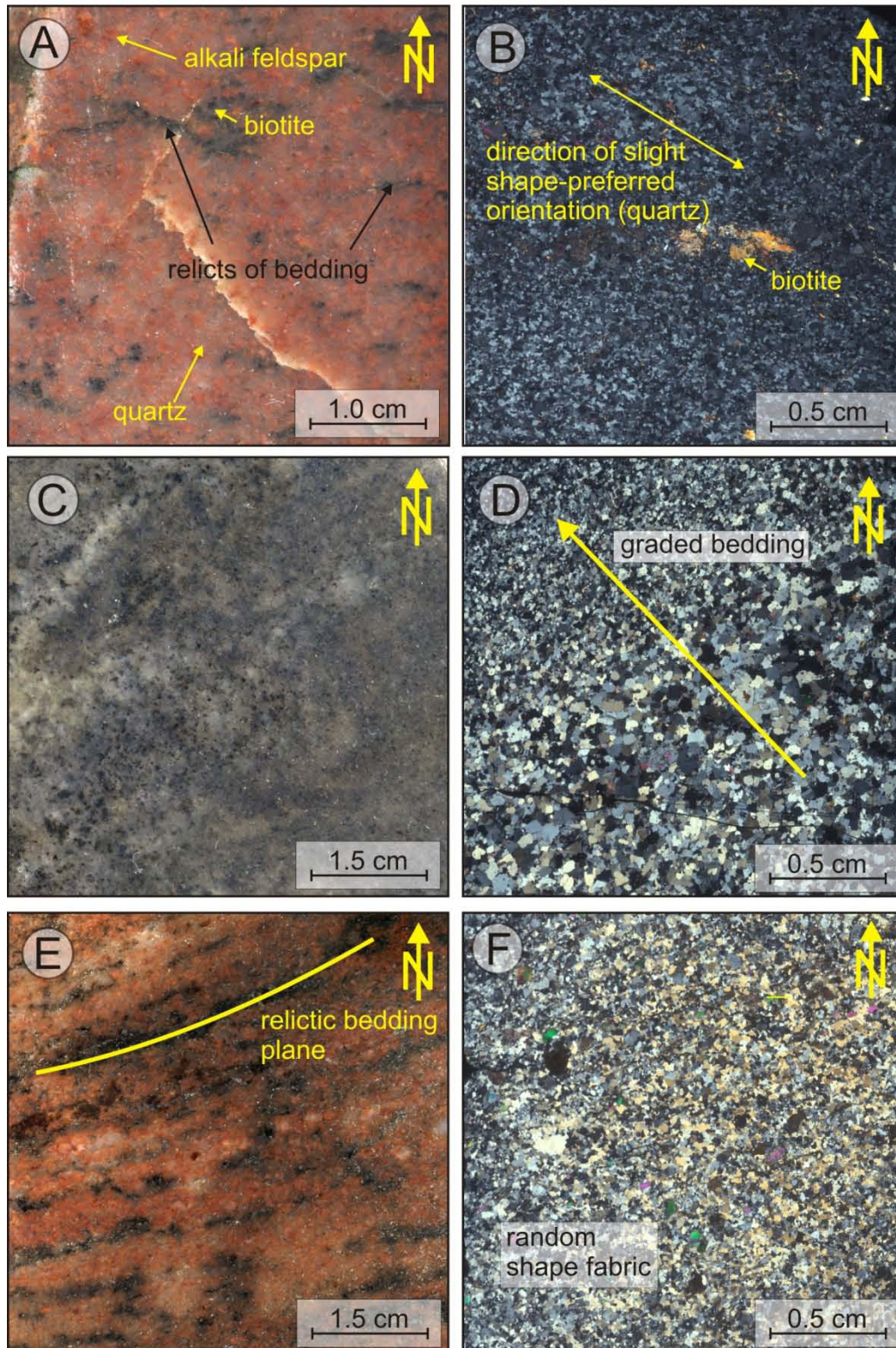
Fig. 3.9 Photographs of polished horizontal slices (left side) and thin sections (right side, all under crossed polars) of the samples of meta-sedimentary rocks.
A&B: Sample 84/2, siliciclastic meta-sedimentary rock. A) The rock contains ~80% quartz, 10% biotite, and 10% alkali feldspar. Relictic bedding is marked by the occurrance of biotite. The average grain size is 0.4 mm. B) Quartz grains exhibit a slight shape-preferred orientation.
C&D: Sample 87, meta-quartzite. C) The rock contains 80-90% quartz, and 10 to 20% plagioclase biotite. The average grain size varies from 0.1 to 0.5 mm. D) The grain-size variation of quartz depicts graded bedding.
E&F: Sample 84, meta-arkose. E) The rock consists of 80% quartz, 10% feldspar (mainly alkali feldspar), and 10% biotite. The average grain size is 0.3 mm. F) The rock is characterised by a random shape fabric.

In the samples, different types of micro-cracks occur. In general, micro-cracks can be classified according to their position and state (Fig. 3.10). Based on position, intragranular (within a grain) and intergranular (between grains) micro-cracks can be distinguished (Fig. 3.10 A). The latter can occur along grain- (between grains of the same mineralogy) and phase-boundaries (between grains of different mineralogy). Based on state, closed and open micro-cracks can be distinguished, where the former can be either healed (filled with the same material as the host grain) or sealed (filled with e.g. precipitation of a material different to the host grain) (Fig. 3.10 B). Sealed grains can usually be recognised by the occurrence of trails of secondary fluid inclusions. When analysing open micro-cracks to determine recent stress directions (Vollbrecht et al., 1994; Zang et al., 1996), cracks related to the preparation process of the sample should be ignored. Furthermore, the formation of micro-cracks is influenced by the properties of the hosting minerals. In general, "crack-resistant" and "crack-sensitive" minerals can be distinguished. "Crack-sensitivity" can be related to pre-existing intragranular features, such as e.g. twin lamellae, flaws, and cleavage planes that cause stress concentrations, which lead to micro-cracking. In general, during micro-cracking pre-existing weaknesses such as these intragranular structures or grain- and phase-boundaries with a favourable orientation in relation to the governing stress regime are exploited (Vollbrecht et al., 1994).
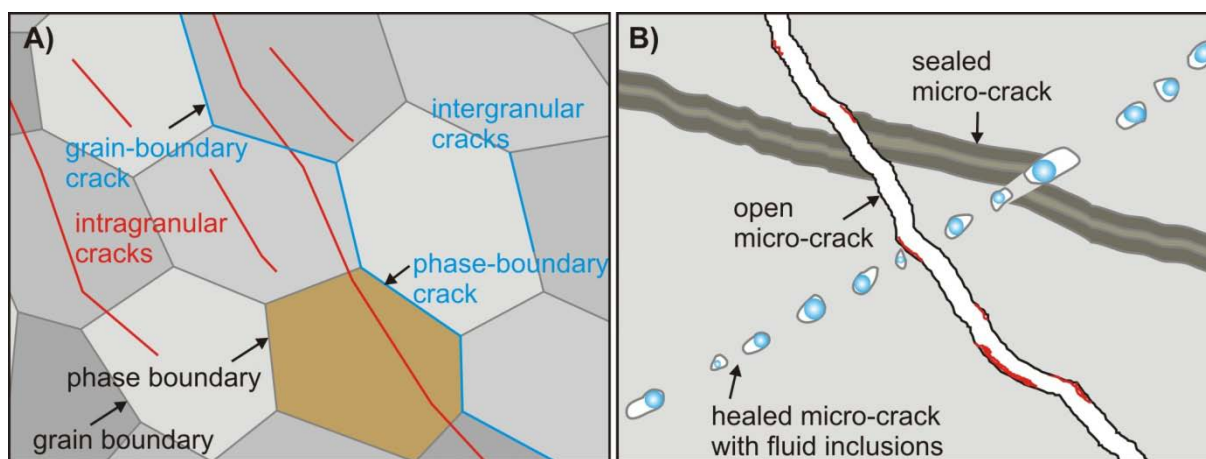
Fig. 3.10: A) Schematic sketch illustrating the difference between inter- and intragranular micro-cracks, grain- and phase-boundary cracks. **B)** Schematic sketch illustrating the terms open, healed and sealed micro-cracks. Modified after Ruedrich and Vollbrecht et al. (2006).

The micro-cracks observed in the samples can be roughly divided into three groups according to their state and related age: (1) the oldest cracks are healed and characterised by lines (planes) of secondary fluid inclusions that are traces of the former cracks, (2) cracks

sealed by mineral precipitation, mainly hematite, and (3) the most recent (recent and sub-recent) cracks that are still open.

In the samples of meta-sedimentary rocks, there are usually no intragranular micro-crack in the quartz grains, while many grain boundaries are marked by hematite precipitation (Fig 3.11 A&C), which indicates sub-recent intergranular micro-cracking. As grain boundaries may be sites of stress concentration (e.g. Kranz, 1983), they are in the fine-grained meta-sedimentary rocks, which contain preferred loci for micro-cracking. Thus, grain-boundary cracks make up the majority of the recent or sub-recent micro-cracks. Consequently, in fine-grained rocks (as in the samples), stress release is preferentially achieved by grain-boundary cracking. In some sample sections, the intensity of mineral precipitation (mainly hematite) along micro-cracks is strongly correlated with the orientation of the grain-boundaries.

In the coarser-grained granitic samples, micro-cracks are mostly intra-granular and controlled by energetically favourable pathways. In all three granitic samples, the abundance of healed micro-cracks is high. These healed micro-cracks are marked by trails of fluid inclusions. In addition, intragranular phase- and grain-boundary cracks occur. The younger micro-cracks are commonly sealed by hematite, while the latest generation of micro-cracks is still open.

Another typical kind of micro-cracks is twin-controlled and therefore mostly bound to feldspar crystals (Figs. 3.11 D & 3.12 E&F). Consequently, micro-cracks in the feldspar crystals are often strictly parallel. This may have a major influence on the total micro-crack distribution and orientation, in particular when feldspar grains display a texture (lattice-preferred orientation), e.g., resulting from flow reorientation in igneous rocks. Cleavage cracking has a similar effect on the distribution of micro-cracks as twin-lamella cracking. This is evident for biotite in granitic samples (Fig. 3.11 D).

Hence, the granitic rock samples show a variety of crack types, while in the fine-grained and quartz-rich meta-sedimentary rocks, micro-cracking is largely controlled by grain and phase boundaries.
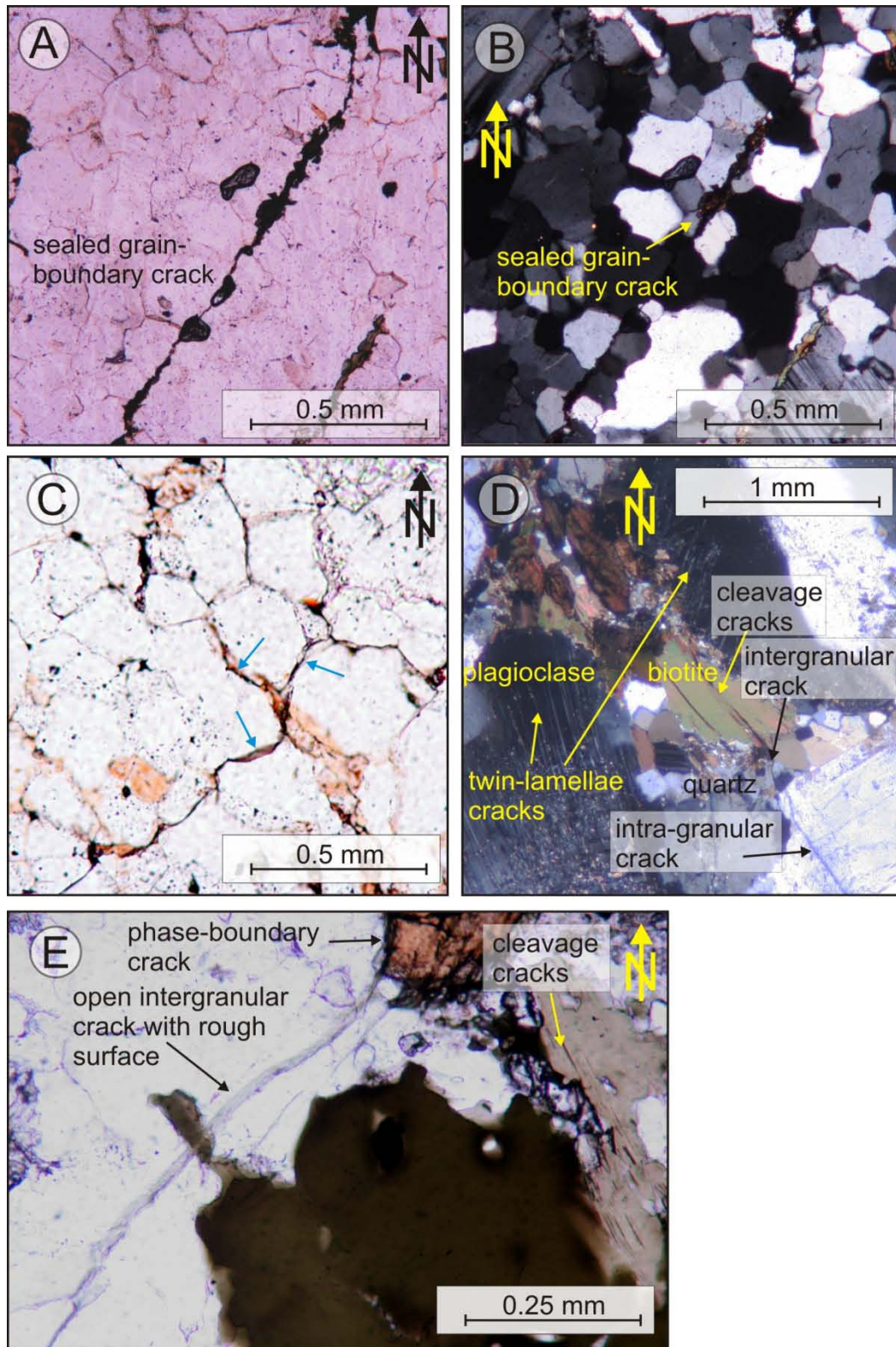
Fig. 3.11: Examples of different micro-crack types, as observed in thin sections of the analysed samples. Images in B and D under crossed polars.
 A&B: Sample 101. Grain-boundary crack, striking NE, sealed with hematite.
C: Sample 104. Sub-recent grain-boundary cracks (exemplarily marked by blue arrows) are coated with hematite.
D: Sample 83. Twin-lamellae cracks in plagioclase. To the right, a „composite" micro-crack changes from an intergranular crack to an intragranular phase-boundary crack to an intragranular cleavage crack.
E: Sample 83. Recent, open micro-crack with a rough surface that changes from an intra-granular to a phase-boundary crack along a biotite crystal.
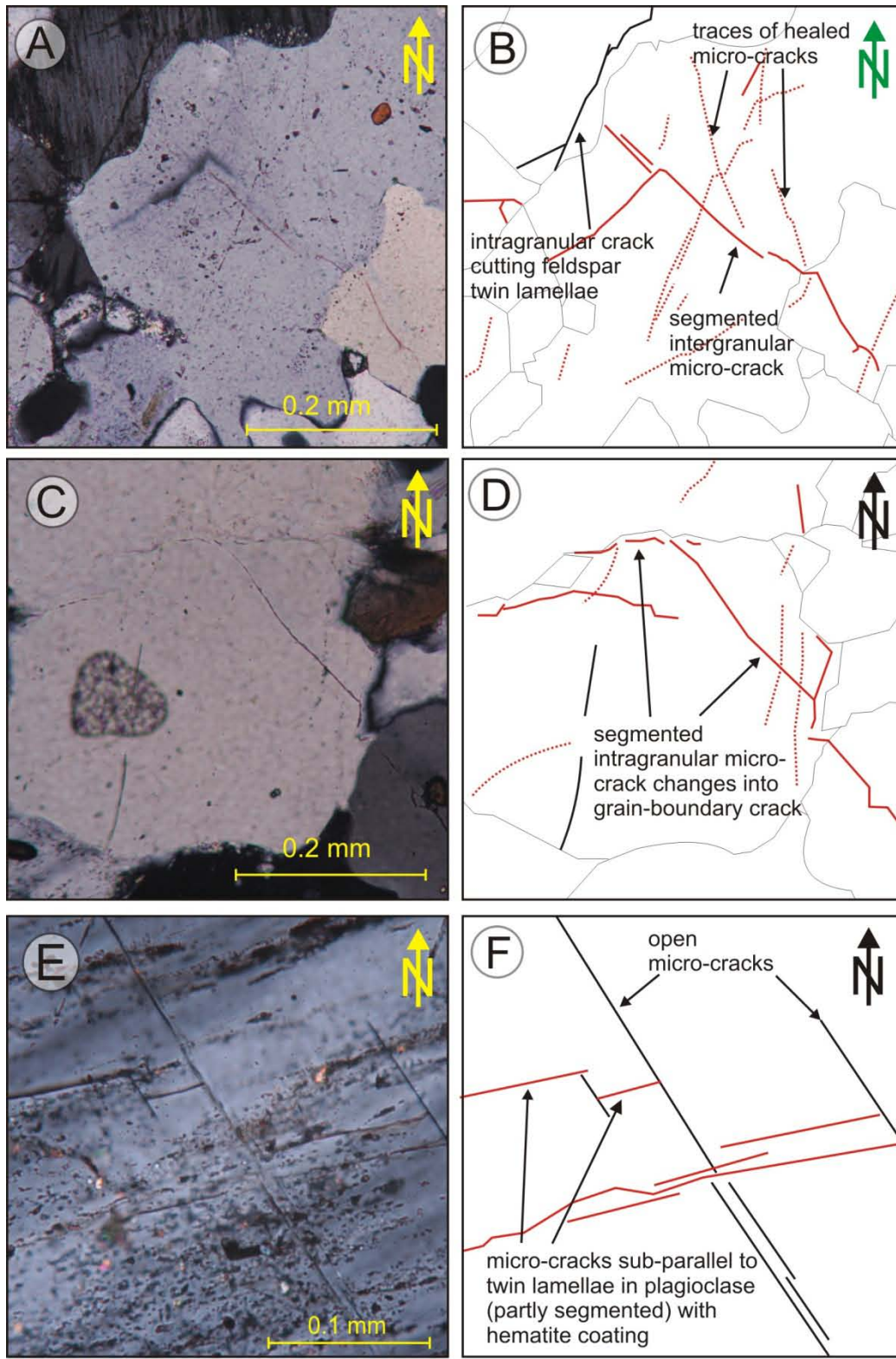
Fig. 3.12 Examples of different micro-crack types, as observed in thin sections of the analysed samples. Left side: photomicrographs under crossed polars. Right side: sketch of grain boundaries (thin, black lines) and micro-cracks (black and red, thick, solid and dashed lines). Note that not all micro-cracks in the photographs are in focus, but still appear in the sketch.
A&B: Sample 87. Healed micro-cracks are traceable as lined up secondary fluid inclusions. Younger cracks are sealed with hematite. Sub-recent, intragranular, open cracks cut plagioclase twin-lamellae at an acute angle.
C&D: Sample 87. Segmented, NW-SE striking, sealed micro-crack branches into an additional boundary crack and changes later completely into a grain-boundary crack.
E&F: Sample 104. Older, sealed micro-cracks, striking ENE are sub-parallel to plagioclase twin lamellae. Younger cracks cut the twin lamellae at a high angle and strike NW.

3.4 Results

3.4.1 Horizontal EMR measurements

In May 2008 and May 2009 horizontal main radiation directions were determined with the EMR-method at 54 locations, distributed over an area of about 1600 km² (Fig. 3.13; Appendix 1). In general, there are only small variations (standard deviation 17°) in the main radiation direction with an average of 135° (cluster analysis; Fig. 3.13). This includes repeated measurements at the same location, as well as for the sum of all measurements performed in the study area. In addition, the intensities of the single pulses and the defining energy vary only over a small range. Few exceptions can be explained by the measuring within fault zones (e.g. close to Valdermarsvik in the LLDZ, Fig. 3.13; cf. Fig. 3.6). In these cases, the main radiation direction differs significantly from the commonly-observed direction and the intensities (number of single pulses and defining energy) are significantly higher.
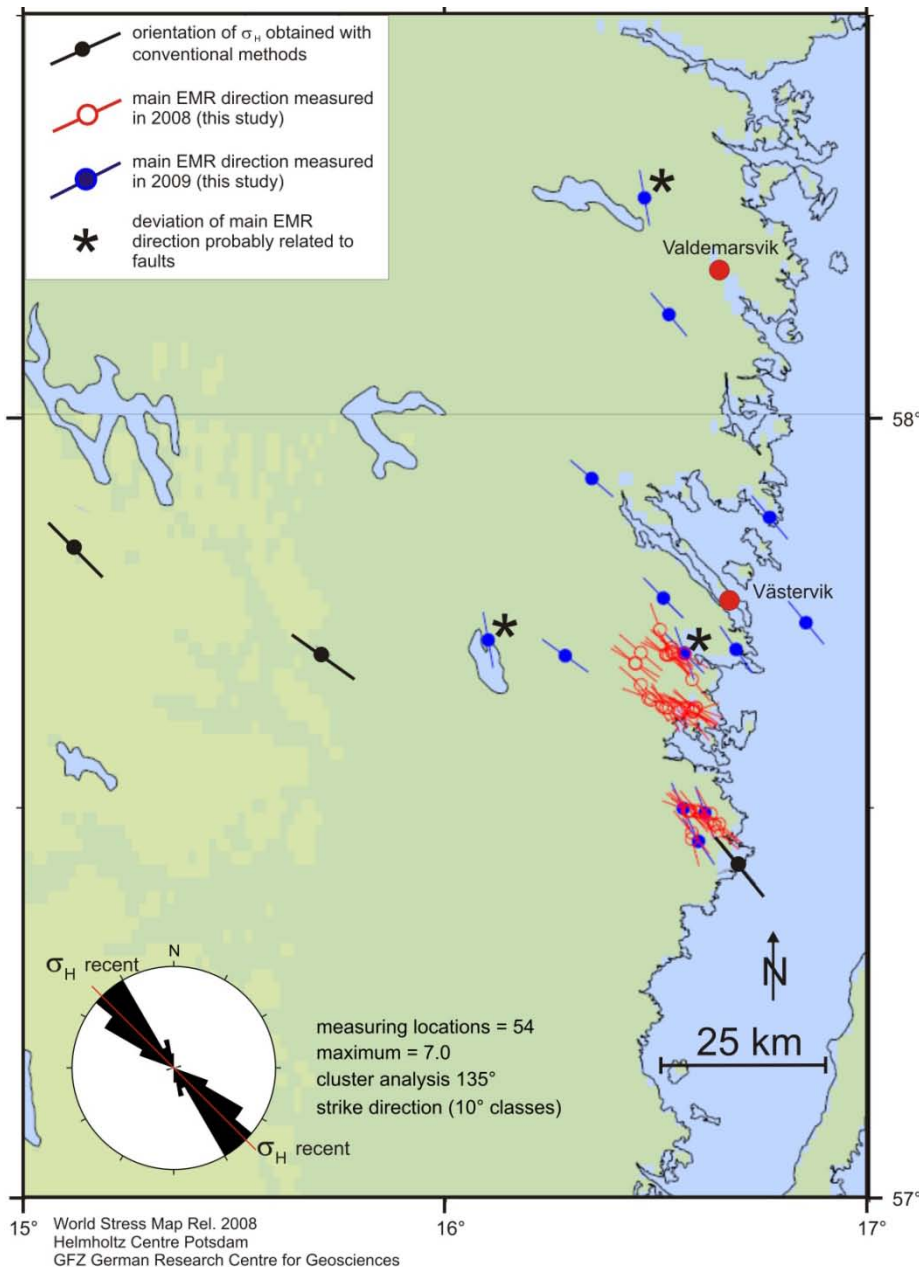
Remarkably, evaluation of the data showed that the patterns of the single pulses were conspicuously asymmetric.

Fig. 3.13: Comparison of WSM data (black symbols) with 108 EMR measurements taken in 2008 (red symbols) and 2009 (blue symbols) at 54 locations. The rose diagram of the 54 determined main EMR directions shows a narrow distribution with only few outliers (marked by an asterisk). Map based on WSM (Heidbach et al., 2008). Projection: Mercator.

3.4.2 Lineaments

Using the SRTM data as map base, 338 lineaments were identified (Figs. 3.14 A&B and 3.15). The length of the lineaments ranges from 0.9 to 25 km (Fig. 3.15 A). Most of the lineaments strike between 085° and 125°. Within this range, three distinct maxima occur: 085-090°, 105-115°, and 120-125° (Fig. 3.15 B&C). This coincides well with the results of a previous lineament analysis by Tirén and Beckholmen (1989). In addition, there are two significant minor sets. Each of them represents about 13% of all lineaments mapped. The first minor set strikes nearly N-S; the strike of the second minor set is ~060.
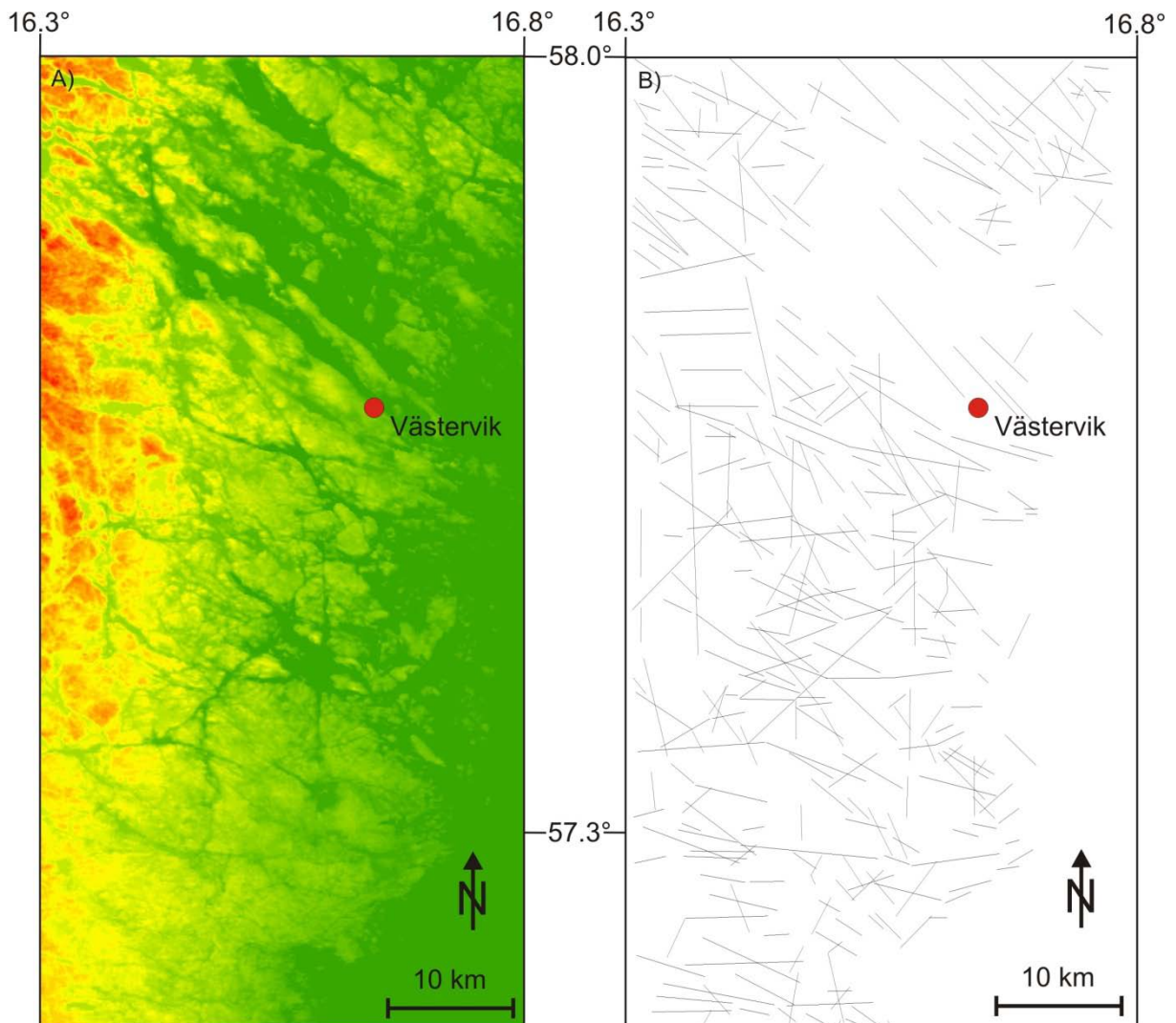
Fig. 3.14: Lineament pattern of the study area. **A)** SRTM image with 90 m cell size. Colour scheme according to height above sea level (green = sea level). **B)** Line map of the 338 mapped lineaments.
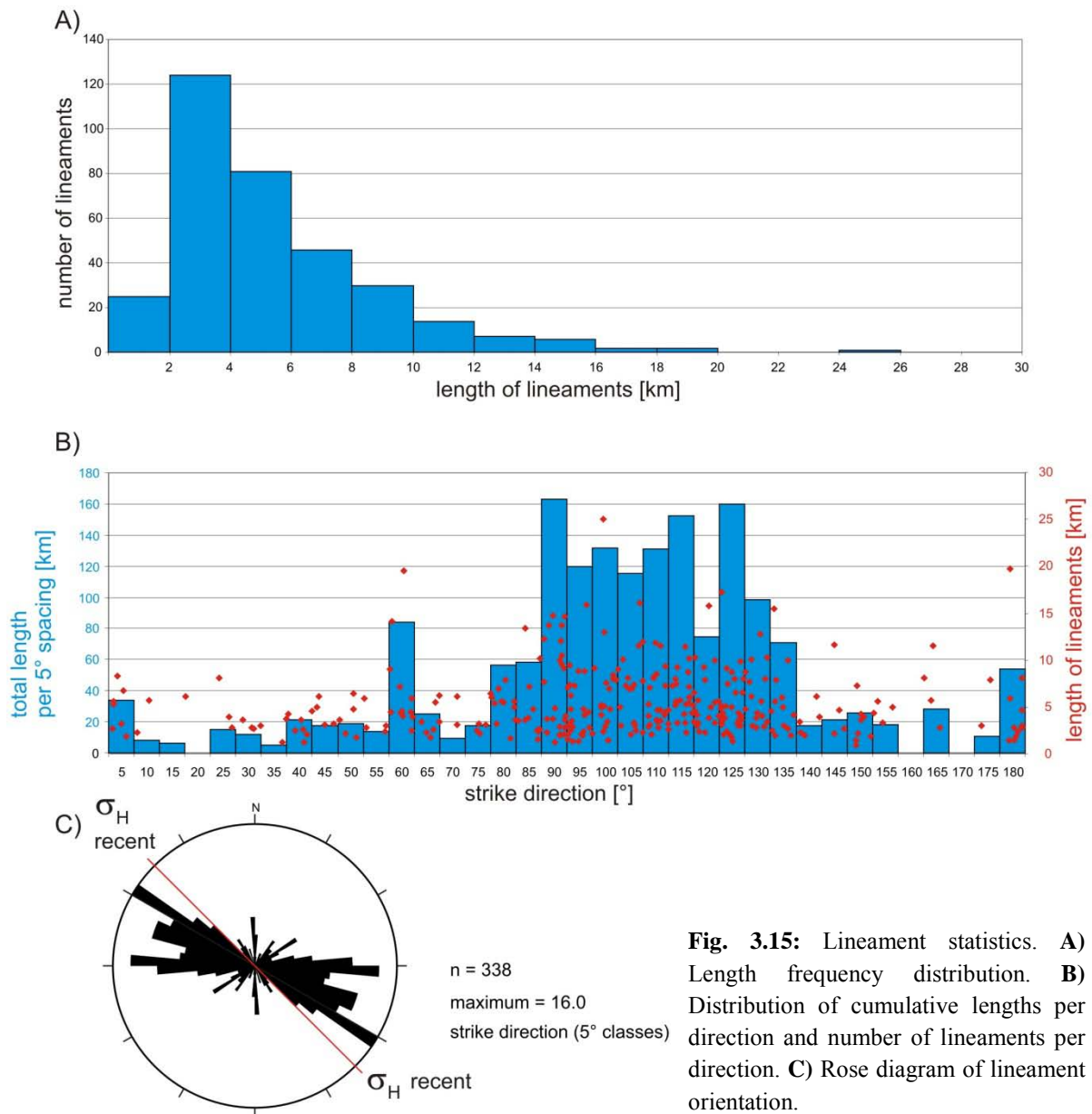
Fig. 3.15: Lineament statistics. **A)** Length frequency distribution. **B)** Distribution of cumulative lengths per direction and number of lineaments per direction. **C)** Rose diagram of lineament orientation.

n = 338

maximum = 16.0

strike direction (5° classes)

3.4.3 Joints

The data used in this study comprises 2174 steeply-dipping joints taken from 34 Diplom mapping reports (Fig. 3.16 A). The data is characterised by two sets with strikes of 060° for the stronger-pronounced main set and 145° for the second major set (Fig. 3.16 B). The distribution of joint orientations over the considered 1600 km^2 does not follow a regular pattern. However, the two main sets occur throughout the area (Fig. 3.16 A). In most of the individual areas these joint sets are oriented more or less perpendicular to each other. In some areas, especially in the south and west, less distinct patterns with a higher number of peaks of joint orientations occur. Furthermore, especially in the northeast, often only one joint direction is developed, while the second main set is missing or under represented.
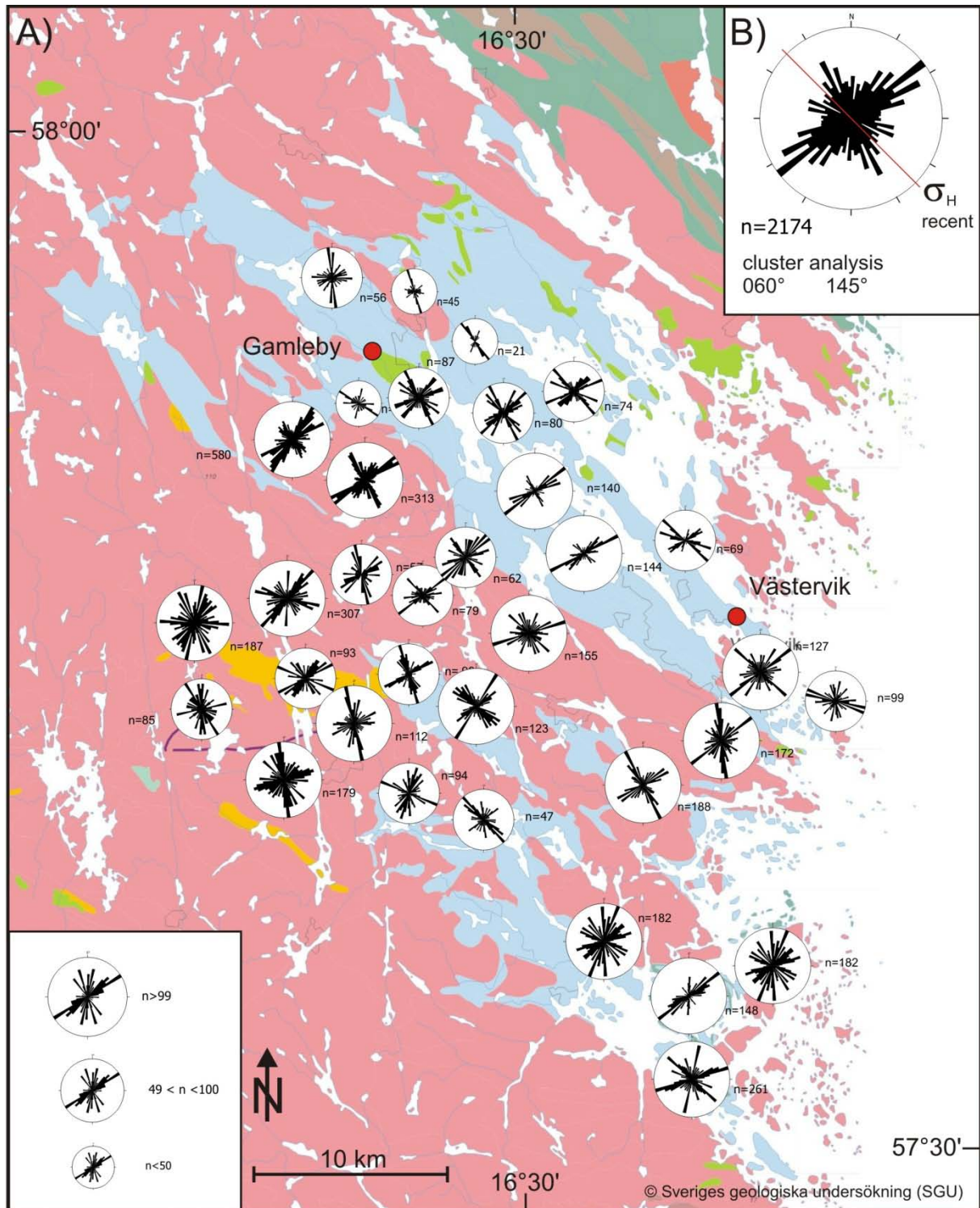
Fig. 3.15: Orientation of steeply-dipping 2174 joints in the study area. **A)** Spatial distribution of the joints displayed in rose diagrams. The size of each diagram reflects the number of measurements per area (see inset). **B)** Composite rose diagram of all joint data. Strike is plotted with sector interval angle of 5°. Base map modified after © Sveriges geologiska undersökning (SGU).

3.4.4 Meso-cracks

The small number of meso-cracks in relation to the surface area does not allow a statistically sound analysis (n = 115 in total for the six samples). Therefore, the results are only included for reasons of completeness.
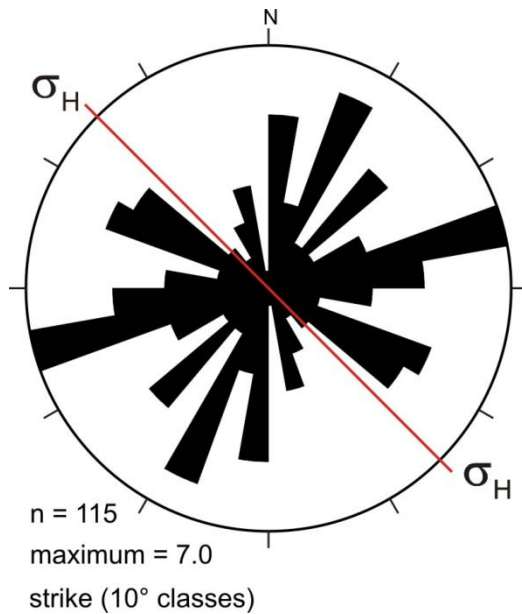
The distribution of the 115 meso-cracks scatter over a wide range (Fig. 3.17). By disregarding the insufficient number of measured meso-cracks, a maximum at 070° could be interpreted, as well as higher densities in the directions of 020° and 120°.

Fig. 3.17: Rose diagram of the strike of 115 meso-cracks measured on horizontal slices of the six samples.

3.4.5 Micro-cracks

On the polished horizontal slices of the samples, a total of 3711 micro-crack orientations (strike) were measured. The number of identified micro-cracks per slice ranges from 581 in sample 84 to 1068 in sample 101. The orientation data are illustrated in Fig. 3.18. If possible, micro-cracks in feldspars and quartz were distinguished. As a result of low-angle overlapping of the grains, it was often not possible to categorise the micro-cracks in an exact way (according to mineralogy; see Section 3.2.4). This problem occurred in sample 84 where the micro-cracks were therefore not classified. As the determination of micro-crack orientation is furthermore limited by the grain size it was not applicable to sample 84/2; the combination of a small grain-size and the resolution of the images inhibited analysis. In addition to the orientation of micro-cracks, the crack-length distribution and the available crack length as a function of strike was determined (Fig. 3.19).

In **sample 83,** three main orientations occur in feldspars and quartz. There is one narrow peak in N-S direction that is somewhat stronger pronounced in quartz, and a minor set striking about 030°. The main set is oriented almost exactly SE-NW. In total, the strike of micro-cracks in feldspars shows a broader distribution than in quartz grains. Furthermore, a sharply bordered E-W striking set occurs predominantly in quartz.

In **sample 84,** where no distinction between cracks in quartz and feldspars was possible because of an extensive red stain of both minerals by hematite, again a sharply bordered, N-S striking set of micro-cracks is present, as well as the narrow E-W striking set, while the bulk of micro-cracks form a NW-SE striking set.

Sample 84/2 shows a more uniform distribution of micro-crack orientations. There is one main peak striking NE-SW and a number of smaller peaks with E-W, NW-SE, and WNW-ESE strikes.

In **sample 87** (contains no significant amount of feldspars), three sets are pronounced: while the N-S striking set is narrow and less distinct, a NE-SW striking set occurs. The third set strikes NW-SE and consist of a pair of similar sets within a 25° range. This subdivided third set represents the main direction of micro-cracks in this sample.

The strike distribution of micro-cracks in **sample 101** is similar in feldspars and quartz with the difference that the sets within quartz have the same intensities, and an additional E-W striking set is developed, while the main set in feldspars strikes N-S. The main orientations are N-S, NE-SW, and NW-SE.

In **sample 104,** the orientation patterns in feldspars and quartz differ from the other samples. While the micro-cracks in feldspars form three distinct, equally pronounced sets that strike around N-S, NE-SW, and NW-SE, only one broad set between 110° and 180° is developed in quartz. The total strike distribution of all micro-cracks in this sample shows a maximum in NW-SE direction, while the other two sets are characterised by a lower maximum as well as narrower strike distribution.

In total, four distinct clusters of micro-crack strikes are developed in all samples. The NW-SE striking cluster is the main orientation direction of micro-cracks and characterised by a broader distribution, while the perpendicularly-oriented NE-SW direction is less distinct. In addition, two sharply bordered clusters with N-S and E-W orientation occur, where the E-W orientated cluster is weaker.

In addition to the preferred orientation of micro-cracks their lengths per direction were also measured (Fig. 3.19). The average crack length ranges from 0.036 mm in sample 84 to 0.066 mm in sample 104. The crack length itself in each sample follows a similar distribution with a considerably higher amount of short micro-cracks. Only sample 104 shows a different distribution with comparatively high amounts of longer micro-cracks. In samples 83 and 84, both feldspars and quartz contribute to the crack length to the same degree, while sample 104 is dominated by micro-cracks in feldspars. In total, the distribution of crack lengths per direction correlates well with the orientation distribution of micro-cracks. In each sample, a

small maximum in N-S direction is pronounced, and a wider maximum between 020° and 060° exists, except in sample 84. The maximum crack length occurs in the range between110° and 150°.
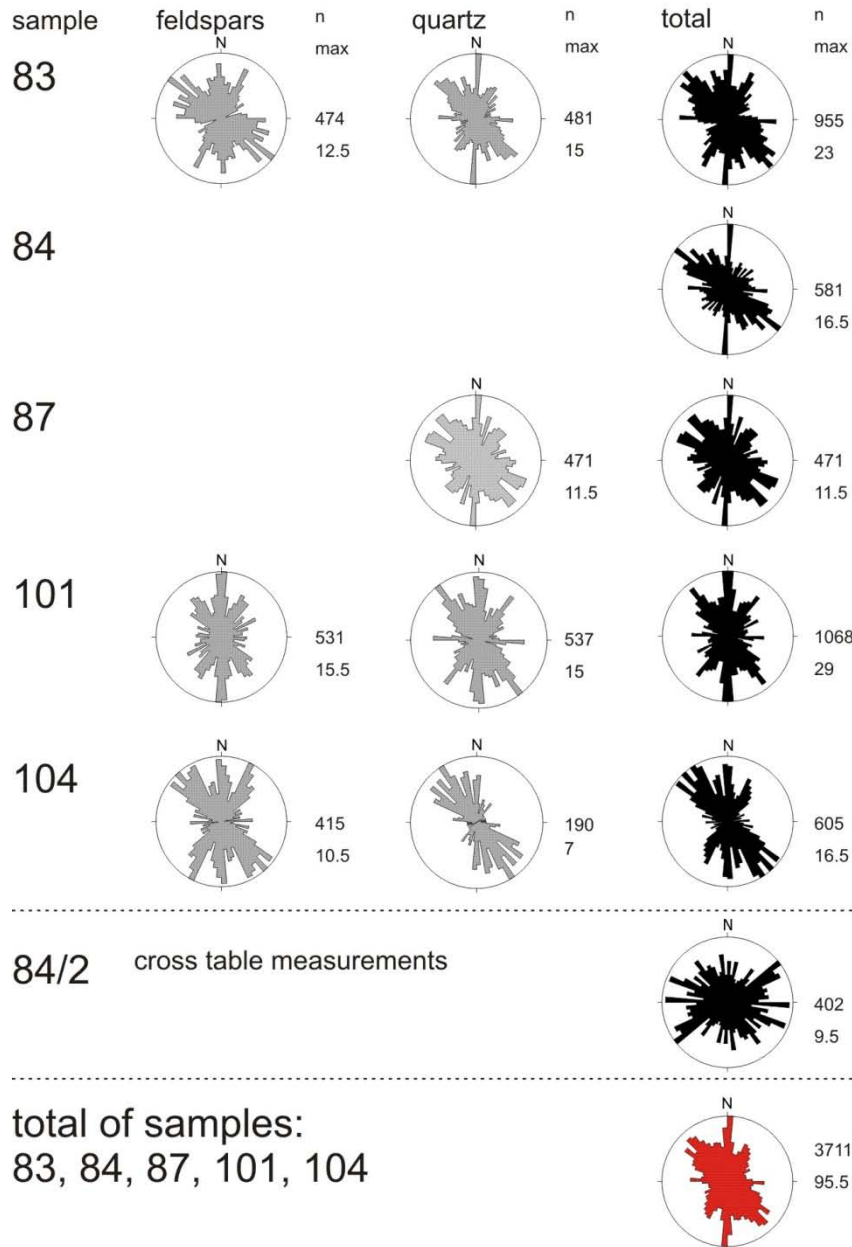
Fig. 3.18: Micro-crack orientation measured on horizontal slices of oriented samples 83, 84, 84/2, 87, 101, and 104, plotted in rose diagrams with 5° spacing. Grey rose diagrams represent separately analysed minerals. Black rose diagrams display all micro-cracks in a sample. Micro-crack orientations of sample 84/2 were obtained by plane-table measurements.

Rose diagram of micro-crack orientations in all samples (except 84/2) in red.
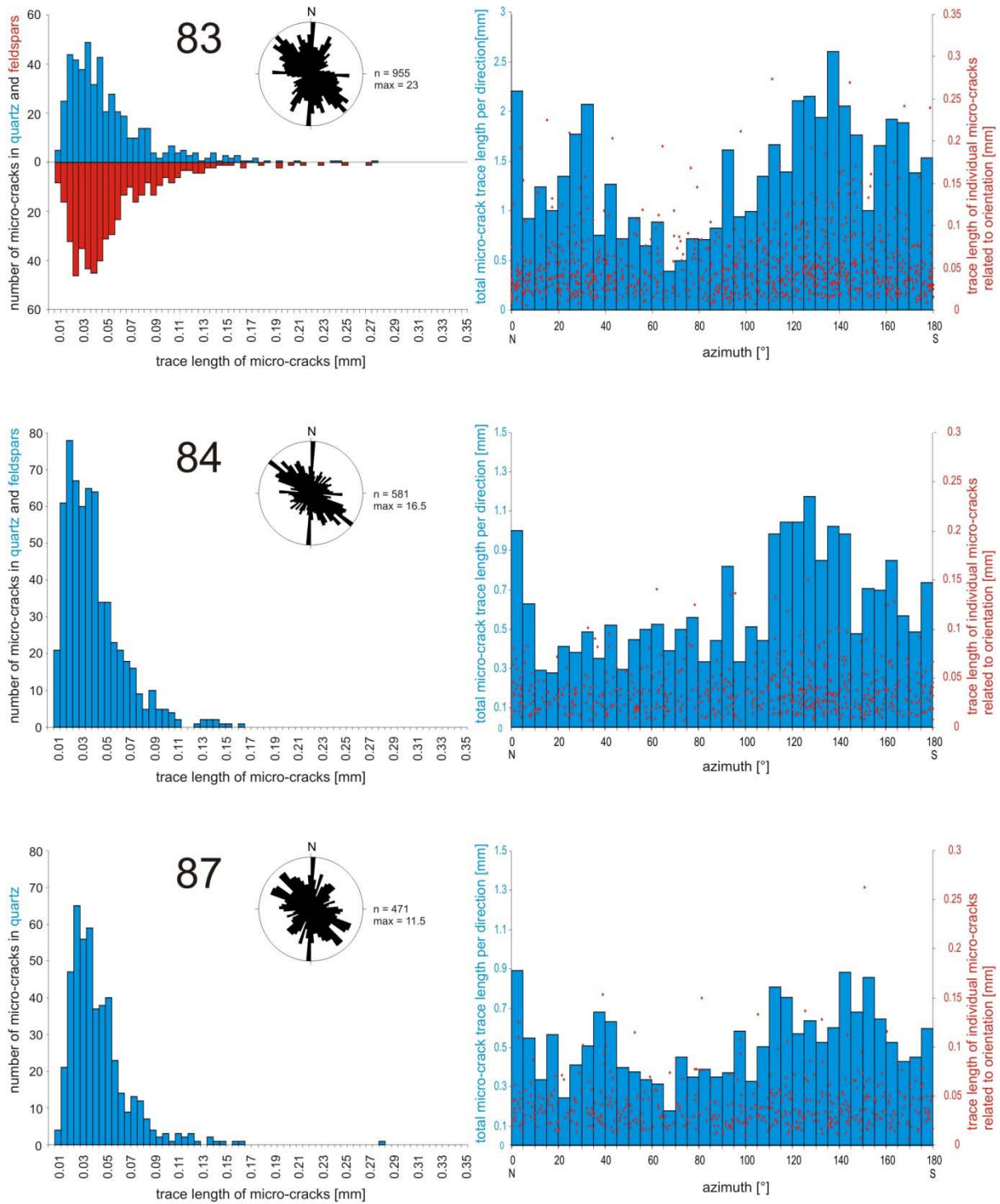
Fig. 3.19: Frequency distribution of micro-crack lengths of the samples 83, 84, 87, 101, and 104. Left side: distribution of micro-crack lengths, if possible separately for quartz and feldspar (data stacked). Rose diagrams as in Figure 3.18 with 5° spacing. Right side: total available length per direction (blue bars). Additionally, the distribution and length of single cracks per direction is plotted (red dots).
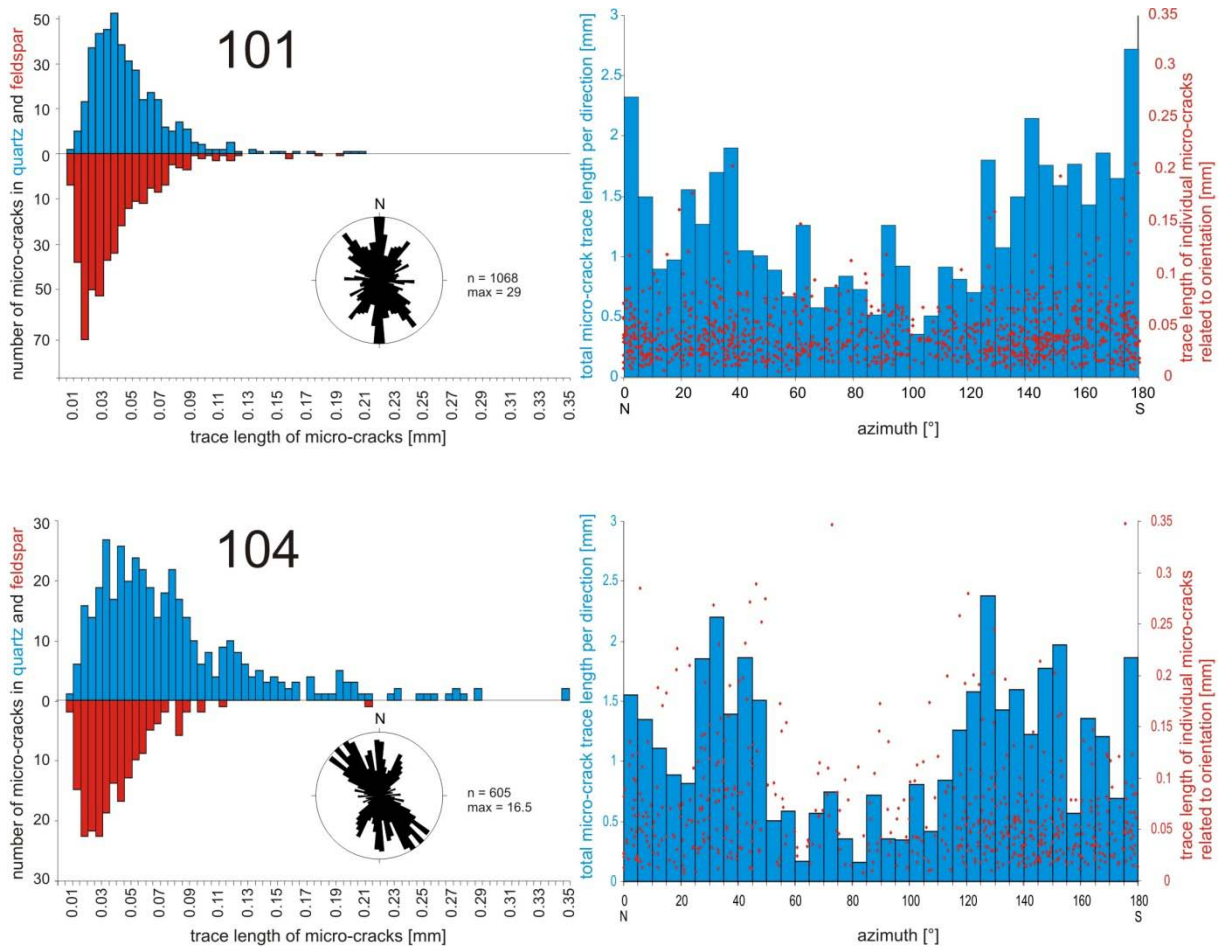
Fig. 3.19: overpage.

3.4.6 Grain- and phase-boundary orientations

After filtering of the grain-boundary data obtained with the "rotating polarizer stage" according to curvature (see Chapter 3.2.5), 38581 grain and phase boundaries and boundary segments remained for interpretation. The number of analysed grain boundaries and segments ranges from 1890 in sample **101** to 5300 in sample **84 2**.

In all samples, two strongly preferred orientations of grain and phase boundaries occur that show only small deviations within individual samples and between the samples with respect to the grain boundary length. To quantify these observations, cluster analyses were performed (Fig. 3.20). The results manifest that the deviations within individual samples are generally insignificant and are highest in sample **83** (12°)**.** The strongest deviations between the samples occur in the group of grain and phase boundaries >0.1 mm. This may result from the lower number of grain boundaries in this range.

The main directions of grain and phase boundaries were calculated using cluster analysis (based on a k-means algorithm with manual determination of the number of clusters) for

individual samples (Fig. 3.20). The results range between 043° and 047° and between 135° and 137°, where the NE cluster is, without exception, stronger developed. Both clusters are oriented exactly perpendicular to each other.
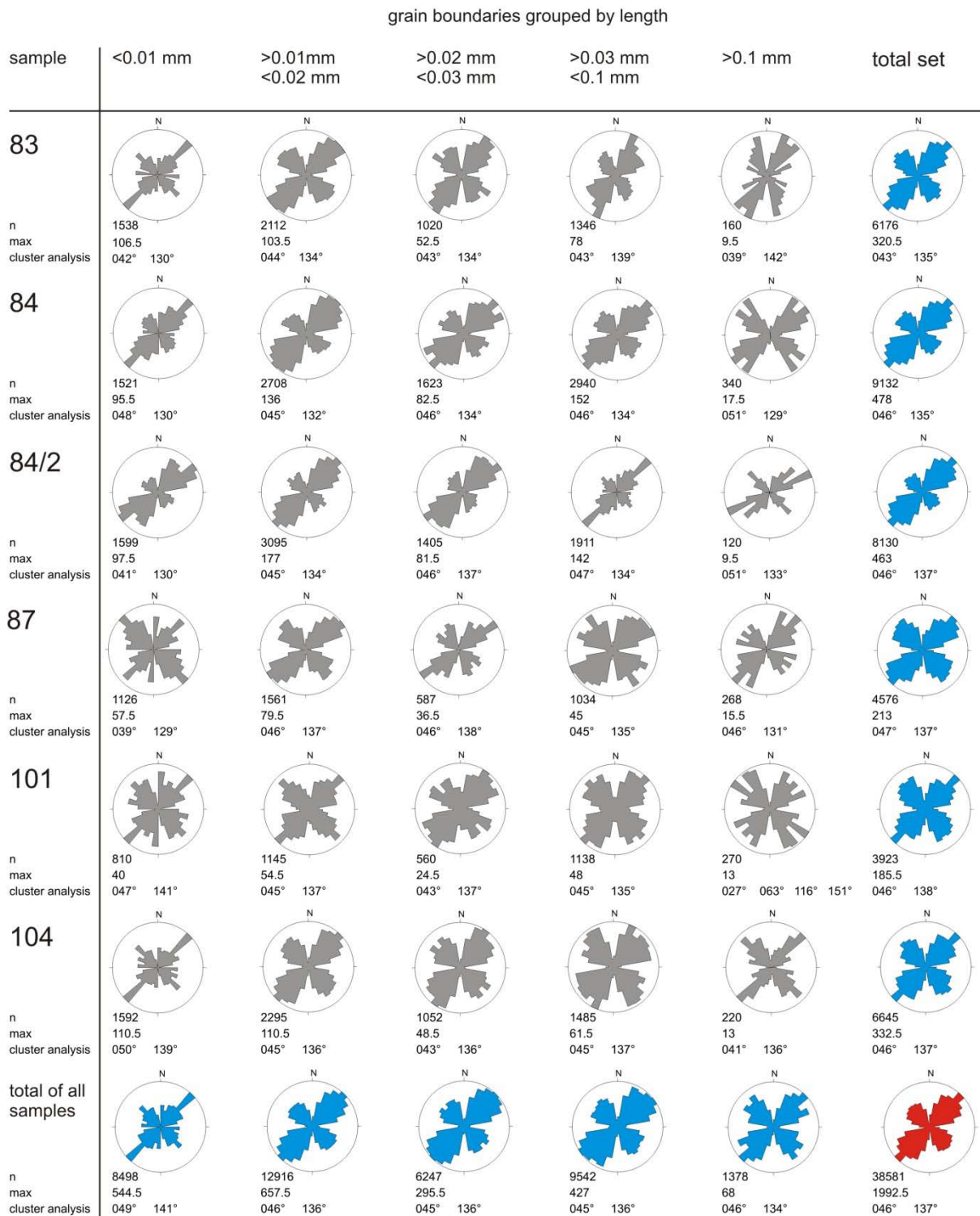
Fig. 3.20: Orientation of grain and phase boundaries of all samples. The distributions of the orientation of grain and phase boundaries are stable within individual samples with respect to their length, as well as between the different samples. According to the results of cluster analyses, the scatter of the main directions are in the range of only few degrees.

The available length of grain boundaries in relation to their strike (Fig. 3.21) shows two distinct maxima that coincide well with the number of micro-cracks per strike direction. In samples **83, 84, and 84 2**, the length maximum lies in the NE direction and coincides with the maximum number of grain-boundaries. In contrast, in samples **87, 101, and 104**, the maximum of grain-boundary lengths are almost identical for the NE and SW direction. In addition, the length-per-direction distribution in samples **84, 84/2, and 101** is symmetric for the single clusters of the samples, while especially in sample **83,** a noticeable, asymmetric pattern occurs.
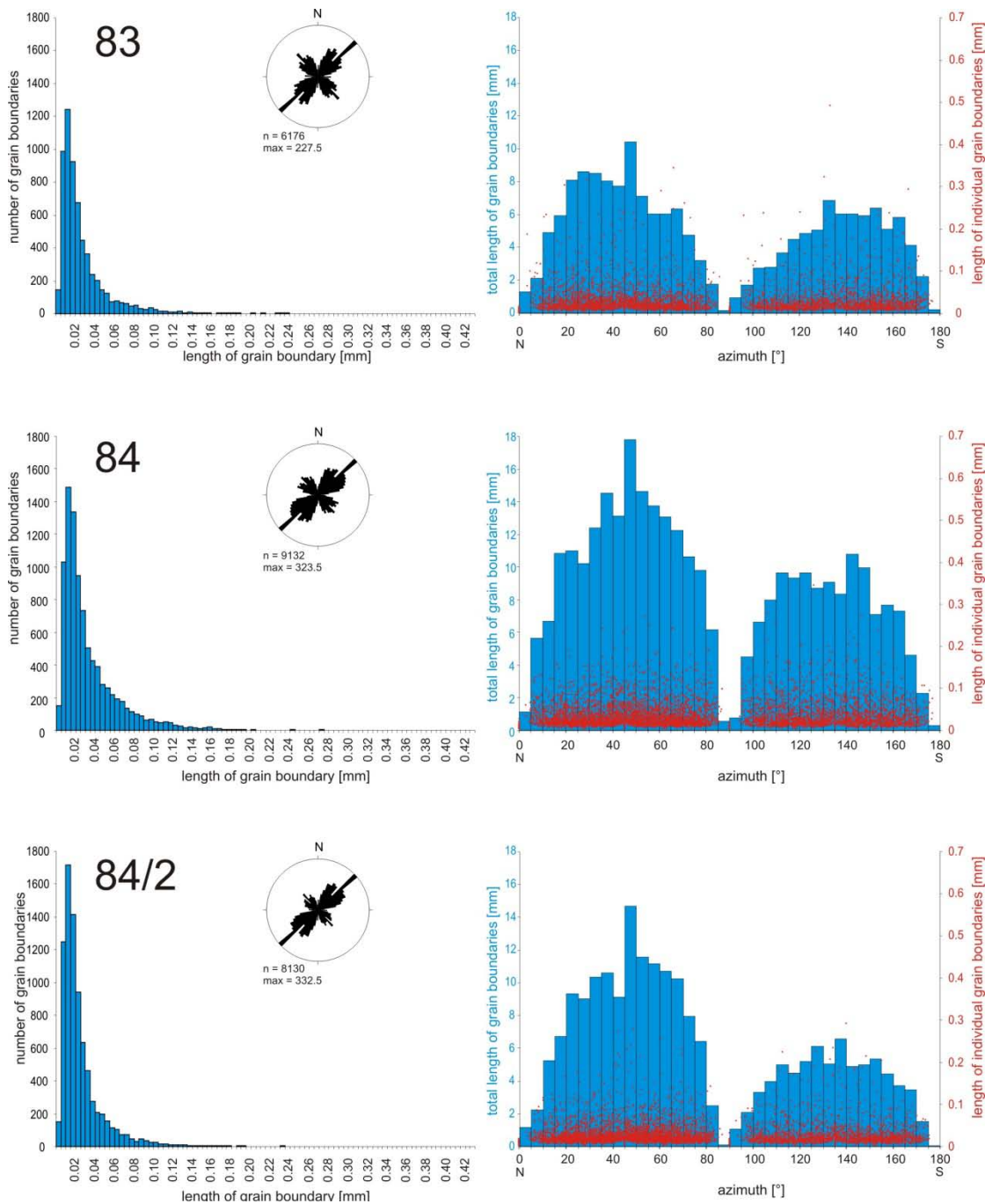
Fig. 3.21: Results of grain-boundary analysis of the samples. Diagrams on the left side show distribution of grain-boundary length. Diagrams on the right side display total available length of grain-boundaries per direction (blue bars). Additionally, the distribution and length of single cracks per direction is plotted (red dots).
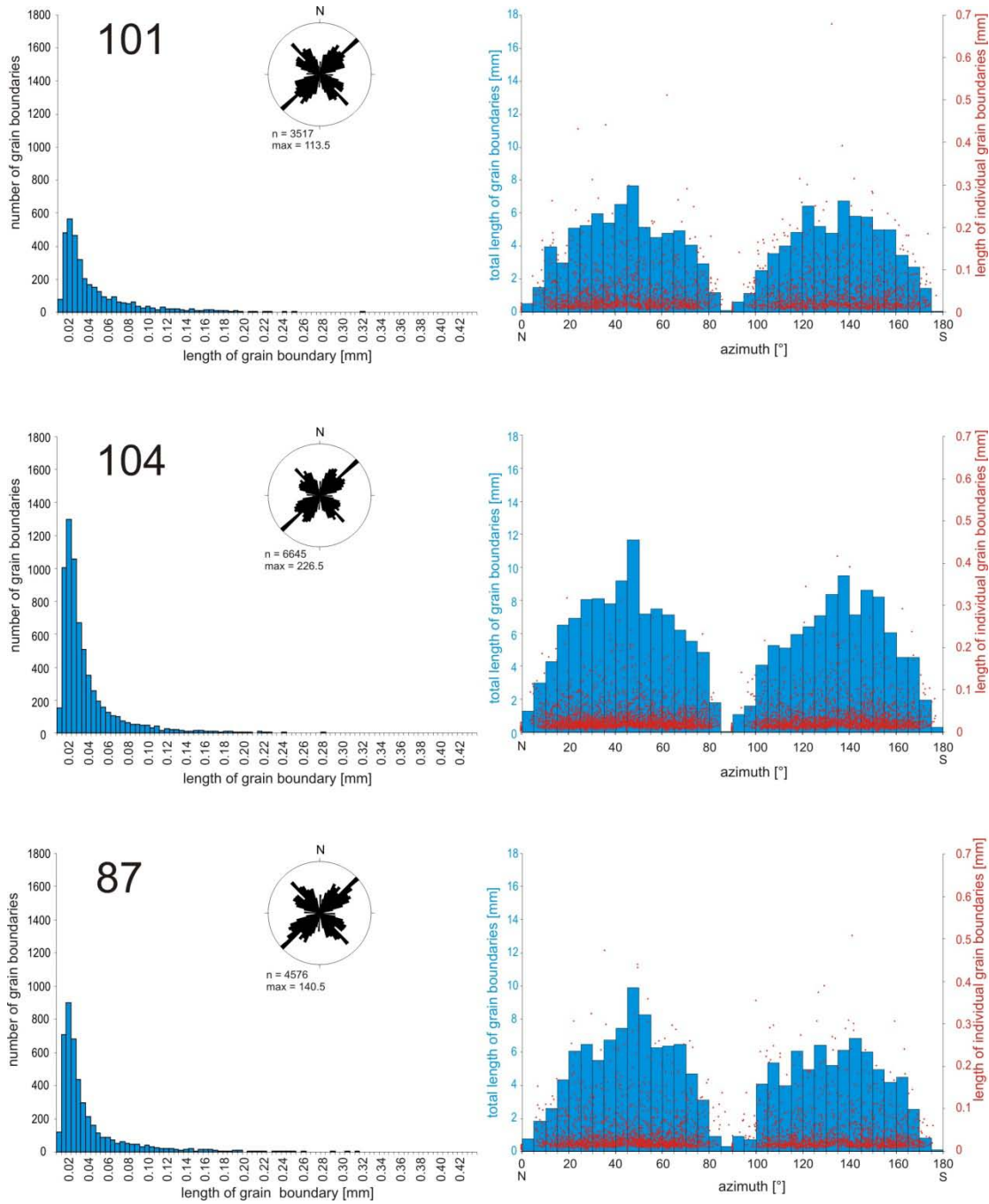
Fig. 3.21: overpage.

3.5 Summary and Conclusions

One aim of this study was to compare the main direction of EMR horizontal measurements as possible indicator of the direction of σ_H with existing stress data and to identify possible EMR-generating structures. For this purpose, directional analysis of brittle structures over a wide range of scales was carried out and compared with EMR measurements at 54 locations distributed over an area of about 1600 km^2. The brittle structures include map-scale faults (or lineaments), joints, micro-cracks, as well as grain and phase boundaries. These data will now

be compared with the direction of recent in-situ stress data and the results of the EMR-measurements of this study (Fig.3.22).
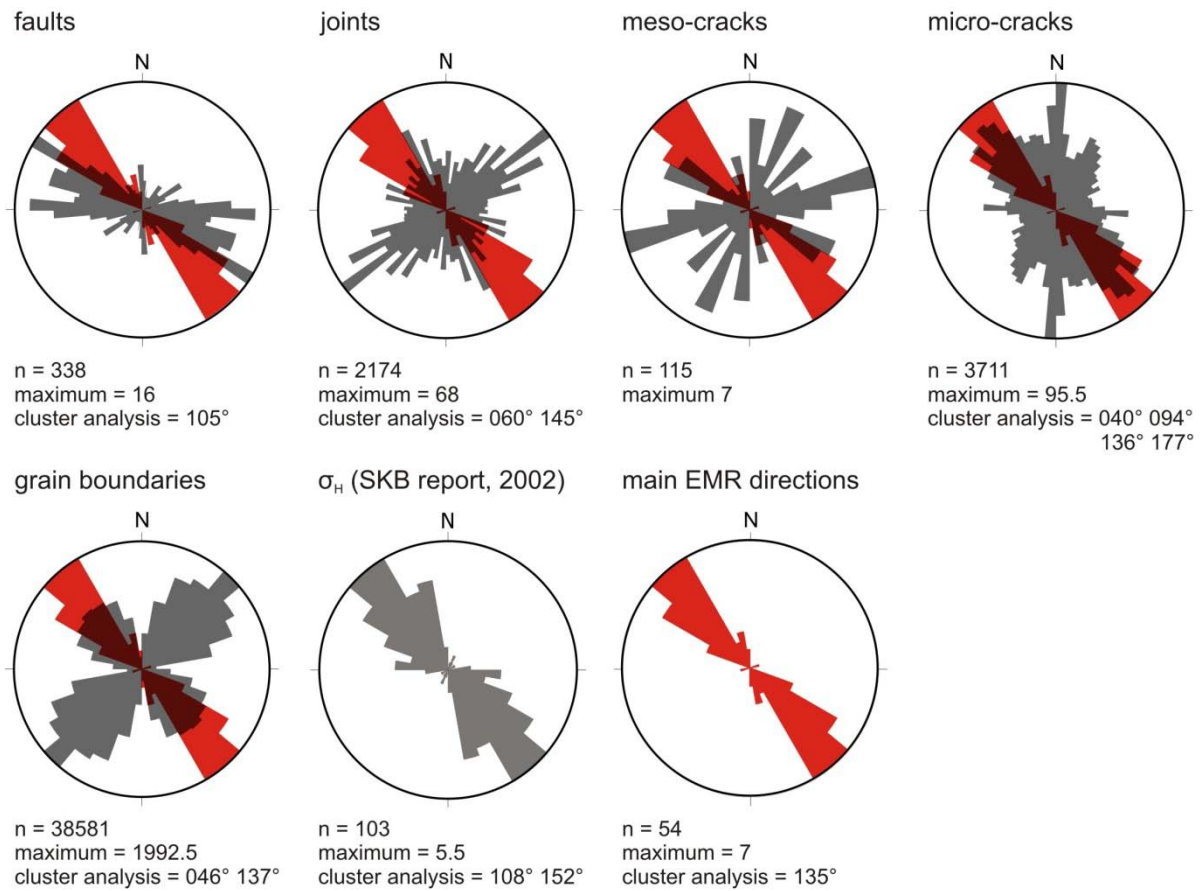
Fig. 3.22: Comparison of the strike orientation of brittle structures at various scales (grey) with main EMR directions (red). In addition, the main direction of in-situ stress data from the area (SKB report, 2002) is displayed for comparison. Rose diagrams with 5° spacing, only in the diagrams of meso-cracks and EMR main directions a 10° spacing was used.

The most reliable in-situ stress data in this area are known from the Äspö Hard Rock Laboratory, only 30 km south of Västervik, close to the town of Oskarhamn. These data comprise a large number of stress measurements obtained from hydraulic fracturing (Bjarnasson et al., 1989; Janson and Stigsson, 2002) and overcoring (Bjarnsson et al., 1989; Klasson et al., 2001; Janson and Stigson, 2002) that are summarised in a model of the Simpevarp region (SKB report, 2002) that includes the Äspö Hard Rock Laboratory. The mean of the analysed stress data in the SKB report (2002) is 132° (Fig. 3.22).

Other data in this area are mostly derived from focal plane mechanisms (Slunga et al., 1984; Arvidsson and Kulhanek, 1994) and also show the common NW-SE orientation of σ_H.

In total, the results of the conventional in-situ stress measurements yield σ_H directions that mostly lie in the range between 130° and 140°, while the average of the EMR data is around 135°, disregarding some outliers. The outliers occur mainly in fault zones, which may explain the deviations from the otherwise stable measuring results (cf. Chapter 6). The main horizontal stress directions determined with the EMR method are therefore in very good agreement with the results obtained by conventional methods in the area. Therefore, the EMR method seems to be a suitable tool to determine main horizontal stress directions in the field.

The orientation of map-scale lineaments (fault zones) is consistent with other studies carried out south of the study area by Tirèn and Beckholmen (1989). The strike of the main set of faults differs with 035° slightly but consistently, from the average EMR main direction. Hence, brittle deformation in the map-scale fault zones is therefore unlikely to control the main EMR.

The joints show two sets striking NE-SW and a NW-SE, scattering over a wide range. The characteristics (shape and size of peaks in comparison to each other, angle between both directions) of both main sets differ over the studied area. More specifically, a switch of the main direction between both sets occurs; or sometimes there is only one pronounced direction recognisable. In some areas, a preferred direction is even missing. This might only in parts be attributed to measuring inaccuracies and varying outcrop conditions. However, in summary the joint patterns do not correlate with the main EMR directions measured in the area. Consequently, these joints are unlikely to emit EMR by a reactivation under the current stress regime.

The main strike of meso-cracks is ENE oriented and does therefore not coincide with the measured main EMR directions. However, the number of measured meso-cracks is too low to allow a significant interpretation in this context.

In contrast, the results of the analysis of the orientation of micro-scale structures, such as intra- and intergranular micro-cracks and grain and phase boundaries support the theory of EMR generation by micro-cracking (Section 2.3.8). The micro-cracks (mainly intragranular) are independent of the lithology and location of the sample in several sets, with a NW-SE striking main set, which coincides with the EMR main direction within the accuracy of both methods. In more detail, about 30% of all intragranular micro-cracks belong to a cluster with a pronounced NW-SE direction with an average of 136°. This is in very good agreement with the main EMR direction.

The orientation of grain and phase boundaries as potential intergranular crack pathways shows an even more articulate accordance among the different samples as well as with the

main EMR directions. In all the samples, two strikes (NE-SW and a NW-SE) are clearly pronounced. Cluster analysis with the software programme "Stereo 32" shows that the main sets of all six samples vary within angles of 043° and 047° for the NE-SW striking set and between 135° and 138° for the SE-NW striking set. Therefore, the NW-SE set coincides extremely well with the main EMR directions. The NE-SW oriented cluster contains 58%, while the NW-SE trending set contains 42% of the total of all analysed grain-boundaries.

Even though the NE-SW oriented set is slightly stronger pronounced than the NW-SE set, the latter has a suitable orientation for a reactivation as mode I cracks in the present-day stress field. This reactivation is thus likely to contribute additionally to the emission of EMR.

In summary, this study supports the applicability of the EMR method in the field. The main horizontal stress directions derived from main EMR directions measured with the Cerescope are in good agreement with the stress orientations determined by conventional methods (SKB-report, 2002 and references therein; Reinecker et al., 2008). Furthermore, the strong alignment of actual brittle structures (open cracks) on the sub-millimetre scale that formed in the present-day stress field seem to be responsible for the EMR main directions. This confirms the results of experiments on laboratory scale, where electromagnetic waves were emitted parallel to the orientation of micro crack propagation (Rabinovitch et al., 1999; Koktavy et al., 2004; Takeuchi and Nagahama, 2006).

Therefore, based on the results of this study, EMR is emitted by (1) the formation of new micro-cracks and (2) the reactivation of old brittle structures (grain- and phase-boundary cracks) with a favourable orientation related to the controlling stress field.

4. Linear EMR measurements

In this chapter, examples of linear EMR measurements to detect fault zones in different geological settings are outlined. The aims of this part of the study are:

(1) to test the applicability of the EMR method under different conditions and to compare the results with conventional tools, such as the measurement of changing radon concentrations above fault zones;

(2) to improve fault-zone detection with regards to the spatial accuracy by combining the Cerescope data in a effective way with exact geographic coordinates; and

(3) to display the combined EMR data and geographic coordinates in such a way to allow a reasonable geological interpretation.

4.1 Correlation between linear EMR measurements and radon emission above fault zones

Increased radon concentrations are known to correlate spatially with faults (e.g. Elster and Geitel, 1902; Kemski, 1993). The detection of faults from increased radon emission is an established method in structural geology. In order to test the applicability of linear EMR-measurements, both methods were simultaneously combined by measuring EMR intensities and radon emission along the same profile.

The increased intensity of radon above faults is the result of two main effects. (1) Radon can only exit from the outermost parts of the minerals or micro-crack surfaces. Due to relative movements along active fault planes, the potential radon emission surface in fault zones is increased by fracturing of minerals. However, this process is expected to be of minor importance (Vogler, 1960; Tanner, 1964). (2) Within and above active and inactive faults, the permeability of the rocks and the overlying soil is lowered and therefore the transport of radon is more effective.

Radon exists as three isotopes, which result from three decay chains. One is ^{219}Radon (Actinon) from the ^{219}Uranium chain. ^{220}Radon (Thoron) is a link in the ^{232}Thorium decay chain, whereas ^{222}Radon (Radon) originates from the decay of ^{238}Uranium. ^{222}Radon is an inert gas and has a half life of 3.82 days. ^{222}Radon decays to ^{218}Polonium (Fig. 4.1).
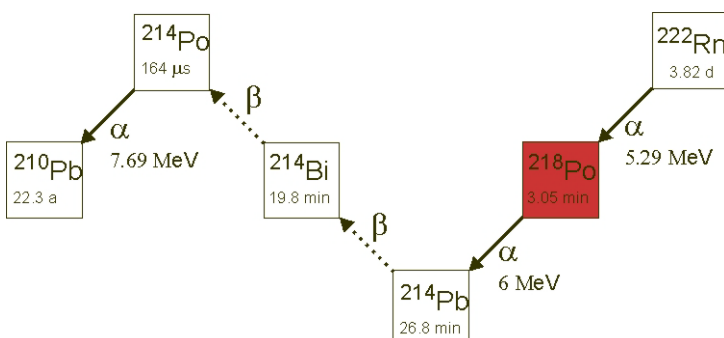
Fig. 4.1: ^{222}Rn decay chain. ^{222}Rn has a half life of 3.82 days. It decays to ^{218}Po. During the field measurements only the short lived ^{216}Po and ^{218}Po decays are counted.

The half life of Thoron, which decays to ^{216}Po (Fig. 4.2) is only 55.6 s, and that of ^{219}Radon is 3.96 s. Due to the short half life time of ^{219}Radon, it is of minor or no importance for radon measurements above faults.
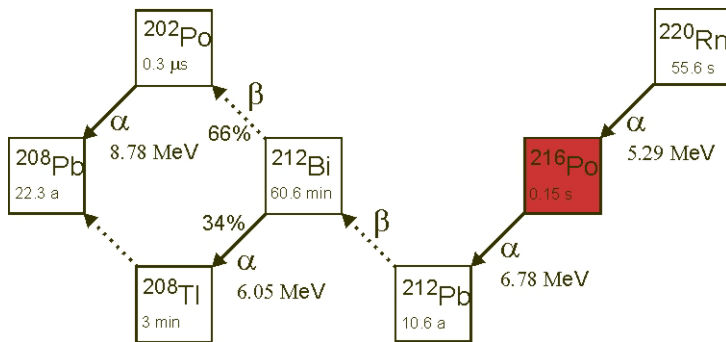
Fig. 4.2: ^{220}Rn (Thoron) decay chain. ^{220}Rn has a half life of 55.6 s. It decays to ^{216}Po.

The radon measurements of this study were carried out with the RAD7 radon detector (Fig. 4.3). This mobile device consists of a metal tube to sample soil gas, a drying tube filled with silica granules to reduce the humidity of the sampled soil gas, and the measurement unit, the RAD7. For each measurement, an appropriate location with at least 30 cm soil thickness was chosen. The metal tube was driven with the opening slots down to a depth of at least 30 cm. Then the soil gas was pumped through the drying tube into the detector for 5 minutes to clean and dry the extracted soil gas. The RAD7 has a "sniffing mode" that pumps soil gas during four 5-minutes-long cycles through the detector, counting the short lived ^{218}Polonium and ^{216}Polonium decays. Therefore, it ensures a response time of the measurement of some minutes (15 min according to the manual). Thus, in contrast to conventional radon measurements that usually run over days or up to months, the RAD7 can obtain results within minutes. It is therefore appropriate for the application in the field.
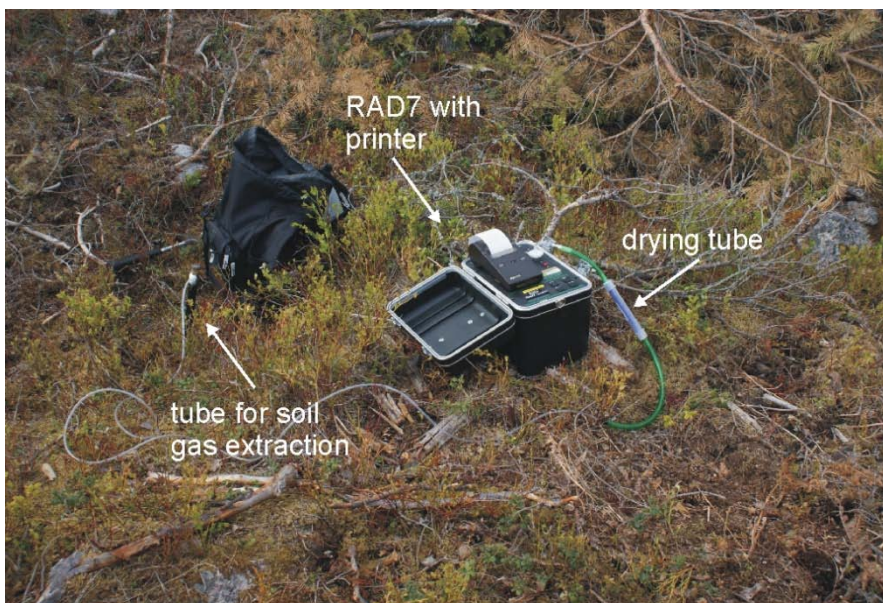
Fig. 4.3: Measuring setup of the RAD7, a mobile measuring device to detect radon emission in soil gas. The soil gas is sampled at least 30 cm below the surface through a metal tube and dried before measurement to increase sensitivity. The results are stored in a non-volatile memory and directly printed.

The profiles along which radon and EMR measurements were carried out is located in the Västervik area, southeast Sweden (for a description of the geological background, see Section 3.3). In this area, supposed faults are demonstrated by the linear arrangement of elongate lakes and sharply-bordered valleys (cf. Section 3.4.2). In case of the chosen profile, east of the Ålsjön, an easily recognisable and previously-mapped fault zone that strikes approximately ESE-WNW was chosen to demonstrate the applicability of linear EMR measurements to detect covered, unexposed faults and fault zones. The selected profile is about 800 m long, strikes N-S to NE-SW, and crosses this fault zone (Fig. 4.4), the trend of which is evident from an incision in the coast line of the Ålsjön and an adjacent sharply-bordered valley. The linear EMR profile was measured twice between 1 and 2 p.m. to ensure reproducible results. The device settings of the Cerescope were amplification of 113 dB, the selected discrimination level was 24, and the used frequency range was between 30 and 35 kHz.

The reproducibility, as shown in Fig. 4.5, is high for both parameters, i.e., the number of single pulses (Fig. 4.5 A) and for the defining energy (Fig. 4.5 B). The negative peak in the centre of the maximum in one profile can be attributed to moving the antenna out of the vertical position while climbing over a fence. Both parameters of the measured EMR are also displayed in Fig. 4.6, linked with exact geographic coordinates (see Section 2.4.2.4). The results show a clear correlation with EMR intensities (single pulses (Fig. 4.6 A) and defining energy (Fig. 4.6 B)) with the supposed location of the fault. From the diagrams (Fig. 4.5), it is obvious that the increase in intensities in both parameters starts at the same point. However, the patterns of increased intensities in both parameters differ from each other. While, the peak in the defining energy is distinct and narrow, the distribution in the single pulses is broader and is not so sharply bordered. To the north, the slope of the EMR intensity increase is slightly steeper than to the south (Fig. 4.5 A). This suggests that the fault dips steeply to the south (cf. Section 2.4.2.1).

The radon measurements were carried out the same day between 1 and 5 p.m. The weather conditions were dry and calm. Errors were only expected to occur at measuring locations 3 and 4, directly above the supposed fault centre, where the soil had a much higher humidity caused by a water channel. This might be important as increased humidity lowers the permeability of the soil and might be responsible for the decrease in detectable radon concentrations.
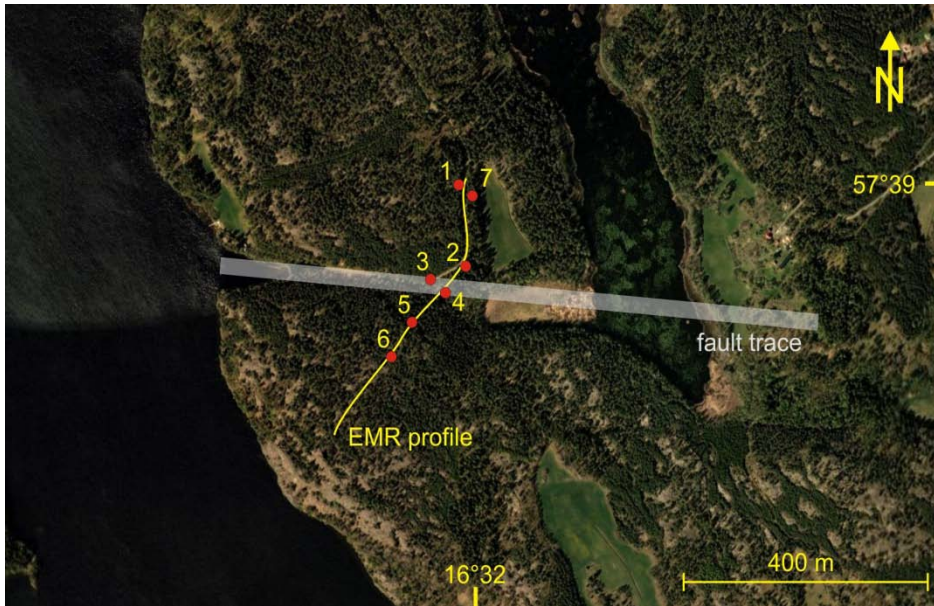
Fig. 4.4: Aerial photograph (provided by Google Earth) of the area of the selected profile at the Ålsjön, southeast Sweden. The profile crosses an ESE-WNW striking fault (trace indicated by a transparent white line). Location of the linear EMR measurements is indicated by a yellow line, while the locations of radon measurements are marked by red dots.
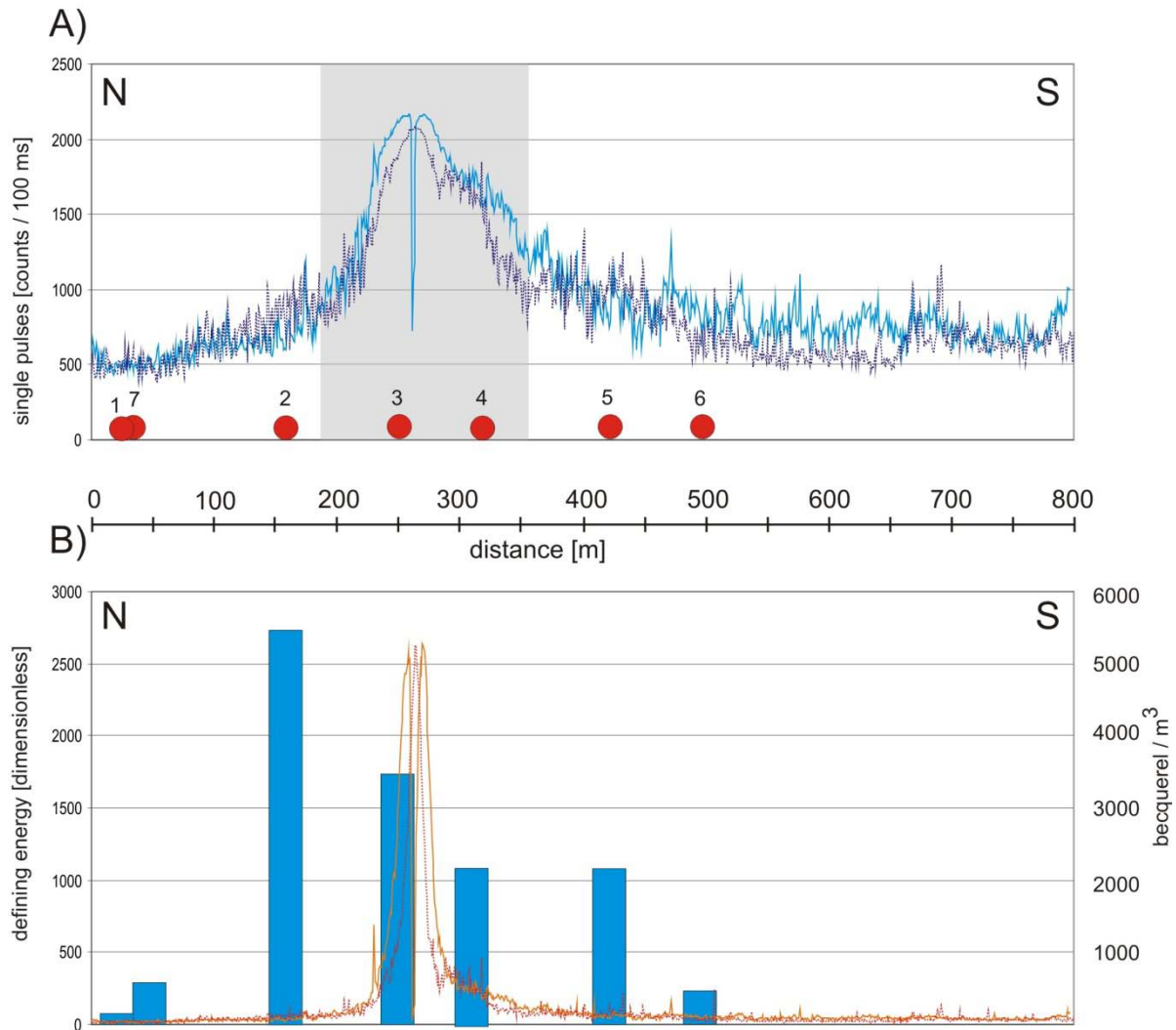
Fig. 4.5: Results of linear EMR and radon measurements along the profile shown in Fig. 4.4. To verify the EMR results, the profile was measured twice. **A)** Intensity distribution of single EMR pulses along the profile with a peak above the estimated fault. The area shaded in grey marks the length of the profile located above the fault trace. Red dots mark the location of radon measurements. **B)** Intensity distribution of the defining energy along the EMR profile (red graph) and measured radioactivity associated with radon decay in [Becquerel/m^3] (blue columns).

The measured radioactivity values associated with radon decay vary between 55 Bq/m^3 (standard deviation 87 Bq/m^3) and 5470 Bq/m^3 (standard deviation 2280 Bq/m^3). The lowest radon concentrations were observed at the northern and the southern end of the profile, while the highest concentrations occurred about 100 m north of the fault (as determined from topography and EMR intensities), at location 2. However, as mentioned above, at locations 3 and 4, the measured radon concentrations are probably lower due to a strong increase of soil moisture. Even if the measurements of the radon concentrations are subject to large errors and only 7 measurements were carried out along the 800 m long profile, it is evident that higher radon concentrations are congruent with higher EMR intensities and decreasing distance to the fault zone.
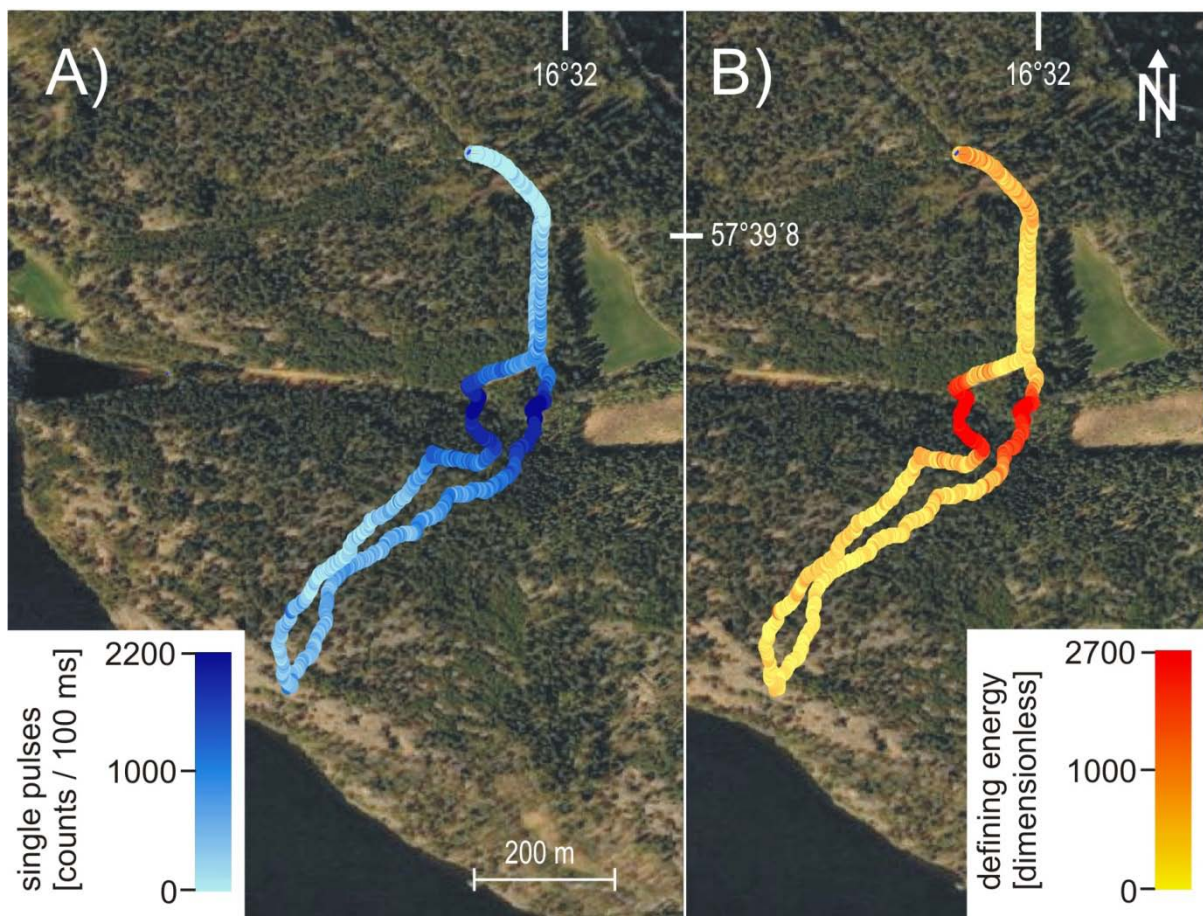
Fig. 4.6: Results of linear EMR measurements along the profile shown in Fig. 4.4 coupled with exact geographic coordinates, plotted on an aerial photograph (source: Google Earth). To verify the EMR results, the profile was measured twice. **A)** Intensity of single EMR pulses along the profile with a peak above the estimated fault. **B)** Intensity of the defining energy along the EMR profile.

This example demonstrates that linear EMR measurements can be a useful tool to detect faults. In analogy with increased radon emission, increased EMR intensities mark the location of the central parts of fault zones. In comparison to radon measurements, linear EMR measurements require less time and effort, are almost unaffected by weather conditions, and

have a much higher spatial resolution. In addition, EMR intensity patterns yield information about the orientation of fault plane underground (dip direction and rough estimate of dip angle).

4.2 Linear measurements in the vicinity of the Götemar Pluton, SE-Sweden

The granitic Götemar Pluton (Fig. 4.6) intruded 1.45 Ga ago (Åhäll, 2001) into 1.8 Ga old granitic rocks of the TIB in southeast Sweden (Fig. 3.6; Section 3.3.1; Wahlgren et al., 2004). The emplacement of the Götemar Pluton and other contemporaneous intrusions were probably tectonically controlled by a long range effect of a NNE-SSW trending shear system (Friese et al., 2009; Cruden, 2008). In map view, the Götemar Pluton displays a circular shape with a diameter of about 5 km. Its surroundings are tectonically largely characterised by faults at all scales, with lengths of up to 25 km (SKB-report, 2002; Section 3.4.2) and several generations of dykes. One of the major fault zones dissects the Götemar Pluton in N-S direction (Fig. 4.7); its length is more than 20 km, while its width, as estimated by remote sensing images, is in some places up to 100 m. In addition to sinistral shear, the western part of the Götemar Pluton was uplifted by several hundred metres along this fault (Kresten and Chyssler, 1976).

As part of this study, part of this N-S trending fault zone was analysed using linear EMR measurements to derive information about its width and internal structure (e.g. dip, degree of fragmentation). For this, four linear EMR profiles striking approximately E-W and positioned between ~5 km north and ~1 km south of the Götemar Pluton were measured (Fig. 4.7). In the following, each profile will be separately discussed.

Profile 1 is about 2200 m long and runs from E to W in the first 1000 m and then changes to a NW-SE orientation. The results are displayed in Figure 4.8. The background intensities are about 600 [counts / 100 ms] for the single pulses and about 40 [dimensionless] for the defining energy. This is in accordance with the other profiles (2, 3, and 4. In general, the peaks of both EMR parameters will be numbered and interpreted for each profile.

The increases in intensities at point (1) are obviously of artificial origin, since the measurements were taken close to a building. At points (2) and (3), the increased intensities correlate with faults identified by field observation, as well as on remote sensing images. The fault at point (2) dips steeply to the W, while at point (3) a sub-vertical dip of the fault can be inferred. At points (4) and (5), the profile crosses a major fault zone bordering a small lake south of the profile. At point (4) the intensities increase strongly and gradually decrease to the background level behind point (5). This supports the existence of a broader fault zone. The EMR intensity pattern indicates a dip to the E. At point (5), this signal is overprinted by the

influence of a power line, marked by a narrow peak. Point (6) shows the result of a combination of signals obviously belonging to a fault, as observed from topography and remote sensing images, and a power line located on the western border of the fault.
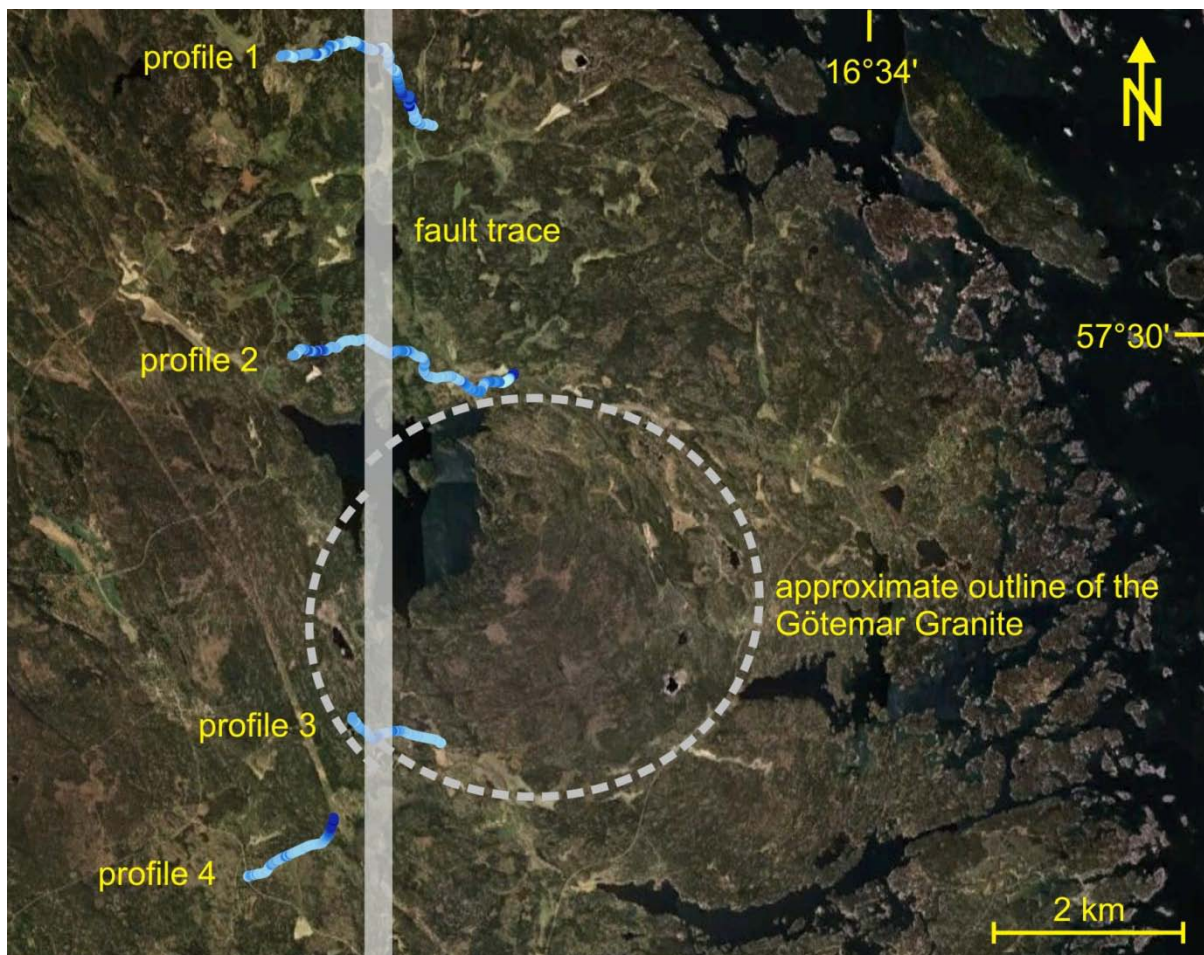
Fig. 4.7: Aerial photograph (source: Google Earth) of the vicinity of the Götemar Pluton (approximate outline of the pluton is indicated by a dashed line). A N-S striking fault (trace indicated by a transparent white line) displaces the Götemar Pluton by sinistral shear. In addition, the western part of the pluton is upthrown along the fault. The four linear EMR profiles are indicated by single-pulse intensities (for colour key see Figs. 4.8-4.11).

Profile 2 is 3300 m long and runs from W to E (Fig. 4.9). The background intensities are between 400 and 500 [counts / 100 ms] for the single pulses and about 25 [dimensionless] for the defining energy. The westernmost part of the profile is marked by two distinct peaks, (1) and (2), that can be correlated with two fault traces inferred from topography and from aerial photographs. Between 900 and 1600 m, the intensities increase before falling to the background level. Within this distance, a double maximum occurs (point 3). The eastern maximum is characterised by a negative peak in its pattern. Both maxima are asymmetric with a steep eastern flank, indicating that the faults dip west.
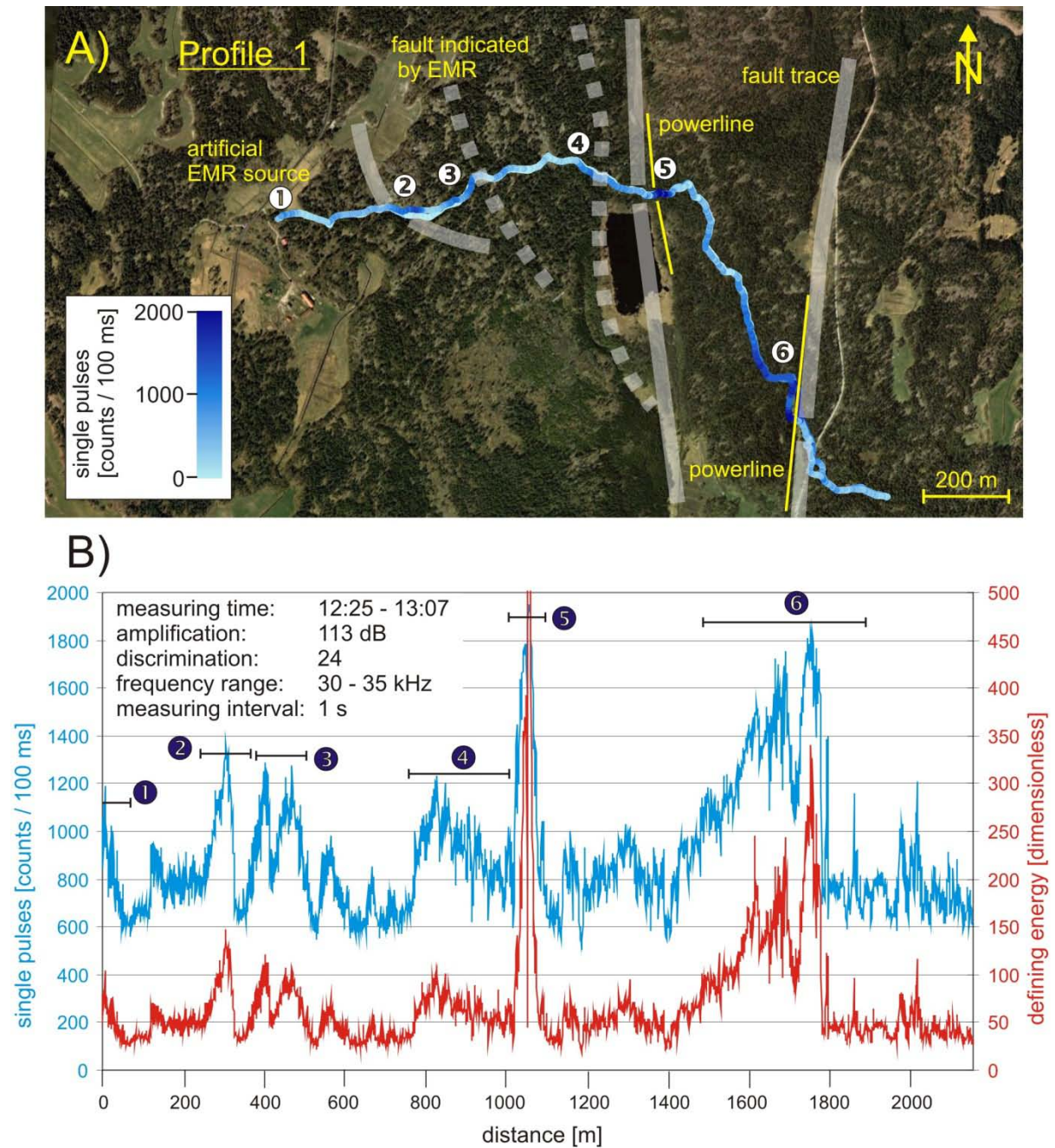
Fig. 4.8: Results of the linear EMR measurement of Profile 1. Numbers indicate peaks in EMR intensities **A)** EMR single-pulse intensities plotted according to their geographic coordinates on an aerial photograph (source: Google Earth). Fault traces identified by remote sensing and EMR peaks (transparent white lines) and identified by EMR only (transparent, dashed lines), as well as sources of artificial disturbances (yellow lines). **B)** Plot of the intensities (single pulses (blue) and defining energy (red)) along the profile are displayed. Bars mark the extent of EMR peaks.

A third peak within (3) that is less distinct might also be interpreted as a fault with a dip to the east. It cannot be identified in the field, but there is a weak indication on aerial photographs. The 300 m long maximum at point (4) coincides with a fault trace identified on aerial photographs. The high intensities at point (5) are caused by a high voltage power line.
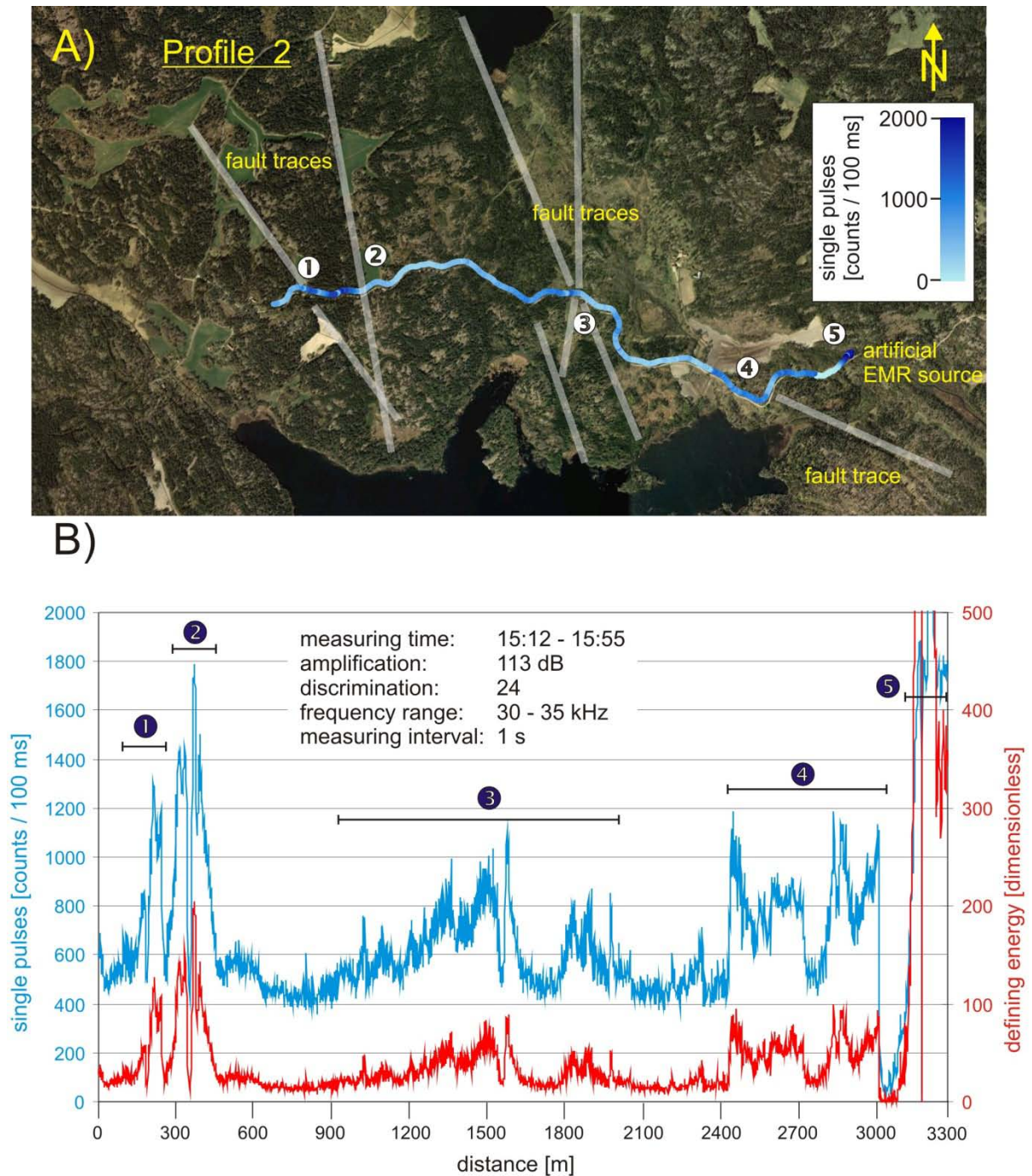
Fig. 4.9: Results of the linear EMR measurement of Profile 2. Numbers indicate peaks in EMR intensities **A)** EMR single-pulse intensities plotted according to their geographic coordinates on an aerial photograph (source: Google Earth). Fault traces identified by remote sensing and EMR peaks (transparent white lines) and sources of artificial disturbances. **B)** Plot of the intensities (single pulses (blue) and defining energy (red) along the profile are displayed. Bars mark the extent of EMR peaks.

In the W–E striking, 1200 m long **Profile 3**, two faults were detected by linear EMR measurements. The background intensities for the single pulses lie in the range between 400 and 600 counts / 100 ms, at a stable level. The same applies to the defining energy with a stable level between 25 and 50 [dimensionless]. The intensities are increased by a factor of about 3 to 4 directly above the faults. The intensity increases associated with the faults start at

a distance of about 100 m to the faults. The western fault (1) is characterised by an asymmetric intensity pattern pointing to a steep westerly dip of the fault. In comparison, at point (2), the asymmetry of the EMR peak is less pronounced, which is an indication for a vertical dip of the fault. In addition, the narrow, negative peak of unknown origin following the maximum is remarkable.

Fig. 4.10: Results of the linear EMR measurement of Profile 3. Numbers indicate peaks in EMR intensities **A)** EMR single-pulse intensities plotted according to their geographic coordinates on an aerial photograph (source: Google Earth). Fault traces identified by remote sensing and EMR peaks (transparent white lines) are marked. **B)** Plot of the intensities (single pulses (blue) and defining energy (red)) along the profile. Bars mark the extent of EMR peaks.

Profile 4 runs from SW to NE with a length of 1200 m. The background levels for the intensities are between 400 and 500 counts / 100 ms for the single pulses and between 20 and 30 [dimensionless] for the defining energy. The increased intensities at point (1) near a road can neither be correlated with geological features nor with artificial sources. Also at point (2), the source of increased EMR is unknown. However, since artificial sources are less likely to occur there than closer to the road, I suppose the increased intensities are associated with a fault that was not identified in the field. The increased intensities at point (3) are clearly related to a fault that was identified by field observation, as well as on remote sensing images. The strong increases at point (4) are related to a high voltage power line. The effect of this power line was recognisable at a distance of 200 m.

4.2.1 Summary of profiles 1-4

A comparison of the results of Profiles 1 to 4 indicates that independent of the measuring time, the background intensities of both evaluated parameters stay constant over the day with the chosen device settings. For the single pulses the background level lies at about 400 counts / 100 ms, while the background level of the defining energy remains at about 25 [dimensionless].

In general, it was possible to identify faults evident in the field and on aerial photographs. The faults coincide with increased intensities of EMR. In addition, the fault dip, or rather steep inclination, can be inferred from the symmetry of EMR intensity patterns. Furthermore, in most cases it is possible to differentiate between signal patterns of natural and artificial origin.

The geological significance of the results include that faulting in the surroundings of the Götemar Pluton is restricted to distinct fault zones with widths of tens of metres. The N-S striking fault dissecting the Götemar Pluton is subdivided into several individual faults. These are in most cases vertical or dip steeply to the west.
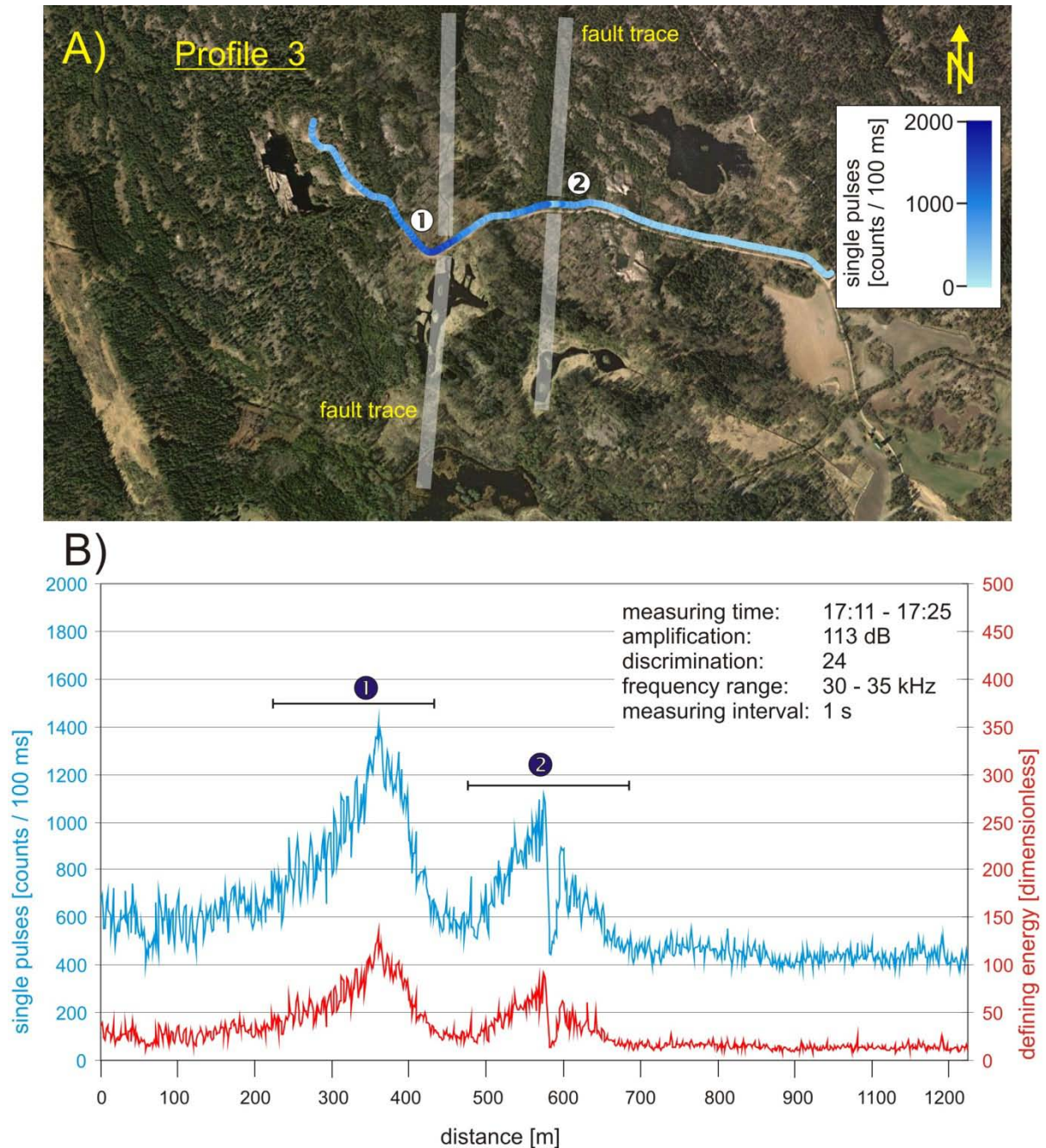
Fig. 4.11: Results of the linear EMR measurement of Profile 4. Numbers indicate peaks in EMR intensities **A)** EMR single-pulse intensities plotted according to their geographic coordinates on an aerial photograph (source: Google Earth). Fault traces identified by remote sensing and EMR peaks (transparent white lines) and identified by EMR only (transparent, dashed lines), as well as sources of artificial disturbances (yellow lines) are marked. **B)** Plot of the intensities (single pulses (blue) and defining energy (red)) along the profile. Bars mark the extent of EMR peaks.
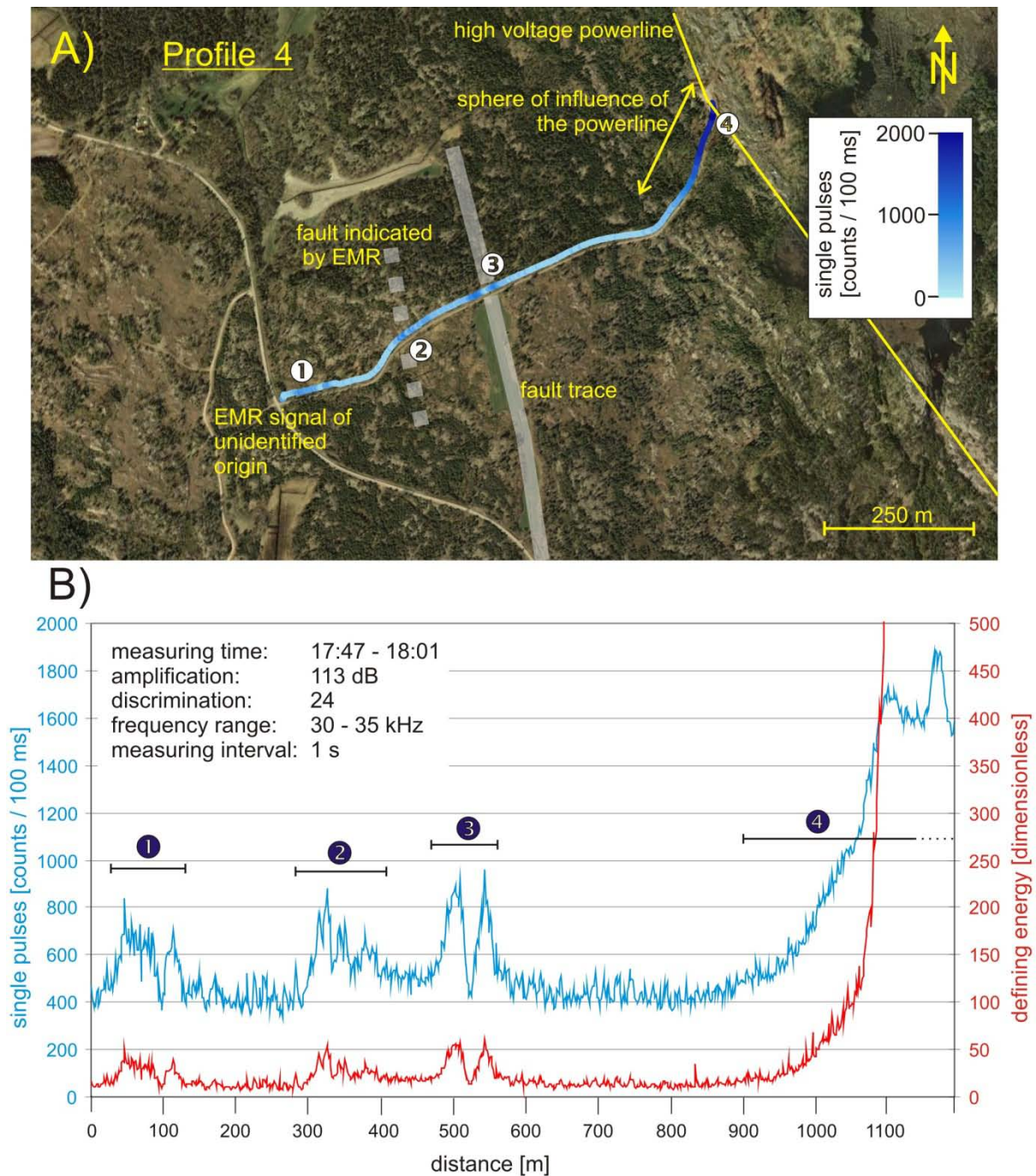
4.3 Linear measurements in the Leinetal Graben, Lower Saxony, Germany

In this section, one exemplary linear EMR measurement on the western shoulder of the Leinetal Graben is outlined to test this method in an area with sedimentary cover. The Leinetal Graben belongs to the intra-continental European rift system and is located in thesouthern part of the North German Basin. The normal faults bordering the graben predominantly strike NNE-SSW. In addition, the Leinetal Graben is characterised by a distinct structural east-west asymmetry. The western faults show considerably lower displacement than the eastern faults. Furthermore, along the NNE-SSW striking faults of the western graben shoulder and in the adjacent horst in the west, basaltic volcanism occurred during early Miocene (Wunderlich, 1968; Wedepohl, 1987). The Grefenberg (Fig. 4.12) is one of these Miocene volcanoes, with the particularity that the Grefenberg is associated with an E-W orientated fault (Nagel et al., 1981).

The measured linear EMR profile is about 3300 m long and crosses the basaltic Grefenberg cone from W to E (Fig. 4.12). The background level for the single pulses lies at about 1700 counts / 100 ms and for the defining energy at about 300 to 400 [dimensionless]. At point (1) the profile runs exactly parallel to the E-W striking fault. The plateau-like maximum of the single pulses could also be explained by an artificial source such as an underground power line. However, the fluctuations in the defining energy at the start and end point of the plateau in relation to the location of the path points to a fault-related signal. The fluctuation in the intensities at point (2) cannot be clearly associated with faults, judging from field evidence, previous mappings, or remote sensing. However, the signal pattern makes artificial sources also unlikely. One reasonable explanation might be a possible stress concentration at the unexposed lithological boundary between the Miocene basalt and the sandstones of the Upper Buntsandstein. At point (3), the EMR signal is similar to the pattern observed at point (1). The plateau in the single pulses does not manifest in the intensity distribution of the defining energy. An explanation for this can only be speculative. On the one hand, the increased intensities have no relation to known structures; on the other hand, the intensity level is too small to be related to artificial sources (cf. Section 2.5.1)

The results of this linear EMR profile indicate that linear EMR measurements may be a suitable tool to detect unexposed faults covered by younger sediments and not outlined by topography. In addition, lithological/rheological contrasts at stratigraphic boundaries might cause stress concentrations and therefore increased micro-cracking. However, an interpretation of the measuring results should in general be taken with care.
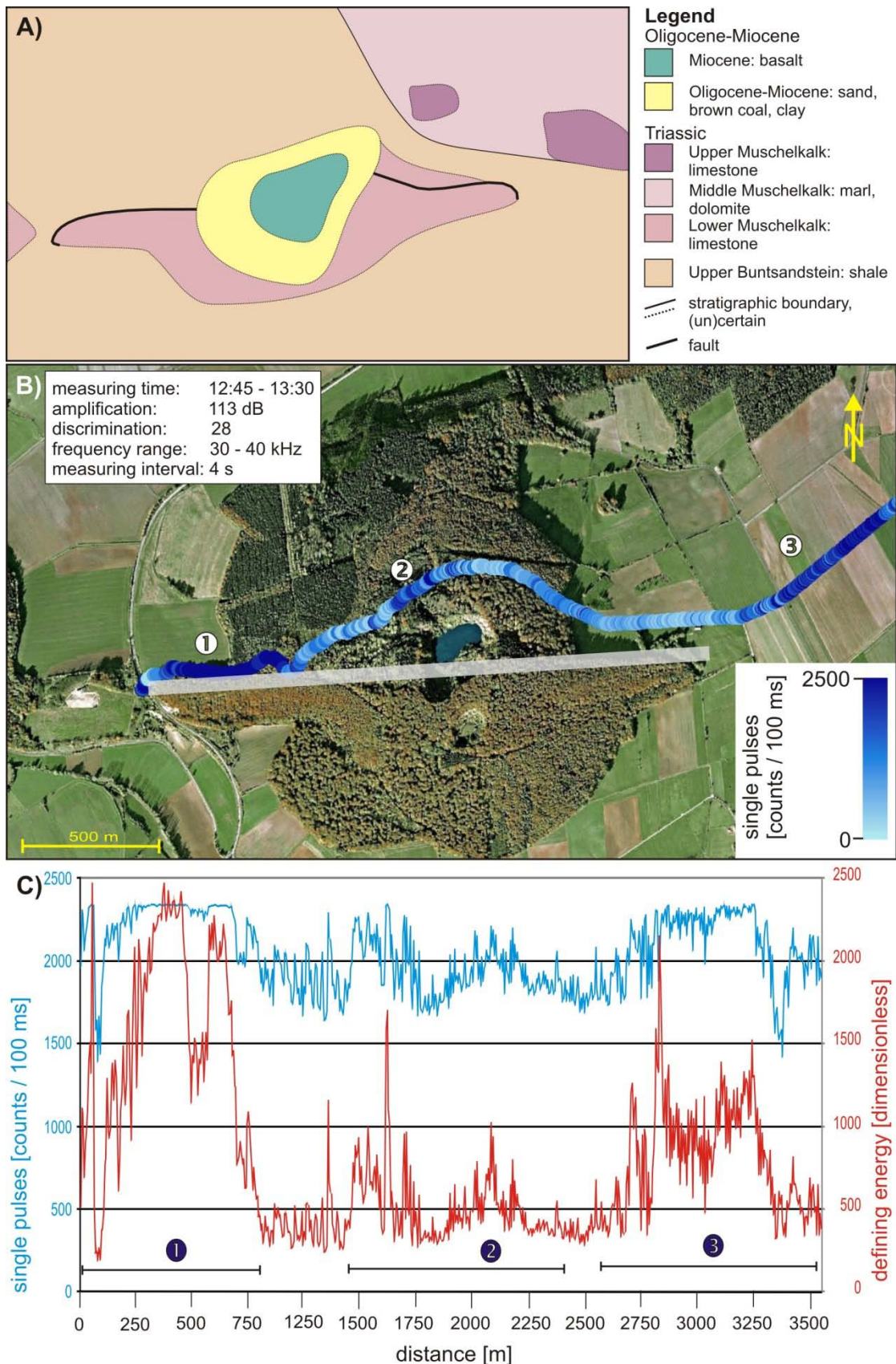
Fig. 4.12: Results of the linear EMR measurement in the Leinetal-Graben area. **A)** Schematic geological map of the Grefenberg, a Miocene basaltic volcano crossed by an E-W striking fault. Map based on Geological Map of Lower Saxony 4424 Dransfeld and Nagel et al. (1981). **B)** EMR single-pulse intensities plotted according to their geographic coordinates on an aerial photograph (source: Google Earth). Numbers indicate peaks in EMR intensities. Fault traces identified by remote sensing, geological maps, and EMR peaks (transparent white lines) are marked. **C)** Plot of the intensities (single pulses (blue) and defining energy (red)) along the profile. Bars mark

4.4 Discussion and conclusions

I demonstrate that linear EMR measurements can detect faults in different geological environments and lithologies. This has been confirmed by the correlation of EMR data with radon emissions, field observations, and remote sensing. Furthermore, the advantage of the combined EMR/GPS measurements, first applied in this study, improve the applicability and precision of the method. It is now possible to display the single measuring points with their exact geographic coordinates.

In detail, I have shown that it is possible to detect faults and make predictions about the dip direction and the strike by combining different linear measurements. In addition, I demonstrate that during one particular day no relevant fluctuations in intensities occur that influence the result or the comparability of different analysed profiles. Furthermore, I have shown that in different settings different background levels of EMR intensities occur and that these intensities are constant over large areas. In the Mesozoic cover rocks in the Leinetal area the intensities of both parameters used are considerably higher than in the crystalline rocks of southeast Sweden. The single pulses are by a factor two to three higher, while the defining energy is about 10 to 20 times higher.

The results support previous studies from e.g. Lauterbach (2005), Lichtenberger (2006) and Mallik et al. (2008), who worked with the Cerescope and other studies such as e.g. Nikoforova et al. (1989) in that they also observed increased EMR above faults.

However, because of possible artificial disturbances, it is recommended to plan field work carefully. Possible disturbances include e.g. roads and paths that are often used for laying cable. However, these disturbances are often first recognised during field work.

5. Spatial and temporal variations of main EMR directions measured with the Cerescope – natural vs. artificial source?

5.1 Introduction

One of the basic aims of this study, apart from testing the applicability of the EMR method in general, was to check the sensitivity of the method and to find out whether it is possible to determine changes of the main horizontal stress direction in the vicinity of faults, using horizontal Cerescope measurements (see Section 2.4.2.2). For this purpose, EMR measurements were carried out in the Leinetal area, in southern Lower Saxony, covering an area of about 1000 km^2, over a time span of two and a half years. No small-scale changes in the main radiation direction, which exceeded the measuring accuracy, were observed in the direct vicinity of faults or within a radius of more than 50 km. By extending the study area to the north, continuous spatial changes of the EMR main direction were measured (Section 5.2; Fig. 5.1). Furthermore, during the measuring periods in the Leinetal area, short-term temporary switches of the main radiation direction were twice observed (Section 5.3).

To evaluate the geological significance and origin of these variations, natural and artificial EMR sources were taken into account (Section 5.4).

5.2 Spatial variations of EMR main directions

Spatial changes of the main radiation direction were first observed along an N-S profile from Göttingen (Germany) to Malmö (Sweden) (Profile 1; Fig. 5.1). In this profile, a main EMR direction of 045±5° occurs in the southern part. Moving north along the profile, pronounced deviations from the directions measured in the Leinetal area occurred east of Hamburg. The northerly directions measured in this area mark the transition to a main EMR direction of 135° in Denmark and southern Sweden. To verify these observations, the study area was extended eastwards by two additional N-S profiles and one E-W profile (Table 5.1), which ran from the Magdeburg area to the island of Rügen (Profile 2), from Rügen to Dresden (Profile 3), and from Dresden to Göttingen (Profile 4; Fig. 5.1). The four profiles have a total length of about 2200 km and comprise 36 measurements with an average spacing of 50 km (Appendix 2). The settings of the Cerescope were kept constant with an amplification of 102 dB, a discrimination level of 20, and a frequency range of 30 – 35 kHz for all measurements.

As illustrated in Figure 5.1, the main EMR direction varies in general from NE-SW in the south to NW-SE in the north. The transition between these directions occurs within a distance of around 100 km in Profile 1 and increases towards the east in Profiles 2 and 3. In Profile 4, the main EMR direction varies from NNE in the east to NE in the west.
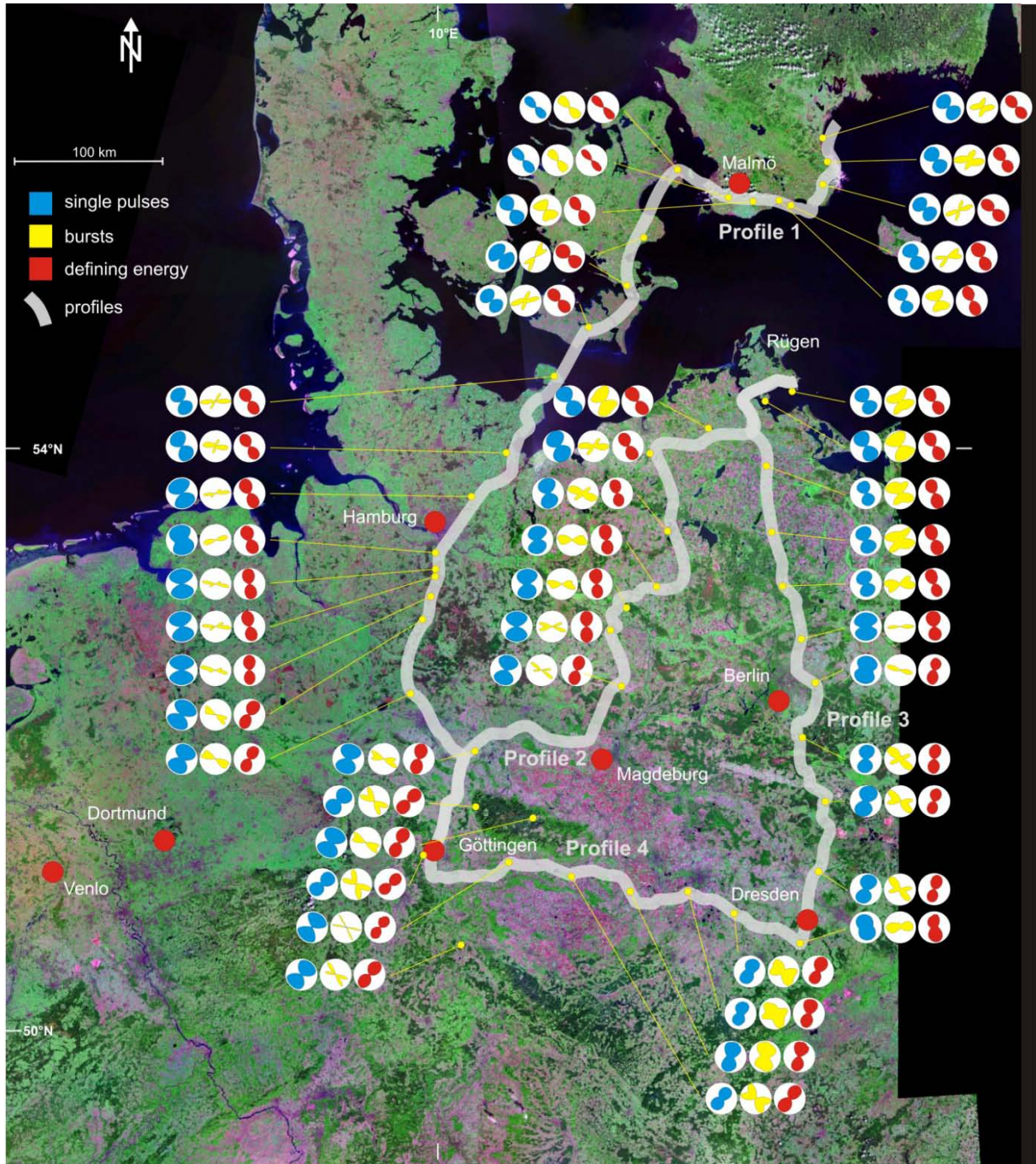
Fig. 5.1: Measuring locations (yellow dots) and observed main EMR directions along three N–S trending profiles. The transition zone between the NE orientation of EMR in the south and the NW orientation in the north occurs within a broader zone in the eastern part of the study area. Device settings were kept constant. Map base: NLT Landsat 7 (Geocover 2000) provided by Nasa World Wind.

The complete dataset of trajectories of the main EMR direction, however, forms a segment of a concentric pattern with a common centre near Emden (northwest Germany). To verify this observation, additional measurements were carried out near Dortmund, Germany, and Venlo, Netherlands. The main EMR directions measured at these locations coincide with the concentric pattern (Fig. 5.2).

Table 5.1: Location and length of EMR profiles as shown in Fig. 5.1.

No.	from	via	to	Distance [km]	Number of measurements
1	Göttingen	Hamburg	Malmö	750	20
2	Göttingen	Magdeburg	Rügen	350	10
3	Rügen	Berlin	Dresden	510	9
4	Dresden		Göttingen	330	6

Fig. 5.2: Map of the trajectories of main EMR directions in Profiles 1- 4. The complete data set forms part of a concentric pattern. Three additional measuring locations in the west confirm this observation. The red trajectories, two in Denmark, one near Göttingen, and one near Dresden are characterised by significantly lower intensities. Additionally, the red trajectories near Göttingen and Dresden deviate from the concentric pattern (see Section 5.4.2). Map base: NLT Landsat 7 (Geocover 2000) provided by Nasa World Wind.

5.3 Temporal variations

In addition to the spatial distribution of main EMR directions, repeated measurements were carried out in the Leinetal area at several points. Measurements in the Mesozoic cover of the Leinetal area were started in spring 2007 (Fig. 5.3). In May 2007, the obtained values were in the range 045 ± 10°. In contrast, at the end of 2007, the main radiation direction was then oriented 150°. Subsequently, at the turn of the year from 2007 to 2008, a rapid change in the main radiation direction from 150° to 045° was observed. This fluctuation was also recorded at Thale, Harz Mountains (station T) around 80 km to the ENE (Fig. 5.3), situated in the Paleozoic basement.
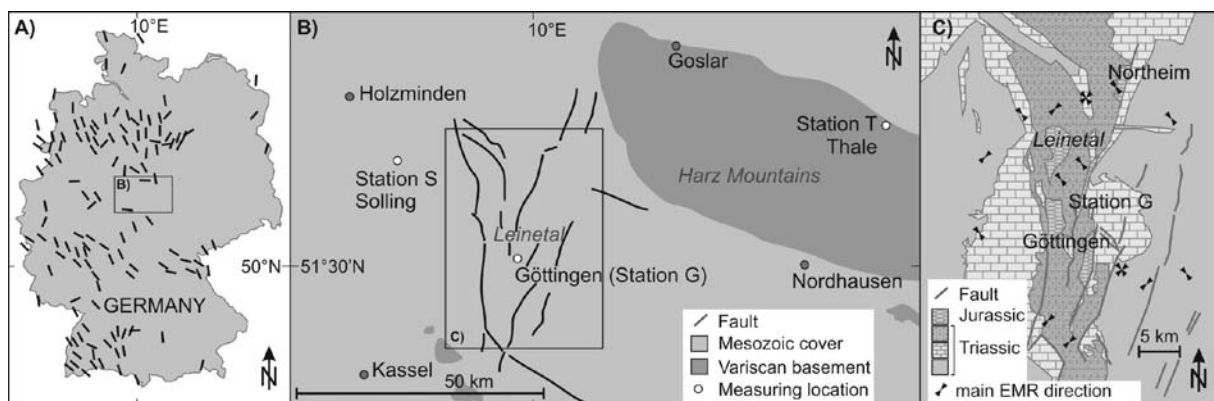
Fig. 5.3: A) Orientation of σ_H in Germany as displayed in the WSM (Heidbach et al., 2008). **B)** Locations of the measuring stations of this study; G (Göttingen), T (Thale), and S (Solling), where temporary changes of the main EMR radiation direction were measured. **C)** Main EMR directions at representative measuring locations in the Leinetal area. The observed main EMR directions are 045 ± 10° and 145 ± 10°. Fig. 5.1 and 5.2 display the NE direction that occurs during most of the year.

To verify and add detail to these observations, the main EMR direction was monitored at weekly intervals at one location (Station G) in the Leinetal Graben, starting in November 2008. These data were compared with intermittent measurements from two additional stations: stations T (Thale) and S (Solling), located around 40 km northwest of station G (Fig. 5.3).

At the turn of the year 2008 to 2009, a similar fluctuation sequence of the main EMR direction was observed in more detail, with more or less constant device settings (amplification, discrimination, frequency range) to keep the results comparable with respect to intensity. The measured direction remained rather constant at station G (with a deviation of ± 5°) over most of the year. However in contrast, the start and the end of the fluctuation sequence (2008-11-23; 2009-03-08) was characterised by a significant change in the orientation of the main EMR direction.
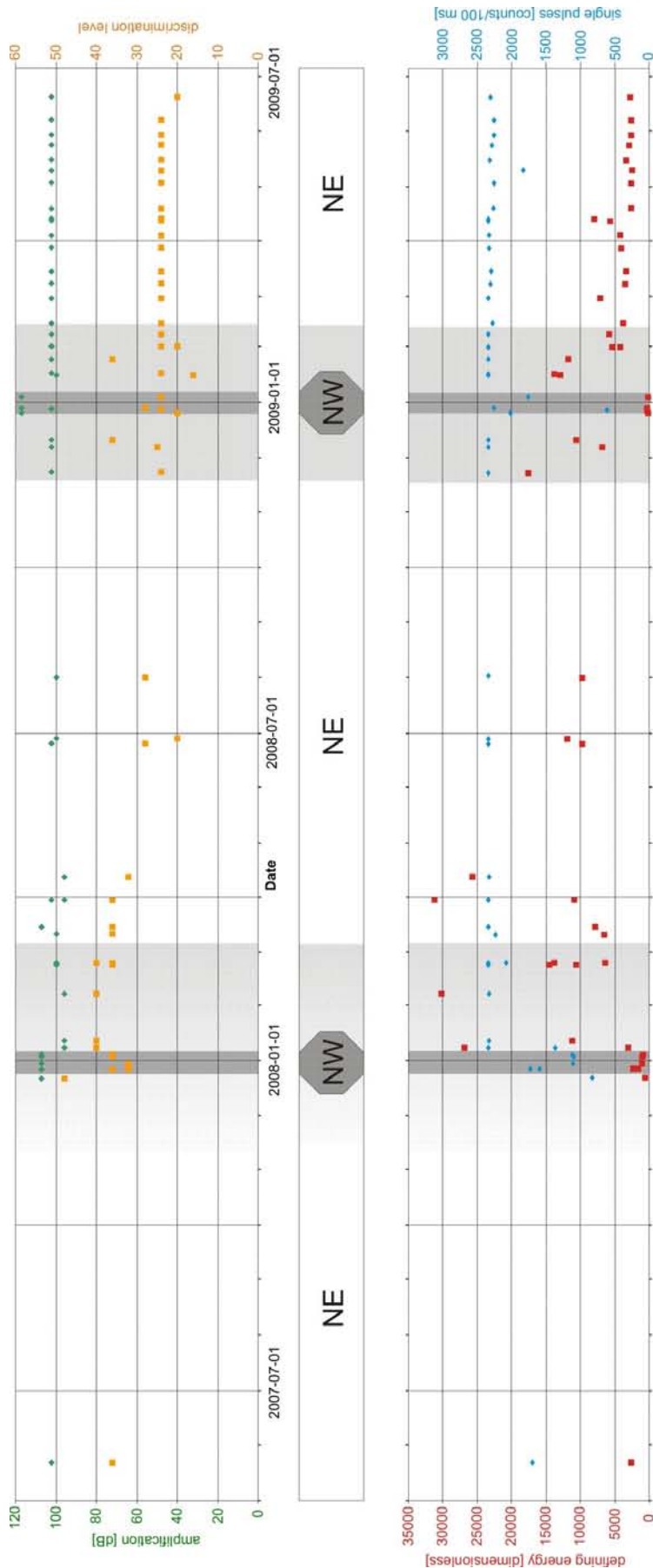
Furthermore, the intensities of EMR changed. At the beginning and the end of the sequence the intensities reached unusually high values for the defining energy, whilst the number of single pulses and the intensity of the defining energy were significantly lower in the middle of the sequence (Fig. 5.4).

Fig. 5.4: Overview of the device settings and observed EMR intensities during the monitoring of the changes of the main radiation direction at station G in the Leinetal area (see Fig. 5.3). In **A)** the device settings, (amplification in green and discrimination in orange) are displayed. An increase in amplification results in an increase of the measured intensity, while a higher discrimination decreases intensities. In **B)**, measured intensities are plotted as a function of time; blue: number of counts per 0.1 s, red: defining energy of the peaks that exceed the discrimination level. Light grey shaded parts around the turn of the year are marked by strongly increased intensities. The narrower dark grey shaded parts at the turn of the year mark the time with a NW main radiation direction with very low intensities despite higher amplifications.

In detail, this fluctuation sequence began with unusually high and fluctuating intensities of the defining energy and number of single pulses and with a directional change from the common 045±5° to 060° (2008-12-07) and 025° (2008-12-11) (Fig. 5.5).
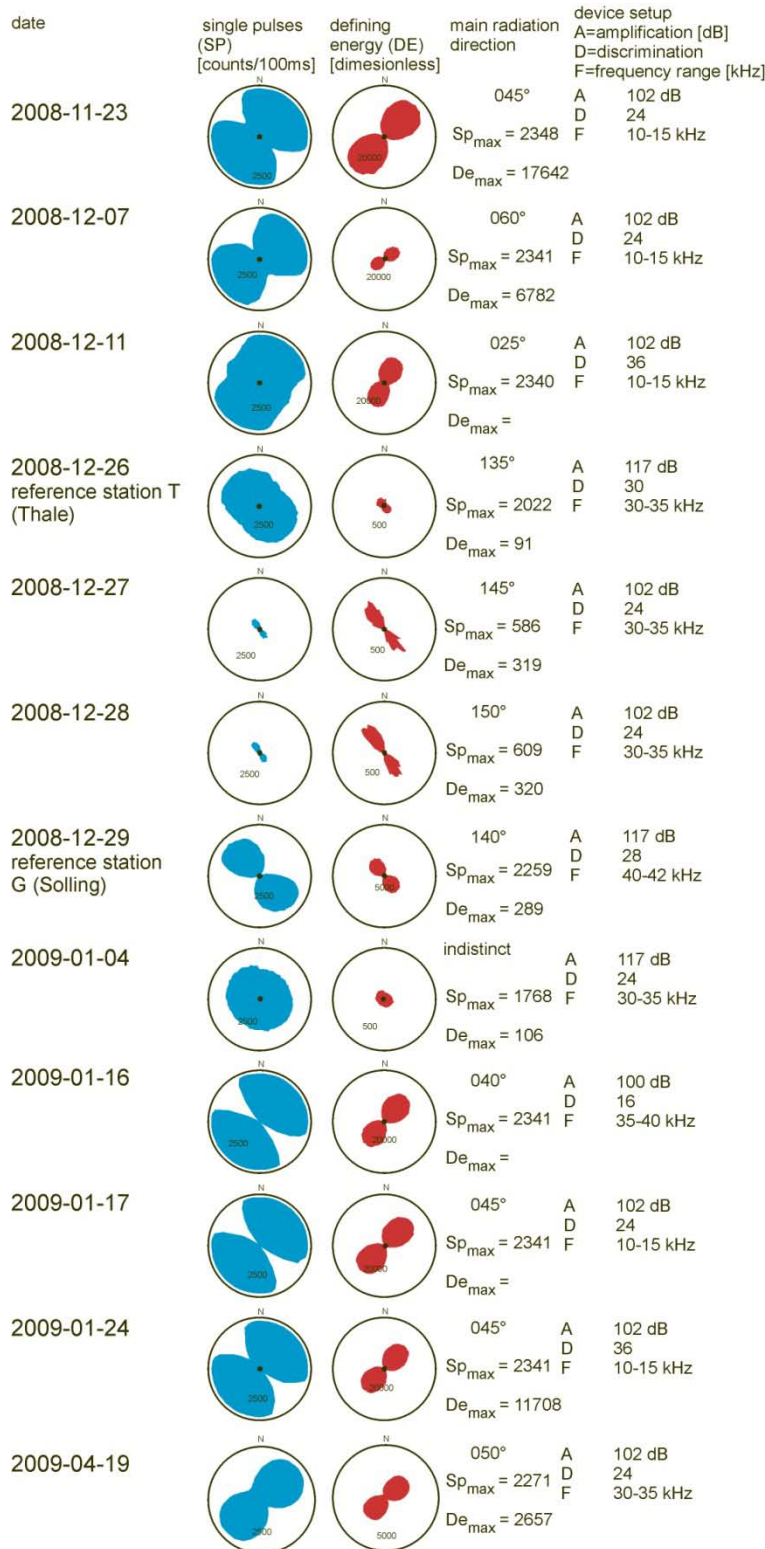
From 2008-12-11 onwards, the main EMR direction switched from 045° to 145 ± 10°. This was additionally observed at stations T (135°) and S (140°). Remarkably, a transition stage occurred during the switch, during which the observed directions were less well pronounced (2008-12-26 and 2008-12-29) or indistinct (2009-01-01).

Fig. 5.5: Temporary changes of the main EMR direction. The sequence started with strongly-increased intensities for the single pulses (SP; blue) as well as the defining energy (DE; red). Furthermore, the NE main EMR direction is unstable at the beginning and the end of the sequence. The second observed direction is NW and characterised by very low intensities compared to the former NE main direction. On 2009-01-04 no distinct direction was established. From the middle of January of 2009 the NE direction re-established and was marked by decreasing intensities and a stabilisation of the main radiation direction back to the stable values measured at the beginning of the sequence.

After the NE main direction of EMR re-established (2009-01-16), it varied between 030° and 065° during a stabilisation phase, which ended at the end of March 2009. Afterwards, the main radiation directions remained stable with values of 045 ± 5°. Moreover, the stabilisation process was characterised by a successive decrease in the intensities for both the defining energy and the number of single pulses until a stable level was reached by the middle of April (e.g. 2009-04-19).

The observed fluctuation of the main EMR direction and of the spatial changes described in Section 5.2 lead to the discussion of related sources of EMR and causes of temporal and spatial variations (Section 5.4).

5.4 Sources of EMR and causes of temporal and spatial variations

5.4.1 Correlation with the World Stress Map (WSM)

The concentric pattern of the main EMR direction cannot be correlated with the regional tectonic stress pattern and hence requires a re-evaluation of the geological significance of the EMR-method as tool for the detection of σ_H orientations. On the WSM (Heidbach et al., 2008) (Fig. 5.6) there are, however, large areas where the main EMR direction coincides with σ_H. This is the case e.g. in parts of north western Germany, Denmark, and southern Sweden.
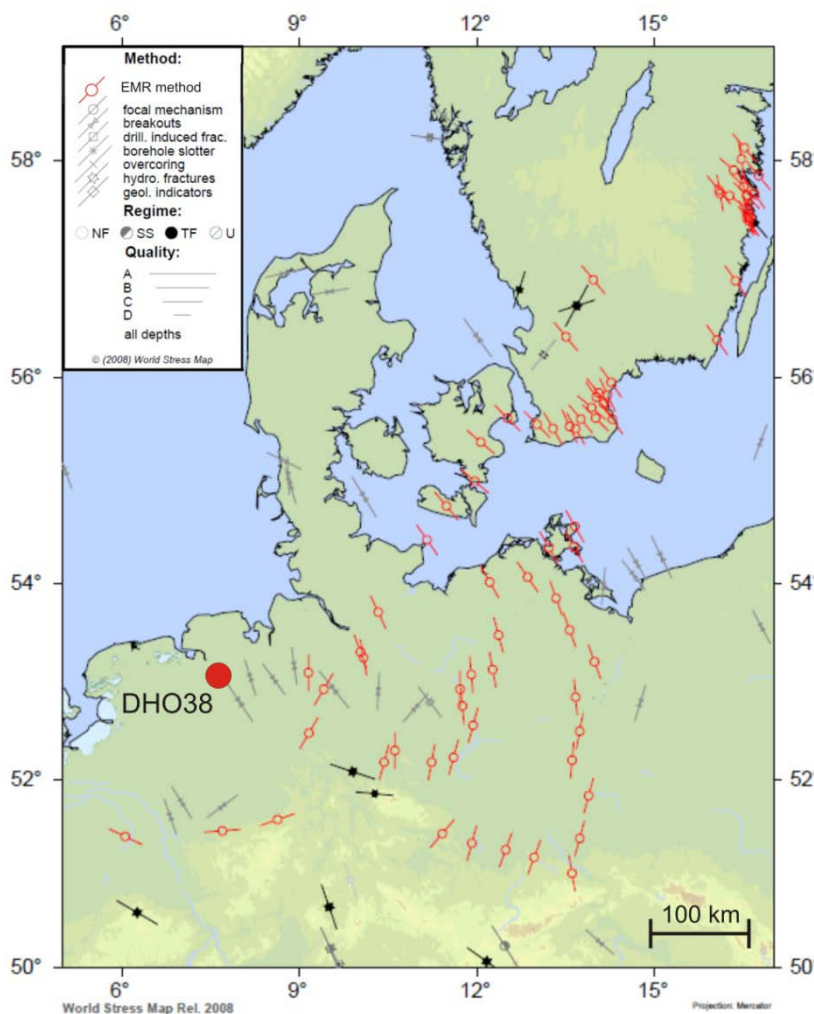
Fig. 5.6: Comparison of the measured main EMR directions (red trajectories) with σ_H trajectories in the WSM (Heidbach et al., 2008). The EMR main directions form a segment of a concentric pattern with a common centre close to the VLF transmitter DHO38 (red dot; see Section 5.4.2). This distribution is in contradiction to the σ_H orientations displayed in the WSM.

Furthermore, a direct comparison of the directions of probable σ_H directions obtained with the EMR method and with those determined with conventional methods is difficult since there is only a limited amount and an uneven distribution of the data in the WSM. Moreover, the error of data in the WSM ranges between $\pm 15°$ and $\pm 40°$, depending on the applied method, which leaves considerable room for interpretation when comparing them with EMR main directions with errors only between $\pm 5°$ and $\pm 10°$. Therefore, it became only necessary to question the geological significance of the EMR results after a large dataset covering an area of 280.000 km^2 had been collected.

5.4.2 Influence of VLF transmitters

For the described dataset, an artificial source of the EMR has also to be considered. The centre of the concentric pattern is located in the area of Emden (Lower Saxony), where the NATO military transmitter "NATO VLF/MSK Marinefunkstelle Rhauderfehn" with the call signal DHO38 is situated (VLF transmitters are named by their call signals below). DHO38 is powered at 0.8 to 1.2 MW and consists of 8 antennas with an omni-directional transmission pattern. The main transmission frequency is 23.4 kHz. Other active European VLF transmitters are listed in Table 5.2; their locations are displayed in Figure 5.7. As most VLF transmitters are military facilities, information is rare and the dataset is probably incomplete.

Table 5.2: Active VLF transmitters in Eurasia with frequency range and status. VLF transmitters can be active at different frequencies and use different call signals at the different frequencies. Therefore, the transmitter frequencies are listed separately according to their status, divided by "/". Based on Jacobsen, 2001.

call signal	country	coordinates		transimission frequency	status
		N	E	[kHz]	
DHO35	Germany	53.13	7.36	18.5	not active
DHO38	Germany	53.13	7.36	23.4 / 0.28	active / not active
GBR	UK	52.22	-1.11	16.0 / 19.6 / 21.22	active / active / not active
GBZ	UK	52.43	-3.02	21.22	not active
GQD	UK	54.53	-3.17	19.00/ 19.6 / 21.22	not active / sporadically active / not active
HWU	France	46.4	1.15	14.5 / 15.1 / 20.9	not active / sporadically active / active
		46.4	1.15	21.05 / 21.75 / 22.6	no info / active / not active
		46.4	1.15	29.0	sporadically active
ICV	Italy	40.55	9.44	20.27 / 20.76	active / sporadically active
JXN	Norway	66.23	13.4	16.4	active
JXZ	Norway	66.23	13.4		
RSDN-20	Russia	45.20	38.15	11.90 / 12.64 / 14.88	acitve / active / active
SAQ	Sweden	57.07	12.23	17.2	sporadically active
TBB	Turkey	37.24	27.19	26.7	active
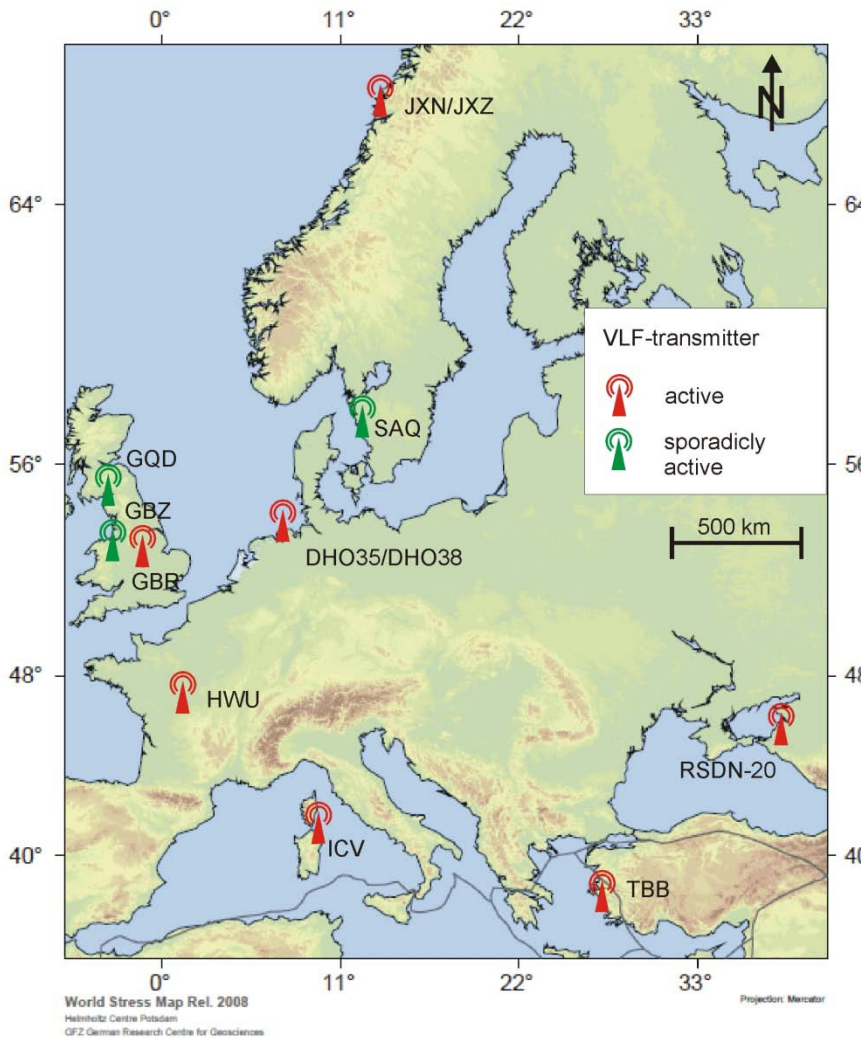
Fig. 5.7: Location of VLF transmitters in Eurasia with active (continuous) broadcasting in red and sporadic broadcasting in green. Base map WSM (Heidbach et al., 2008).

DHO38 is monitored by an amateur station (American Association of Variable Star Observers (AAVSO), observer code A118) in southern France near Toulouse. The distance of this station to DHO38 is 1167 km on an bearing of 021°. The aim of this station is to detect Sudden Ionospheric Disturbances (SIDs) caused by solar flares that manifest in disturbances of the received signal strength of VLF transmitters. The dataset of this monitoring station can be found at http://sidstation.lionelloudet.homedns.org/home-en.xhtml. On this site the recorded signal is displayed in real time.

The archive contains data from December 2005 to present. As shown in Figure 5.8, the signal strength varies considerably over the day, depending on the altitude of the sun. While during the daytime variations are small, the received signal strength varies over a wider range from sunset to sunrise. Every day between 7:00 a.m. and 8:00 a.m. UTC an intermission in the regular operation of DHO38 is operated.
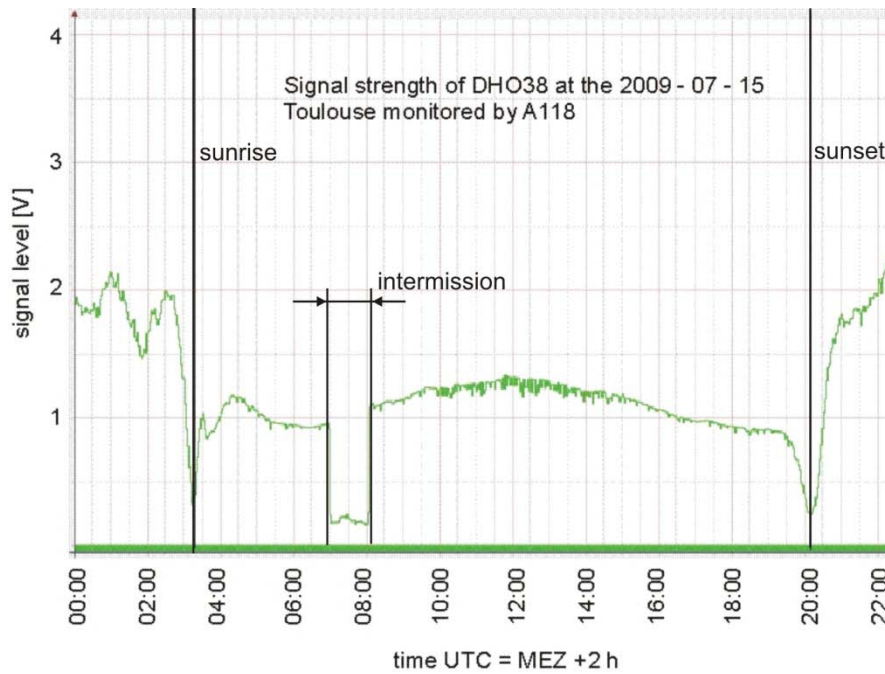
Fig. 5.8: Signal strength variation of DHO38 as received near Toulouse on 2009–07–15. Between sunrise and sunset the received signal strength is nearly constant. During night, sunrise, and sunset the received signal strength varies over a wide range. Between 07:00 and 08:00 UTC DHO38 is turned off. Modified after Loudet, 2009).

For a further verification of the influence of the transmissions of DHO38 on EMR measurements with the Cerescope, time-triggered measurements were carried out during the turn-off and turn-on times of DHO38, combined with horizontal measurements prior to and during the intermission on 2009–07–15 (Figure 5.9). The device settings during the horizontal measurements prior to the turn-off time and the time-triggered measurements during the turn-off time were kept constant with an amplification of 100 dB, a discrimination level of 24, and a frequency range between 5 and 12 kHz. The main EMR direction prior to the intermission was 030°. The following time-triggered measurement started at 6:47 a.m. (UTC) with a measurement interval of 30 s for the first three measurements and 60 s intervals for the ensuing time. The antenna was oriented parallel to the main EMR direction. During the first 13 minutes no changes in intensities or the frequency occurred, however the 7:00 and 7:01 a.m. measurements had increased intensities for the single pulses and the defining energy, while the burst rate and the frequency remained stable. From 7:02 a.m. onwards, the intensities were near zero. Only at 7:18 a.m. a peak in the defining energy was observed. The frequency varied in a wider range than before turn-off. For the measurement of the main EMR direction during the intermission, the device settings had to be changed to a higher amplification (107 dB); the discrimination level was increased to 24, the frequency range again kept the same. The determined main EMR direction was 165°. Furthermore, the intensities of the defining energy decreased considerably in relation to the number of single pulses per direction.
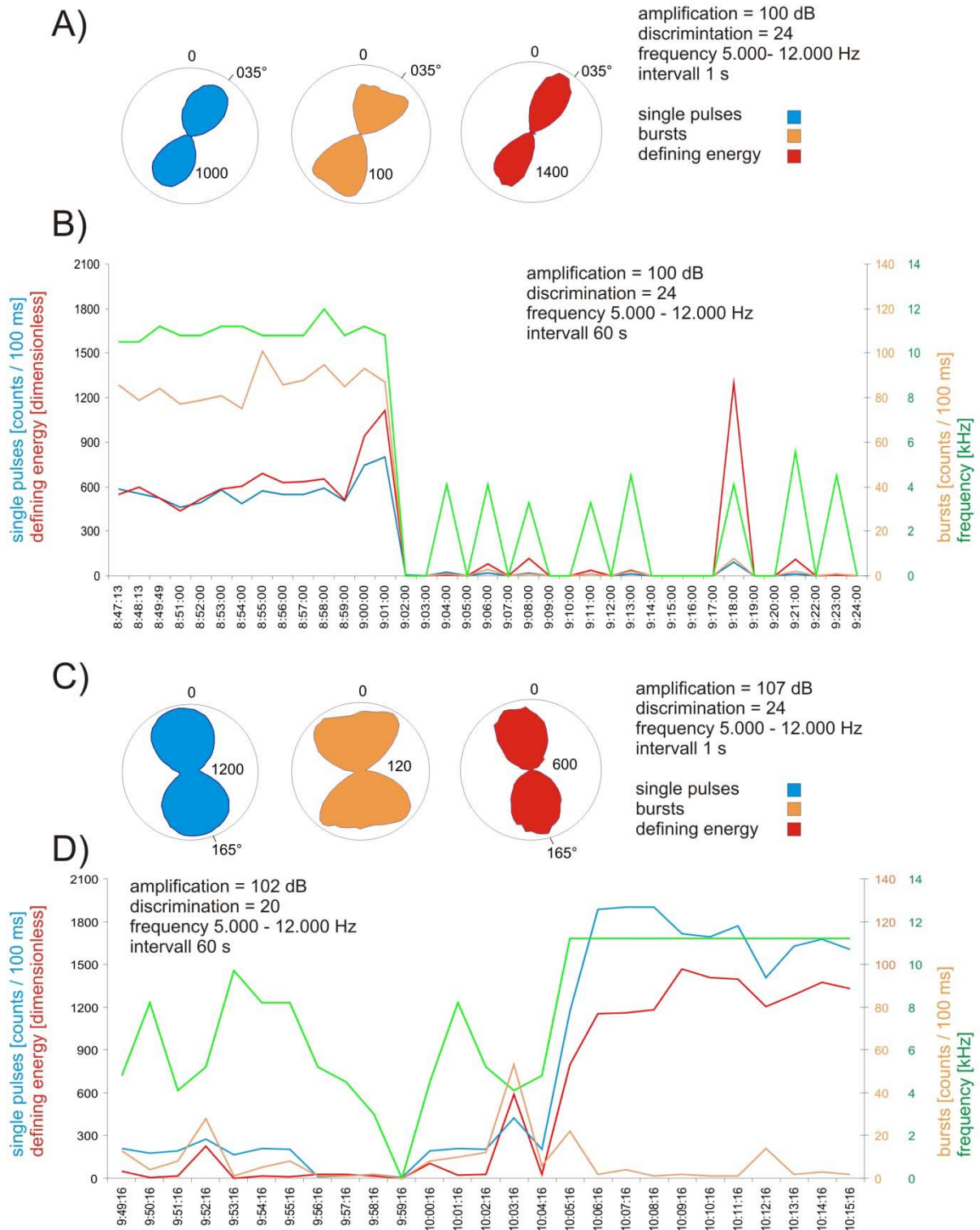
Fig. 5.9: Daily intermission in the regular broadcasting of DHO38, recorded with the Cerescope on the 2009-7-15 near Göttingen. **A)** Horizontal measurements (Chapter 2.4) show the regularly-observed pattern with a main EMR direction at 030°, i.e. perpendicular to the bearing to DHO38, intensities are at the common level. **B)** Measurement during the turn-off of DHO38. Exactly at the turn-off time, the received signals decreased to nearly zero at the given device settings. **C)** Results of a horizontal measurement of EMR during the intermission. The main EMR direction is 165° and the intensities are, despite the higher amplification, lower than in A) before the intermission. **D)** Time-triggered measurement during the turn-on of DHO38. The amplification is higher than in B). Therefore the intensities and especially the frequency could be evaluated during this period.

The time-triggered measurement during the turn-on time was carried out with the same settings as during the turn-off, with the exception that the amplification was increased to 102 dB. Furthermore, the discrimination level was lowered to 20 to get evaluable values during the intermission. The intensities for single pulses, the defining energy and the bursts stayed on a more or less constant level between 7:49 a.m. and 8:04 a.m., with one exception at 8:03 a.m. After the turn-on of DHO38, the intensities for the single pulses and the defining energy immediately increased to a stable level, and the number of bursts stayed constant. The frequency varied during the turn-off time and became stable at the end of the intermission.

In addition to the daily intermission of DHO38 between 7:00 a.m. and 8:00 a.m., there is an intermission at the turn of the year that starts in the middle of December and ends in the first week of January. The signal pattern received by the monitoring station A118 suggested that these intermissions are used for maintenance work. This intermission completely explains the temporary fluctuations described in Section 5.3., while the second direction observed during the intermission can be explained by HWU, another VLF transmitter located in France (see Fig. 5.7).

In Figure 5.10, the maximum intensities of the defining energy and the single pulses during the measurements of the profiles shown in Fig. 5.1 and 5.2 are plotted in relation to the distance to DHO38. The dataset is extended with representative measurements taken in 2009 in the Västervik area (see Chapter 3). There is a clear trend (in Fig. 5.10), which implies that decreasing intensities correlate with increasing distance to DHO38. In Profile 2, at a distance of about 500 km, it was necessary to increase the amplification to obtain acceptable values; the same applies to the measurements in Profile 3 at a distance of about 700 km to DHO38. Consequently, some of the outliers (displayed in Figure 5.10) can be explained by their time and the measuring conditions. Outliers 5 and 6 were taken during the daily intermission of DHO38, the low intensities of outlier 7 can also be explained by the measuring time, i.e., exactly during the sunset when the signal strength is generally low (see Fig. 5.8). Outlier 3 was measured after sunset. The high intensities of outliers 1, 2, and 4, which were measured between 8:17 a.m. and 1:12 p.m., cannot be explained by the intermission of DHO38 or the altitude of the sun. Therefore, I assume that these measurements were taken above a fault or a fault zone.
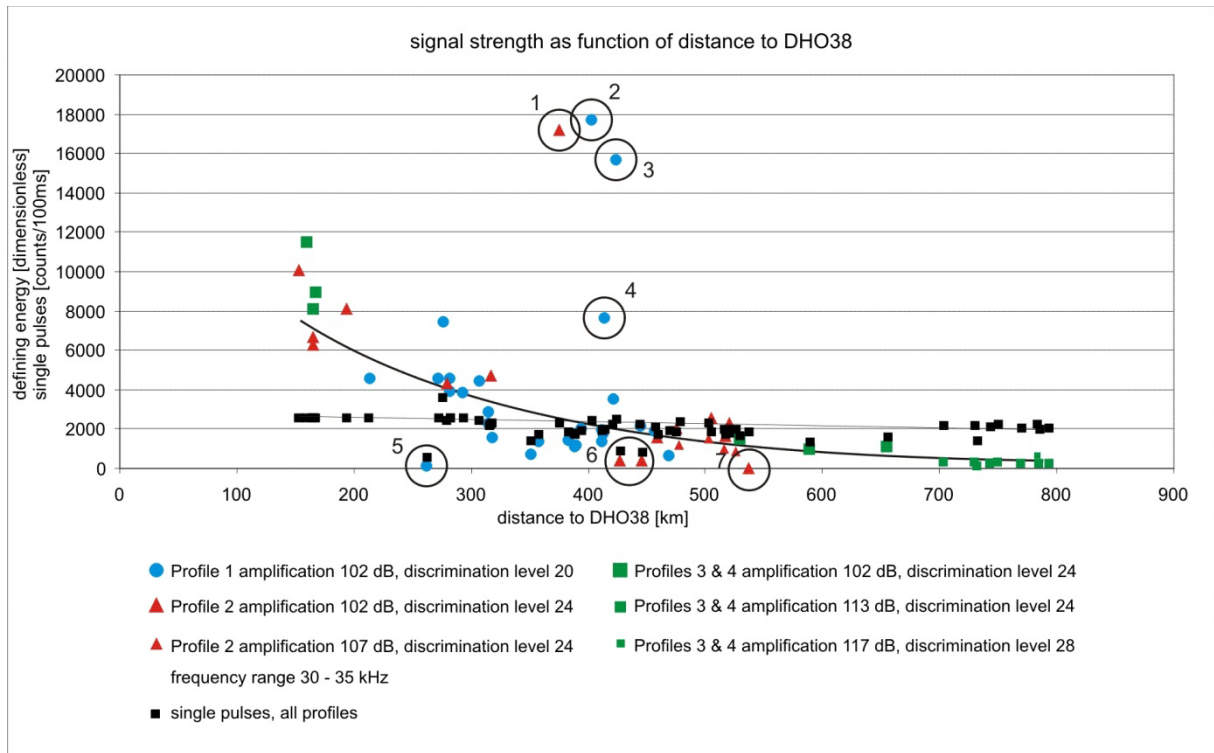
Fig. 5.10: Maximum intensities of the defining energy of EMR as a function of the distance to DHO38. The general trend is that intensities decrease with increasing distance to DHO38. Outliers (encircled) were usually measured during the intermission time of DHO38 or during sunset or sunrise. Only outliers 1, 2, and 4 cannot be explained by the time of measuring. The most likely explanation is that these measurements were carried out above faults or fault zones. For profile numbers see Fig 5.1. Note that the number of single pulses remains relatively constant independent of distance and device settings.

Another, problematic observation is based on some EMR measurements on Lanzarote, Canary Islands, Spain, where even by using the highest amplifications available on the Cerescope, only weak signals could be observed, correlated with only weakly pronounced main directions (Fig. 5.11; Appendix 3). These, however, are again of an orientation that could be explained with DHO38, and are also consistent with some geological structures that give rise for a main horizontal principle stress directions that coincides with the measured main EMR direction. If the signal is controlled by DHO38, this means that at least at a distance of about 3500 km to DHO38 the signal strength of the VLF transmitter is higher than the natural EMR and therefore the maximum amplification of the Cerescope might be too low to receive the geogene EMR.
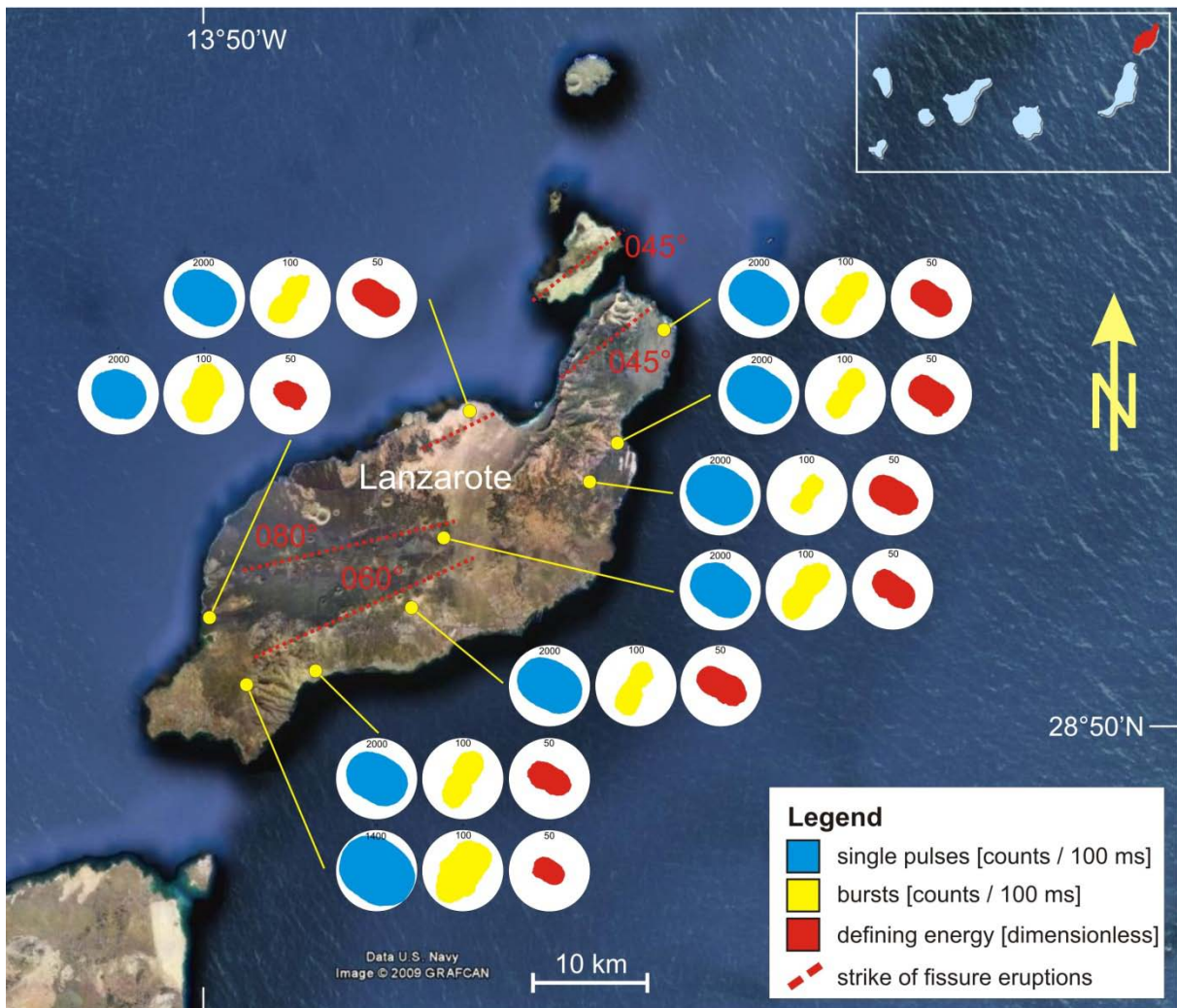
Fig. 5.11: Spatial distribution of main EMR directions on the island of Lanzarote, Canary Islands, Spain. The Cerescope setup used included an amplification of 120 dB, discrimination of 20, and a frequency range between 40 and 45 kHz. Map base provided by Google Earth.

5.5 Consequences

In general, the signal of DHO38 is evidently a constant source of disturbance, which forms a narrow peak in the frequency spectrum recordable with the Cerescope, even if it has only been identified as the source of this peak during this study. Consequently, all measurements taken during this study excluded the 23.4 kHz signal.

In principle, the signal of DHO38 should not influence Cerescope measurements because of several filter mechanisms that allow a specification of the evaluated frequency range and automatically reject periodic signals (see Section 2.4.1). Hence, any influence of artificial signals should be prevented. However, as demonstrated in Section 5.4.2, I attribute the recorded main EMR directions to DHO38. The results of test measurements at different

frequency ranges (Fig. 5.12) demonstrate that not only is the automatic filter for periodic signals unable to reject the signal of DHO38, but also the bandpass filter. The filter mechanisms probably cannot compensate, maybe as a result of the high signal strength, compared to the natural EMR.
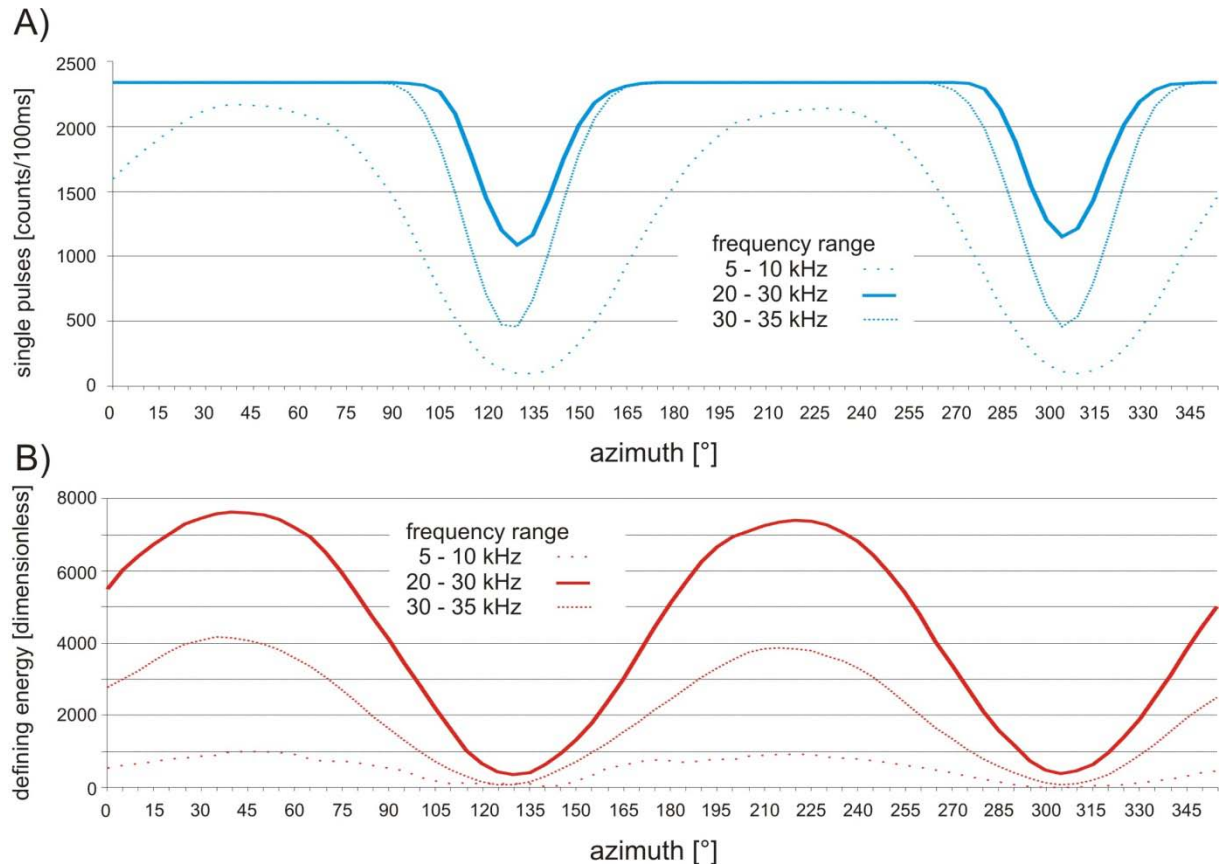
Fig. 5.12: Comparison of three horizontal measurements with the same device settings; amplification 107 dB, discrimination level of 24. **A)** Intensities of single pulses (blue) and **B)** defining energy (red) vs. the azimuth. Only the frequency range was changed. Highest intensities are observed with antenna orientated perpendicular to DHO38 at every frequency band.

In detail, the results of three measurements at different frequencies taken within 15 minutes of each other (Fig. 5.12) show that the bandpass filter was unable to eliminate the influence of the VLF transmitter. Not only the measurements at a range of 20 to 30 kHz, which comprise the transmitter frequency (23.4 kHz), but also the measurement at 5 to 10 kHz and 30 to 35 kHz show the influence of DHO38.

The observations may also explain a "phenomenon" that was observed during further EMR measurements, namely the observed maxima of the single pulses. During the horizontal measurements an upper limit of 2341 single pulses per 100 ms was regularly observed (see Fig. 5.10). In contrast to the defining energy, the number of single pulses per time is not as strongly affected by the distance to DHO38. The number is relatively stable even with

changing settings of the measuring device. Furthermore, 2341 is exactly a tenth of the transmission frequency of 23.4 kHz, with respect to the measuring time of 100ms. This is an additional argument for DHO38 as a source of the measured EMR. Thus, the relationship between the number of single pulses and the defining energy is a function of the distance to the VLF transmitter. This additional information might be useful for further studies, and more important in identifying the location or distance to the disturbance source than the relationship between defining energy and distance to the disturbing source. However, further verification of this is necessary.

5.5 Discussion and Conclusions

Several observations associated with EMR measurements with the Cerescope give cause for serious concern about the applicability of this method for detecting crustal stress directions. These observations include: (1) a concentric pattern of main EMR directions around a common centre, which correlate with the NATO VLF transmitter DHO38 (Section 5.2); (2) temporary variations in the main EMR directions observed twice around the turn of the year, coinciding with an intermission of the broadcasting of DHO38 (Section 5.3); (3) daily variations, coinciding with the daily intermission of DHO38; (4) decrease of the EMR intensities with distance to DHO38 (Section 5.4.2); (5) daily fluctuations of EMR intensities, which can be correlated to the altitude of the sun, with respect to the distance to DHO38 (Section 5.4.2), and (6) the typical maximum number of single pulses that coincides with the transmitting frequency of DHO38.

Furthermore, the beam antenna is not most sensitive in its longitudinal direction, but in its "broadside" direction. Thus no influence to the horizontal measurements is expected, but certainly to vertical measurements, as described in e.g. Lichtenberger (2006a, b). As in vertical measurements the tip of the antenna is rotated perpendicular to the tunnel axis, the intensities distribution attributed to points on the tunnel wall and used to measure stress concentrations on the same. With the knowledge that the antenna is most sensitive along its "broadside", I expect that the measuring direction is along the tunnel axis. However, some measurements of Lichtenberger (2005; 2006a, b), which show asymmetric patterns, are in contradiction to this, but might be explained by the curvature of the tunnel axis.

For linear measurements where the antenna is vertical, it is essential to keep this measuring configuration, even though the antenna is not most sensitive orientated towards the ground. During horizontal use of the antenna the orientation to the VLF transmitters will become dominant and the intensities will depend mostly on the orientation of the antenna to DHO38. Nevertheless, several investigations of linear measurements and profiles have shown that it is possible to reliably detect faults with the Cerescope (see Chapter 4). Therefore, I expect that the detection of faults with the Cerescope belongs to the well established VLF method (Fig. 5.13), and the vertical orientation of the antenna is essential to detect the secondary electromagnetic field of the VLF transmitters generated at zones of increased electric conductivity as faults. The operating mode of the VLF method uses the electromagnetic far-field of VLF transmitters (primary field), where the magnetic component propagates horizontally and induces an electrical current in structures of higher electrical conductivity (e.g. faults). These electrical currents are accompanied by their own electromagnetic field (secondary field), where the magnetic component is perpendicular (vertical) to the primary magnetic field (horizontal) and therefore the antenna is most sensitive when orientated to the magnetic component of the secondary electrical field. The secondary magnetic field is phase-shifted. As the generation of the secondary electromagnetic field is not only restricted to one point, but to several locations with different electric conductivities, this results in multiple phase-shifted electromagnetic fields with a vertically orientated magnetic component. Each of these electromagnetic fields still contains the properties (frequency) of the primary field and therefore the number of measured single pulses is multiplied as well as the defining energy.

Fig. 5.13: Principle mechanism of the VLF method. The secondary electromagnetic field, generated along structures of higher electrical conductivity (e.g. faults) is the result for increased EMR intensities above faults.
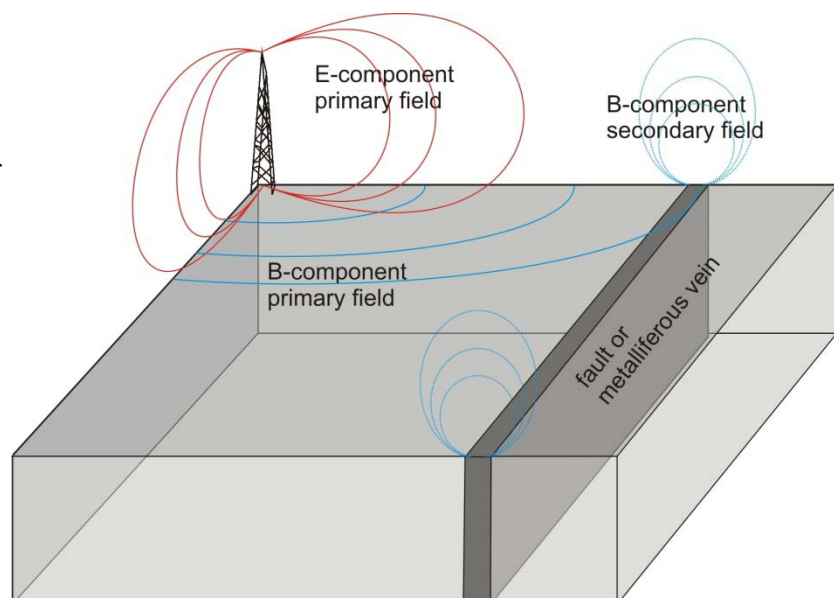
As the observations outlined in this chapter demonstrate, there is a strong influence of VLF transmitters on the EMR method. Its applicability, limitations, and the impact on further field studies needs to be discussed. However, since the concept of the method is still convincing and the laboratory investigations undoubtedly prove the existence of natural EMR and their relationship to micro-cracking, it is necessary to make further efforts to make the method applicable under field conditions (see Chapter 6).

6. Summary, discussion, conclusions, and outlook

6.1 Summary

This study focuses on the possibility to infer in-situ stress directions and the existence of faults from natural Electro-Magnetic Radiation measured in the field (EMR method) with a Cerescope. The basic concept of this method is that natural EMR mainly results from the movement of charge carriers related to the growth of micro-cracks and hence should show a directional dependence on the local stress field. This comparatively new kind of application is so far only accepted by a small circle of geoscientist, despite a number of promising first results. Previous studies applied the method only locally, with the exception of an investigation by Reuther and Moser (2009) and over short periods of time. The results could not explain the relationship between probable EMR-emitting structures and measured signals in a satisfying way. So far, a comprehensive study to evaluate the applicability of the method over a large area and a long time period has been missing. Moreover, stress orientations inferred from EMR data had never been critically compared with data obtained by conventional in-situ stress measurements in a systematic way.

The main aim of this study was, thus, to evaluate the applicability of the EMR method, and the different measuring procedures in the field. For this purpose, it was necessary to investigate the relationship between potential EMR-emitting brittle structures and the measured EMR itself. For this, a comprehensive field study was carried out in the Västervik area in southeast Sweden, in which the orientation of brittle structures at all scales were compared with the direction of σ_H inferred from EMR data to identify the structures most likely responsible for EMR. The Västervik area was chosen because of the large database of high quality in-situ stress measurements carried out in the Äspö Hard Rock Laboratory and the existence of numerous diploma map theses that collected an immense dataset of structural geology features. The results of this study are outlined in detail in Chapter 3 and summarised in the following Section 6.1.1.

Another major aim was to test the EMR method as a tool for the identification of geological structures, such as faults, by linear EMR measurements. For this purpose, several fault structures in southeast Sweden, as well as in the Leinetal Graben in central Germany, were investigated (Chapter 4). One exemplary study compared EMR intensities with radon emissions associated with a fault to compare the EMR method with an established method for the fault detection. Moreover, the data of linear measurements taken with the Cerescope were

combined for the first time with GPS data to improve the accuracy of the method and its applicability under difficult field conditions. The results are summarised in Section 6.1.2.

Further investigations were done to examine the spatial resolution of the EMR method (Chapter 5). As part of this study, the main EMR direction that is supposed to correspond to σ_H was determined between the Leinetal Graben area in the south and the Västervik area in the north, to compare the pattern of main EMR directions with the data contained in the World Stress Map. In addition, temporal variations of the EMR properties were first realised and then monitored at weekly intervals. The results of these investigations are summarised in Section 6.1.3.

6.1.1 Implications of a multi-scale analysis of brittle structures in southeast Sweden for the generation of Electro-Magnetic Radiation (EMR)

Directions of σ_H were determined with the EMR method in an area of about 1600 km^2. The results of the EMR measurements are, with an average orientation of 135°, in good agreement with σ_H orientations obtained by conventional methods. The only outliers measured lay within fault zones.

The map-scale lineaments (crustal-scale faults and fault zones) strike predominantly E-W to SE-NW, forming three distinct sets. In addition, two minor sets with a N-S and a NE-SW orientation occur. None of these main sets coincides with the orientation of the EMR data. Thus, map-scale faults do probably not contribute significantly to the measured EMR.

The orientation of joints in the area is characterised by an inhomogeneous pattern with two main sets that strike generally 60° (NE-SW) and 145° (NW-SE). The strike of the minor set (NW-SE) differs only by about 10° from the main EMR/σ_H directions. However, because of this deviation, together with the large scatter of their strikes, it is unlikely that actual fracture propagation along these joints is responsible for the EMR emissions under the current stress field.

Inspite of different rock composition and locations, the orientation of micro-cracks is the same for all samples, with a main strike of SE-NW. In total, the micro-cracks of all samples have exactly the same orientation as σ_H obtained with the EMR method and conventional in-situ measurements. In addition, the trace lengths of micro-cracks are largest in NE-SW direction.

Likewise, the strike directions of grain-boundaries as preferred planes for micro-cracking are consistent in all samples within the range of a few degrees. Two strongly pronounced

maxima occur with a major set striking NE-SW, with a minor set striking exactly perpendicular to it in SE-NW direction. The major set coincides also with the direction of maximum grain-boundary length. The direction of the minor SE-NW striking set correlates well with the inferred σ_H orientation. So, for the investigated area, it can be concluded that it is most likely to attribute stress-related EMR to the combination of newly-formed intragranular cracks and crack propagation along pre-existing grain- and phase boundaries at a suitable orientation to the actual stress field.

This first comprehensive study that compares the orientation of brittle structures over a large range of scales with horizontal EMR measurements supports the applicability of the method. Furthermore, the accurate concordance of the orientation of structures on the sub-millimetre scale with the EMR main directions support the results of laboratory studies that proved small-scale structures to be responsible for the emission of EMR in centimetre-size samples.

6.1.2 Linear measurements

For all three case studies, the Cerescope was coupled with a GPS during recording, so that the measured EMR signals could be accurately referenced with their locations. This coupling makes it possible to display the measured EMR intensities in a reasonable and intelligible way that facilitates geological interpretation.

The first case study (Section 4.1) compares radon emission above a fault with known location (from remote sensing and field observations) in southeast Sweden with the results of a linear EMR profile. Both the EMR method, as well as the radon measurements, came to comparable results, which supports the applicability of linear EMR measurements for fault detection. In comparison with the detection of radon emission, the EMR method is carried out with less effort and yields higher resolution results quicker.

In Section 4.2, four linear EMR profiles that crossed a major fault zone in the vicinity and within the Götemar Pluton, southeast Sweden are outlined. The results demonstrate the ability of linear EMR measurements to detect faults and, under favourable circumstances, the attitude of the faults. However, disturbances by artificial EMR sources (e.g. power lines) can occur, so that critical examination of the results during fieldwork, as well during the later interpretation. is necessary. The geologically significant parts of the linear profiles in the Götemar area accurately show the location and, also in some cases, the attitude of the crossed faults.

The result of a linear EMR measurement in the Leinetal Graben, Germany, is presented in Section 4.3. The EMR profile shows accurately the location of faults as indicated by

geological maps, which also confirms linear EMR measurements as a useful tool to detect faults, in particular in areas where it is difficult to detect faults topography or stratigraphic offset.

In general, during linear EMR measurements, increased intensities indicate the location of faults or fault zones. Variations of the intensities within broader fault zones may yield implications about their internal structure. Accordingly, the dip of faults can be determined, if the linear EMR measurements are performed along a profile at high angle to the strike of the fault.

6.1.3 Spatial and temporal variations of main EMR directions measured with the Cerescope – natural vs. artificial sources?

Chapter 5 includes a compilation of horizontal Cerescope measurements that cover the area between central Germany and southern Sweden. Furthermore, the results of long-term monitoring of the main horizontal EMR direction taken at weekly intervals are described.

Although the horizontal measurements in northern Germany and southern Sweden are in large parts consistent with the WSM (Heidbach et al., 2008), the overall pattern of the main EMR direction determined with the Cerescope forms a concentric pattern with a common focus near Emden, where the VLF transmitter DHO38 is situated. I suggest that determinations of σ_H using the Cerescope are influenced by this artificial source. The intensity of the defining energy is a function of the distance to DHO38, while the number of recorded single pulses stays relatively constant. Furthermore, the typical maximum value of the single pulses corresponds to the transmitting frequency of DHO38.

The weekly horizontal measurements have shown that during the turn of the year from 2008 to 2009, after a constant increase in intensities, the intensities decreased rapidly. This coincides with a temporary intermission in the broadcasting of DHO38. After this, the main EMR direction switched from the commonly observed NW-SE direction to NE-SW direction characterised by comparatively low intensities, before re-establishing the NW-SE main EMR direction. The main EMR direction observed during the turn of the year corresponds obviously to HWU, a VLF transmitter near Le Blance (France).

Other observed fluctuations of EMR can also be explained with the time of day the measurement was taken, regarding the known dependence of VLF transmissions on the altitude of the sun. While during daytime the signal strength (defining energy) is constant, during sunrise and sunset, lows in the intensities can be observed, whereas during the night the intensities are much higher. In addition, there is a daily broadcasting intermission of

DHO38 for one hour, during which a deviating EMR main direction is measured. However, it is unclear if this deviating main direction is of natural origin.

Therefore, it can be concluded that, at the present stage of development, the identification of σ_H by the measurement of EMR with the Cerescope is not yet applicable, because the influence of artificial signals from VFL transmitters cannot be ruled out. Presently, the filters of the Cerescope are not able to remove such signals. This applies to the bandpass filter, as well as to the electronic filter that should reject signals of artificial origin, by periodicity and shape.

Furthermore, the Cerescope antenna has not the directional properties as envisaged, which makes vertical measurements invalid and complicates horizontal measurements. It also implies that the measuring setup during linear measurements is correct, by classifying the EMR method at the actual stage as VLF method. These results show that the method has to be revised and previous studies have to be reviewed.

6.2 Discussion

Since I identified that artificial VLF signals influence EMR measurements even at distances of several thousand kilometres from the VLF transmitters, the results of previous studies need to be re-evaluated. As the amount of studies using the Cerescope is still small and limited to two PhD theses and five research papers, the results of these studies will be discussed in the following separately for the individual studies (Sections 6.2.1 to 6.2.5). Additionally, possible implications of the findings of this study for other studies that consider the generation of EMR in context with the EMR method as a tool for earthquake prediction, will be discussed.

6.2.1 Discussion of Reuter et al. (2002)

The first research paper that described the EMR method used under field conditions was published by Reuther et al. (2002). The work was carried out in southeast Sicily, Italy, on the Hyblea-Malta Platform in 2001. The conducted EMR measurements were compared with previous results of doorstopper- and borehole-breakout measurements (Heidbach et al., 2008; Fig. 6.1). The neotectonic stress regime is controlled by the northwestward motion of Africa since late Miocene (Dewey et al., 1989) and is therefore dominated by NW to NNW main horizontal stress directions (Adam et al., 2000) that are characteristic for most parts of Sicily. In contrast, in the north of the Hyblean Platform, the main horizontal stress direction changes to NE as a result of gravitational forces (Adam et al., 2000; Reuther et al., 2002). The results

of the EMR measurements by Reuther et al. (2002) show that the main EMR directions and are in good agreement with stress directions inferred from borehole-breakout measurements and doorstopper measurements. This accounts for both observed main radiation directions and therefore supports the applicability of the EMR method.

However, these two directions may also be explained by signals from VLF transmitters, where DHO38 (distance about 1900 km, bearing 345°) could explain the ENE-direction in the northern part of the Hyblean Platform, and the NNW-direction could be explained by DSDN 20-F1 (distance 2170 km, bearing 057°) near Krasnodar (Fig. 6.1; Table 5.2). Both observed main EMR directions are roughly perpendicular to the two transmitters, which is in accordance with the observations described in Chapter 5. However, it is unlikely that one of the transmitters was turned off exactly during the EMR measurements in the southernmost part of Sicily, while the second main EMR direction was measured. It cannot be completely excluded that the two observed directions are of artificial origin.
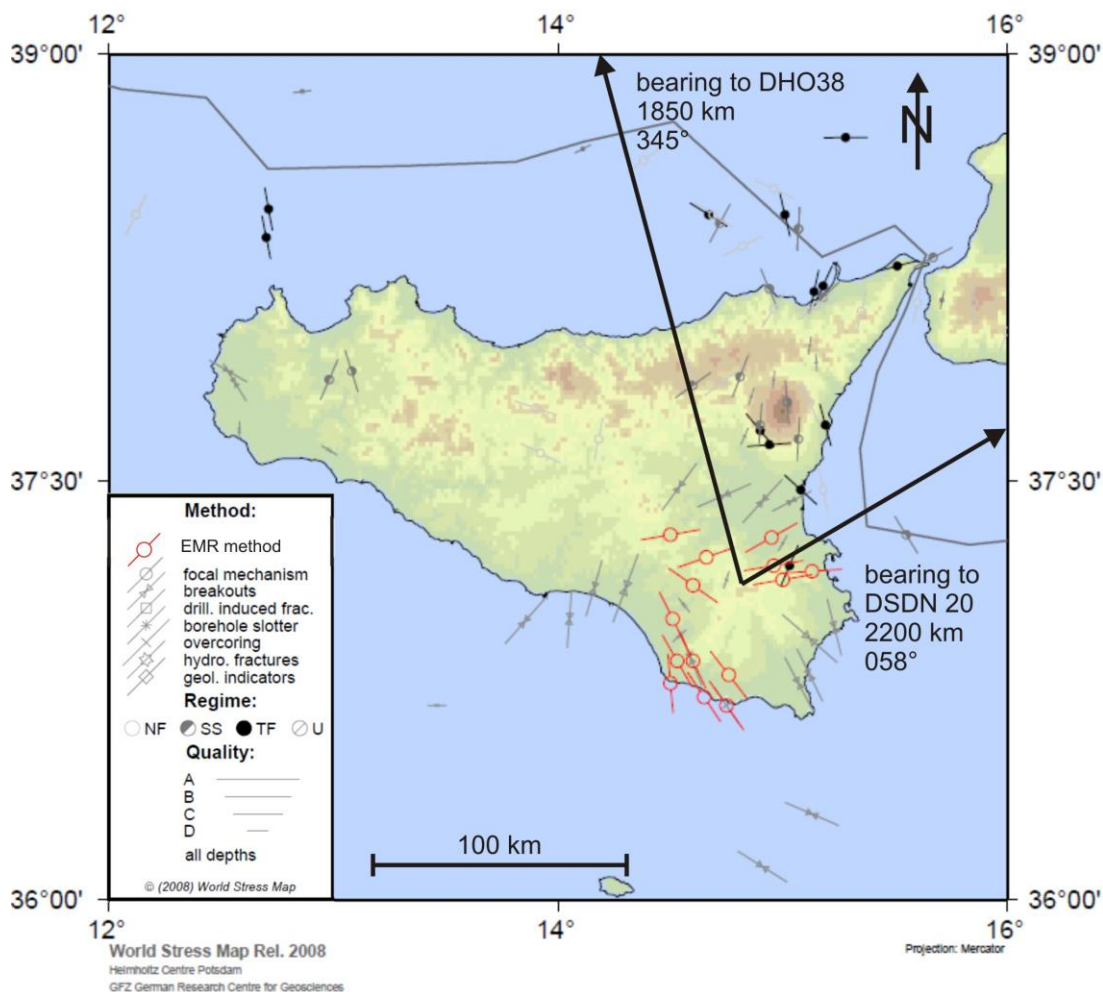
Fig. 6.1: Section of the WMS (Heidbach et al. 2008) of Sicily, Italy, including main EMR directions measured by Reuther et al. (2002). Black arrows indicate bearings to VLF transmitters.

6.2.2 Discussion of Lauterbach (2005)

Lauterbach (2005) mapped landslides and carried out horizontal measurements mainly in southern Germany. In addition, he carried out some laboratory experiments and recorded the diurnal cycle of the EMR with the Cerescope. The results show that the detection and mapping of landslides is a well-working application of the EMR method. In contrast, the horizontal measurements are mostly inconsistent with the stress data of the WSM (Fig. 6.2). The WSM shows a clear NW-SE trend of σ_H in the study area, with only one exception in the south. However, this outlier is classified in the WSM with a high error (accuracy within $\pm 25°$ to $40°$) and therefore questionable.
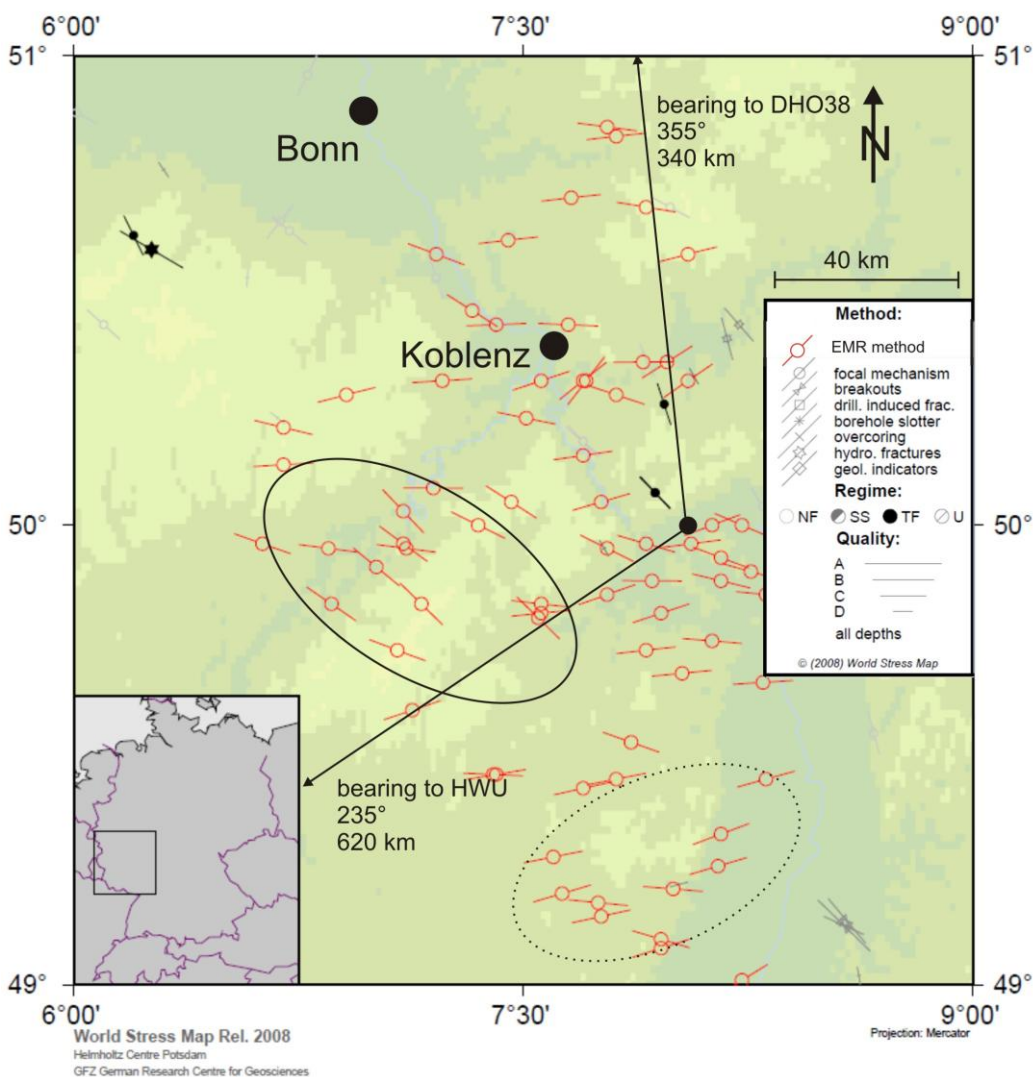
Fig. 6.2: Section of the WMS (Heidbach et al. 2008) of the area around Koblenz, western Germany, including main EMR directions measured by Lauterbach (2005). Black arrows indicate bearings to VLF transmitters. The data enclosed by a solid black ellipse are in accordance with the directions of σ_H in the WSM, but might be also explained by signals from the VLF transmitter HWU. The data in the dotted ellipse are consistent with a stress measurement classified as questionable in the WSM.

The majority of Lauterbach's (2005) main EMR directions scatter around an E-W strike and therefore exhibit considerable deviation from σ_H directions of the WSM. Part of the variation within the data can certainly be attributed to the data acquisition in the time-triggered mode which causes a decrease in accuracy. Most of the measurements were conducted at a longitude between 7° and 8° and are therefore exactly south of the VLF transmitter DHO38. The distance of these measurements to DHO38 ranges from 320 km in the northern part to 450 km in the southern part of the study area.

The diurnal cycle of EMR (Fig. 6.3) was recorded by Lauterbach (2005) from 2002-04-28 to 2002-05-03. On 2002-04-29 and 2202-05-03 a rapid increase and decrease of the intensities were identified as artificial noise (shaded in grey), while the rest of the data were explained as the diurnal cycle of the Earth's magnetic field. The maxima between 5 and 9 a.m. and between 5 and 11 p.m. were interpreted to be due to interaction between tidal forces and the effect of the Sun's radiation on the ionosphere.
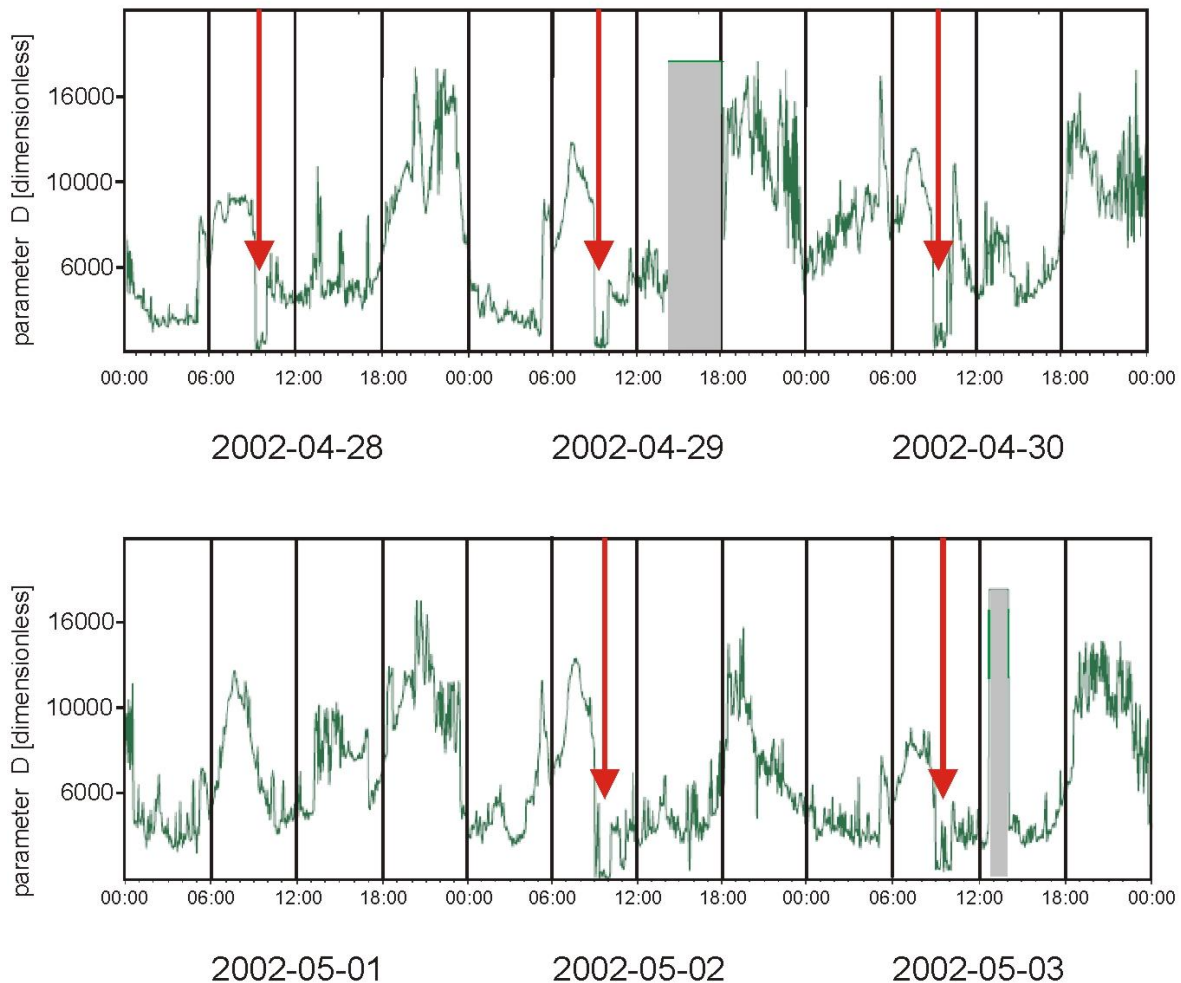
Fig. 6.3: Diurnal cycle of EMR. Areas shaded in grey are artificial disturbances. The red arrows mark the time between 9:00 and 10:00 a.m., were DHO38 is turned off, resulting in a sharp bordered decrease in intensities (cf. Fig. 5.8). The diurnal cycles are roughly consistent with the transmission pattern of DHO38 (see Fig. 5.8). Modified after Lauterbach (2005).

The sunrise on the 2002-05-01 was at 6:08 a.m. and at 08:39 p.m. Especially, the first recorded maximum coincides very well with the sunrise, while the second maximum starts about 1.5 h before sunset. Between 9 a.m. and 6 p.m. a plateau with relatively low intensities occured. Furthermore, at all days (except 2002-05-01) a strong and sharply-bordered decrease in intensities were observed (marked with red arrows in Fig. 6.3) that exactly falls at the time of the daily intermission of DHO38 and suggests that the recorded signals were broadcasted by DHO38, the signal of which varies according to a diurnal cycle depended on the altitude of the sun (Fig 5.8).

The detection and mapping of landslides, or the determination of the most active parts within landslides using linear EMR measurements by Lauterbach (2005) is consistent with former engineering geological investigations and remote sensing studies on aerial photographs of the area. Based on the results of this study about the influence of the artificial VLF transmitters on EMR measurements (cf. Chapter 5), it has to be taken into account that the detection of landslides, as well as the detection of faults, might be related to the well-established VLF method. Accordingly, the electric properties of the ground that might be related to higher water saturation in the case of landslides are also able to explain measurement of increased EMR intensities above active or inactive landslides.

In addition, Lauterbach (2005) carried out some borehole measurements using an especially designed antenna to record EMR intensities in a vertical profile. Six different boreholes were analysed with Cerescope measurements up to a depth of 50 m with different device settings. An artificial origin of the signal would result in a continuous decrease of the signal strength with depth. Three of the borehole measurements show this decrease of intensities with depth; other measurements show different patterns. Therefore, no final conclusion of the origin of the measured EMR in the boreholes can be given at this point. Lauterbach (2005) himself proposed that the EMR borehole profiles should be evaluated with respect to the groundwater situation and expected that with increased groundwater flow, the intensities of EMR should increase. He concluded furthermore that the EMR is composed of different effects, such as e.g. piezoelectricity and streaming potentials.

6.2.3 Discussion of Lichtenberger (2005, 2006a, b)

Lichtenberger (2005, 2006a,b) mainly worked on the determination of stress directions and magnitudes with the EMR method in underground facilities such as tunnels, but also at the surface. The main study areas include the Odenwald, western Germany (Fig. 6.4), and central Sweden (Fig. 6.5).

Lichtenberger (2006a) observed different main EMR directions in his study area in Germany. Some of his measurements show two or three maxima within a single horizontal measurement. The most detected direction is about 070±10° (perpendicular to the bearing to DHO38), while the second most observed direction is about 150±10° (perpendicular to the bearing to HWU). To interpret his results of horizontal EMR measurements, Lichtenberger (2006a) used the bisectrix of the two strongest measured EMR directions to calculate σ_H under the precondition that the different directions belong to a system of conjugate micro-cracks. Using this approach, main EMR directions with a north-westerly strike (120-145°) were derived, which is consistent with the WSM data (Fig. 6.4). However, it is difficult to explain why the two directions within one conjugate system are active at different times. Furthermore, the angles within a conjugate set of micro-cracks are under surface conditions, where tensional cracking is preferable, commonly small and lie in a range of 20°. The angles between the main EMR directions observed by Lichtenberger (2006a) are about 40° and therefore unusually high.

These main EMR directions (120° to 145°) cannot be explained with signals from DHO38 (bearing to the transmitter 075°). An influence of HWU in France is more probable, but the main EMR directions differ consistently with an angle of about 10° to 15° from the bearing to HWU. However, if the original data of the horizontal measurements before interpretation is used, the two main EMR directions measured can be attributed to the signals of both HWU and DHO38 (Fig. 6.4). Lichtenberger's (2006a) main EMR directions measured in Sweden are mainly consistent with the WSM (Fig. 6.5); however, stress data for this area is scarce so that an influence of VLF transmitter signals cannot be excluded.

Further observations by Lichtenberger (2006a) include that during surface measurements strong fluctuations in intensities and main EMR directions occurred several times and sometimes no main radiation direction developed. These disturbances occurred at the same time at different measuring locations over the whole frequency range. The duration of these disturbances was 5 min up to 5 hours. He explained these observations as erratic disturbances of atmospheric origin. In addition, Lichtenberger (2006a) observed that, in general, the EMR intensities increase when leaving a tunnel at the entrance. This underlines a possible influence of VLF transmitters on Cerescope measurements and that artificial signals might not penetrate the overburden, so that EMR measured in the tunnels are of natural origin and can be used to determine regional stress directions.
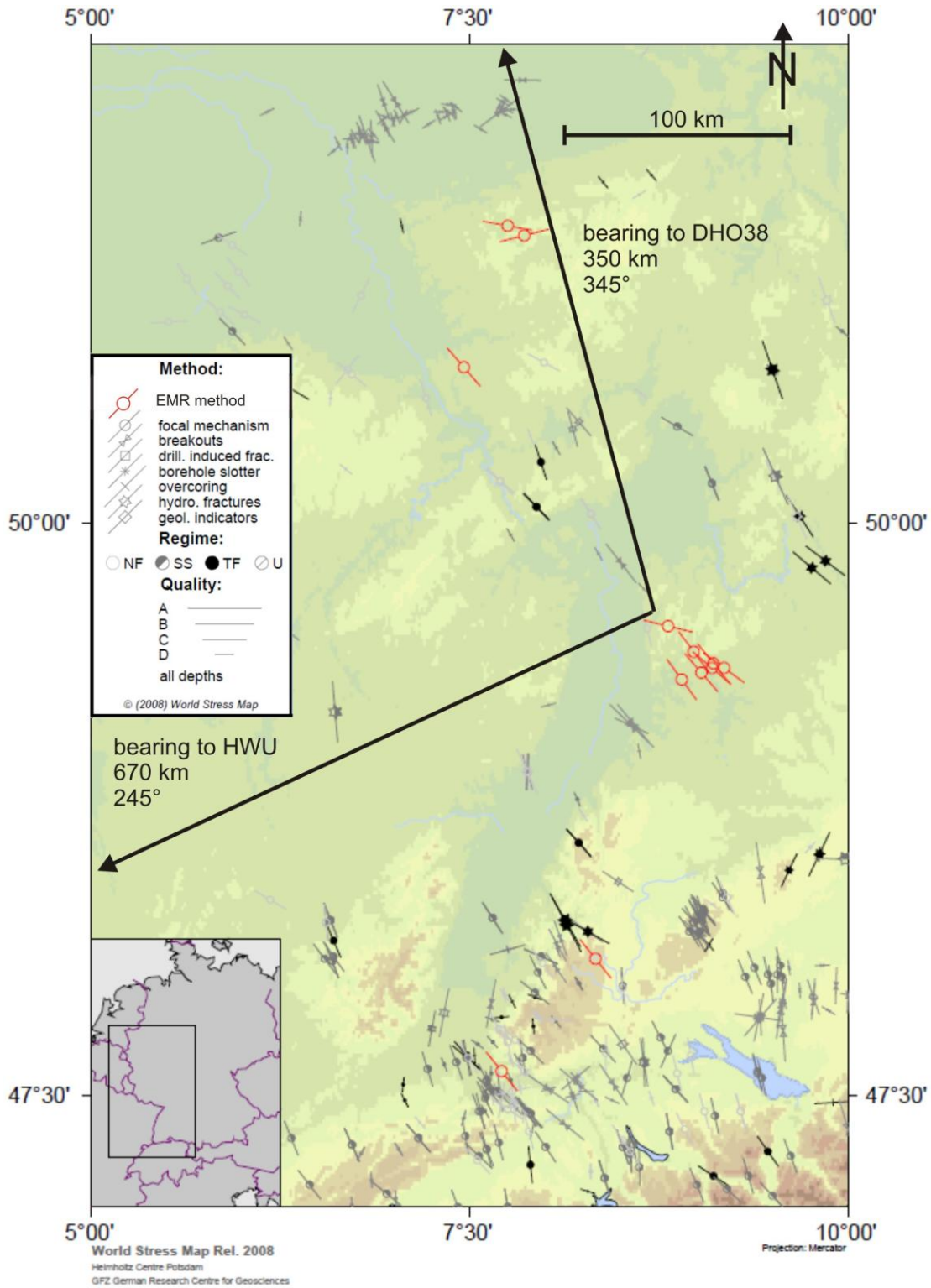
Fig. 6.4: Section of the WMS (Heidbach et al. 2008) of southwest Germany, east France, and north Switzerland, including main EMR directions measured by Lichtenberger (2005, 2006a,b). Black arrows indicate bearings to VLF-transmitters.
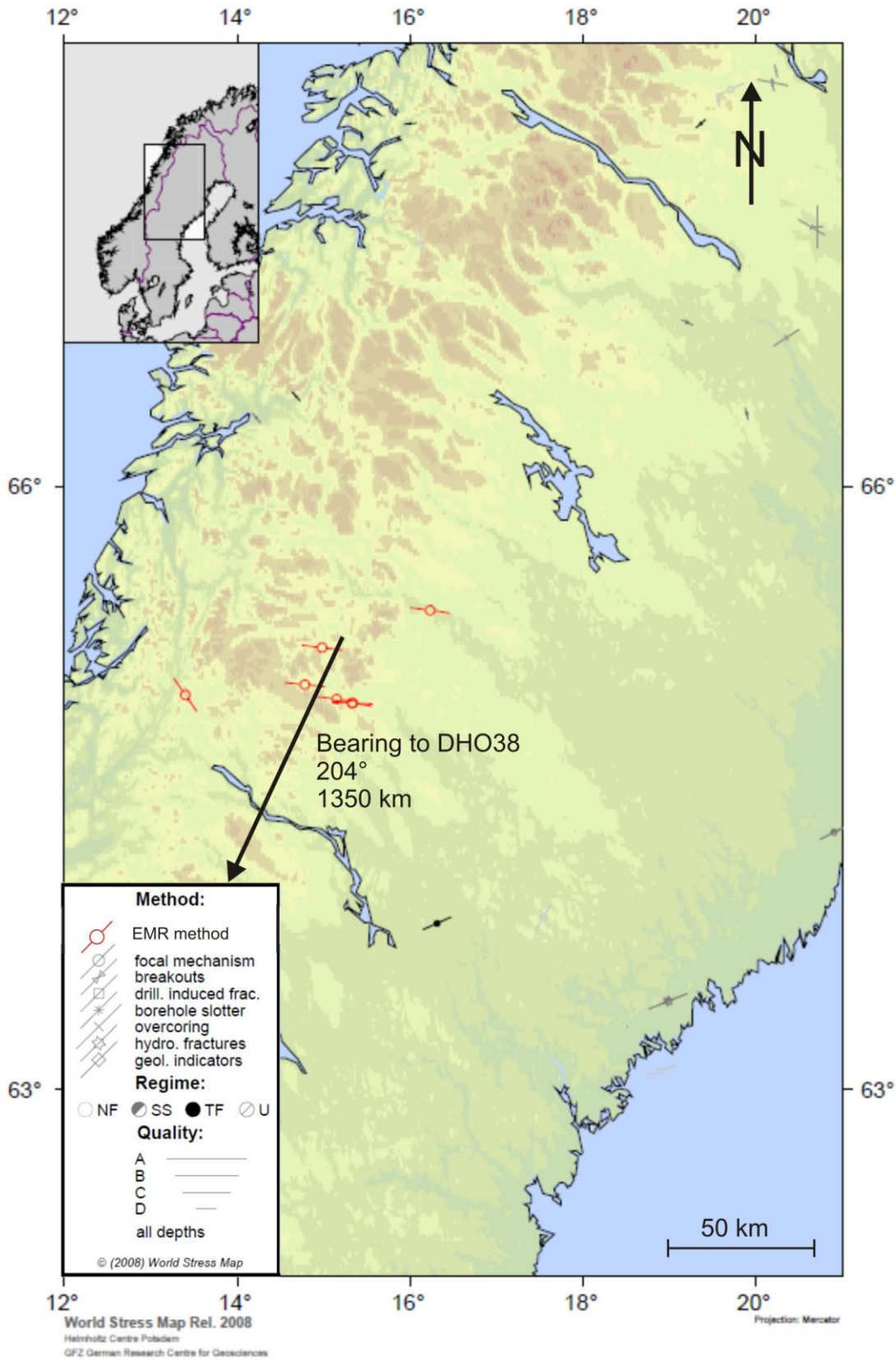
Fig. 6.5: Section of the WMS (Heidbach et al. 2008) of central Sweden and Norway, including main EMR directions measured by Lichtenberger (2006a). Black arrows indicate bearings to VLF transmitters.

Furthermore, Lichtenberger (2005, 2006a, b) carried out subsurface investigations with the aim to determine magnitudes of σ_H with respect to the distribution of EMR intensities along the tunnel using cross-sectional EMR measurements (see Section 2.4.2.3). However, based on the knowledge that the Cerescope antenna is not most sensitive at its tip, the database used for the stress calculations is wrong. Even if the methodological approach might be right, the applicability of these measurements must be re-evaluated with redesigned equipment.

6.2.4 Discussion of Mallik et al. (2008)

The study area of Mallik et al. (2008) was situated in the Kachchh Basin in western India. In this study, active fault systems were successfully investigated with the EMR method. The Kachchh region represents a pericratonic rift basin that became inverted since the Indian plate collided with the Eurasian plate during the Mid Tertiary (Biswas, 1987; Mathew et al., 2006). The inversion is ongoing with reactivation of normal faults, folding and increasing seismicity (Biswas, 1987; Mathew et al., 2006). The general strike of faults and folding in the area is E-W, attributed to a N-S main stress direction, caused by the collision of India and Eurasia. The N-S orientated main horizontal stress direction is known from focal plane solutions from a depth of 9 to 15 km and borehole breakouts (Heidbach et al., 2008). These measurements indicate an orientation of σ_H striking NNE (Fig. 6.6). The results of horizontal EMR measurements by Mallik et al. (2008) gave a main radiation direction of about 060 ± 10°, which with one exception, has a deviation of -20°. In average the results differ with an angle with 50° to 60° from the WSM data. This deviation was explained by Malik et al. (2008) by stress rotations between depth (where σ_H was determined with focal plane solutions; Heidbach et al., 2008) and the surface (where EMR measurements were carried out). I suggest that the measured main EMR directions might also be caused by signals from a VLF transmitter, in this case VTX near Vijaya Narayanam, southern India.

A micro-crack analysis of Mallik et al. (2008) comprised 77 micro-cracks (Fig. 6.7). Two NNE and E-W trending sets of micro-cracks were interpreted as a conjugate set, where the acute bisectrix of both sets is consistent with the EMR main direction. However, this bisectrix has a relatively large angle of 60° between the two sets of a conjugate system. Disregarding th fact that the number of micro-cracks of this study was very small and the maximum strike directions are therefore indistinct, two more acute bisectrices could be determined (Fig.6.7 A), where the N-S striking direction could be explained with the expected N-S orientation of σ_H as shown in the WSM.
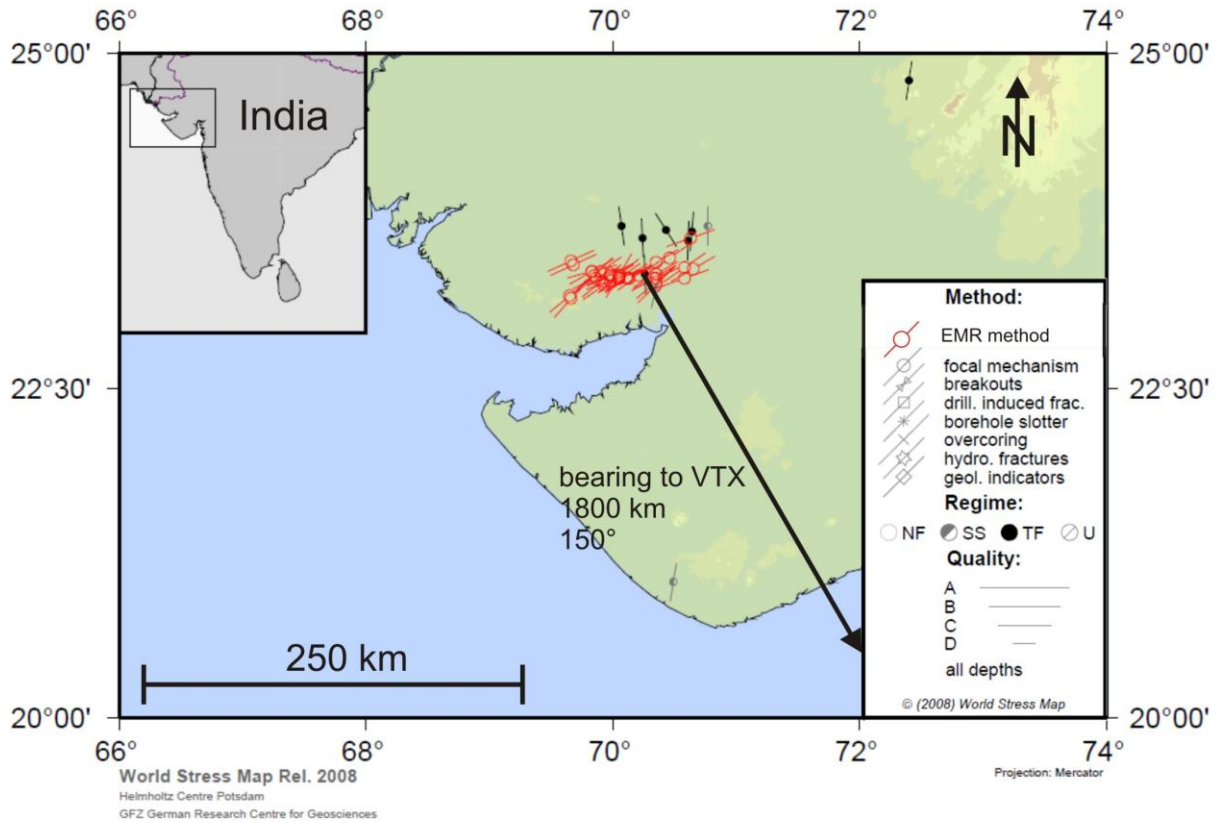
Fig. 6.6: Section of the WMS (Heidbach et al. 2008) of northwest India, including main EMR directions measured by Mallik et al. (2008). Black arrows indicate bearings to VLF transmitters.
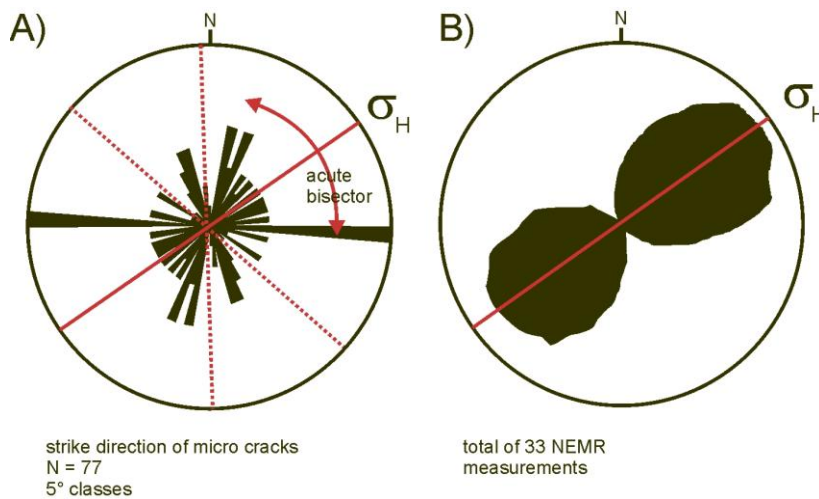
Fig. 6.7: Comparison of the strike of 77 micro-cracks with a total of 33 horizontal EMR measurements. The determined acute bisectrix coincides with the measured EMR main direction. Modified after Mallik et al. (2008).

6.2.5 Discussion of Reuther and Moser (2009)

The stress field in the Patagonian segment of South America is mostly influenced by the subduction of the Nazca plate and the Antarctic plate under the South American plate at the western Pacific coast. In the east, Patagonia is bordered by a passive continental margin.

In 2006, Reuther and Moser (2009) measured EMR main directions at 140 locations. In this area, they distinguished 5 basic stress domains. These domains coincide roughly with existing data published in the WSM (Fig. 6.8). However, the determined stress trajectories also show a roughly circular or semicircular pattern. An evaluation of the significance of their data is difficult since the location and especially the broadcasting time of VLF transmitters in the southern hemisphere cannot be exactly determined. Therefore, an analysis of their study lies beyond the scope of this thesis.
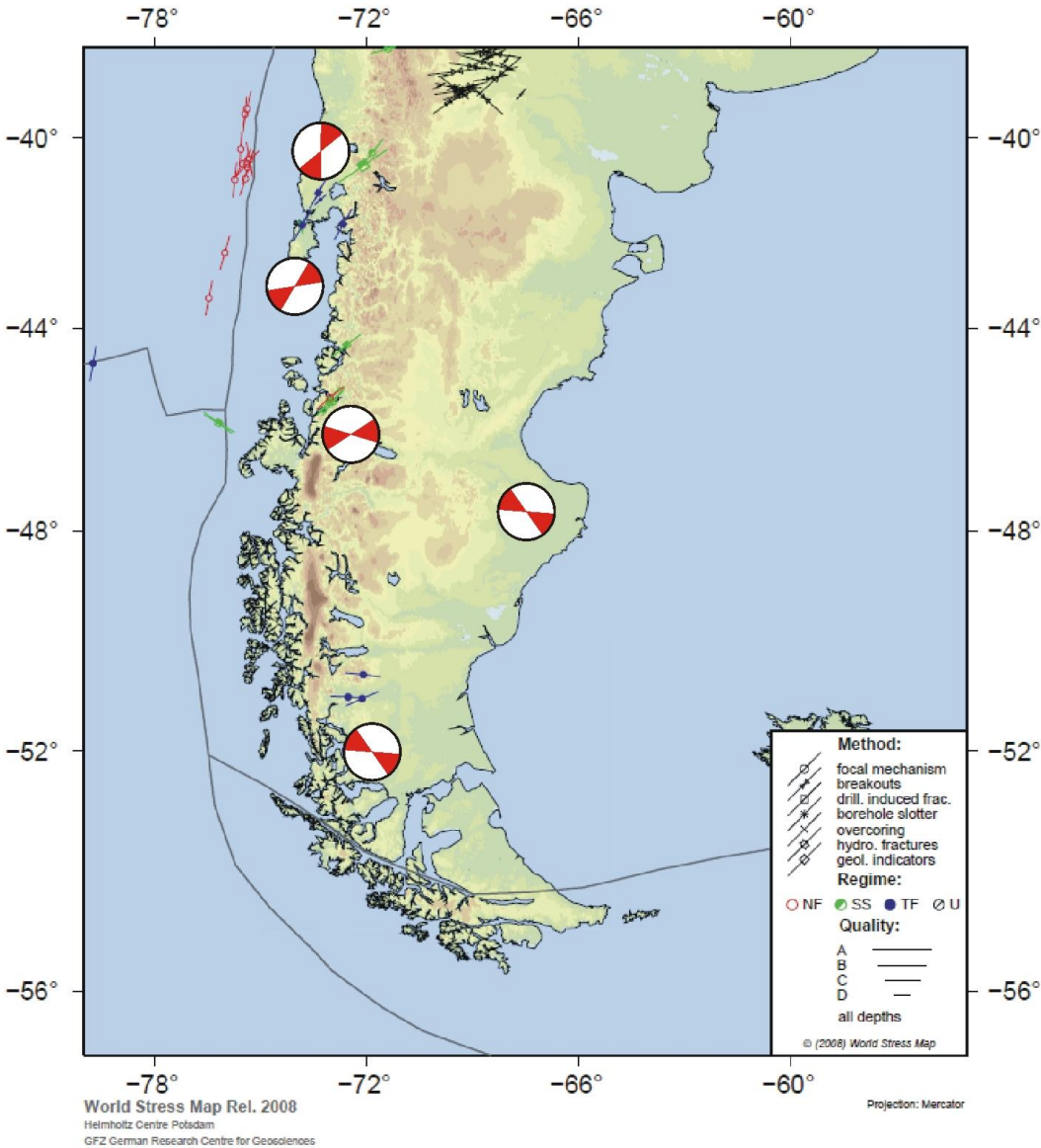
Fig. 6.8: Section of the WMS (Heidbach et al. 2008) of southern South America, including main EMR directions measured by Reuther and Moser (2009).

Furthermore, in addition to horizontal measurements, Reuther and Moser (2009) carried out a cross-sectional measurement at each measurement location to determine the orientation

of σ_1. However, since the directionality of the antenna does not allow this procedure, these determinations are incorrect. At a few locations, also significantly higher EMR intensities occurred with a vertical antenna orientation. According to the results of this thesis (see Chapter 5), these measurements were probably carried out above structures with increased electric conductivities.

6.2.6 Further discussion

In the following, the results of this thesis will be discussed with respect to studies about the application of the EMR method to forecast earthquakes and volcanic eruptions. These studies can be roughly divided into two categories. The first category analyses EMR as a result of natural processes (e.g. Kawate et al., 1998; Kawada et al., 2007; Morgounov and Malzev, 2007), while the second category includes the results of monitoring anomalies in artificial signals modified by natural processes (e.g. Bella et al., 1998; Molchanov et al., 1998; Biagi et al., 2001). However, a comparison and evaluation of the different approaches remain difficult, because different frequency ranges and antenna designs were used, as well as different experimental setups and data evaluation methods.

The problems in using EMR as precursors for earthquakes and volcanic eruptions are widespread and discussed in detail by, e.g., Geller et al. (1997), Tzanis and Gruszow (1998), and Sevgi (2007). In general, the main problems include:

(1) An overall physical model that explains the generation of electric currents, and therefore EMR, is still missing.

(2) Signal shapes used for an identification of the EMR signal as precursor of an earthquake or eruption are different, and might therefore be of different origin.

(3) Sometimes EMR precursors do not occur.

(4) Temporary correlations between EMR anomalies and earthquakes are difficult if sometimes days or weeks lie in between the observation of the precursors and the earthquakes themselves.

(5) A differentiation between natural and artificial signals is difficult and sometimes questionable (Morgounov and Malzev, 2007).

(6) An upscaling of EMR observed in laboratory experiments to field conditions is problematic (Tzanis and Vallianatos, 2001).

To avoid these basic problems, artificial EMR signals, such as those from VLF transmitters, should be regarded and monitored as tool to forecast earthquakes. By using this approach, no new model would be necessary for the generation of electrical currents (1).

Changes in signal strength and pulse numbers can be easily explained with short time changes in the electrical properties of the underground by, e.g., changes in groundwater levels, well known before earthquakes. (2) Different signal shapes might belong to the different sources, in this case transmitters. (3) The occasional lack of EMR precursors can be explained by an unfavourable spatial arrangement of transmitter, earthquake preparation zone, and monitoring station. Problems (4) to (6) are obsolete using this explanation; for problem (5), changes in the known behaviour of the diurnal variations in the signal strength of the artificial sources have to be taken into account.

Taking artificial sources of EMR associated with earthquakes and volcanic eruptions into account does not exclude the existence of naturally-generated electric currents and associated EMR. However, at the current state of the art, artificially-generated EMR as a tool for earthquake prediction is to be preferred, since artificial signals can explain observations much better. In general, this should be analysed in more detail regarding e.g. a favourable setup for EMR monitoring in the vicinity to earthquake-preparation zones or volcanoes.

6.3 Conclusions and outlook

According to the aims presented in Section 1.1, this study has succeeded in the following points:

(1) A systematic procedure was developed for the interpretation of recorded Cerescope data (Section 2.4.2.2).

(2) The graphic evaluation and spatial resolution of the method was enhanced by combining Cerescope measurements with exact geographical coordinates (Section 2.4.2.4). This allows a more accurate detection and mapping of faults (e.g. Chapter 4).

(3) Micro-cracks within grains and along-grain and phase boundaries have been identified as the structures that potentially emit natural EMR in the field when oriented favourably with respect to the governing stress field (see Chapter 4).

(4) Horizontal EMR measurement have been carried out in southern Sweden (Section 4.4.1) and compared with existing stress data obtained with conventional methods (Section 3.5).

(5) Linear Cerescope measurements were carried out in areas with known locations of faults (Chapter 4). The results demonstrate the practicability of this method to identify and map faults. A comparison with the method of radon emission above faults supports the applicability of linear Cerescope measurements (Section 4.1).

(6) A systematic measurement of main EMR directions using horizontal Cerescope measurements was carried out over a large area of Germany, eastern Denmark, and southern Sweden (Section 5.2) and compared with stress data published in the WSM (Section 5.4.2). The results indicate that stress determination with the EMR method in its present state is not possible because the Cerescope measures artificial signals from VLF transmitters instead of natural EMR (Section 5.5).

(7) Major EMR directions were monitored over a longer period of time to identify temporal variations (Section 5.3). The recorded variations support an influence of artificial signals from VLF transmitters (Section 5.4.2).

To conclude, this thesis demonstrates that the current state of the EMR method does not allow the measurement of main stress directions using horizontal and vertical Cerescope measurements. This is due to an ineffective function of the filter mechanisms of the measurement device. Hence, the EMR method at its present state fails in measuring the geogene signal, but instead records artificial signals from VLF transmitters. At the moment, the Cerescope is only useful for the detection and mapping of faults and fault zones. However, this procedure can be attributed to the well-established VLF method.

To adjust the method for the correct measurement of geogene EMR, the technical equipment needs further development. The required hardware improvements mostly affect the antenna design, as the ferrite core used in the actual antenna of the Cerescope is most sensitive perpendicular to its long axis. Hence, the antenna has an omni-directional receiving pattern and is not most sensitive in direction at its tip. Therefore, it might be useful to experiment with loop antennas. Loop antennas exhibit distinct directional properties and are used preferably in the long wavebands. Furthermore, the efficiency of the bandpass filters has to be increased to filter unwanted frequency ranges. In addition, the electronic filter that filters signals according to periodicity and shape needs reworking.

In addition, the findings of this thesis indicate that the EMR recorded prior to and during earthquakes and volcanic eruptions might be of artificial origin by an interaction of VLF signals and changes in the water table. This knowledge may be useful for research of EMR as earthquake and eruption forecasting tool (see Section 6.2.6).

Observations by Lichtenberger (2005, 2006a, b) and the author (unpublished data) of EMR in tunnels indicate that the artificial VLF signal is dampened underground. Hence, further research has to be carried out first in tunnels at sufficient depths, where no influence of VLF transmitters is to be expected. In order to prove the applicability of the EMR method, EMR

has to be monitored continuously in tunnels over longer time spans to identify signal strength and shape of natural EMR. These measurements should also be complemented by other methods, e.g. acoustic measurements. Following hard- and software improvements and underground measurements, the applicability tests of the EMR method can be resumed at the surface.

7. References

Abdullabekov, K. N., Bezuglaya, L. S., Golovkov, V. P. and Skovorodkin, Y. P., 1972. On the possibility of using magnetic methods to study tectonic processes. Tectonophysics **14**, 257-262.

Adam, J., Reuhter, C. D., Grasso, M. and Torelli, L., 2000. Active fault kinematics and crustal stresses along the Ionian margin of southeastern Sicily. Tectonophysics **326**, 217-239.

Andersson, U. B., 1991. Granitoid episodes and mafic-felsic magma interaction in the Svecofennian of the Fennoscandian shield, with main emphasis in the 1.8 Ga plutonics. Precambrian Research **51**, 127-149.

Andersson, U. B., Högdahl, K., Sjöström, H. and Bergman, S., 2006. Multistage growth and reworking of the Palaeoproterozoic crust in the Bergslagen area, southern Sweden: evidence from U–Pb geochronology. Geological Magazine **143**, 679. doi: 10.1017/S0016756806002494.

Andersson, U. B., Rutanen, H., Johansson, Å., Mansfeld, J. and Rimsa, A., 2007. Characterization of the Paleoproterozoic Mantle beneath the Fennoscandian Shield: Geochemistry and Isotope Geology (Nd, Sr) of ~ 1.8 Ga Mafic Plutonic Rocks from the Transscandinavian Igneous Belt in Southeast Sweden. International Geology Review **49**, 587-625. doi: 10.2747/0020-6814.49.7.587

Arvidsson, R. and Kulhanek, O., 1994. Seismodynamics of Sweden deduced from earthquake focal mechanisms. Geophysical Journal International **116**, 377-392.

Asada, T., Baba, H., Kawazoe, M. and Suguira, M., 2001. An attempt to delineate very low frequency electromagnetic signals associated with earthquakes. Earth Planets Space **53**, 55-62.

Ashton, A. W., 1901. Note on the electrification of Dielectrics by Mechanical Means. Proceedings of the Physical Society of London **17**, 751-754.

Åhäll, K. I., 2001. Åldersbestämning av svårdaterade bergarter i sydöstra Sverige. SKB-R-01-60, Swedish Nuclear Fuel and Waste Management Co, Stockholm, Sweden, pp. 24.

Bahat, D., Rabinovitch, A. and Frid, V., 2001. Fracture characterization of chalk in uniaxial and triaxial tests by rock mechanics, fractographic and electromagnetic radiation methods. Journal of Structural Geology **23**, 1531-1547.

Bahat, D., Rabinovitch, A. and Frid, V., 2005. Tensile fracturing in rocks-tectonofractographic and electromagnetic radiation methods. Springer, 570 pp.

Bahat, D., Frid. V., Rabinovitch, A. and Palchik, V., 2002. Exploration via electromagnetic radiation and fractographic methods of fracture properties induced by compression in glass-ceramic. International Journal of Fracture **116**, 179-194.

Bazhenov, V. A., 1961. Piezoelectric properties of Wood. Consultants Bureau Enterprises, New York, 180 pp.

Bella, F., Biagi, P. F., Caputo, M., Cozzi, E., Della Monica, G., Ermini, A., Plastino, W. and Sgrigna, V., 1998. Field strength variations of LF radio waves prior to earthquakes in central Italy. Physics of the Earth and Planetary Interiors **105**, 279-286.

Beunk, F. F. and Page, L. M., 2001. Structural evolution of the accretional continental margin of the Paleoproterozoic Svecofennian orogen in southern Sweden. Tectonophysics **339**, 67-92.

Biagi, P. F., Piccolo, R., Ermini, A., Martelucci, S., Bellecci, C., Hayakawa, M., Capozzi, V. and Kingsley, S. P., 2001. Possible earthquake precursors revealed by LF radio signals. Natural Hazzards and Earth System Sciences **1**, 99-104.

Bishop, J. R., 1981a. Piezoelectric effects in quartz-rich rocks. Tectonophysics **77**, 297-321.

Bishop, J. R., 1981b. Estimating quartz fabrics from piezoelectric measurements. Mathematical Geology **13**, 261-289.

Biswas, S. K., 1987. Regional tectonic framework, structure and evolution of the western marginal basins of India. Tectonophysics **135**, 307-327.

Bjarnsson, B., Klasson, H., Leijon, B., Strindell, L. and Öhman, T., 1989. Rock stress measurements in boreholes KAS02, KAS03 and KAS05 on Äspö. SKB PR 25-89-17, Svensk Kärnbränslehantering AB.

Blenkinsop, T., 2000. Deformation Microstructures and Mechanisms in Minerals and Rocks. Kluwer Academic, Dordrecht, 164 pp.

Brady, B. T. and Rowell, G. A., 1986. Laboratory investigation of the electrodynamics of rock fracture. Nature **321**, 488-492.

Breiner, S., 1964. Piezomagnetic effect at the Time of Local Earthquakes. Nature **202**, 790-791.

Campbell, J. B., 1996. Introduction to Remote Sensing. The Guilford Press, 626pp.

Carlsson, A. and Olsson, T., 1982. Rock stresses as a consequence of glaciations. Nature **298**, 739-742.

Carmichael, R. S., 1968. Remanent and transitory effects of elastic deformation of magnetite crystals. Philosophical Magazine **17**, 911-927.

Carmichael, R. S., 1977. Calculation of piezomagnetic effect for earthquake prediction. Earth and Planetary Science Letters **36**, 309-316.

Claesson, S. and Lundqvist, T., 1995. Origins and ages of Proterozoic granitoids in the Bothnian Basin, central Sweden; isotopic and geochemical constrains. Lithos **36**, 115-140.

Clint, O. C., 1999. Electrical potential changes and acoustic emissions generated by fracture and fluid flow during experimental triaxial rock deformation. Ph.D. Thesis University of London, 237pp.

Cress, G. O., Brady, B. T. and Rowell, G. A., 1987. Sources of electromagnetic radiation from fracture of rock samples in the laboratory. Geophysical Research Letters **14,** 331-334.

Cruden, A. R., 2008. Emplacement mechanisms and structural influences of a younger granite intrusion into older wall rock-a principal study with application to the Götemar and Uthammar granites. SKB-R-o8-138, Swedish Nuclear Fuel and Waste Managment Co, Stockholm, Sweden, 48pp.

Derr, J. S., 1986. Luminous phenomena and their relationship to rock fracture. Nature **321**, 470-471.

Dewey, J. F., Cande, S. and Pitman, W. C. III., 1989. Tectonic evolution of the India/Eurasia collision zone. Eclogae Geologicae Helvetiae **82**, 717-734.

Dologlou, E., 1993. Thermally stimulated currents in rocks.II. Tectonophysics **224**, 175-180.

Dyer, R., 1988. Using joint interactions to estimate paleostress ratios. Journal of Structural Geology **10**, 685-699.

Egorov, P. V., Ivanov., V. V. and Kolpakova, L. A., 1988. Patterns in the electromagnetic pulsed radiation of alkali halide crystals and rocks. Journal of Mining Science **24**, 58-61.

Eisbacher, G. H., 1996. Einführung in die Tektonik. Ferdinand Enke Verlag, Stuttgart, 374 pp.

Elster, J. and Geitel, J., 1902. Über die Radioaktivität der im Boden enthaltenen Luft. Physikalische Zeitschrift **3**, 574-577.

Engelder, T. and Geiser, P. A., 1980. On the use of regional joint sets as trajectories of paleostress fields during the development of the Appalachian Plateau, New York. Journal of Geophysical Research **85**, 6319-6314.

Enomoto, Y. and Hashimoto, H., 1990. Emission of charged particles from indentation fracture of rock. Nature **346**, 641-643.

Enomoto, Y. and Hashimoto, H., 1992. Transient electrical activity accompanying rock under indetation loading. Tectonophysics **211**, 337-344.

Eyal, Y., Gross, M. R., Engelder, T. and Becker, A., 2001. Joint development during fluctuation of the regional stress field in southern Israel. Journal of Structural Geology **23**, 279-296.

Fatkullin, M. N., Zelenova, T. I. and Legenka, A. D., 1989. On the ionospheric effects of asthenospheric earthquakes. Physics of the Earth and Planetary Interiors **57**, 82-85.

Fieldskaar, W., Lindholm, C., Dehls, J. F. and Fieldskaar, I., 2000. Postglacial uplift, neotectonics and seismicity in Fennoscandia. Quaternary Science Review **19**, 1413-1422.

Fifolt, D. A., Petrenko, V. F. and Schulson, E. M., 1993. Preliminary study of electromagnetic emissions from cracks in ice. Philosophical Magazine B **67**, 289-299.

Freund, F., 2000. Time resolved study of charge generation and propagation in igneous rocks. Journal of Geophysical Research **15**, 11001-11019.

Freund, F. T., 2002. Charge generation and propagation in igneous rocks. Journal of Geodynamics **33**, 543-570.

Freund, F. T., 2003. Rocks that crackle and sparkle and glow: strange pre-earthquake phenomena. Journal of Scientific Exploration **17**, 37-71.

Freund, F. T., Takeuchi, A. and Lau, B. W. S., 2006. Electric currents streaming out of stressed rocks – A step towards understanding pre-earthquake low frequency EM emissions. Physics and Chemistry of the Earth **31**, 389-396.

Freund, F. T., Takeuchi, A., Lau, B. W. S., Post, R., Keefner, J., Mellon, J. and Al-Manaseer, A., 2004. Stress induced changes in the electrical conductivity of igneous rocks and the generation of ground currents. TAO **15**. 437-467.

Frid, V., 1997a. Rockburst hazard forecast by electromagnetic radiation excited by rock fracture. Rock Mechanics Rock Engineering **30**, 229-236.

Frid, V., 1997b. Electromagnetic radiation method for rock and gas outburst forecast. Journal of Applied Geophysics **38**, 97-104

Frid, V., 2000. Electromagnetic radiation method water-infusion control in rockburst-prone strata. Journal of Applied Geophysics **43**, 5-13.

Frid, V., Rabinovitch, A. and Bahat, D., 1999. Electromagnetic radiation associated with induced triaxial fracture in granite. Philosophical Magazine Letters **79**, 79-86.

Frid, V., Rabinovitch, A. and Bahat, D., 2003. Fracture induced electromagnetic radiation. Journal of Physics D: Applied Physics **36**, 1620-1628.

Frid, V., Rabinovitch, A. and Bahat, D. 2006. Crack velocity measurement by induced electromagnetic radiation. Physics Letters **356**, 160-163.

Frid. V., Bahat, D., Goldbaum, J. and Rabinovitch, A., 2000. Experimental and theoretical investigations of electromagnetic radiation induced by rock fracture. Israel Journal of Earth Science **49**, 9-19.

Friese, N., Vollbrecht, A., Tanner, D. C., Fahlbusch, W. and Weidemann, M., 2009. Multistage emplacement of the Götemar Pluton, SE Sweden – a layered laccolith intrusion. In prep.

Gaal, G. and Gorbatschev, R., 1987. An outline of the Precambrian evolution of the Baltic Shield. Precambrian Research **35**, 15-52.

Gavelin, S., 1984. The Västervik area in south-eastern Sweden. Studies in Proterozoic Sedimentation, high-grade metamorphism and granitization. Sveriges Geologiska Undersökning **32**, 1-172.

Geller, R. J., Jackson, D. D., Kagan, Y. Y. and Mulargia, F., 1997. Earthquakes cannot be predicted. Sciences **275**, 1616-1617.

Geological Map of Lower Saxony (GK25) 4424 Dransfeld, 2009. Landesamt für Bergbau, Energie und Geologie.

Gershenzon, N. and Bambakidis, G., 2001. Modeling of seismo-electromagnetic phenomena. Russian Journal of Earth Sciences **3**, 247-275.

Gershenzon, N. and Gokhberg, M., 1993. On the origin of electrotelluric disturbances prior to an earthquake in Kalamata, Greece. Tectonophysics **224**, 169-174.

Gershenzon, N. I., Gokhberg, M. B. and Yunga, S. L., 1993. On the electromagnetic field of an earthquake focus. Physics of the Earth and Planetary Interiors **77**, 13-19.

Gershenzon, N., Zilpimiani, D. and Maguladze, P., 1985. Electromagnetic radiation from crack tip during ionic crystal fracture. Doklady Akademii Nauk **248**, 1077-1081.

Gershenzon, N. I., Zilpimiani, D., Mandzhgaladze, P. V., Pokhotelov, O. A. And Chelidze, Z. T., 1986. Electromagnetic emission of the crack top during rupture of ionic crystals. Dokladi Akademii Nauk SSSR **288**, 75-78.

Ghomshei, M. M. and Templeton, T. L., 1989. Piezoelectric and a-axes fabric along a quartz vein. Physics of the Earth and Planetary Interior **55**, 374-386.

Gokhberg, M. B., Kolosnitsyn, N. I. and Nikolaev, A. I., 2007. Tidal deformations and the electrokinetic effect in a two-layer fluid-saturated porous medium. Izvestiya, Physics of the Solid Earth **43**, 702-706.

Gokhberg, M. B., Nekrasov, A. K. and Shalimov, S. L., 1994. A new approach to the problem of the lithosphere-ionosphere coupling before the earthquakes. In: Hayakawa, M., Fujinawa, Y. (Eds.), Electromagnetic Phenomena Related to Earthquake Prediction. TERRAPUB, Tokyo, 259-263.

Gokhberg, M. B., Morgunov, V. A., Yoshino, T. and Tomizawa, I., 1982. Experimental measurement of electromagnetic emissions possibly related to earthquakes in Japan. Journal of Geophysical Research **87**, 7824-7828.

Gold, R. M., Markov, G. and Mogila, P. G., 1975. Pulsed electromagnetic radiation of minerals and rocks subjected to mechanical loading. Physics of the Solid Earth **7**, 109-111.

Goldbaum, J., Frid, V., Bahat, D. and Rabinovitch, A., 2003. An analysis of complex electromagnetic radiation signals induced by fracture. Measurement Science and Technology **14**, 1839-1844.

Gorbatschev, R. and Bogdanova, S., 1993. Frontiers in the Baltic Shield. Precambian Research **35**, 3-22.

Gregersen, S., Korhonen, H. and Eystein, S. H., 1991. Fennoscandian dynamics: Present-day earthquake activity. Tectonophysics **189**, 333-344.

Hadjicontis, V., Mavromatou, C. and Ninos, D., 2004. Stress induced polarization currents and electromagnetic emission from rocks and ionic crystals, accompanying their deformation. Natural Hazards and Earth System Sciences **4**, 633-639.

Hancock, P. L., 1985. Brittle microtectonics: principles and basics. Journal of Structural Geology **7**, 437-457.

Hancock, P. L. and Engelder, T., 1989. Neotectonic joints. Geological Society of America Bulletin **101**, 1197-1208.

Heidbach, O., Tingay, M., Barth, A., Reinecker, J., Kurfeß, D. and Müller, B., 2008. The World Stress Map database release 2008 doi:10.1594/GFZ.WSM.Rel2008.

Hobbs, W. H., 1912. Earth Features and Their Meaning: An Introduction to Geology for the Student and General Reader. Macmillan, New York, 347 pp.

Högdahl, K., Andersson, U. B. and Eklund, O., 2004. The Transscandinavian Igneous Belt (TIB) in Sweden: a review of its character and evolution. Geological Survey of Finland, Special Paper **37**, 125 pp.

Horn, R. G. and Smith, D. T., 1992. Contact electrification and adhesion between dissimilar materials. Science **256**, 362-365.

Hudson, J. A. and Harrison, J. P., 2000. Engineering Rock Mechanics. An Introduction to the Principles. Elsevier Science, Oxford, 456 pp.

Huang, L. and Deng, H., 1979. Earthquake light. Earthquake Press, Bejing, in Chinese.

Jacobsen, T., 2001. WUN – Worldwide Utility News – ELF and VLF Guide Version 1.0. ALFLAB, 29 pp.

Jagasivamani, V. and Iyer, K. J. L., 1988. Electromagnetic emission during fracture of heat-treated spring steel. Material Letters **6**, 418-422.

Janson, T. and Stigsson, M., 2002. Test with three different stress measurement methods in two orthogonal bore holes. SKB R-02-26, Svensk Kärnbränslehantering AB.

Kamogawa, M. and Ohtsuki, Y., 1999. Plasmon model for origin of earthquake related electromagnetic wave noises. Proceedings of the Japan Academy, Ser. B: Physical and Biological Sciences **75**, 186-189.

Karabacak, D. M., Ekinci, K. L., Gan, C. H., Gbur, G. J., Ünlü, M. S., Ippolito, S. B., Goldberg, B. B. and Carney, P. S., 2007. Diffraction of evanescent waves and nanomechanical displacement detection. Optics Letters **32**, 1881-1883.

Kawada, Y., Nagahama, H. And Nakamura, N., 2007. Time-scale invariances in preseismic electromagnetic radiation, magnetization and damage evolution of rocks. Natural Hazards and Earth System Sciences **7**, 599-606.

Kemski, J., 1993. Radonmessungen in der Bodenluft zur Lokalisierung von Störungen im Neuwieder Becken (Mittelrhein). Bonner Geowissenschaftliche Schriften **8**, 144p.

Kepic, A., Russell, R. D., Maxwell, M. and Butler, K. E., 2001. Underground tests of the radio pulsed effect seismoelectric method at the Lynx Mine, Canada. Exploration Geophysics **32**, 107-112.

Khatiashvili, N. G., 1984. The electromagnetic effect accompanying the fracture of alkaline halide crystals and rocks. Izvestija Earth Physics **20**, 656-661.

Khatiashvili, N. G. and Perel´man, M. E., 1989. On the mechanism of seismo-electromagnetic phenomena and their possible role in the electromagnetic radiation during periods of earthquakes, foreshocks and aftershocks. Physics of the Earth and Planetary Interiors **57**, 169-177.

King, C.-Y., 1983. Electromagnetic emissions before earthquakes. Nature **303**, 377.

Kirsch, G., 1898. Die Theorie der Elastizität und die Bedürfnisse der Festigkeitslehre. Zeitschrift des Vereins Deutscher Ingenieure **42**, 797-807.

Klasson, H., Persson, M. and Ljunggren, C., 2001. Overcoring Rock Stress Measurements at the the Äspö HRL – Prototype Repository: Borehole KA3579G (Revised data) and K-tunnel: Borehole KK0045G01. SKB IPR-02-03, Svensk Kärnbränslehantering AB.

Knuffel, W. and Pizzi, A., 1986. The piezoelectric effect in structural timber. Holzforschung – International Journal of the Biology, Chemistry, Physics and Technology of Wood **40**, 157-162.

Kawate, R., Molchanov, O. A. and Hayakawa, M., 1998. Ultra-low-frequency magnetic fields during the Guam earthquake of 8 August 1993 and their interpretation. Physics of the Earth and Planetary Interiors **105**, 229-238.

Koktavy, P., Pavelka, J. and Sikula, J., 2004. Characterization of acoustic and electromagnetic emission sources. Measurement Science and Technology **15**, 973-977.

Kormiltsev, V. V., Ratushnyak, A. N. and Shapiro, V. A., 1998. Three-dimensional modelling of electric and magnetic fields induced by the fluid flow movement in porous media. Physics of the Earth and Planetary Interiors **105**, 109-118.

Koshevaya, S., Grimalsky, V., Kotsarenko, A., Pérez-Enríquez, R., Siquieros-A. J. and Gutierrez, D. E., 2007. Transparency change of the ionosphere for cosmic radio waves caused by acoustic pulse of ultra low frequency range. Tectonophysics **431**, 241-247.

Krakovetzky, Y. K., Nadubovich, Y. A., Popov, L. N. and Shumilova, A. B., 1984a. Study of spatial distribution of polar aurora. Doklady Akademii Nauk SSSR **279**, 580-582 (in Russian).

Krakovetzky, Y. K., Degtyarov, V. I., Platonov, O. I., Popov, L. N. and Chagarov, L. M., 1984b. Spatial distribution of aurorae near Norilsk. Geomagnetism and Aeronomy **24**, 362-365.

Kranz, R. L., 1983. Microcracks in rocks: a review. Tectonophysics **100**, 449-480.

Kresten, P. and Chyssler, J., 1976. The Götemar massif in south-eastern Sweden: a reconnaissance survey. Geologiska Föreningens I Stockholm Förhandlingar **98**, 155-161.

Lahtinen, R., Korja, A. and Nironen, M., 2005. Paleoproterozoic tectonic evolution. In: Lehtinen, M., Nurmi, P. A., Rämö, O. T. (Eds.), Precambrian Geology of Finland - Key to the Evolution of the Fennoscandian Shield. Elsevier, Amsterdam, pp. 481–532.

Larkina, V. I., Migulin, V. V., Molchanov, O. A., Kharkov, I. P., Inchin, A. S. and Schetcova, V. B., 1989. Some statistical results on very low frequency radiowave emissions in the upper ionosphere over earthquake zones. Physics of the Earth and Planetary Interiors **57**, 100-109.

Lauterbach, M., 2005. Beurteilung der Eignung der NPEMFE-Methode (Natural Pulsed Electromagnetic Field of Earth) mit dem "Cereskop" in Rutschungen und in Locker- und Festgesteinen mit Spannungsänderungen im Mittel- und Hochgebirge. Ph.D. Thesis University of Mainz, 243 pp.

Lichtenberger, M., 2005. Regional stress field as determined from electromagnetic radiation in a tunnel. Journal of Structural Geology **27**, 2150-2158.

Lichtenberger, M., 2006a. Bestimmen von Spannungen in der Lithosphäre aus geogener elektromagnetischer Strahlung. Ph.D. Thesis University of Heidelberg, Gaea Heidelbergensis **16**, 140 pp.

Lichtenberger, M., 2006b. Underground measurements of electromagnetic radiation related to stress-induced fractures in the Odenwald Mountains (Germany). Pure and Applied Geophysics **163**, 1661-1677.

Lindh, A. and Bylund, G., 1987. Proterozoic Geology of southern Sweden. Excursion Guide, 64 pp., unpublished.

Liperovsky, V. A., Pokhotelov, O. A., Liperovskaya, E. V., Parrot, M., Meister, C. V. and Alimov, O. A., 2000. Modification of sporadic E-layers caused by seismic activity. Surveys in Geophysics **21**, 449-486.

Lorne, B., Perrier, F. and Avouac, J., 1999. Streaming potential measurements 1. Properties of the electrical double layer from crushed rock samples. Journal of Geophysical Research **104**, 857-877.

Loudet, L., 2009. SID monitoring station A118. http://sidstation.lionelloudet.homedns.org/

Lowell, J. and Rose-Innes, A. C., 1980. Contact electrification. Advances in Physics **29**, 947-1023.

Lyakhov, A. N. and Zetser, Y. I., 2008. Observation of Low-Frequency Oscillations of the Ionospheric Electric field over Fractures in the Earth´s Crust. Doklady Earth Sciences **420**, 620-623.

Mallik, J., Mathew, G., Angerer, T. and Greiling, R. O., 2008. Determination of directions of horizontal principal stress and identification of active faults in Kachchh (India) by electromagnetic radiation (EMR). Journal of Geodynamics **45**, 234-245.

Mansfeld, J., 1995. Crustal evolution in the southeastern part of the Fennoscandian shield. Medd. Stockholms Universitet, Institution för Geologie och Geokemi, 289 pp.

Mansfeld, J., 1996. Geological, geochemical and geochronological evidence for a new Palaeoproterozic terrane in southeastern Sweden. Precambrian Research **77**, 91-103.

Markov, G. A. and Ipatov, Y., 1986. Method of electromagnetic radiation for rockburst forecast on apatite mines. Engineering Geology **3**, 54-57.

Mathew, G., Singhvi, A. K. and Karanth, R. V., 2006. Luminescence chronometry and geomorphic evidence of active fold growth along the Kachchh mainland fault (KMF), Kachchh, India, Seismotectonic implications. Tectonophysics **422**, 71-87.

Meloni, A., Mele, G. and Palangio, P., 1998. Tectonomagnetic field observations in central Italy 1989-1995. Physics of the Earth and Planetary Interiors **105**, 145-152.

Milne, J., 1980. Earthquakes in connection with electric and magnetic phenomena. Transactions of the Seismological Society of Japan **15**, 135-163.

Miroshnishenko, M. and Kuksenko, V., 1980. Emission of electromagnetic pulses during nucleation of cracks in solid insulators. Soviet Physics-Solid State **22**, 895-896.

Misra, A., 1975. Electromagnetic effects at metallic fracture. Nature **254**, 133-134.

Misra, A., 1977. Theoretical study of the fracture-induced magnetic effect in ferromagnetic materials. Physics Letters A **62**, 234-236.

Misra, A. and Gosh, S., 1980. Electromagnetic radiation characteristics during fatigue crack propagation and failure. Applied Physics **23**,387-390.

Misra, A. and Kumar, A., 2004. Some basics of electromagnetic radiation during crack propagation in metals. International Journal of Fracture **127**, 387-401.

Mizutani, H., Ishido, T., Yokohura, T. and Ohnishi, S., 1976. Electrokinetic Phenomena associated with earthquakes. Geophysical Research Letters **3**, 365-368.

Mognaschi, E. R., 2002. On the possible origin, propagation and detectability of electromagnetic precursors of earthquakes. Atti Ticinensi di Scienze della Terra **43**, 111-118.

Molchanov, O. A., Hayakawa, M. Oudoh, T. and Kawai, E., 1998. Precursory effects in the subionospheric VLF signals for the Kobe earthquake. Physics of the Earth and Planetary Interiors **105**, 239-248.

Molchanov, O., Fedorov, E., Schekotov, A., Gordeev, E., Chebrov, V., Surkov, V., Rozhnoi, A., Andreevsky, S., Indin, D., Yunga, S., Lutikov, A., Hayakawa, M., Biagi, P. F., 2004. Lithosphere-athmosphere-ionosphere coupling as governing mechanism for preseismic short-term events in athmosphere and ionosphere. Natural Hazards and Earth System Sciences **4**, 757-767.

Molotskii, M. I., 1980. Dislocation mechanism for the Misra Effect. Soviet Technical Physics Letters **6**, 22-23.

Morgounov, V. A. and Malzev, S. A., 2007. A multiple fracture model of pre-seismic electromagnetic phenomena. Tectonophysics **431**, 61-72.

Morgounov, V. and Zdorov, A., 2007. Electromagnetic emission precursors of landslides and earthquakes. Geophysical Research Abstracts **9**, 01357.

Mori, Y. and Obata, Y., 2008. Electromagnetic emission and AE Kaiser effect for estimating rock in-situ stress. Report of the Research Institute of Industrial Technology, Nihon University **93**, 1-16.

Mueller, R. J. and Johnston, M. J. S., 1998. Review of magnetic field monitoring near active faults and volcanic calderas in California: 1974-1995. Physics of the Earth and Planetary Interiors **105**, 131-144.

Muller, O. H. and Polard, D. D., 1977. The stress state near Spanish Peaks, Colorado, determined from dike pattern. Pure and Applied Geophysics **115**, 69-86.

Muto, J., Nagahama, H., Miura, T. and Arakawa, I., 2005. Electric discharge plasma from frictional natural quartz: one origin of seismo-electromagnetic radiation. Proceedings of the International Workshop on Seismology and Electromagnetics 2005, 269-272.

Muto, J., Nagahama, H., Miura, T. and Arakawa, I., 2007. Frictional discharge at fault asperities: Origin of fractal seismo-electromagnetic radiation. Tectonophysics **431**, 113-122.

Nagamato, H., Fukushima, T., Ida, Y., Matsudo, Y. and Hayakawa, M., 2008. Disturbances in VHF/UHF telemetry links as a possible effect of the 2003 Hokkaido Tokachi-oki earthquake. Natural Hazards and Earth System Sciences **8**, 812-817.

Nagel, U., Ritzkowski, S. and Schunke, E., 1981. Geologisches und orohydrographisches Blockbild der Umgebung von Dransfeld (b. Göttingen). Schriften der Wirtschaftswissenschaftlichen Gesellschaft zum Studium Niedersachsens e.V., 79 pp.

Nardi, A., Caputo, M., De Natale, G. and Scarascia Mugnozza, G., 2003. Evidence for electromagnetic emissions during rock loading and fracture: a way towards earthquake forecast. GNGTS-Atti del 22° Convegno Nazionale / 06.22.

Nekrasov, A. K.; Shalimov, S. L.; Shukla, P. K. and Stenflo, L., 1995. Nonlinear disturbances in the ionosphere due to acoustic gravity waves. Journal of Athmospheric and Terrestrial Physics **57**, 732-742.

Nikiforova, N. N.; Yudakhin, F. N. and Toktospiev, A. M., 1989. Studies of electromagnetic emissions of seismotectonic origin in the Kirghiz S.S.R. Physics of the Planetary Interiors **57**, 68-75.

Nironen, M., 1997. The Svecofennian Orogen: a tectonic model. Precambrian Research **86**, 21-44.

Nitsan, V., 1977. Electromagnetic emission accompanying fracture of quartz-bearing rocks. Geophysical Research Letters **4**, 333-336.

Nolte, N., 2006: Geochemische Charackterisierung granitoider Gesteine der Västervik-Region (SE-Schweden). Unpublished diploma thesis, University of Göttingen.

Obermeyer, H., 2001. Handbuch zur Anwendung der NPEMFE-Methode mittels des Cereskops. Ceres GmbH, Staffort, 32 pp.

Obermeyer, H., 2005. Measurement of natural pulsed electromagnetic radiation (EMR) with the Cerescope. Ceres GmbH, Staffort.

O´Keefe, S. O. and Thiel, D. V., 1995. A mechanism for the production of electromagnetic radiation during fracture of brittle materials. Physics of the Earth and Planetary Interiors **89**, 127-135.

Ogawa, T. and Utada, H., 2000. Electromagnetic signals related to incidence of a teleseismic body wave into a subsurface piezoelectric body. Earth Planets Space **52**, 253-260.

Ogawa, T., Oike, K. and Miura, T., 1985. Electromagnetic radiation from rocks. Journal of Geophysical Research **90**, 6245-6249.

Parkhomenko, E. S., 1959. The symmetry of piezoelectric textures of quartz containing rocks. Bulletin of the Academy of Sciences of the USSR - Geophysical Series, 536-540.

Parkhomenko, E. S., 1971. Electrification Phenomena in Rocks. Plenum Press, New York, 314 pp.

Parks, G. A., 1965. The isoelectric point of solid oxides, solid hydroxides, and aqueous hydroxo complex system. Chemical Reviewies **65**, 177-198.

Parrot, M., 1994. Statistical study of ELF/VLF emissions recorded by low altitude satellite during seismic event. Journal of Geophysical Research **99**, 339-347.

Perelman, M. and Khatishvili, N., 1981. Radiowave radiation during brittle fracture of dielectrics. Doklady Akademii Nauk **256**, 824-826.

Pertsev, N. N. and Shalimov, S. L., 1996. Excitation of athmospheric gravitiy waves in a seismically active region and their ionospheric effect. Geomagnetism and Aeronomy **36**, 111-118.

Petrenko, V. F., 1993. On the nature of electrical polarization of materials caused by cracks – Application to ice electromagnetic emission. Philosophical Magazine B **67**, 301-315.

Pollard D. D. and Aydin, A., 1988. Progress in understanding jointing over the past century. Geological Society of American Bulletin **100**, 1181-1204.

Popov, L. N., Krakovetzkiy, Y. U., Gokhberg, M. B. and Pilipenko, V. A., 1989. Terrogenic effects in the ionosphere: a review. Physics of the Earth and Planetary Interior **57**, 115-128.

Price, N. J., 1966. Fault and Joint Development in Brittle and Semi-brittle Rocks. Oxford University Press, Oxford, 176 pp.

Rabinovitch, A., Bahat, D. and Frid, V., 2002. Similarity and dissimilarity of electromagnetic radiation from carbonate rocks under compression, drilling and blasting. International Journal of Rock Mechanics and Mining Sciences **39**, 125-129.

Rabinovitch, A., Frid., V. and Bahat, D., 1998. Parameterization of electromagnetic radiation pulses obtained by triaxial fracture of granite samples. Philosophical Magazine Letters **77**, 289-293.

Rabinovitch, A., Frid, V. and Bahat, D., 1999. A note on the amplitude-frequency relation of electromagnetic radiation pulses induced by material failure. Philosophical Magazine Letters **79**, 195-200.

Rabinovitch, A., Frid, V. and Bahat, D., 2007. Surface oscillations – a possible source of fracture induced electromagnetic radiation. Tectonophysics **431**, 15-21.

Rabinovitch, A., Frid, V., Bahat, D. and Goldbaum, J., 2000. Fracture area calculation from electromagnetic radiation and its use in chalk failure analysis. International Journal of Rock Mechanics and Mining Sciences **37**, 1149-1154.

Rabinovitch, A., Frid., V., Goldbaum, J., and Bahat, D., 2003. Polarization-depolarization process in glass during percussion drilling. Philosophical Magazine **83**, 2929-2940.

Ragg, S., Grasso, M., and Müller, B., 1999. Patterns of tectonic stress in Sicily from borehole breakout observations and finite element modelling. Tectonics **18**, 669-685.

Red´kin, V., Kuprijanov, A. S. and Bufalov, V. V., 1985. Geophysical devices for distance rock burst control. In: V. Smirnov (Ed.), Geophysical Methods of Stress and Deformation Control. Novosibirsk, 81-82.

Reuther, C. and Moser, E., 2009. Orientation and nature of active crustal stresses determined by electromagnetic measurements in the Patagonian segment of the South America Plate. International Journal of Earth Science **98**, 585-599.

Reuther, C., Obermeyer, H., Reicherter, K., Reiss, S., Kaiser, A., Buchmann, T., Adam, J., Lohrmann, J., and Grasso, M., 2002. Neotektonik und aktive Krustenspannung in Südost-Sizilien und ihre Beziehung zur regionalen Tektonik im Zentralen Mittelmeer. Mitteilungen Geologisches Paläontologisches Institut, Universität Hamburg **86**, 1-24.

Rikitake, T., 1968. Geomagnetism and earthquake prediction. Tectonophysics **6**, 59-68.

Rozhnoi, A., Solovieva, M., Molchanov, O., Biagi, P., F. and Hayakawa, M., 2007. Obsevation evidence of atmospheric Gravity Waves induced by seismic activity from analysis of subionospheric LF signal spectra. Natural Hazards and Earth System Sciences **7**, 625-628.

Ruedrich, J. and Vollbrecht, A., 2006. Geowissenschaftliche Bedeutung von Mikrorissen in Kristallingestein. In: Philipp, S., Leiss, B., Vollbrecht, A., Tanner, D. and Gudmundsson (Eds.), 11. Symposium „Tektonik, Struktur- und Kristallingeologie", 185-187, Universitätsdrucke Göttingen.

SKB-report, 2002. Simpevarp-site descriptive model version 0. Swedish Nuclear Fuel and Waste Management Company, SKB-R-02-35. Stockholm, Sweden.

Scitovich, V. P. and Lazarevich, L. M., 1985. Estimation of stress condition of rock massive by EMR. In: V. Smirnov (Ed.), Geophysical methods of Stress and Deformation Control. Novosibirsk, 65-66.

Scott, D. F., Williams, T. J. and Knoll, S. T., 2004. Investigation of Electromagnetic Emissions in a Deep Underground Mine. In: Peng, S. S., Mark, C., Finfinger, G., Tadolini, S., Khair, A. W. and Heasley, K. (Eds.), Proceedings of the 23rd International Conference on Ground Control in Mining, Morgantown, West Virginia, August 3-5, 2004, 125-132.

Sevgi, L., 2007. A Critical Review on Electromagnetic Precursors and Earthquake Prediction. Turkish Journal of Electrical Engineering and Computer Sciences **15**, 1-15.

SGU, 1994. Major Tectonic Units in the Bedrock of Sweden. SGU Ba 1994.

Shalimov, S. L., 1992. Lithosphere-ionosphere relationship: A new way to predict earthquakes? Episodes: Journal of International Geoscience **15**, 252-254.

Shalimov, S. L. and Gokhberg, M., 1998. Lithosphere-ionosphere coupling mechanism and its application to the earthquake in Iran on June 20, 1990. A review of ionospheric measurements and basic assumptions. Physics of the Earth and Planetary Interiors **105**, 211-218.

Shaw, D. J., 1978. Introduction to Colloid and Surface Chemistry. Butterworths, London, 236pp.

Shridar, S., Giannakopoulos, A. E., Suresh, S. and Ramamurty, U., 1999. Electrical response during indentation of piezoelectric materials: A new method for material characterization. Journal of Applied Physics **85**, 380-387.

Slifkin, L., 1993. Seismic electric signals from displacement of charged dislocations. Tectonophysics **224**, 149-152.

Slifkin, L., 1996. A dislocation model for seismic electric signals. In: Lighthill, J. (Ed.), A critical review of VAN: earthquake prediction from seismic electric signals. World Scientific, Singapore, 97-104.

Slunga, R., Norrman, P. and Glans, A. C., 1984. Seismicity of Southern Sweden. FOA Rapport C2 C 20543-T1.

Sobolev, G. A. and Demin, V. M., 1980. Mechanoelectrical phenomena in the earth. Moscow, NAUKA, in Russian with English abstract.

Sobolev, G. A., Demin, V. M., Narod, B. B. and Whaite, P., 1984. Tests of piezoelectric and pulsed-radio methods for quartz vein and base-metal sulfides prospecting at Giant Yellowknife Mine, N. W. T., and Sullivan Mine, Kimberley, Canada. Geophysics **49**, 2178-2185.

Somasundaran, P. and Kulkarni, R. D., 1973. A new streaming potential apparatus and study of temperature effects using it. Journal of Colloid and Interface Science **45**, 591-600.

Srilakshmi, B. and Misra, A., 2005. Secondary electromagnetic radiation during plastic deformation and crack propagation in uncoated and tin coated plain-carbon steel. Journal of Materials Science **40**, 6079-6086.

Stavrakas, I., Triantis, D., Agioutantis, Z., Maurigiannakis, S., Saltas, V., Vallianatos, F. and Clarke, M., 2004. Pressure stimulated currents in rocks and their correlation with mechanical properties. Natural Hazard and Earth System Sciences **4**, 563-567.

Stepanow, A., W., 1933. Über den Mechanismus der plastischen Deformation. Zeitschrift für Physik A Hadrons and Nuclei **81**, 560-564.

Stephansson, O., Ljunggren, C. and Jing, L., 1991. Stress measurements and tectonic implications for Fennoscandia. Tectonophysics **189**, 317-322.

Takahashi, T., 1983. Electric charge separation during ice deformation and fracture under a temperature gradient. Journal of Physical Chemistry **87**, 4122-4124.

Takeuchi, A., 2008. Positive Holes Flowing through Stressed Igneous Rocks. IEEJ Transactions of Fundamentals and Materials **128**, 307-310.

Takeuchi, A. and Nagahma, H., 2001. Voltage changes induced by stick-slip of granites. Geophysical Research Letters **28**, 3365-3368.

Takeuchi, A. and Nagahma, H., 2002. Interpretation of charging on fracture or frictional slip surface rocks. Physics of the Earth and Planetary Interiors **130**, 285-291.

Takeuchi, A. and Nagahma, H., 2006. Electric dipoles perpendicular to a stick-slip plane. Physics of the Earth and Planetary Interiors **155**, 208-218.

Takeuchi, A., Lau, B. W. S. and Freund, F. T., 2006. Current and surface potential induced by stress-activated positive holes in igneous rocks. Physics and Chemistry of the Earth **31**, 240-247.

Talwani, P. and Kovach, R. L., 1972. Geomagnetic observations and fault creep in California. Tectonophysics **14**, 245-256.

Tamatani, M., 2002. Contact electrification phenomena on phosphor particle surfaces. Journal of Luminescence **100**, 317-323.

Tanner, A. B., 1964. Radon migration in the ground: a review. In: Adams, J. A. S. and Lowder, W. M. (Eds.), The natural environment **I**, 161-190.

Tate, J. and Daily, W., 1989. Evidence of electro-seismic phenomena. Physics of the Earth and Planetary Interior **57**, 1-10.

Teisseyre, R., 1992. Earthquake premonitory processes: Evolution of stresses and electric current generation. Terra Nova **4**, 509-513.

Teisseyre, R. and Ernst, T., 2002. Electromagnetic radiation related to dislocation dynamics in a seismic preparation zone. Annals of Geophysics **45**, 393-398.

Teisseyre, R., Varotsos, P. A. and Rozluski, C., 2004. Electromagnetic excitation and seismicity in the natural time domain: simulations with theoretical model. Acta Geophysica Polonica **52**, 477-496.

Tirén, S. A. and Beckholmen, M., 1989. Block faulting in southeastern Sweden interpreted from digital terrain models. Geologiska Föreningens I Stockholm Förhandlingar **111**, 171-179.

Trigunait, A., Parrot, M., Pulinets, S. and Li, F., 2004. Variations of the ionospheric electron density during the Bhuj seismic event. Annales Geophysicae **22**, 4123-4131.

Tuck, G. J., Stacey, F. D. and Starkey, J., 1977. A search for piezoelectric effect in quartz-bearing rocks. Tectonophysics **39**, T7-T11.

Tzanis, A. and Gruszow, S., 1998. On the problem of identification and discrimination of electrical earthquake precursors. Physics and Chemistry of The Earth **23**, 939-944.

Tzanis, A. and Vallianatos, F., 2001. A critical review of Electric Earthquake Precursors.Annali di Geofisica **44**, 429-442.

Utada, H., 1993. On the physical background of the VAN earthquake prediction method. Tectonophysics **224**, 153-160.

Vogler, G., 1960. Ursachen emanomanetrischer Anomalien. Zeitschrift für Geophysik **26**, 57-71.

Vollbrecht, A. and Leiss, B., 2008: Complex fabric development in Palaeoproterozoic meta-quartzites oft he Västervik Basin, SE Sweden. Geologiska Föreningen I Stockholm Förhandlingar **130**, 41-45.

Vollbrecht, A., Rust, S. and Weber, K., 1989. Mikrorißgenerationen in der KTB-Vorbohrung und im Umfeld. KTB-Report **89**, 111-119.

Vollbrecht, A., Stipp, M. and Olesen, N. Ø., 1999. Crystallographic orientation of microcracks in quartz and inferred deformation processes: a study on gneisses from the German Continental Deep Drilling Project (KTB). Tectonophysics **303**, 279-297.

Vollbrecht, A., Dürrast, H., Kraus, J. and Weber, K.. 1994. Paleostress directions deduced from microcrack fabrics in KTB core samples and granites from the surrounding field. Scientific Drilling **4**, 233-241.

Wahlgren, C. H., Ahl, M., Sandahl, K. A., Berglund, J., Petersson, J., Ekström, M., Persson, P. O., 2004. Oskarshamn site investigation. Bedrock mapping 2003 – Simpevarp subarea. Outcrop data, fracture data, modal and geochemical classification of rock types, bedrock map, radiometric dating. Swedish Nuclear Fuel and Waste Management Company. SKB-R-04-102. Stockholm, Sweden.

Warwick, J. W., Stoker, C. and Meyer, T. R., 1982. Radio emission associated with rock failure: possible application to the great Chilean earthquake of May 22, 1960. Journal of Geophysical Research **87**, 2851-2859.

Wedepohl, K. H., 1987. Kontinentaler Intraplatten-Vulkanismus am Beispiel der tertiären Basalte der Hessischen Senke. Fortschritte der Mineralogie **65**, 19-47.

Wellmer, F. W., 1971. An approximation method for evaluation of the third-rank piezoelectric tensor of the symmetry 3:2 and its application in petrofabric studies. Mathematical Geology **3**, 375-378.

Whiteworth, R. W., 1975. Charged dislocations in ionic crystals. Advances in Physics **24**, 203-204.

Wunderlich, H. G., 1968. Der Hohe Hagen – ein Basaltschlot im niedersächsischen Bruchschollengebirge. Der Aufschluß, Sonderheft **17**, 121-128.

Yamada, I., Masuda, K. and Mizutani, H., 1989. Electromagnetic emission associated with rock fracture. Physics of the Earth and Planetary Interiors **57**, 157-168.

Yoshida, S. and Ogawa, T., 2004. Electromagnetic emissions from dry and wet granite associated with acoustic emissions. Journal of Geophysical Research **109**, B09204, DOI: 10.1029/2004JB003092.

Zang, A., Lienert, M., Zinke, J. and Berckhemer, H., 1996. Residual strain, wave speed and crack analysis of crystalline cores from the the KTB-VB well. Tectonophysics **263**, 219-234.

Zlotnicki, J. and Bof, M., 1998. Volcanomagnetic signals associated with the quasi-continuous activity of the andesitic Merapi volcano, Indonesia: 1990-1995. Physics of the Earth and Planetary Interiors **105**, 119-130.

Zlotnicki, J. and Cornet, F. H., 1986. A Numerical Model of Earthquake-Induced Piezomagnetic Anomalies. Journal of Geophysical Research **91**, 709-718.

Websites

http://earth.google.de/

http://sidstation.lionelloudet.homedns.org/

http://worldwind.arc.nasa.gov/java/

8. Appendix 1: EMR data Västervik

No.	Latitude	Longitude	main EMR direction [°]	single pulses max. values [counts/100ms]	defining energy max. values [dimensionless]	time	date	amplification [dB]	discrimination	frequency range lower [kHz]	frequency range upper [kHz]
1	57,37814	16,30661	140	1958	1640	16:15	06.05.2008	113	28	30	40
2	57,38293	16,29085	130	1933	1221	16:45	06.05.2009	113	28	30	40
3	57,41059	16,26857	160	1847	1002	17:40	06.05.2009	113	28	30	40
4	57,39963	16,35090	140	1660	217	11:00	08.05.2008	113	28	30	40
5	57,42262	16,32066	130	1672	248	11:40	08.05.2008	113	28	30	40
6	57,41949	16,31623	140	1777	275	12:20	08.05.2008	113	28	30	40
7	57,41762	16,31225	115	2100	536	12:35	08.05.2008	113	28	30	40
8	57,41680	16,31314	130	1835	301	12:45	08.05.2008	113	28	30	40
9	57,41698	16,31641	120	1805	283	13:00	08.05.2008	113	28	30	40
10	57,41834	16,32269	145	1947	394	13:20	08.05.2008	113	28	30	40
11	57,41743	16,33823	120	2038	572	13:40	08.05.2008	113	28	30	40
12	57,37687	16,35475	110	1868	395	14:10	08.05.2008	113	28	30	40
13	57,37687	16,35475	125	1195	121	15:05	08.05.2008	113	28	30	40
14	57,37390	16,35029	70	2257	2528	15:30	08.05.2008	90	24	30	40
15	57,36858	16,34811	140	1990	352	15:50	08.05.2008	113	24	30	40
16	57,37662	16,34253	120	2037	339	16:05	08.05.2008	113	24	30	40
17	57,37671	16,33727	120	1930	279	16:20	08.05.2008	113	24	30	40
18	57,37381	16,33089	130	1863	253	16:30	08.05.2008	113	24	30	40
19	57,37658	16,31621	140	1943	295	16:50	08.05.2008	113	24	30	40
20	57,37655	16,31206	150	1951	334	17:00	08.05.2008	113	24	30	40
21	57,37824	16,30657	120	1868	235	17:15	08.05.2008	113	24	30	40
22	57,38387	16,28725	110	1968	360	17:35	08.05.2008	113	24	30	40
23	57,39396	16,27671	130	1808	239	17:55	08.05.2008	113	24	30	40
24	57,41073	16,26857	120	1842	253	18:15	08.05.2008	113	24	30	40
25	57,29777	16,34346	130	2004	370	15:35	09.05.2008	113	24	30	40
26	57,29819	16,34463	110	1992	307	10:45	09.05.2008	113	24	30	40
27	57,29810	16,34613	140	2176	731	10:50	09.05.2008	113	24	30	40
28	57,29818	16,34696	130	1960	326	11:10	09.05.2008	113	24	30	40
29	57,29708	16,35769	140	2071	527	11:45	09.05.2008	113	24	30	40
30	57,29797	16,35610	115	2113	523	12:15	09.05.2008	113	24	30	40
31	57,29584	16,37589	150	2032	460	12:45	09.05.2008	113	24	30	40
32	57,28776	16,38741	130	2051	480	13:45	09.05.2008	113	24	30	40
33	57,28277	16,38543	130	2027	356	14:35	09.05.2008	113	24	30	40
34	57,28719	16,38110	125	2041	400	14:45	09.05.2008	113	24	30	40
35	57,27652	16,34886	165	2136	279	15:40	09.05.2008	113	24	30	40
36	57,28148	16,34834	140	2150	439	16:00	09.05.2008	113	24	30	40
37	57,41891	16,27644	130	2042	387	16:55	09.05.2008	113	24	30	40
38	57,37545	16,35145	135	1881	259	17:30	09.05.2008	113	24	30	40
39	57,37445	16,35093	120	1835	249	17:35	09.05.2008	113	24	30	40
40	57,37357	16,35002	120	2073	547	17:45	09.05.2008	113	24	30	40
41	57,29655	16,36720	170	1175	102	14:25	19.05.2009	113	24	30	35
42	57,29985	16,33674	155	1869	283	16:15	19.05.2009	113	24	30	35
43	57,27468	16,35848	145	2015	313	17:00	19.05.2009	113	24	30	35
44	57,41805	16,33847	135	2008	313	09:55	20.05.2009	113	24	30	35
45	57,41805	16,33847	160	1880	344	13:00	20.05.2009	113	24	30	35
46	57,41642	16,16947	125	1890	303	13:30	20.05.2009	113	24	30	35
47	58,07620	16,31699	140	1809	263	10:30	21.05.2009	113	24	30	35
48	58,01639	16,28221	170	2026	646	11:10	21.05.2009	113	24	30	35
49	57,52152	16,45909	140	1761	243	12:00	21.05.2009	113	24	30	35
50	57,55078	16,20727	130	1845	235	12:45	21.05.2009	113	24	30	35
51	57,46022	16,30825	135	1742	226	13:15	21.05.2009	113	24	30	35
52	57,42853	16,06020	170	1942	494	13:50	22.05.2009	113	24	30	35
53	57,44165	16,05103	140	1881	283	14:15	22.05.2009	113	24	30	35
54	57,42143	16,41151	145	1876	278	15:30	22.05.2009	113	24	30	35

No.	Latitude	Longitude	main EMR direction [°]	single pulses max. values [counts/100ms]	defining energy max. values [dimensionless]	time	date	amplification [dB]	discrimination	frequency range lower [kHz]	upper [kHz]	profile
1	55,55031	14,1854	145	1662	785	18:38	27.04.2009	102	28	30	35	1
2	55,49675	14,01350	145	1581	1919	10:27	30.04.2009	102	24	30	35	1
3	55,51706	14,03871	140	1755	2279	13:33	30.04.2009	102	20	30	35	1
4	55,43851	13,56745	130	1659	2544	15:12	30.04.2009	102	24	30	35	1
5	55,36800	14,17705	140	1517	1637	16:35	30.04.2009	102	24	30	35	1
6	55,31461	13,17579	145	1483	1584	08:42	01.05.2009	102	24	30	35	1
7	55,33067	13,01827	135	613	382	09:04	01.05.2009	102	24	30	35	1
8	55,35992	12,31095	135	629	360	09:44	01.05.2009	102	24	30	35	1
9	55,20250	10,37350	130	2112	17199	10:20	01.05.2009	102	24	30	35	1
10	54,46867	11,29306	140	2012	4702	11:34	01.05.2009	102	24	30	35	1
11	54,26281	11,09848	150	2236	4298	13:20	01.05.2009	102	24	30	35	1
12	54,05559	10,45599	150	1919	2771	14:00	01.05.2009	102	24	30	35	1
13	53,43096	10,20137	155	2340	8090	14:48	01.05.2009	102	24	30	35	1
14	53,19955	10,02496	165	2339	6692	15:34	01.05.2009	102	24	30	35	1
15	52,56853	9,52564	30	2341	10081	16:34	01.05.2009	102	24	30	35	1
16	52,29276	9,49768	35	2341	6259	17:14	01.05.2009	102	24	30	35	1
17	53,06608	9,59056	180	2341	11483	08:15	18.05.2009	102	24	30	35	1
18	53,15210	10,05297	170	2341	8963	08:37	18.05.2009	102	24	30	35	1
19	52,44220	9,40470	165	2340	8095	20:30	23.05.2009	102	24	30	35	1
20	51,33230	9,57020	140	2294	2921	12:55	24.05.2009	102	24	30	35	1
21	52,11956	10,26678	25	2340	4576	08:19	16.06.2009	102	20	30	35	2
22	52,18450	10,37561	25	2341	4562	08:47	16.06.2009	102	20	30	35	2
23	52,14525	11,36246	30	2341	3915	10:00	16.06.2009	102	20	30	35	2
24	52,34009	11,56245	15	2335	3853	10:53	16.06.2009	102	20	30	35	2
25	52,46532	11,45108	60	3383	7441	11:29	16.06.2009	102	20	30	35	2
26	53,05319	11,54069	175	2323	4578	12:26	16.06.2009	102	20	30	35	2
27	53,08331	12,16635	170	2212	4440	13:14	16.06.2009	102	20	30	35	2
28	53,29721	12,22669	165	1942	2320	13:57	16.06.2009	102	20	30	35	2
29	54,01009	12,13293	155	1993	2906	15:11	16.06.2009	102	20	30	35	2
30	54,04672	12,51675	145	1510	1363	15:48	16.06.2009	102	20	30	35	2
31	54,34159	13,39564	5	2295	15664	20:34	16.06.2009	102	20	30	35	2
32	54,22564	13,38077	150	1737	1951	10:04	17.06.2009	102	20	30	35	3
33	54,21528	13,13046	150	1491	1171	10:58	17.06.2009	102	20	30	35	3
34	53,51370	13,20004	160	1626	1422	11:58	17.06.2009	102	20	30	35	3
35	53,13031	13,59434	160	2046	3522	13:18	17.06.2009	102	20	30	35	3
36	52,51237	13,40010	175	2206	17706	14:30	17.06.2009	102	20	30	35	3
37	52,30477	13,44856	10	1736	7676	15:12	17.06.2009	102	20	30	35	3
38	52,12495	13,36390	10	1789	1750	15:55	17.06.2009	102	20	30	35	3
39	51,50780	13,53336	15	2013	2150	16:34	17.06.2009	102	20	30	35	3
40	51,23291	13,44832	15	1909	1868	17:19	17.06.2009	102	20	30	35	3
41	51,01613	13,36622	170	1670	675	09:54	18.06.2009	102	20	30	35	4
42	51,11814	12,58044	20	1709	1354	10:37	18.06.2009	102	20	30	35	4
43	51,16652	12,29442	15	1581	1130	11:12	18.06.2009	102	20	30	35	4
44	51,20830	11,55377	15	1156	722	11:48	18.06.2009	102	20	30	35	4
45	51,26161	11,25590	40	2059	1569	12:18	18.06.2009	102	20	30	35	4
46	51,34715	10,30600	45	2338	25733	19:40	12.04.2008	96	36	30	45	4
	51,28788	7,4216	90	2113	1805	18:00	12.07.2009	102	24	45	50	
	51,24171	6,04026	120	2274	5890	19:40	12.07.2009	102	24	30	35	
	51,35264	8,38817	240	2341	8450	22:51	12.07.2009	102	24	30	50	
	51,36725	10,19822	135	2310	2470	14:12	13.06.2009	102	20	30	50	
	51,01783	10,1725	130	2348	9695	11:13	25.06.2008	102	28	30	40	
	51,45428	11,05106	25	2342	8034	10:40	13.04.2009	102	24	30	15	

No.	Latitude	Longitude	main EMR direction [°]	single pulses max. values [counts/100ms]	defining energy max. values [dimensionless]	time	date	amplification [dB]	discrimination	frequency range	
										lower [kHz]	upper [kHz]
2	28,5505	-13,461	130	1392	25	11:55	19.02.2009	120	20	40	45
3	28,5429	-13,4416	125	1592	34	12:50	19.02.2009	120	20	40	45
4	28,5814	-13,3925	130	1731	40	13:15	19.02.2009	120	20	40	45
5	29,0236	-13,3711	135	1617	32	14:00	19.02.2009	120	20	40	45
6	29,0758	-13,3555	125	1644	35	14:30	19.02.2009	120	20	40	45
7	29,0438	-13,2924	120	1713	41	15:20	19.02.2009	120	20	40	45
8	29,0716	-13,275	125	1671	31	15:50	19.02.2009	120	20	40	45
9	29,1226	-13,2523	125	1664	33	16:28	19.02.2009	120	20	40	45
10	28,5618	-13,495	125	1540	31	18:32	19.02.2009	120	20	40	45

11. Acknowledgements

Als erstes möchte ich mich bei meiner Referentin und meinem Korreferenten für ihre Unterstützung bedanken: bei Sharon Webb für die Übernahme des Referates, die technischen Unterstützung. Den größten Dank verdient jedoch Axel Vollbrecht für den Anstoß zur dieser Arbeit, die Motivation, die viele Zeit, die wir mit Diskussionen verbracht haben, und dafür, dass er mit seiner fachkundigen Hilfe und kritischen Fragen jederzeit zur Verfügung stand, auch in kulinarischen Dingen.

Weiterhin möchte ich den vielen Kollegen des Geowissenschaftlichen Zentrums danken, die immer bereit waren, mit mir über fachliche Dinge zu diskutieren. Ganz besonders hervorzuheben sind dabei Bernd Leiss, David Tanner, Jens Walter und Klaus Wemmer, die mich auf vielfältige Weise unterstützt haben und durch ihre fachliche Kompetenz einen wichtigen Beitrag zum Gelingen meiner Arbeit geleistet haben. Man kann sich keine besseren Kollegen wünschen als Euch!

Nicole Nolte danke ich dafür, dass Sie für mich bei fachlichen Dingen und beim Lösen von technischen Problemen so oft unterstützt hat. Für die Hilfe bei ArcGis-Problemen möchte ich mich bei Frithjof Bense, Stefan Löbens und Bianca Wagner bedanken. Außerdem möchte ich den vielen ehemaligen Diplomkartierern sowie bei Marian Schütz und Sebastian Rauch für die Zurverfügungstellung der Schweden-Daten bedanken.

Die Abteilung Mineralogie hat mir immer hilfreich zur Seite gestanden und mich fachlich sowie logistisch unterstützt. Besonders bedanken möchte ich mich deshalb bei Burkhard Schmidt, Roland Stalder und Ursula Köhler.

Außerdem gilt mein Dank an Bent Hansen und Werner Kreisel, sowie Brigitte Groneberg für ihre Unterstützung in schwierigen Zeiten.

Mein Dank geht an die vielen anderen Mitarbeiter, die immer bereit waren, mir mit Ihrem Fachwissen und ihrem Handwerklichen Geschick zu helfen. Das gilt besonders für Günter Tondock aus der Abteilung Strukturgeologie, Axel Dierschke aus der Abteilung für Isotopengeologie, Herr Schulz von der Metallwerkstatt und Friedrich Güthoff aus der Physikalischen Chemie.

Für ihre große Hilfe bei verwaltungstechnischen Dingen danke ich Gudrun Asic, Ines Ringel, Petra Wolfrath, Brigitte Hinz und Marie-France Hesse. Ganz besonders Marie-France Hesse hat einen großen Anteil daran, hat das ich diese Arbeit beenden konnte.

Nicht vergessen möchte ich auch meine Freunde, die mir während der Zeit in Göttingen jegliche erdenkliche Hilfe und den ein oder anderen Hektoliter Kaffee haben zukommen

lassen. Besonderer Dank geht also an Alexander Gehler, Malte Drobe, Wiebke Bäro, Mike Reich, Brigitte Dietrich, Nicole Nolte, Andreas Moser, Nadine Friese und Chris Schneeberg.

Bei Stefanie Heidrich, die mich während vieler Jahre während meines Studiums sehr unterstützte und immer eine große Hilfe war, bedanke ich mich.

Letztendlich möchte ich Steffi Burchardt für die Hilfe besonders während der Korrekturphase und für die Unterstützung bei der Geländearbeit danken.

Curriculum Vitae

Vor- und Zuname:	Michael Krumbholz
Geburtsdatum und –ort:	08.07.1974 in Quedlinburg
Nationalität:	deutsch
Familienstand:	ledig

Ausbildung

01/2010	Promotion mit dem Thema „Electromagnetic radiation as a tool to determine actual crustal stresses – applications and limitations", Universität Göttingen
04/2006	Diplom Geowissenschaften, Universität Göttingen Diplomarbeit: „Volcano-tectonic evolution of the Geitafell Volcano, Southeast Iceland" Diplomkartierung: „Report of the structural geology map of the Eastern Monte Freddone area, Alpi Apuane, Northern Apennine, Italy at the scale of 1:5000"
07/2004	Bachelor of Science Geowissenschaften, Universität Göttingen Bachelorarbeit: „Dyke emplacement in Tenerife (Canary Islands): Field studies and numerical models"
10/1999 – 04/2006	Studium der Geowissenschaften an der Georg August Universität Göttingen
06/1993	Abitur am staatlichen Gymnasium Thale, Thale

_____   _____
Ort, Datum   Unterschrift